Universidade do Minho
Escola de Engenharia

Vipin Richhariya

Design and Development of Multi-Functional Surfaces to Control Frictional Behaviour in the Presence of Ice

January 2025

Design and Development of Multi-Functional Surfaces to Control Frictional Behaviour in the Presence of Ice

Vipin Richhariya

UMinho | 2025

REPÚBLICA PORTUGUESA
fct Fundação para a Ciência e a Tecnologia
NORTE2020
PORTUGAL 2020
UNIÃO EUROPEIA
Fundos Europeus Estruturais e de Investimento



Universidade do Minho
Escola de Engenharia

Vipin Richhariya

Design and Development of Multi-Functional Surfaces to Control Frictional Behaviour in the Presence of Ice

Doctoral Thesis

Doctoral Programme in Mechanical Engineering

Research carried out under the supervision of

Professor Filipe Samuel Silva

Professor Óscar Carvalho

Professor Ashis Tripathy

January 2025

DIREITOS DE AUTOR E CONDIÇÕES DE UTILIZAÇÃO DO TRABALHO POR TERCEIROS

Este é um trabalho académico que pode ser utilizado por terceiros desde que respeitadas as regras e boas práticas internacionalmente aceites, no que concerne aos direitos de autor e direitos conexos.

Assim, o presente trabalho pode ser utilizado nos termos previstos na licença abaixo indicada.

Caso o utilizador necessite de permissão para poder fazer um uso do trabalho em condições não previstas no licenciamento indicado, deverá contactar o autor, através do RepositóriUM da Universidade do Minho.

Licença concedida aos utilizadores deste trabalho



Atribuição-NãoComercial-SemDerivações

CC BY-NC-ND

https://creativecommons.org/licenses/by-nc-nd/4.0/

University of Minho, 22/01/2025

Signature: _____

DEDICATIONS & ACKNOWLEDGMENTS

I would like to start by thanking Professor Filipe for his unwavering confidence in me, believing that I could deliver what had never been attempted here before. His conviction in the idea, motivating nature, and wits made it possible for me to seek his advice and favours and the man never uttered the word "no" to me. Next, I want to acknowledge Professor Óscar, the guy with myriad ideas and a fine sense of engineering, with whom I learnt the concepts to kick start my experimentations that would have taken me long to understand on my own. Then, there's Professor Ashis, one directional man and that's hard work and commitment. I learnt from him to aim for excellence and never settle for mediocrity, despite uncertainties.

There are few in one's life that we can truly call dear friends, nevertheless, list is immense. Usha (dear friend and because of whom I am here), Bruno and Hélder (whom I consider close to brothers), and Francisca (the most unjealous person I have ever met), easy to talk Narayan, and my besties Mayank, Deepak, Rakesh, and Rajnish without whom no journey would be worthwhile. This journey would have been very hard if not impossible without the support of the Gören family, who did for me what only family would do. I also thank all my colleagues who made me feel at home, especially friends like João, Nuno, and Daniel who helped me at the time of need.

There is another Filipe, beside Prof. Filipe, to whom I owe many of my ideas and successes in achieving goals I once thought unattainable. Filipe's support, both as a friend and as a human being, in my personal and professional life, is unparalleled and beyond words. I also want to thank Eng. Sergio, Flavio Junior, and Prof. Gomes for their help in obtaining and optimising results. My gratitude extends to Prof. Dusan for his motivation for support to start my publication career. Lastly, I would like to thank Prof. Zille, Sónia, Marta, Edith, Madam Sandra, Maria Luísa for their help and availability whenever needed.

I have no words to show my gratitude towards my dearest family to whom I can literally lay down my life and dreams especially my parents and handsome nephews, Sarthak and Tejas, who never had any ideas other than that I am doing a PhD and except Tejas asking, "Did you finish that 200-300 pages thing that will end your PhD". I cannot thank enough, Sara as she panics for me, struggles for me, adores me, and always wishes only the best for me.

I dedicate this chapter of my life to all the friends and foes who believed in me or doubted me, for making me realise that it was all worth it. In the end, I dedicate this to the wrinkles on the faces of my parents' faces that got deeper while I was attempting this to work out here for six plus years, and to the one without whose sacrifices, this would still be just a dream. I dedicate this to *"HER"*.

I thank FCT (UI/BD/150939/2021) for providing me financial freedom and support to keep up the work and livelihood.

"The only thing that never finishes is the one that never starts"

STATEMENT OF INTEGRITY

I hereby declare having conducted this academic work with integrity. I confirm that I have not used plagiarism or any form of undue use of information or falsification of results along the process leading to its elaboration.

I further declare that I have fully acknowledged the Code of Ethical Conduct of the University of Minho.

University of Minho, 22/01/2025

_____

Vipin Richhariya

RESUMO

Projeto e Desenvolvimento de Superfícies Multi-Funcionais para Controlo do Comportamento à Fricção na Presença de Gelo

Escorregamentos e quedas (SFs, Slips and Falls) em superfícies de gelo escorregadias, durante o inverno, causam mais de 350000 mortes, num total de 20 milhões de lesões que necessitam de cuidados médicos a nível mundial. Os custos com cuidados de saúde, seguros e cuidados intensivos são preocupantes, ultrapassando os 100 mil milhões de dólares globalmente, sem contar com a perda de profissionais qualificados na indústria, amputação de membros, traumas e perda de vidas humanas. Uma camada de água com espessura nanométrica sobre o gelo, conhecida como Camada Quase Líquida (QLL, Quasi Liquid Layer), que resulta do derretimento superficial provocado pela pressão e atrito, é a principal causa dessas lesões. A maioria das lesões por SFs poderia ser evitada através do uso de solas antiderrapantes eficazes. As soluções antiderrapantes atualmente disponíveis focam-se na hidrofobicidade do material da sola para repelir água, ou no desenho de ranhuras para remover a QLL. Soluções mais avançadas baseiam-se em dispositivos antiderrapantes, como pitões, crampons e correntes, que empregam fibras de carbono ou outros materiais antiderrapantes, com o objetivo de aumentar o atrito em gelo escorregadio. No entanto, solas hidrofóbicas e avançadas falham na resposta à constante regeneração da QLL causada pelo contacto entre a sola e o gelo e pelo derretimento da superfície, levando à perda de eficácia ao longo do tempo. Para além disso, estes dispositivos antiderrapantes não são adequados para uso em ambientes interiores, nem para indivíduos de todas as idades, especialmente aqueles com mobilidade reduzida.

A ideia desta tese surgiu da observação da aderência capilar das patas antiderrapantes de rãs e geckos. Elas captam e usam a QLL para formar pontes capilares, ao absorver e congelar rapidamente a água em microcanais, criando um bloqueio mecânico. A tese introduz a fabricação de uma Superfície Multifuncional (MFS, Multi-Functional Surface) hidrofílica, através da modificação físico-química de borracha de silicone, reforçada com nanopartículas de zircónia/titânia e microtexturização a laser, permitindo alcançar uma ultrarrápida absorção e congelamento da QLL em microcavidades. O estudo avalia o efeito de concentrações altas e baixas de nanopartículas de zircónia nas propriedades de molhabilidade e nos coeficientes de atrito estático e dinâmico. Adicionalmente, a titânia é introduzida na criação de uma MFS hidrofílica devido às suas propriedades antibacterianas e hidrofílicas superiores. A zircónia e a titânia são comparadas com base nas suas propriedades mecânicas, químicas e hidrofílicas, bem como no seu desempenho friccional em gelo molhado.

Esta ideia abre caminho para o desenvolvimento de *designs* biomiméticos combinados com modificações de materiais, com o objetivo de criar uma MFS capaz de controlar o comportamento do atrito, culminando na preservação de vidas e dos seus meios de subsistência.

Palavras-chave: Biomimética; Capilaridade; Atrito; Hidrofílico; Texturização de Superfície a Laser (LST); Camada Quase-Líquida (QLL); Escorregamento e Queda (SF); Nanocompósito de Zircónia/Titânia.

ABSTRACT

Design and Development of Multi-Functional Surfaces to Control Frictional Behaviour in the Presence of Ice

Slips and falls (SFs) on slippery ice during winters claim more than 350,000 lives out of 20 million worldwide injuries requiring medical attention. The expenses in healthcare, insurance, and intensive care are staggering, far exceeding $100 billion globally excluding the loss of skilled individuals for industries, permanent loss of limbs, trauma, and lives. A nanometre-thick layer of water on ice called as the Quasi-Liquid Layer (QLL) is the primary cause of these injuries resulting from surface melting (due to pressure and friction). Most SF injuries can be prevented with an effective anti-slipping shoe sole. Current anti-slipping solutions focus either on the hydrophobicity of the sole material to repel water or on tread designs to drive out interfacial QLL. More advanced solutions take inspiration from anti-slipping devices like cleats, crampons, and chains, introducing carbon fibres or other slip-resistant materials to increase friction on slippery ice. However, hydrophobic and advanced soles fail to address the constantly regenerating QLL caused by sole-to-ice contact and surface melting, losing effectiveness over time. Anti-slipping devices, meanwhile, are unsuitable for indoor use and for individuals of all ages, especially the physically challenged.

The idea of this thesis has budded from observing the capillary adhesion in the slip-resistant footpads of frogs and geckos. It harnesses the QLL to form capillary bridges by quickly absorbing and freezing water inside micro-channels providing mechanical interlocking. Thesis introduces the fabrication of a hydrophilic Multi-Functional Surface (MFS) through the physicochemical tailoring of silicone rubber reinforced with zirconia/titania nanoparticles and laser surface micro-texturing, to achieve ultrafast imbibition and freezing of QLL in micro-cavities. The study assesses the effects of high and low zirconia nanoparticle loadings on wettability and the static and dynamic coefficients of friction. Additionally, titania is introduced to create a superhydrophilic MFS due to its superior antibacterial and hydrophilic properties. Zirconia and titania are compared for their mechanical, chemical, and hydrophilic properties, alongside their frictional performance on wet ice.

This idea paves the way for biomimicking designs coupled with material modifications to develop an MFS that controls frictional behaviour, ultimately saving lives and livelihoods.

Keywords: Biomimic; Capillary; Friction; Hydrophilic; Laser Surface Texturing (LST); Quasi Liquid Layer (QLL); Slip and Fall (SF); Zirconia/Titania Nanocomposite.

CONTENTS

Dedications & Acknowledgments iii

Resumo v

Abstract vi

Contents vii

List of abbreviations and symbols x

List of figures xiii

List of tables xxi

Chapter 1 Introduction 1

1.1. Background 2

1.1.1. Context of slip and fall on ice and snow 3

1.1.2. What causes slips and falls on ice 4

1.2. Limitations of superhydrophobic surfaces and adhesion as a solution 6

1.3. Motivation behind the study 8

1.4. History of biomimicking 11

1.5. Objective of the thesis 13

1.6. Structure of the thesis 13

Chapter 2 Literature Review 2

2.1. Emergence and determination of slippery layer on ice 3

2.2. Adhesion and friction 6

2.3. Elements affecting adhesion and friction on ice 9

2.3.1. Temperature 10

2.3.2. Surface area of contact and roughness 11

2.3.3. Sliding speed and normal load 14

2.3.4. Wettability 16

2.4. Existing shoe-sole solutions for anti-slipping 19

2.4.1. Anti-slipping devices 20

2.4.2. Tread design-based strategy 22
2.4.3. Materials-based strategy 25
Chapter 3 Materials and Experimental Section 32
3.1. Materials 33
3.1.1. Silicone Rubber 33
3.1.2. Zirconium oxide and titanium dioxide 33
3.2. Experimental section 34
3.2.1. Synthesis of zirconia/titania nanopowder reinforced silicone rubber 34
3.2.1.1. Preparing silicone rubber 35
3.2.1.2. Obtaining dehumidified nanopowder of zirconia and titania 36
3.2.1.3. Mechanical shear mixing 37
3.2.1.4. Final mixing of pre-mixed compound 38
3.2.2. Vulcanisation of nanoparticle-reinforced silicone rubber compound 38
3.2.3. Role of laser in optimisation and surface modification 40
3.2.3.1. Laser photolithography 40
3.2.3.2. Laser surface texturing 41
3.3. Advanced characterisation and friction tests 43
3.3.1. Morphological and dimensional, analyses of surface 44
3.3.2. Strength and elasticity analyses 44
3.3.3. Surface hardness 45
3.3.4. Fourier Transform Infrared Spectroscopy 45
3.3.5. Wettability and capillarity 46
3.3.6. Bacterial adhesion 47
3.3.7. Sliding friction test 48
Chapter 4 Results & Discussions 50
4.1. Morphology and topology 51
4.1.1. Surface morphology and roughness analyses 51
4.1.2. Topographical analysis 55
4.1.3. Dimensional analyses 57
4.2. Wear resistance and hardness 65

4.3. Strength and elasticity analyses 68
4.4. Advanced material characterisations 72
4.4.1. Chemical analyses through FTIR and EDS 73
4.4.2. X-Ray diffraction analysis 75
4.5. Anti-bacterial evaluation 77
4.6. Significance of water imbibition 79
4.6.1. Wettability 79
4.6.2. Capillarity 85
4.6.2.1. Diffusion theory 88
4.6.2.2. Dynamics of capillarity 88
4.7. Sliding friction test 92
4.7.1. Relevance of tribological test for friction on ice 92
4.7.2. Static and dynamic coefficient of friction 94
4.7.2.1. Static and dynamic coefficient of friction for higher zirconia loadings 94
4.7.2.2. Static and dynamic coefficient of friction for lower loadings 98
4.7.2.3. Significance of dynamic coefficient of friction 104
Chapter 5 Recommendations and perspectives on future works 107
5.1. Limitations and further optimisation of the work 108
5.2. Towards the extension of the work 108
5.3. Bridging nature with science and safety 110
5.4. Conclusions 111
Thesis based publications, conferences, and patents 114
References 115

LIST OF ABBREVIATIONS AND SYMBOLS

CA	Contact Angle
CF	Carbon Fibre
CNT	Carbon Nano Tubes
COF	Coefficient of Friction
DCOF	Static Coefficient of Friction
EDS	Energy Dispersive Spectroscopy
EVA	Ethylene Vinyl Acetate
FTIR	Fourier Transform Infrared Spectroscopy
GF	Glass Fibre
GNP	Graphene Nano Particles
LST	Laser Surface Texturing
MFS	Multi-Functional Surface
NBR	Natural Butadiene Rubber
NR	Natural Rubber
PBO	Poly-Phenylene-Benzobisoxazole
PDMS	Polydimethylsiloxane
PGQLL	Perpetually Generating Quasi Liquid Layer
PU	Polyurethane
PVC	Polyvinyl Chloride
QLL	Quasi Liquid Layer
SBR	Styrene Butadiene Rubber
SBS	Styrene Butadiene Styrene
SCOF	Static Coefficient of Friction
SEM	Scanning Electron Microscopy
SF	Slip and Fall
SHS	Super Hydrophobic Surface
Silica	Silicon dioxide
SPU	Special Polyurethane
SR	Silicone Rubber
Titania	Titanium dioxide (TiO_2)

TPE	Thermoplastic Elastomer
TPR	Thermoplastic Rubber
TPU	Thermoplastic Polyurethane
UTM	Universal Testing Machine
wt%	Percentage weight
XRD	X-Ray Diffraction
Zirconia	Zirconium oxide (ZrO_2)
ZnO	Zinc oxide
ρ_1, ρ_2	Density of ice and shoes-sole asperities, respectively
$\ddot{z}$	Acceleration in axial direction or in z - direction
$\dot{z}$ or v	Velocity in axial direction or in z - direction
μ_m	Reduced mass of atoms in bonds
β	Contact Angle
ν	Kinematic viscosity
ρ	Density of the fluid i.e., water
σ	Surface tension
μ	Coefficient of friction
τ_v	Shear stress
a	Radius or half of equivalent diameter or capillary radius
A	Spot area
A	Clausius-Clapeyron constant
b	Width of contact
D	Diffusion constant
D_{eq}	Equivalent diameter or characteristic length
E	Laser pulse energy
F	Laser fluence
F	Force constant of the bond
f	Vibrational frequency
g	Gravitational acceleration
h	Length of the diffusion path/capillary height
h_{sf}	Latent heat of melting
K	Thermal conductivity

l	Thickness of quasi liquid layer or water thickness layer
n	Number of contacts dur to uneven contact surface
N	Normal force
P	Average power
P_d	Power density
t	Time
T	Transmittance
t_μ	Time taken to develop fully developed flow
T_g	Glass Transition Temperature
u_r	Velocity profile
V	Speed of penetration of shoe-sole into ice or asperities
z	Capillary rise
I, I_0	Intensity, incidental intensity

LIST OF FIGURES

Chapter 1

Figure 1.1 – A schematic progression of midstance (complete foot contact) from (a) initial contact at the dry ice surface, (b) generation of QLL due to friction, and pressure melting at the contact of shoe-sole and ice, (c) initial slip over slippery QLL while moving forward that makes heel to slide, (d) further rotation of heel when slip becomes fall. 6

Figure 1.2 – Evolution of rolling effect: superhydrophobic shoe-sole surface in contact with PGQLL. The air which can be the mixture of entrapped atmospheric air and water vapour of the ice neither lets water enter the tread/micro-roughness nor drive out interfacial QLL without initial impact. However, PGQLL with entrapped air creates a gas-liquid (air-water) interface and produces rolling effect. (the foot-sole represents the shoe-sole surface) 8

Figure 1.3 – Concept behind the thesis work in which adaptation of capillary enhanced adhesion from frog and gecko toepads; (a) produced micro-cavities with micropillars accommodate at the shoe-sole, (b) micro-cavities will imbibe nanolayer of QLL and smaller amount help in quick filling-freezing resulting in mechanical interlocking, (c) peeling off results in deadhesion of the structures. 11

Figure 1.4 – Historical timeline of the major events in biomimicry and some recent development in the field of adhesion. 12

Chapter 2

Figure 2.1 – A pictorial depiction of different mechanisms of adhesion and the forces in play. These forces are also the major phenomena present in the natural world; (a) van der Waals, (b) capillary, (c) electrostatic or Coulomb, (d) mechanical interlocking, (e) suction or vacuum, (f) chemical or molecular, (g) diffusion, and (h) magnetic. 7

Figure 2.2 – A graphical representation of rubber polymers sliding on polished ice. Sliding speed is 0.1 mm/sec and normal load at 2.2 N [81]. 11

Figure 2.3 – A graphical representation of Stribeck curve depicting lubricating regimes and the effect of roughness for with the generation of quasi liquid layer [93]. 13

Figure 2.4 – Graphical representation of the effect of sliding velocity on coefficient of friction [102]. 15

Figure 2.5 – Progression of wettability states shown on textured surfaces resembling micro roughness. 17

Figure 2.6 – Commonly used anti-slipping devices used for ice/snow; (a) crampons, (b) chains, (c) studs, (d) spikes, (e) cleats. (nomenclatures are interchangeable depending on places and applications). 21
Figure 2.7 – Sequential gait cycle in a stroll over a surface; (a) initial contact (heel-strike), (b) loading (flatfoot), (c) midstance, (d) terminal stance, (e) pre-swing, (f) initial swing, (g) mid swing, and (h) terminal swing. Surface are of contact is represented by as [137]. (the foot sole represents the shoe-sole) 21
Figure 2.8 – Five tread designs (micro-embedded macro-treads) before and after the wear representing for; (a) Hexagonal-triangle (Brand – Keuka, Model - Galley 55014), (b) Star-shaped (Brand – SafeTstep , Model - Apollo 140060), (c) Square-square (Brand – Shoes for Crews, Model – Falcon 6007), (d) Rectangular-square (Brand – SR Max, Model – SRM 3500), (e) Hexagonal-trapezoidal (Brand – TredSafe, Model – M151044BU). Macro treads yield deep and wide tread channels which carry maximum amount of liquid, whereas micro treads construct shallow and narrow channels. Micro treads do not specifically serve to drain out liquid instead provide initial pressure on the ice/snow to attain most area of contact [158], [162]. 24
Figure 2.9 – Strategies to alter material of shoe-sole to exploit roughness, hardness compounding with fillers/reinforcements; (a) hybrid rubber patterned surface footwear outsole consisting smooth and rough rubber blocks to provide high SCOF and DCOF under wet and dry conditions both, and channels to help in dispersion of fluid from sole-floor interface, (b) SEM of composite of soft Poly-Phenylene-Benzobisoxazole (PBO) and protruding hard carbon fibres, protruded hard fibres, accommodated in shoe-sole, (c) SEM of rubber and glass fibre composite inserted at the heel of shoe-sole [176], [177], [178]. 29
Figure 2.10 – SEM of Propylene (PP) and rubber textured surfaces; (a) SEM of 2D Graphene Nano-platelets (GNP) and hexagonal Boron Nitride Nano-sheets (BNNS) before and after the abrasion on ice; (i) GNP before abrasion, (ii) GNP after abrasion, (iii) BNNS before abrasion, (iv) BNNS after abrasion, (b) (i) only micro-textured PP, (ii) hierarchical micro-micro textured PP, (iii) protected micro-micro hierarchical PP textures [179], [187]. 31

Chapter 3

Figure 3.1 – Schematic representation of compounding method to fabricate nanoparticle-reinforced SR composite; (a) initial mastication of high consistency silicone rubber to small crumbs in two roll-mill and finally into a thin strip, (b) preparation of zirconia or titania nanopowder to mix with silicone rubber prepared after initial mastication. Zirconia is available in micro-agglomerates and needs to

be binder removed followed by storage in vacuum vessel. Titania is already in nano form and just requires removing moisture contents before mixing, (c) mechanical shear mixing in mini extruder to initially blend nanopowder with silicone rubber to avoid material loss, (d) final mixing of silicone rubber with nanoparticles in two roll-mill..... 35
Figure 3.2 – An image of two roll-milling machine used for producing composite. Supplied by: Porfil – Mechanical Metalworking industry suppliers of machines for the jewellery industry from Pereira Gomes & Sons Lda, Portugal. 36
Figure 3.3 – An image of chamber muffle furnace (maximum temperature = 1380°C) used to deagglomerate zirconia micro-agglomerates to nanoparticles and dehumidify titania. Supplied by: Thermolab Fornos Electricos Lda, Portugal..... 37
Figure 3.4 – SEM micrographs showing morphology and relative size of the nanoparticles; (a) zirconia micro-agglomerates and magnified version of the nanoparticles, (b) titania nanopowder and magnified version of nanoparticles..... 38
Figure 3.5 – Vulcanisation set-up and mould; (a) hot co pression moulding machine for vulcanisation, (b) aluminium moulding plate in assembled position with punches at the top. 39
Figure 3.6 – A visual reference that resembles the concept of conical and cylindrical cavities formed using laser photolithography. 41
Figure 3.7 – Experimental set up of laser surface texturing for nanopowder-reinforced silicone rubber composite. 42
Figure 3.8 – LST of vulcanised composite; (a) laser machine setup, (b) cutting strategy i.e., parallel lines at 10 μm apart to attain desired cut (capillary cavity), (c) LST structures produced showing conical cavities. 42
Figure 3.9 – Schematic set up of UTM for elasticity tests; (a) silicone rubber composite, (b) silicone rubber composite in dog-bone shape, (c) fixture of the specimen in the UTM machine, (d) fractured silicone rubber composite specimen after reaching its ultimate tensile strength..... 45
Figure 3.10 – Schematic set up of a functional friction tribometer modified for the purpose of sliding test on ice. 49

Chapter 4

Figure 4.1 – SEM micrographs to show the geometry obtained for zirconia specimens for different weight percentages with optimum texturing geometry of 500×200; (a) 0wt% zirconia, (b) 1wt% zirconia, (c) 3wt% zirconia, (d) 5wt% zirconia, (e) 7wt% zirconia, (f) 9wt% zirconia. White circles show the location of nanoparticles visible from the images. 53

Figure 4.2 – SEM micrographs magnifying microfibrillar pillar surface of nanoparticle-reinforced composite of 0.3wt% 500×200; (a) morphology of zirconia-reinforced SR composite, (b) morphology of titania-reinforced SR composite. 53
Figure 4.3 – SEM micrographs for the textured hydrophilic SR composite with their successive operations (textured specimen before and after the ice adhesion friction tests; (a) top view of the textured microfibrillar structures (approximately remains similar for all loadings before friction tests), (b) representative top view of the textured microfibrillar structures after the ice friction test for 0wt% to 5wt% of zirconia and all lower loadings for both zirconia and titania, (c) condition of surface after sliding friction tests on ice for 7wt%, and (d) condition of surface after sliding friction test on ice for 9wt%..... 55
Figure 4.4 – Optical profilometer 3D images of the surface of composites; (a) 0wt% reinforcement vulcanised plain SR surface with average roughness of 0.09 μm and maximum roughness of 0.17 μm, (b) 0wt% reinforcement vulcanised textured SR surface with average roughness of 0.23 μm and maximum roughness of 0.40 μm, (c) 0.1wt% zirconia reinforced vulcanised textured SR composite surface with average roughness of 1.32 μm and maximum roughness of 1.5 μm, (d) 0.5wt% zirconia reinforced vulcanised textured SR composite surface with average roughness of 2.06 μm and maximum roughness of 2.45 μm, (e) 0.9wt% zirconia reinforced vulcanised textured SR composite surface with average roughness of 3.75 μm and maximum roughness of 4.86 μm, (f) 0.1wt% titania reinforced vulcanised textured SR composite surface with average roughness of 1.36 μm and maximum roughness of 1.48 μm, (g) 0.5wt% titania reinforced vulcanised textured SR composite surface with average roughness of 1.72 μm and maximum roughness of 1.92 μm, (h) 0.9wt% titania reinforced vulcanised textured SR composite surface with average roughness of 2.07 μm and maximum roughness of 2.23 μm. 56
Figure 4.5 – Variations of depth of the cut of cavities and volume of material removed obtained through LST for higher loadings of zirconia; (a) depth of cut/cavity, (b) material removal/unit width. 59
Figure 4.6 – SEM micrographs to show the geometry obtained for zirconia specimens for different weight percentages and textured dimension. Three textured dimensions 500×150, 500×200, 500×250 are shown with numbers (i), (ii), and (iii), respectively below the zirconia weight percentages; (a) 0.1wt% zirconia, (b) 0.3wt% zirconia, (c) 0.5wt% zirconia, (d) 0.7wt% zirconia, and (e) 0.9wt% zirconia..... 61

Figure 4.7 – SEM micrographs to show the geometry obtained for titania specimens for different weight percentages and textured dimension. Three textured dimensions 500×150, 500×200, 500×250 are shown with numbers (i), (ii), and (iii), respectively below the zirconia weight percentages; (a) 0.1wt% titania, (b) 0.3wt% titania, (c) 0.5wt% titania, (d) 0.7wt% titania, and (e) 0.9wt% titania. 61
Figure 4.8 – Variations of depth of the cut of cavities and volume of material removed obtained through LST for zirconia and titania; (a) material removal/unit width for zirconia weight percentages, (b) material removal/unit width for titania weight percentages, (c) depth of cut for zirconia loadings, (d) depth of cut for titania loadings. 64
Figure 4.9 – Variations of Shore A hardness measured through durometer for nanoparticle-reinforced untextured composites; (a) Shore A hardness for zirconia composite for 0%, 1%, 3%, 5%, 7%, and 9% weight percentages, (b) Shore A hardness for zirconia and titania composite for 0.1%, 0.3%, 0.5%, 0.7%, and 0.9%. 67
Figure 4.10 – Stress vs strain plots to obtain elasticity modulus via compression tests; (a) curves for 1wt% to 9wt% reinforced zirconia nanocomposites, (b) illustration to measure the slope of the curve by fitting a line segment at the linearity zone. 69
Figure 4.11 – Stress vs strain plots to obtain elasticity modulus via tensile tests; (a) curves for 0.1wt% to 0.9wt% reinforced zirconia nanocomposites, (b) curves for 0.1wt% to 0.9wt% reinforced titania nanocomposites. 70
Figure 4.12 – Individual stress vs strain curves obtained from tensile tests for; (a) zirconia-reinforced nanocomposites, (b) titania-reinforced nanocomposites. 72
Figure 4.13 – Chemical composition analyses to gather the presence of zirconia nanoparticles in SR under loading conditions; (a) FTIR plots of zirconia-reinforced nanocomposite for high amount zirconia loading, (b) EDS of zirconia-reinforced nanocomposite (c) EDS of titania-reinforced nanocomposite. 74
Figure 4.14 – Chemical composition analyses to gather the presence of nanoparticles in SR nanocomposites under different loading conditions for; (a) zirconia, (b) titania. 75
Figure 4.15 – X-Ray Diffraction spectrum plot of Intensity vs 2θ depicting Miller indices for crystallographic lattice structures for zirconia and titania. 77
Figure 4.16 – Graphical representation of the performance of nanoparticle-reinforced composites with and without laser texturing in terms of Colony Forming Unit/millilitre (CFU/mL); (a) zirconia

untextured and textured bacterial adhesion, (b) titania untextured and textured bacterial adhesion. The textured surface is with 500×200 configuration. 79
Figure 4.17 – Contact angle measurement using the sessile drop method with a goniometer and capillary suction tests for pure SR (plain and textured) and SR with five different weight percentages of zirconia nanoparticles for 500 μm × 200 μm samples; (a) water CAs for plain SR without any loading to comprehend the importance of physical structures, individually, (b) CAs measured and classified into different wettability states: Cassie-Baxter, Wenzel, Cassie impregnated, and superhydrophilic, (c) capillary suction experiments conducted against gravity. The specimens were glued with superglue on a flat surface with the textured side facing down. A pipette with water (resembling QLL) was then brought close to the surface until an appropriate distance was achieved to establish contact between the squeezed-out water and the textured surface. The droplet's behaviour upon contact—whether it wets, does not wet, or is completely suctioned was observed. Three frames, each approximately 0.5 milliseconds apart, were used to demonstrate the capillary effect. (All tests involving water and ice were conducted using normal tap water to simulate natural conditions, as natural molten ice typically contains impurities such as mineral salts, organic matter, dissolved gases, particulate matter, chemical pollutants, and biological contaminants)..... 84
Figure 4.18 – Contact angle measurement using the sessile drop method with a goniometer and capillary suction tests for zirconia and titania for five different weight percentages; (a) CAs measured and classified into with their numerical values, (b) capillary suction experiments conducted against gravity. The specimens were glued with superglue on a flat surface with the textured side facing down. A pipette with water (resembling QLL) was then brought close to the surface until an appropriate distance was achieved to establish contact between the squeezed-out water and the textured surface. The droplet's behaviour upon contact—whether it wets, does not wet, or is completely suctioned was observed. Three frames, each approximately 0.5 milliseconds apart, were used to demonstrate the capillary effect. (All tests involving water and ice were conducted using normal tap water to simulate natural conditions, as natural molten ice typically contains impurities such as mineral salts, organic matter, dissolved gases, particulate matter, chemical pollutants, and biological contaminants). 86
Figure 4.19 – Capillary regimes covered during the rise of water and the nature of their variations. The summation of all the regimes determines the time for suction of fluid in capillary tube of a micrometre to mm size..... 91

Figure 4.20 – Imagery of the concept; (a) the concept of anti-slipping using biomimicked enhanced adhesion during the process of movement illustrating heel strike, full contact, and peeling off or termination of contact. This shows the suction of QLL into the cavities at the start of contact, leading to full contact, and then the release of ice peaks during termination, (b) the manifestation of adapted concept in terms of micro-structures produced incorporating frog and gecko toepads' properties to perform capillarity followed by the representation of leftover pillars on wet ice. The colour was introduced to visualise the presence of micropillars of ice. Coloured images are the images taken after vertical impact of specimen on the QLL and then removing it vertically to see frozen pillars. 96

Figure 4.21 – Experimental results for sliding friction tests performed on higher zirconia loading (from plain SR, textured SR, and 1wt% to 9wt%) specimens; (a) COF curves obtained for the optimised zirconia-reinforced nanocomposites i.e., 500×200 LST, (b) SCOF for all specimens i.e., plain SR, plain textured SR, and reinforced textured specimens with 500×150, 500×200, and 500×250, (c) DCOF for all specimens i.e., plain SR, plain textured SR, and reinforced textured specimens with 500×150, 500×200, and 500×250. Sliding tests were performed at the speed of 5 mm/sec for 100 mm span. 97

Figure 4.22 – COF curves with their corresponding SCOF values created by averaging the values obtained from three specimens, with five tests conducted for each specimen obtained after averaging five repetitions of each for three specimens under similar experimental conditions at 0.05 Hz (5 mm/sec for 100 mm stroke length) 100

Figure 4.23 – COF curves with their corresponding SCOF values created by averaging the values obtained from three specimens, with five tests conducted for each specimen obtained after averaging five repetitions of each for three specimens under similar experimental conditions at 0.1 Hz (10 mm/sec for 100 mm stroke length). 103

Figure 4.24 – Graphical representation of overall obtained values for SCOF and DCOF for the visualisation of comparison (zirconia is on the left, titania is on the right); (a) SCOF for zirconia-reinforced nanocomposite at 0.05 Hz (5 mm/sec), (b) SCOF for titania-reinforced nanocomposite at 0.05 Hz (5 mm/sec), (c) DCOF for zirconia-reinforced nanocomposite at 0.05 Hz (5 mm/sec), (d) DCOF for titania-reinforced nanocomposite at 0.05 Hz (5 mm/sec), (e) SCOF for zirconia-reinforced nanocomposite at 0.1 Hz (10 mm/sec), (f) SCOF for titania-reinforced nanocomposite at 0.1 Hz (10 mm/sec), (g) DCOF for zirconia-reinforced nanocomposite at 0.1 Hz (10 mm/sec),

(h) DCOF for titania-reinforced nanocomposite at 0.1 Hz (10 mm/sec). Sliding tests were performed at the speed of 5 mm/sec and 10 mm/sec for 100 mm stroke length..... 106

Chapter 5

Figure 5.1 – Imagery of the concept employed in real application; (a) accommodation of softer nanocomposite micro-structures as an MFS to place on shoe-sole with tread channels, (b) hexagonal tread channels (mainly resembling frog toepad structures) designed on harder shoe-sole. The harder shoe-sole tread patterns cut in shoe-sole protect the softer MFS by keeping them few mm inside, (c) hexagonal tread channels, (d) triangular tread channels, (c) circular/cylindrical tread channels. Several tread channels can be implemented in the shoe-sole for appropriate drainage of access interfacial liquid. The produced palettes can also be accommodated inside the cavities of any kind of tread channels without changing the cylindrical shape of the produced specimens..... 109

LIST OF TABLES

Chapter 2

Table 2.1 – Different adhesion mechanisms, their presence around us, their nature. 8

Table 2.2 – Polymers, their ingredients, and deliverable properties for their selection. 25

Chapter 3

Table 3.1 – Standard characteristics of silicone rubber with working temperature range of –55°C to 200°C. 33

Table 3.2 – Standard physical and chemical properties of TZ-3YSB-E yttria stabilised zirconia nanopowder. 34

Table 3.3 – Standard physical and chemical properties of titania nanopowder (Titanium(IV), Oxide, Anatase). 34

Table 3.4 – Optimised preliminary and finalised laser process parameters for textures. 43

Table 3.5 – Number of specimens for each percentage of nanopowder and LST. 43

Chapter 4

Table 4.1 – Dimensions of pillars and cut/cavities for zirconia weight percentages (higher loadings). 58

Table 4.2 – Dimensions of pillars and cut/cavities for zirconia weight percentages (small loadings). 62

Table 4.3 – Dimensions of pillars and cut/cavities for titania weight percentages (lower loadings). 63

CHAPTER 1

INTRODUCTION

The following chapter aims to highlight the purpose and motivation behind this PhD project by encompassing the detailed background and context of the problem, elaborative objectives, followed by an outline on the structure of the thesis.

1.1. Background

"**Friction is Omnipresent**". Requirement for tailoring the friction as a phenomenon depends on its desirable effects whether safe and slip-resistant locomotion/walking require high friction, or lubricating parts of engine or water bodies that need low values to reduce fuel consumption and emissions. Surfaces as the first to contact their counterparts participate in frictional occurrence. Regardless of the smoothness of the surfaces, asperities (surface roughness) exist at micro/nano level, and they interlock, rupture, penetrate, and dislodge during the contact. The close contact between surfaces results in adhesion by virtue of van der Waals, electrostatic/coulomb, magnetic forces, or hydrogen bonds. These forces of adhesion behave like glue points and resist the sliding of surfaces effortlessly. Tailoring the surfaces to utilise the friction to our own advantage has been a constant human endeavour and different surface modification techniques have been adopted or adapted in past decades. Surface modifications ranging from coatings, surface texturing, chemical treatments, material deposition, and various other treatment processes trended for centuries. Implementing a single method to alter (enhance or reduce) the surface friction as per the requirements follows a cumbersome and arduous journey through the knowledge and deep understanding of surface chemistry, reactions, and behaviour at the atomic level. Hence, it is crucial not to change the favourable properties of the materials while obtaining desirable frictional surfaces.

Surfaces in contact with fluids, especially with water go through extraordinary changes physically, chemically, electrostatically, and biologically. All these changes lead to alter the friction at the water-surface interface. Physical changes such as surface roughness or erosion, and swelling can change friction depending on the material and environment. Water exposure leading to chemical changes like corrosion or oxidation tend to roughen the surface that increases friction, or the dissolution of protective coatings, which can expose more friction-prone materials. Variation in surface charges results in electrostatic effects affecting wettability. The surfaces requiring reduction in friction lead to the wettability aspect in the form of water repulsion to decrease the surface area of contact and direct exposure. Finally, biological factors such as biofouling, where micro like initial conditioning from bacterial adhesion followed by macro-organisms like algae or barnacles attach to the surface offering drastic increase in surface roughness and friction. Reduction or enhancement of friction is a highly subjective and often related to the place of application rather than its usual behaviour such as desirability of increment in friction on wet slippery surfaces e.g. winter vehicle tyres and footwear, airport runways, marine decks, surgical

grips etc. Friction on wet slippery surface relates to handling the interfacial water either by the attraction (hydrophilicity) or repulsion (hydrophobicity) to it. The dynamic changes, and combination of numerous variables together contribute to a complex nature of friction at water-contacting surfaces. This thesis deals with one such dynamic and complex problem that has been highly underestimated i.e. Slip and Fall (SF) on slippery ice. Seeing SFs as a surface occurrence and providing a good grip shoe-sole tailoring its friction with the help of a Multi-Functional Surface (MFS) can prevent these mishaps.

An MFS is a combination of properties into a single material/composite to serve multiple functions that are usually not inherent to the base material. These functionalities go deeper than basic properties of the principal material offering different intensities of water attraction or repellence, anti-bacterial, antimicrobial, electric conductivity, and self-cleaning. The desirability of the combinations of different functionalities is at its peak in recent decades and must serve the required effect. Creation of an MFS is a challenging task as they interact directly with the other surfaces and experience interfacial chemical, physical, biological, and other phenomena at the interaction. Therefore, an MFS must tolerate the interfacial stresses of all kinds and must keep its integrity at the same time. For almost a century, several approaches have been developed to generate MFSs for specific applications. These approaches vary from altering surface chemistry to physical structures, to topographical modifications, to most recently association of nanomaterials. The PhD work stimulates thought on the significance of SFs and explores a possible solution inspired by nature.

1.1.1. Context of slip and fall on ice and snow

The gravity of SFs in today's world needs attention and a more mindful perspective, hence, this thesis work is an effort to elaborate, emphasise, and provide a solution in a scientifically engineered approach. SFs are the second leading cause of occupational health injuries encompassing 29% of total injuries and ranks just after cardiovascular, respiratory, and road traffic accidents [1]. Additionally, SFs outweigh any other cause of non-fatal injuries and are the leading cause of musculoskeletal, spinal and back, hip and pelvic injuries, brain trauma, amputation, and permanent disability [2], [3]. Nearly half of these SFs occur on ice/snow because of accretion of ice/snow on the streets, pavements, and roads that pose severe threat during locomotion [4], [5]. SFs not only result in personal losses but also long term financial and economic losses at industrial, national, and international levels. Scandinavian and Nordic nations, UK, USA, Canada, Iceland, and any place where it snows, SFs occur inevitably. Centres for Disease Control and Prevention,

USA recorded approximately 17,000 fatal injuries occur in one million hospitalisations (every year) in the USA, because of SFs on ice and snow in winters. Health and Safety Executive, UK (HSE - UK)reports half a million SFs cases leading to the thousands of fatal injuries every year making it the leading cause of injuries [6]. SF on ice is a major issue in Canada as nearly 9000 people reportedly got hospitalised with life threatening accidents and thousands perished during 2016-17 according to the Canadian Institute for Health Information for severe injuries. Nearly 1,40,000 grave injuries in Finland and Sweden resulting in thousands of casualties and more than $3 billion capital loss on healthcare, loss of insurance [7], [8], [9], [10], [11]. The burden on the hospitals is about $50 billion in the USA only, apart from the additional billions on other healthcare and insurance firms [12], [13]. National Safety Council - USA archives more than $50 billion spendings on account of SFs [14]. HSE - UK states employers' loss of £500 million, about £42 million capital loss for employees only excluding the lost income without considering the expenses on health insurances, social securities, which compiles to billions [8], [9], [10], [11], [15]. The intensity with which SFs participates in losses can be comprehended by the statistics that show 83% of total accidents occurring only during winters in Russia [16]. Ageing world population, and vulnerability of elderlies and kids make SF more problematic as it results in losing skilled workers or employees for the firm, breadwinners of the family, job loss, livelihoods, and lives. Moreover, burden on insurance companies, social securities, healthcare, industries, economy, and career disruption impose hundreds of billions globally every year.

This work encompasses the surface modification methods to attain an MFS to tailor friction in the presence of ice. Produced MFS is a combination of physical and compositional modifications of Silicone Rubber (SR) polymer adapted from frog and gecko toepads. This study on ice can be extended to other applications and interfacial surfaces like wearable sensors, wound healing, and drug delivery. Anti-slipping shoe-soles also deal with different slipping scenarios mainly by the dint of fluidic substances on the walking surfaces like oils, grease, contaminations, and other fluids. Shoe-soles are the first point of contact with the slippery surface and command the speed of walking, intensity of slip, body balance, and vulnerability. An effective and efficient slip-resistant shoe-sole can prevent most of these slip accidents.

1.1.2. What causes slips and falls on ice

Snowfall during winters results in combination its dry and wet phases of ice. Generally, ice stays dry at sub-atmospheric temperatures (below −5°C or less) and approaches wetting close to melting point temperatures (above −5°C). Other factors such as salinity of water, impurities,

environmental temperature and humidity, and composition also participate in the changes of surface of ice/snow [17], [18], [19], [20], [21]. Dry ice is comparatively less slippery than wet ice but becomes wet due to the surface contact while ambling due friction, pressure, or surface melting. Wet ice indicates the presence of a nanometre thin layer of water popularly known as Quasi Liquid Layer (QLL) [22]. The QLL obstructs the contact between the hard solid ice and shoe-sole as it works as a lubricating medium that reduces the friction. The reduction in friction makes wet ice extremely slippery. Figure 1.1 depicts progression of the generation of a QLL during walk over ice (though formation of QLL starts as soon as sole touches the ice), where already presented liquid layer or simultaneous formation occurs based on the factors such as atmospheric temperature, sunlight, and conditions related to pedestrian footpaths. SF is an interactive occurrence between two solids and a liquid at the interface due to physical and chemical mechanisms of melting. Melting and liquification of icy surface is inevitable due to surface interaction, pressure, and friction caused by weight of an individual, temperature rise, wear, and speed of walking [23].

The surface contact (shoe-soles or vehicle tyres) produces heat energy that causes ice/snow to melt due to the absorption of heat energy that in turn participates in gaining enough kinetic energy by the molecules to overcome the hydrogen bonds holding them in a fixed crystalline structure. Water molecules are arranged in a hexagonal lattice in ice, where each molecule forms hydrogen bonds with its neighbouring molecules. These bonds are responsible to keep the water molecules in place creating the rigid, crystalline form of ice. The temperature rise by the added heat energy causes the water molecules to vibrate more vigorously. Eventually, the molecular vibrations become strong enough to break the hydrogen bonds. This transition from a structured solid to a more disordered liquid state occurs because the molecules start moving freely, though they still retain some of their hydrogen bonds in the liquid state, but in a much looser arrangement. Nevertheless, chemical structure remains intact throughout melting process [22], [24], [25], [26].

When a shoe-sole encounters an icy or snowy surface, it has to deal with the already existing or immediately formed QLL, repel/channel it, and create better contact for non-slip walking. However, this contact results in the formation of a Perpetually Generating Quasi Liquid Layer (PGQLL). PGQLL is when small amount of ice constantly melts after each interaction and after bulk melting due to molecular changes. The initial impact required to repel the QLL only happens at the first contact, and the subsequent impact is insufficient to handle PGQLL making any shoe-sole prone to SFs [27].

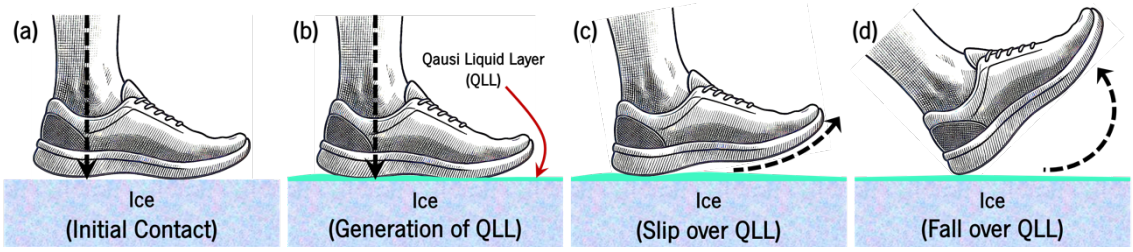


Figure 1.1 – A schematic progression of midstance (complete foot contact) from (a) initial contact at the dry ice surface, (b) generation of QLL due to friction, and pressure melting at the contact of shoe-sole and ice, (c) initial slip over slippery QLL while moving forward that makes heel to slide, (d) further rotation of heel when slip becomes fall.

1.2. Limitations of superhydrophobic surfaces and adhesion as a solution

The role of surfaces in natural world, performing specific tasks is an ancient and integral part of nature. The first point of contact between two entities always begins with their surfaces. Thus, this work focuses on enhancing and imparting specific properties to the shoe-sole surface for better interaction with ice or snow. The generation of a QLL on ice is inevitable and a winter shoe-sole must manage this melting liquid. Regardless of their adoption or adaptation methods, anti-slipping surfaces mostly followed the similar route of enhancing friction i.e. by repelling the interfacial water and increase solid-to-solid contact. No current winter anti-slip shoe-sole technology operates on surface adhesion, instead, they work on the development of hydrophobicity. Shoe-sole drives out the QLL driving out through the normal force applied by the wearer attempting to stick to the dry, solid part of the ice. Superhydrophobic materials or tread patterns (such as hexagonal, trigonal, square, or biomimicked designs) have shown some success in increasing friction. However, after extensive studies on hydrophobic surfaces used in anti-slip shoe soles, the drawbacks including their vulnerabilities and limitations must be emphasised [27].

Various physical and chemical methods are employed to achieve Superhydrophobic Surface (SHS) including chemical etching, solution immersion, laser electrodeposition, template deposition, spray coating, compression moulding, flow plating, spin coating, calcination, plasma treatment, and chemical vapor deposition. The degree of hydrophobicity, ranging from hydrophobic to superhydrophobic depends on the techniques used to create an SHS. The performance of an SHS is also influenced by surface characteristics such as oxidation level, chemical composition, thickness, and bulk properties. Chemical surface modification techniques exploit the polar nature of fluids like water to generate the repulsive force necessary for hydrophobicity. However, chemically modified SHSs can lose effectiveness over time, as they may develop an affinity for water or form weaker hydrogen bonds allowing exchange between the liquid and the surface.

Additionally, repeated contact between shoe-soles and ice can eventually wear down, erode, or alter the coatings. The primary advantage of SHS lies in its ability to avoid QLL not using it. Physical methods of creating hydrophobicity involve modifying the surface texture or morphology to induce irregularities or designs that generate a superhydrophobic effect. These surface textures trap air within cavities preventing water from filling them and causing repulsion. The presence of air in these cavities resulting hydrophobicity (evident from the high wettability angles), no matter how small, prevents liquid penetration forcing the water to be repelled [28].

Unlike chemical techniques, physical methods for altering surfaces to achieve SHSs are more durable and do not affect the bulk properties of the material. Chemical modifications sometimes can alter the overall properties of the material such as hardness, elasticity, wear resistance making them less suitable for certain applications. In contrast, physical surface alterations are less likely to compromise these core properties. The common belief that SHSs repel interfacial fluids (such as those at the interface of shoe-sole and ice) and enhance solid-to-solid contact is partially accurate. While solid-to-solid contact does increase friction reducing the likelihood of slipping, however, SHSs do not provide a long-term solution. SHSs produced for condenser coils, cryogenic cylinders, railway tracks, airplanes, power transmission cables, wind turbine blades, and roofs represent typical cases of ice accretion in a moist atmosphere. The accumulation of ice/snow on these surfaces is the evidence of the failure of SHSs, because of humidity, temperature, environment, and constant exposure to the moisture. These factors promote ice adhesion rather than repelling it. Contrary to these applications, where the surface remains stationary and ice accretion occurs, the interaction between a shoe-sole and ice operates in the opposite manner. Here, the shoe-sole moves across the ice, and while no accumulation takes place, the dynamics of the shoe-sole-to-ice interaction are influenced by various factors, such as age, weight, gait pattern, body biomechanics, walking speed, overall physical health, and QLL. As a result, human movement on icy or snowy surfaces becomes a complex kinetic situation with additional impact from the environmental conditions [29], [30], [31]. At the junction of SHS shoe-sole and QLL, a rolling effect takes place by virtue of air entrapment inside the hydrophobic sole. Figure 1.2 shows the scenario where trapped air does not drive out active PGQLL due to lack of impact [32]. Drawbacks of existing solutions are marred by the limitations of SHSs rather than using the freezing interfacial liquid to create adhesion.

The limitations of SHSs to deal with PGQLL and producing rolling effect leading to worsening of SF is a sign to use QLL rather than repelling it. QLL is inherent to icy surface and

constant repulsion of it poses a limitation on SHSs as shoe-soles. Moreover, wear of the shoe-sole structures causes the loss of hydrophobicity accompanied by temperature hardening and ice adhesion with time. The constant contact of shoe-sole and ice producing PGQLL needs more than a water repelling surface i.e. adhesion. Establishing the relationship between adhesion and friction is central to this work as existing solutions treat these phenomena as separate issues in the context of SFs on ice. Therefore, thesis introduces the idea of preventing SF accidents by changing the approach to modify winter anti-slipping shoe-soles. Instead of repelling, the surface structures of shoe-sole can have locations with comparatively softer hydrophilic micro-cavities that will produce capillary bridges by absorbing the QLL and immediately freezing it that to form mechanical interlocking (filling-freezing effect). Frog toepads maintain adhesion by forming capillary bridges with mucus, while gecko's soft spatulae generate adhesion through their unique structures. By adapting the material properties and structural features of these creatures, one can replicate their capillary adhesion mechanism to guide us toward an effective solution [33].

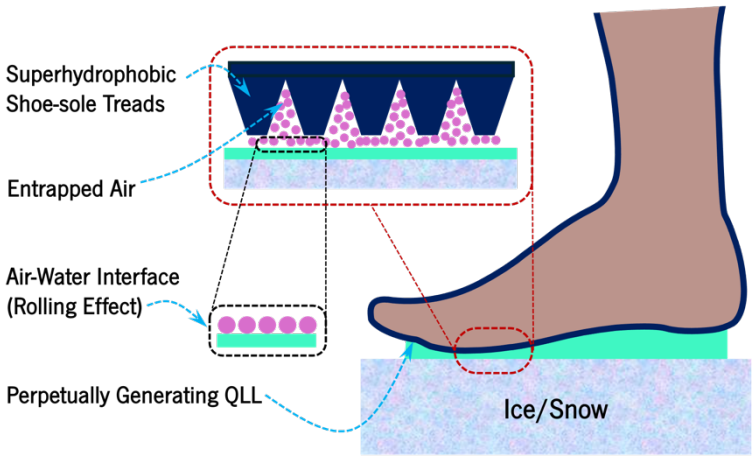


Figure 1.2 – Evolution of rolling effect: superhydrophobic shoe-sole surface in contact with PGQLL. The air which can be the mixture of entrapped atmospheric air and water vapour of the ice neither lets water enter the tread/micro-roughness nor drive out interfacial QLL without initial impact. However, PGQLL with entrapped air creates a gas-liquid (air-water) interface and produces rolling effect. (the foot-sole represents the shoe-sole surface)

1.3. Motivation behind the study

My profound belief in "**Whoever saves one life, saves the world entire**" serves as the driving force behind my pursuit of addressing what may seem like an ordinary problem, yet one that wreaks significant havoc in society i.e. SF accidents. These accidents are often underestimated and dismissed with laughter and mockery, but can inflict severe pain, physical injury, and emotional trauma on individuals. Despite the gravity of their impact such accidents are frequently

downplayed, which underscores the necessity of approaching this issue with both scientific rigour and a deep sense of responsibility. My motivation to pursue this research sprouts from a firm conviction that solutions to even the most complex problems are often found in the natural world. "**Nature always has a solution; if we look close enough**" has been an inspiring mantra guiding this work. Over the past two decades, SHSs gained much attention for their potential in anti-icing, anti-fouling, anti-bacterial, and anti-slipping applications. Yet, despite their promises, SHSs repeatedly struggled to provide effective solutions in dynamic environments particularly when it comes to locomotion over ice or snow.

Wetting is the force of nature and atmospheric wet content (humidity, precipitation) wets everything and anything about it. All the anti-icing surfaces eventually fail to perform in extreme conditions like aeroplane wings, condenser coils, cryogenic equipment, and several other places where ice can accrue. If we have atmosphere, we will have the source of life, water. Capillarity in plants give life to plants and direct absorption to creatures. If we cannot get rid of wetness, then we must thrive to use it like animal kingdom have been doing in their evolution of millions of years. The idea to explore this topic for my Ph.D. was sparked by the realisation to mimic toepads of torrent frog and gecko involving both their material properties and physical structure. There is already plethora of studies to explore shark's skin, lotus leaf, octopus suction cups, and geckos and frog toepads, however, produced surfaces can generally overlook that these natural surfaces replenish and replicate from time-to-time as they are alive. Self-cleaning and replenishing surfaces generally perform with chemical changes with physical tailoring. The adoption of biological designs, such as the hexagonal footpads of frogs or the spatulae-shaped footpads of gecko has shown promise in shoe-sole tread designs.

Learning from nature, we recognised capillarity formation of liquid bridges in moist or watery environments, is a common denominator among these creatures, all of whom thrive in humid or aquatic habitats. Torrent frogs use mucus in extremely wet environments, geckos utilise capillary suction to thrive in moist conditions, and octopus' soft suction cups create vacuum to stick underwater, all leveraging capillary bridges to create adhesion. Unlike artificial designs that rely on repelling liquids, these natural systems embrace hydrophilic surfaces to absorb moisture creating stronger adhesion through mechanical interlocking. By using capillary bridges to create a mechanical interlocking effect, a higher coefficient of friction can be achieved that is essential for anti-slip surfaces in icy conditions. My research explores a unique application of this idea taking

advantage of the freezing temperature of ice to freeze water in small quantities much like how a drop of water immediately freezes on near-dry ice.

While some current anti-slipping shoe-sole designs use materials like glass fibres mixed into the sole to pierce wet ice creating a temporary mechanical interlock like crampons or studs. These materials wear out quickly and become brittle in icy conditions. On the other hand, we focus on capillary tube-like structures inspired by the flexible, spatulae-like fibrillar pillars of geckos combined with the hydrophilic properties of frog toepads. The goal is to create an anti-slip surface that doesn't rely on temporary penetration but instead uses hydrophilic surfaces to draw in the QLL on ice enabling stronger and lasting mechanical interlocking. Adhesion by mechanical interlocking and deadhesion by peeling off are the key factors of the development. Figure 1.3 illustrates the fundamental concept of biomimicked microfibrillar textured pillars absorbing, creating mechanical interlocking followed by deadhesion during peeling off process. The thesis does not only cover the basis for anti-slipping applications but also present a bird eye view of hydrophilicity as a solution for winter gloves, medical facility anti-bacterial shoes, implants, drug delivery patches, and wearable sensor systems to deal with bodily exudations. Example of surfaces that need to absorb water and increase friction or enhance adhesion such as sports equipment (grips on rackets, handlebars, golf clubs, cue sticks, bats, gloves), footwear, brakes, food packaging, and medical devices. The surfaces by virtue of hydrophilicity increase friction through the absorption of sweat, water, and other interfacial fluids. An MFS can play a major role to attain desirable results, and this work explores the options by tailoring physical and chemical aspect of the surfaces keeping the bulk properties intact to this goal.

The mimicking is based on two facts; (i) adapting the mechanical properties of the frog and gecko footpads' like elasticity, hardness, and conformability but not exactly the dimensions of their footpad geometries (properties closer to frog toepads can be replicated with soft polymer rubber and can resemble high conformability) and (ii) the idea of capillary suction of humidity without any mucus or wetness like gecko that has ability to handle humidity and limited amount of moisture. The work proposes capillary rise purely as material plus structural feature to take care of limited amount of interfacial liquid and not necessarily flooded conditions. This liquid handling proved to be useful in case of limited amount of liquid of QLL without any prior existence of any kind of mucus, instead absorbing existing liquid only. Additionally, as ice can be dry and wet both it can also take advantage of van der Waals, capillary, and increasing surface area. Hence both the

creatures can lead to an appropriate shoe-sole material tailored to handle QLL with long lasting material properties [33], [34].

The PhD project focuses on adapting these biological principles to develop a hydrophilic rubber that is inherently hydrophobic further mimicking the desired effects of nature's most efficient adhesion systems. Through this Ph.D. work, we aim to contribute a solution to a problem that, though often unacknowledged, holds the potential to significantly reduce the incidence of life-altering injuries caused by SFs on ice and snow. By exploring the intersection of biology, materials science, and engineering, this research holds the promise of providing a more effective, long-lasting, and environmentally conscious solution to an age-old problem.

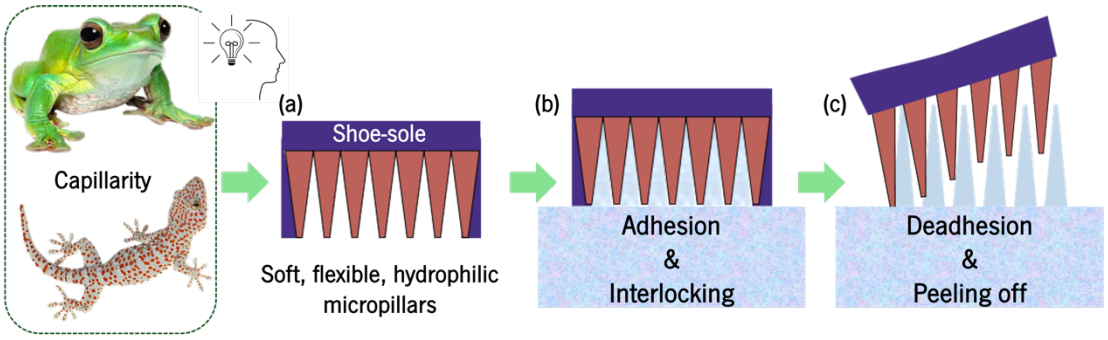


Figure 1.3 – Concept behind the thesis work in which adaptation of capillary enhanced adhesion from frog and gecko toepads; (a) produced micro-cavities with micropillars accommodate at the shoe-sole, (b) micro-cavities will imbibe nanolayer of QLL and smaller amount help in quick filling-freezing resulting in mechanical interlocking, (c) peeling off results in deadhesion of the structures.

1.4. History of biomimicking

Biomimicking has been a constant source of solutions to our day-to-day lives. Figure. 1.4. shows a history of more than five centuries where nature-inspired solution changed the course of the human history. Adhesion is one of the key elements and started taking roots with the Mestral's revolutionary Velcro or even before that when Niemiec's detailed octopus's suckers' adhesion in his PhD thesis [35]. Major breakthrough came in 1990 and 2002 when Smith and Kier presented elaborate adhesive and structural mechanisms of octopus suckers [36].

Another crucial feat was the study of kinematic features of polar bears to explore the anti-slipping on ice/snow. To achieve that, Pocock studied the feet and other external features of the polar bear families Canidae and Ursidae [37]. He discussed the ability of polar bears to walk on the ice under –40°C or below in 1914. Following Pocock's work, in 1998, Renous and his team illustrated a kinematic analysis of locomotion of the Ursus Maritimus family performed in

experimental and natural conditions [38]. Further down the time, a breakthrough came in 1991, when Hannah and Barnes performed detailed adhesion and deadhesion experiments for finding out the wet adhesion of tree frog. Whereas, in 2000, biologists Full and Autumn solved the mystery of gecko adhesion when they explored the phenomenon of van der Waals adhesion of gecko using setae-spatulae (micro-nano) arrangement [39], [40]. In the area of anti-slipping, gecko and frog footpad became the symbol of extraordinary interest as how small creature like gecko without any mucus secretion produce such a high amount of traction force or frog produce its friction drag in extremely flooded atmosphere.

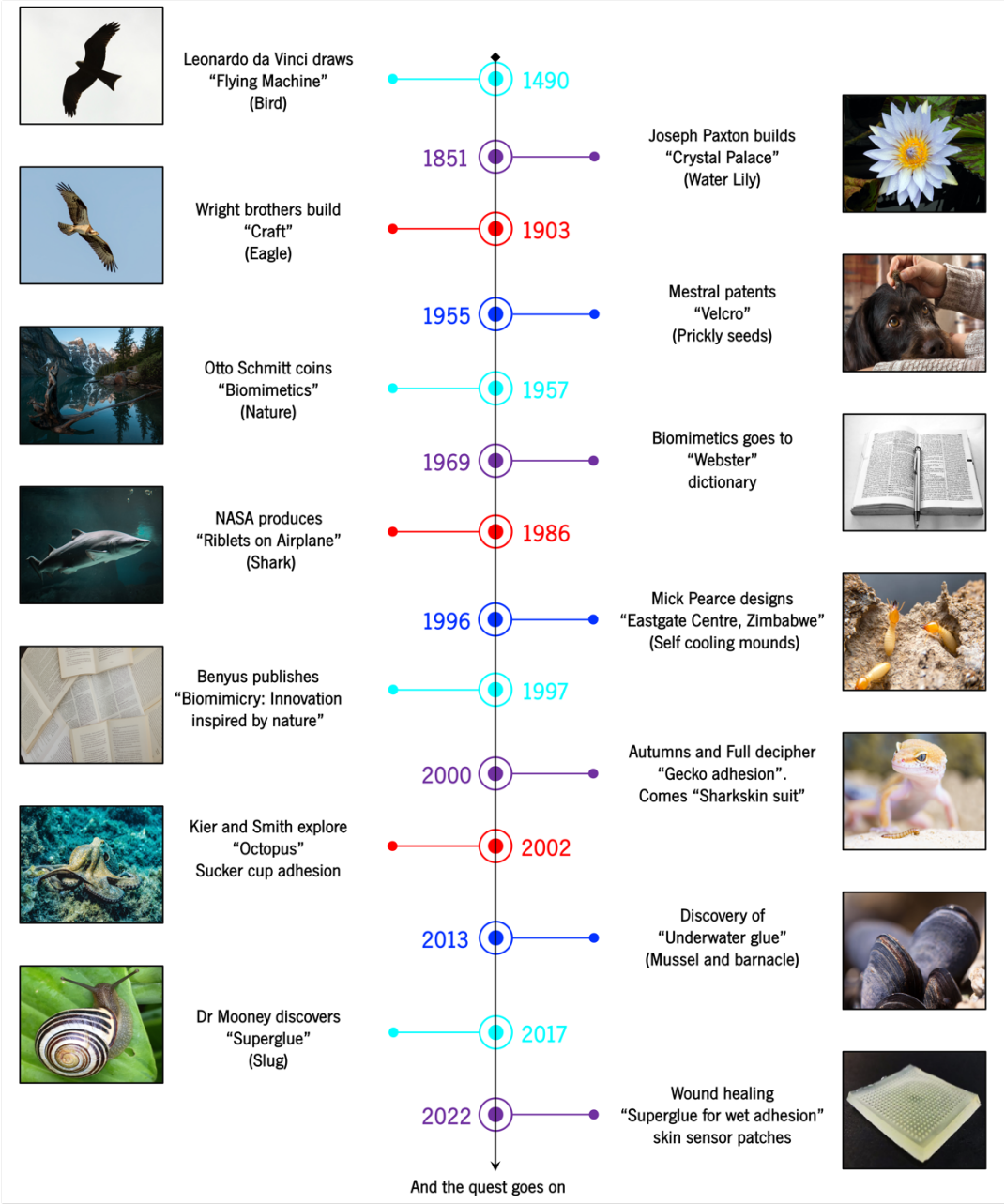


Figure 1.4 – Historical timeline of the major events in biomimicry and some recent development in the field of adhesion.

1.5. Objective of the thesis

The present thesis aims to develop an MFS for anti-slipping winter shoe-soles to enhance friction on wet icy surfaces. The specific objectives of this research are;

1. **Review existing solutions**: Conducting a comprehensive review of current anti-slipping shoe-sole materials, structures, designs, and their performance.
2. **Study of the nature-inspired solutions**: Analyse biomimetic and nature-inspired technologies available in the market for anti-slipping purposes.
3. **Establishing concept of hydrophilicity**: Formulation of the concept based on hydrophilicity and capillarity for improved friction in icy conditions.
4. **Material selection for fabrication**: Identifying suitable materials with necessary physical, mechanical, and chemical properties to produce composites with the desired qualities.
5. **Development of the nanocomposite**: Selection of zirconia (ZrO_2) and titania ((TiO_2)) based on their excellent hydrophilicity and bacterial resistant properties. Preliminary experiments will optimise nanoparticle contents to achieve efficient performance in addition to surface textures produced by laser.
6. **Synthesis of the nanocomposite**: Development of a methodology for the preparation of nanocomposites including material-powder amalgamation and vulcanisation into desired shapes and sizes of specimens.
7. **Laser Surface Texturing (LST)**: Optimisation of LST parameters to expose nanoparticles and achieve effective capillary suction. Evaluate different capillary cavity geometries for optimal water imbibition with a focus on conical shapes. Laser photolithography was used to decide the shape and dimensions of the capillary cavities before LST for synthesised material.
8. **Wettability and capillarity**: Elaborate analyses of wettability and capillary suction inside the fabricated microstructures of nanoparticle-reinforced polymer composite.
9. **Sliding friction tests and performance evaluation**: Performing friction tests on wet ice using a Peltier-based refrigerating tribometer to assess the effectiveness of the developed surface in improving grip on ice.

1.6. Structure of the thesis

The thesis is structured in a conventional way comprising five chapters. Each chapter is formulated based on their compilation and contents. The **first chapter** of the thesis is detailed collection of backgrounds of the problem discussed and the reasons behind it. It gives the glimpse and gravity of the situation and why is it important to address it. This chapter also underlines the

limitations of existing solutions Furthermore, the chapter ends with the motivation behind the task taken up and the objectives of the thesis.

The **second chapter** deals with comprehensive literature review on the existing developments in the field of the study involving materials and methods adopted to produce desired effect. The chapter covers the formation of the QLL, parameters affecting adhesion and friction. Furthermore, it divides the existing anti-slipping solutions in three categories i.e., anti-slipping devices, material-based, and design-based strategies.

The **third chapter** consists of materials and methodology used for fabrication. Here, material properties, process parameters, equipment used are discussed in detail. Additionally, the details about advanced characterisations' equipment and methods are compiled in this section.

Being the kernel point of the thesis; **fourth chapter** elaborates on results based on characterisation techniques. The results in this chapter are accompanied elaborate discussions on morphological, mechanical, physical, chemical, anti-bacterial, wettability, and frictional behaviour of the MFS produced.

The **fifth chapter** gives a glimpse of the future scopes and extension of the work with limitations of this study. Additionally, major findings are recorded in conclusions that were observed during the development of the nanocomposite to design the MFS.

CHAPTER 2

LITERATURE REVIEW

This section presents a comprehensive state-of-the-art discussion on various aspects of slips and falls on ice, encompassing the reasons behind the generation of quasi liquid layer, principles of ice adhesion and friction, and variables affecting. The chapter further develops a theme of adhesion mechanisms observed in nature and classifies existing anti-slipping shoe-sole solutions into three categories of anti-slipping devices, design-based, and material-based.

Ice as a naturally slippery surface owes its slipperiness primarily to the formation of the QLL that is unavoidable and inevitably forms on glossy icy or hard snowy surfaces. To effectively address and mitigate issue of SFs on ice, it is crucial to have a deep understanding of the complex nature of the icy surface and the mechanisms that govern its slipperiness. This includes examining the quantity of liquid water, thickness of the QLL, environmental, and physical factors that influence the formation and properties of this layer. The following literature review provides an in-depth exploration of the nature of ice drawing from extensive studies to offer insights into these factors. Additionally, a comprehensive discussion on adhesion forces and their relationship with slipping failures is also included liaising between surface adhesion, friction, and the dynamics of walking on ice. Adhesion forces especially on ice or wet surfaces vary with parameters like temperature, contact area, sliding speed, normal load, wettability, and roughness. These variables need a thorough understanding to comprehend nature of the interfacial phenomenon. There are numerous solutions acquired to prevent SFs on ice or common wet surfaces and these solutions can be summarised in three broad categories namely, anti-slipping devices, design-based solutions, and material-based solutions, therefore, all three categories are also analysed in detail.

2.1. Emergence and determination of slippery layer on ice

The role of interface in terms of fluids, gases, vacuum, or normal atmospheric conditions is invaluable for deciding which adhesion/bonding will prevail. Therefore, this work develops a deep understanding of the properties of natural surfaces in contact especially slip-resistant with focus on QLL and contacting surface before getting into the solution phase. Friction, pressure, and surface melting are the three broad classifications to realise physicochemical nature of the formation of QLL. Melting is a key aspect for the success ski/sled as these use a microlayer of water at their interface for successful skiing or sledging on the ice, contrary to winter shoe-soles that are designed to increase friction [27], [28]. The slippery layer is created by friction melting of ice by body weight with sufficient speed and pressure produced for better gliding. In dry conditions, ice provides better friction on the surface but given time and contact area characteristics, frictional heating occurs leading to surface melting implying the direct effect of the friction as heating and melting of surface [29], [30]. A group of physicists (1930) emphasized that the friction between ice and another material produces heat, which melts the ice's surface similar to how rubbing hands (abrasion) together warms us on a cold day [41]. Therefore, frictional heating is the dominant cause of ice/snow melting among pressure and surface melting. Normal load of an individual is not the only parameter deciding the intensity of friction melting but also the speed of locomotion,

surface contact area, interfacial temperature, and shoe-sole characteristics [28], [32], [34]. More melting means more quantity of water, that makes surface slipperier and shoe-sole requires dealing with more liquid, therefore, it is vital to obtain thickness of existing QLL.

Determination of the thickness of QLL through hydrodynamic frictional mechanism is a complex scenario because of the inaccessibility of the temperature increment of the interface. Hence, Couette's flow i.e., flow of fluid between two parallel plates, one stationary and another fixed (resembling QLL between flat shoe-sole and ice) proved useful to determine the thickness of the interfacial QLL. In the absence of actual temperature rise and its relation to generation of QLL, energy conservation yields satisfactory results [42]. It states that "the frictional energy generated must be equal to the energy conducted to the ice and to the shoe-sole from the contact surface plus energy for the melting of ice." The layer thickness (l) can be given by Equation 2.1.

$$l = \frac{1}{h_{sf}\rho}\left(\frac{\mu N}{nb} - \sqrt{\frac{L}{2u}}\left(\Delta T_1\sqrt{k_1 c_1 \rho_1} + \Delta T_2\sqrt{k_2 c_2 \rho_3}\right)\right) \qquad \text{Equation 2.1}$$

Where; l = Water layer thickness, n = Number of contacts (due to non-uniform contact), N = Normal force h_{sf} = Latent heat of melting, u = Velocity of the slider (slider moves on smooth ice), ρ_1 and ρ_2 = Density of ice and asperity of the shoe-sole, respectively, b = Width of the contact, L = Sliding distance and equals to the length of the contact, ρ = Density of liquid water, μ = Coefficient of Friction (COF) between the ice and contact surface, ΔT_1 and ΔT_2 = Difference between the contact surface temperature and ice, and contact surface and sole, respectively, k_1, c_1 and k_2, c_2 = Thermal conductivity and specific thermal capacity of ice and asperity, respectively. ΔT_1 (Ice) > ΔT_2 (Shoe-sole). Equation 2.1 can produce the QLL thickness for friction melting.

Unlike friction melting (shear driven, constant velocity, no pressure gradient), pressure melting is a function of normal load and actual contact area ($P=N/A_c$), however, calculating actual contact area is a tedious task due to shoe-sole asperities and patterns. Friction melting causes ice to melt by a relative rubbing, whereas, for pressure melting, normal load must be high enough to increase substantial temperature and melt the ice. Adrian Bejan pioneered contact melting laws on icy surface proposing mathematical determination of thickness of the QLL due to pressure melting. His experiments based on Poiseuille's flow (QLL between stationary shoe-sole and an ice block) considered only normal movement (no lateral movement like friction melting's Couette's model) for different surface geometries pressurised against ice. Both the models assume no-slip,

Newtonian, laminar, incompressible, and viscous flow [43], [44]. The thickness of QLL can be determined by Equation 2.2 based on pressure melting.

$$\frac{l}{b} = \left(\frac{24\eta k_2}{\rho h_{sf} A b^2}\right)^{1/4} (\xi - \xi^2)^{1/4} \qquad \text{Equation 2.2}$$

Where; l = Water layer thickness, b = Body width of contact, η = Viscosity of liquid water, k_2 = Thermal conductivity of liquid water, ρ = Density of liquid water, h_{sf} = Latent heating of melting, V= Speed of penetration of shoe-sole into ice (used to calculate applied force), A = Physical constant (Clausius-Clapeyron constant) = $\frac{-dP}{dT_m}$, and $\xi = \frac{x}{L}$, where, x = axial direction of L. Equation 2.2 is driven from the correlation of applied pressure, melting speed, and body width [45], [46], [47].

Pressure melting is closely connected to ice sintering, which occurs when ice is subjected to pressure. The pressure lowers its melting point and causes localised melting at points of contact between ice particles. Pressure-induced melting can facilitate the bonding of ice particles by generating small amounts of liquid water e.g., QLL at contact points that can further refreeze strengthening the bond as the pressure is relieved. This dynamic interaction plays a critical role in the frictional behaviour of ice at low sliding velocities, where the pressure from contact with surfaces as shoes-soles or tyres can lead to temporary melting, reducing friction and increasing the likelihood of slips. As the ice refreezes, it can also contribute to the healing of flaws in weak layers, further complicating the behaviour of ice under pressure and influencing its interaction with surfaces [20], [41], [48].

Another important aspect of QLL is surface melting that is a complex bulk phenomenon as ice can have a liquid layer even below the freezing temperatures. Water layer of about 200 Å was observed at all temperatures due to surface melting including triple point. A layer melts followed by another layer by bulk ice's molecular movement towards the surface to decrease the surface energy and also high vapour pressure that makes ice sublime quickly [49]. Surface ice melting is a molecular phenomenon, however, arguable whether chemical or physical [50]. Michael Faraday (1859) performed experiments deducted that dangling hexagonal structures of ice at the free surface contain less energy and melt without any friction. He also suggested that the presence of QLL on ice below freezing temperatures is majorly a chemical outcome [51].

2.2. Adhesion and friction

Adhesion refers to the molecular attraction between surfaces, which creates resistance to movement. This resistance, especially at microscopic contact points contributes to static friction that needs to be overcome to initiate motion. In dynamic situations, kinetic friction also benefits from adhesion though the forces are typically weaker than in static friction. Adhesion forces can vary from weak forces like van der Waals, electrostatic to strong forces such as mechanical interlocking, vacuum, capillary, magnetic, or diffusion. Using these adhesive forces every day is fundamental to the nature. Figure 2.1 depicts adhesion mechanisms and forces as their results, depicting two surfaces interacting with each other and creating weak or strong bonding depending on the nature of interface. Creatures walking on slippery surfaces use one or another of these forces and mostly the combinations for their anti-slipping locomotion. Friction and adhesion both are actual area dependent directional forces against external forces as adhesion representing normal force while friction representing tangential force. The Coefficient of Friction (COF) between the shoe sole and ice is generated primarily by the shearing effect caused by adhesion at the points of close contact, rather than solely by the frictional properties of the shoe-sole [19], [26], [52].

Water layer is used intelligently in the form of capillary adhesion where liquid rises inside cavities to carry supplements for plants and similarly for anti-slipping that creates mechanical interlocking, electrostatic, adsorption, and other adhesive forces that are inexistent in dry adhesion. Frank P. Bowden (1957) documented that solids with superior COFs commonly demonstrate stronger adhesive properties. Surfaces in nature largely depend on attaining higher adhesion with the help from creating large contact area during the application of normal force. This phenomenon occurs when a tree frog presses its toepads against a drenched tree branch, increasing the surface area of contact while forming mucus-based capillary bridges within the hexagonal patterns on its skin [53], [54]. A gecko exhibits a similar behaviour but with a different approach, where its toepads absorb small amounts of moisture and cover a phenomenally large surface area using millions of spatulae located at the ends of its setae [55], [56].

Adhesion forces like suction and mechanical interlocking are crucial in overcoming wet and slippery surfaces. Suction adhesion operates on pressure differences, where a cavity generates a low-pressure zone, and atmospheric pressure on the exterior creates a suction effect, as seen in octopi's suckers and clingfish. Recent studies reveal that octopus suction cups also possess fine hairs forming hierarchical structures that enhance adhesion by facilitating closed contact between their acetabulum and infundibulum during vacuum generation. In contrast, mechanical interlocking

relies on physical interactions between contact surfaces, often influenced by micro or macrostructures like surface roughness such as gecko spatulae, the claws of polar bears or arctic foxes, and the stiff, wire-like furs of seals penetrating icy surfaces, showcasing varied mechanisms of adhesion across nature.

Chemical adhesion involves molecular interactions, such as hydrogen and covalent bonds, which are the characteristic of certain adhering surfaces, like the mucus secreted by frogs, mussels, and spiders. On the other hand, magnetic adhesion relies on magnetic polarity to produce reversible adhesion whereas, diffusion adhesion occurs through capillary rise, where fluids diffuse into capillaries to create adhesion, as in the case of water striders. Nature effectively combines these adhesion mechanisms, rarely relying on just one. For instance, frogs utilise mucus for stickiness while their soft hexagonal toepads form capillary bridges and expel liquid to enhance solid-to-solid contact. Thus, bioinspired surfaces mimic nature by adapting and integrating multiple adhesion forces to suit specific applications. Table 2.1 is a detailed account of various adhesion mechanisms, principle behind them, and the creatures that effectively utilise these mechanisms to their advantage [36], [52], [53], [54], [56].

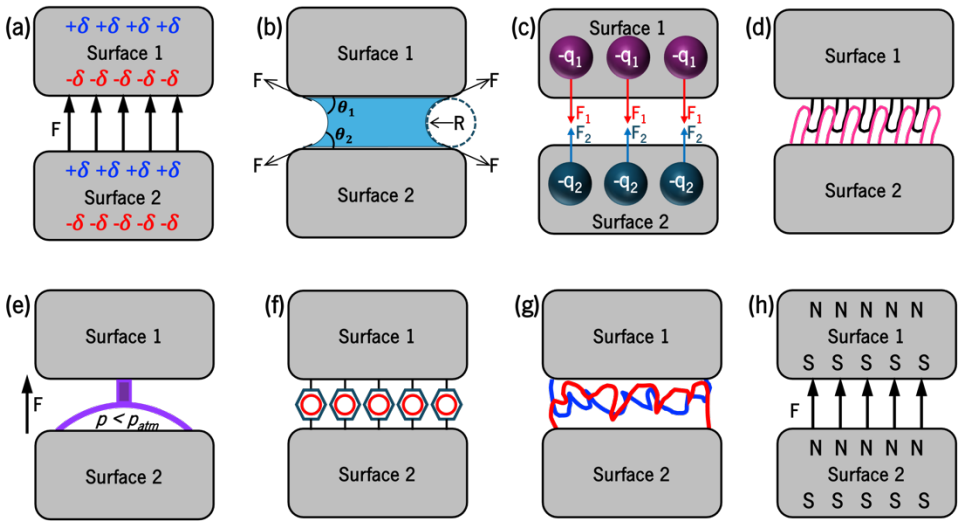


Figure 2.1 – A pictorial depiction of different mechanisms of adhesion and the forces in play. These forces are also the major phenomena present in the natural world; (a) van der Waals, (b) capillary, (c) electrostatic or Coulomb, (d) mechanical interlocking, (e) suction or vacuum, (f) chemical or molecular, (g) diffusion, and (h) magnetic.

Though the connection between adhesion and friction appears unidirectionally linear, nevertheless, is complex because of the nature of interface of shoe-sole and ice. Walking over ice means constant momentary adhesion-deadhesion in kinetic conditions where normal force results

in adhesion and peeling in detachment. In natural world, physical structure evolved far more than chemical and switchable reversible adhesion found in nature can provide us a solution.

Table 2.1 – Different adhesion mechanisms, their presence around us, their nature.

Adhesion mechanism	Present in	Phenomenon
(a) Van der Waals Force (Discovery - J. D. van der Waals, 1873) [34]	Gecko, Frog, arthropods.	-weak intermolecular force. -can be attractive or repulsive -depend on the instantaneous/temporary dipole induced interactions between adjacent apolar molecules. -independent of wettability. -can switch due to rapid changes in dipole. -general values are 0.2 nm.
(b) Capillary Force (Discovery – Francis Hawksbee, 1709) [57]	Gecko, Frog, paper towel in water, dock beetles, water strider, polar bear, seal.	-wet adhesion. -capillary bridges form between two surfaces in the presence of water. -pressure difference between the capillary bridge and the surroundings creates adhesion strength.
(c) Coulomb Force (Electrostatic Force) (Discovery – C. A. Coulomb, 1785) [58]	Seal skin fur, polar bear pad hairs, arctic fox pad hairs.	-electrostatic force between two charged bodies at rest. -can be attraction or repulsion depending on the charge of the particle. -a non-contact type force.
(d) Mechanical Interlocking and Friction Force (Discovery – G. Amonton, 1699) [59]	Snake, frog, dragonflies, beetles, polar ear, gecko, arctic fox.	-joining two bodies together with screws/rivets or welding -micro and nano scale interlocking due to surface roughness, perturbance, and asperities. -kinds; dry, wet/fluid, lubricated, skin, and internal friction.
(e) Suction (Vacuum) Force (Discovery – O. V. Guericke, 1654) [58]	Octopus, clingfish, leech, beetles, chitons.	-results from the pressure difference between inside and outside a cavity. -adhesion is independent of the surface orientation. -can take heavy loads. -more of a geometric phenomenon rather than a surface dependent phenomenon. -sealing is important to get suction.
(f) Chemical Force (Discovery – E. Frankland, 1852) [60]	Frog, beetles, sea anemones, centipedes.	-covalent, metallic, and ionic bonds. -electron sharing between the atoms is a covalent bond. -electrostatic attractive force between positive ions and conduction electrons is metallic force. -ionic bonds are the electrostatic attraction between oppositely charged ions, or between two electronegative atoms.
(g) Diffusion Force (Discovery – T. Graham, 1829) [61]	Perfume spread, food colouring, CO_2 diffusion from the soda to the air, breathing, etc.	-diffusion is the movement of atoms, ions, molecules to energy from higher to lower gradient. -slow process.

		-can cause permanent joining. -can increase peeling force up to 50-70%.
(h) Magnetic Force (Discovery – H. C. Oersted, 1820) [62]	Compass, MRI scanner, electrical motor, speaker, door catch.	-when electrically charged particles move -can be attraction or repulsion. -magnetically charged particles between two bodies. -magnetic polarity and strength decide the strength of magnetic force. -kinds; permanent (magnets) and electromagnets (electric induction).

2.3. Elements affecting adhesion and friction on ice

Ice as a surface poses significant challenges when it encounters a variety of materials such as shoe-soles, skates, skis, tires, concrete structures, heat exchanger tubes, aircraft wings, and other structures [63], [64], [65]. The complexity arises from the multi-layered and dynamic interaction between ice and these surfaces influenced by various factors [66]. These factors operate dynamically rather than in isolation influencing how surfaces behave on ice. Not only ice and surface characteristics but also physical, chemical, and thermal elements like the speed of movement, applied pressure, temperature, COF, and the duration of contact [67], [68], [69]. Moreover, environmental conditions such as ambient temperature and humidity can significantly affect the behaviour of the interface, particularly by affecting the formation of QLL on the ice. The COF plays a major role in capturing the complexities and improving adhesion-deadhesion to mitigate the SFs. Amontons' (1699) classical theory on law of friction states that frictional force, $F = \mu . N$, where μ is COF and N is normal applied load, does not hold true in case of ice as it assumes only Static Coefficient of Friction (SCOF) and no sliding speed. However, sliding speed will never be zero in case of walking on ice, hence, kinetic friction comes into the picture [70].

Moreover, the classical law of friction is independent of sliding speed, apparent area of contact, and temperature but do not necessary hold true for slippery ice/snow. Ice adhesion on entities like pavement blocks, concrete structures, condenser coils encounter SCOF and mainly vary with materials' surface properties, icy temperature influenced by surface and surroundings, atmospheric pressure, alloying, impurities, coatings, and surface roughness. Large number of research driven by hydrophobicity and ultra smooth surfaces (slipping of moisture and deadhesion of accrued ice) considered as favourable options throughout the century. But the nature of wettability around these entities still makes them vulnerable and ice eventually adheres to these surfaces. A variety of factors affecting the friction on ice are compiled here, especially in the context of SFs and their role in their prevention [58], [71], [72], [73].

2.3.1. Temperature

Not only temperature of the ice but also the freezing, ambient, and glass transition temperature (T_g) of the contacting material play a mutual role in ice adhesion and slipperiness. The combined effect of these factors alongside temperature derives the final complex ice adhesion mechanism. Studies show that ambient temperature has more significant influence on adhesion than freezing temperature. Ice adhesion strength improved substantially (69.31% for aluminium and 69.61% for stainless steel), when atmospheric temperature dropped from −5°C to −10°C keeping freezing temperature constant at −5°C. On the other hand, for the same drop in ambient temperature by keeping atmosphere at −5°C, the adhesion strength increment was 23.91% for aluminium and 22.24% for stainless steel [74], [75]. Being an amorphous layer, the molecules are in excitation state for QLL that further contribute to electrostatic adhesion of ice. At low freezing temperatures, these liquid-layer molecules become less excited making van der Waals adhesion forces stronger. Ice adhesion to metals is different than polymers because of the T_g. Polymers like rubber near their T_g exhibit higher internal friction due to their viscoelastic properties because they can still deform and dissipate energy while sliding resulting better frictional adhesion on ice. However, rubber hardens, stiffens like brittle glassy material and shrinks at very low temperatures that makes it unable to deform leads to slipping. Above T_g, the amount of melting of liquid layer and the speed of movement plays predominant roles [76], [77]. At supercooled temperatures (well below 0°C), the work of adhesion for ice increases. This is attributed to a rise in surface tension in turn decreasing the contact angle and surface tension of water on supercooled surfaces. Therefore, very low temperatures pose a severe limitation to the use of polymer because of their inherent natures and work of adhesion. For the ceramics, the effect follows entirely different route like in silicon carbide, glass, model ice skates, at low temperatures, COF follows Arrhenius-type equation indicating frictional behaviour that is governed by the thermally activated motion of surface ice molecules. Above −20°C, friction increases due to ploughing and deviates from Arrhenius behaviour. This happens when the ceramic slider plastically deforms the ice surface making it harder and leading to deeper penetration, which raises the friction coefficient as the slider moves through the ice [78].

Figure 2.2 shows sliding experiments done by A. D. Roberts to understand the adhesion phenomenon of polymers especially rubbers like silicone, nitrile butadiene, and isoprene. These tests were performed at low speeds and small normal loads to gather the information on COF that varies along the temperature scale. It was observed that as temperature approaches near to zero

and ice starts melting in bulk, COF for all the rubber polymers reaches to same small values. However, at start of the sliding test, silicone and isoprene exhibit extremely high COF marks and then sharply decrease near the melting point temperature of ice as supported by the other modern studies as well. On the other hand, nitrile rubber remains at low friction even at the −30°C dry ice then rises gradually nearing melting then gradually drops and meets the same end as other polymers. Very high friction at about −35°C is the function of softness and resilience of the material and the material that remains soft at these low temperatures like silicone and isoprene compared to nitrile [79], [80], [81].

Schallamach waves were present during peeling off for soft rubber sliding process, whereas for nitrile they were not present. Schallamach waves are surface waves that form on rubber at low sliding speeds and high friction conditions, when it slides against another surface like ice especially during stick-slip motion. As the rubber sticks and then slips, elastic energy is released in the form of waves that propagate in the opposite direction of the sliding. These waves help reduce friction by temporarily detaching parts of the rubber from the surface lowering the contact area [77], [82], [83].

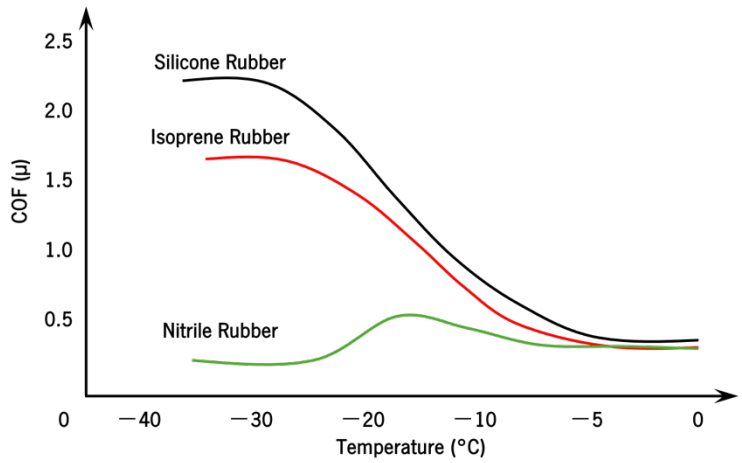


Figure 2.2 – A graphical representation of rubber polymers sliding on polished ice. Sliding speed is 0.1 mm/sec and normal load at 2.2 N [81].

2.3.2. Surface area of contact and roughness

Area of contact is a multidimensional situation when it comes to contacting ice/snow because it does not obey the classic law of friction that says COF is independent of area of contact. Contrary to that, contact area is important to determine the adhesion and friction on ice/snow. Number of studies on sliding objects (mainly metals or ski) established that the real area of contact is much smaller than apparent area of contact. Small surface areas have asperities closer to each

other than large surfaces and that melts more ice due to frictional heating resulting lower COF compared to large surfaces where asperities are scattered over more area [20]. A ski to smoothly slide over an ice at −20°C, considering tiny real contact area (due to roughness of the surface) of ski, pressure melting will not be enough to produce QLL. Frictional heating with COF of 0.05 can generate enough heat to melt ice at localised points with small real area of contact despite most of this heat is lost to surrounding snow through conduction. Unlike the skis where extra heat is supplied by frictional heating to melt the ice, adhesion/friction for anti-slip shoe-soles requires less frictional, pressure, and surface melting, however, the area of contact in these cases of foot sole is large and not scattered along a line like skis. Therefore, large surface roughness and concentrated contact area can generate enough friction melting accompanied by pressure and surface melting. Nevertheless, large surface areas of toepads of frogs and geckos with stimulated material characteristics of wettability offer large contact area to increase friction as well. High surface roughness does not surely create better adhesion by capillary bridges under wet condition [84], [85]. Contrary to that, it was found that capillary bridges/adhesion forces between two comparatively parallel plates increased when surfaces became smoother. Because finer roughness offers larger real contact areas where the liquid bridge forms increasing the mean curvature, contact radius, and neck radius of the bridge. In contrast, rough surfaces create smaller contact areas for the liquid resulting in larger contact angles that indicates a more hydrophobic surface. Micro to nano scale roughness is the reason behind the smooth looking frog/gecko toepads that create anti-slipping properties with capillary bridges and wettability [86], [87].

To understand the depth of the microstructural roughness and contact area, case of polar bear footpad can be considered with all its papillae and soft muscular pad. Its footpad's adaptation to increase contact area for slip-resistant movement on ice using roughness by increasing papillae height by 1.5 times and contact area by 1.3 times compared to other species of bears is an example anti-slipping feature. The power spectral density analysis reveals that the polar bear paw pads show a distinct increase in surface area due to the roughness at both its papillae and smaller length scales. Capillary adhesion is inherent when polar bear steps on snow, the snow compresses into the rough surface of the paw pad creating complete contact between the pad's roughness and the compressed snow. Heat from the paw generates a QLL at the contact points filling in finer roughness features that don't directly contribute to the interaction. For slippage/deadhesion to occur, the paw must slide across the true contact area, which is where the pad and snow are in

direct contact. Additionally, fracture of the snow can happen across its cross-sectional area affecting traction [88], [89].

QLL can appear at very low temperatures about any values above −35°C depending on the contact pressure. The thickness of the QLL can determine the type of lubrication regime for ice as well [90], [91]. Lubrication regimes are defined based on the roughness height i.e., dry lubrication (inexistent QLL and very rare for ice tribology), mixed lubrication when the interfacial temperature is high enough to melt ice but the thickness of liquid layer still remains less than characteristic height of surface roughness, and the hydrodynamic lubrication where the interfacial temperature reaches above melting temperature of ice and melts so much that QLL engulfs the surface roughness of contacting surface [92]. Under dry/mixed regimes, generally higher roughness results in higher friction, whereas decreases in hydrodynamic conditions. Critical studies also showed that decrease in COF with high roughness in flooded hydrodynamic regime is due to the free flow QLL in wider asperities [93]. Although roughness and contact area significantly affect the adhesion and friction, and temperature, sliding velocity, normal load plays vital roles as well. Figure 2.3 is a graphical representation of Stribeck curve drawn to manifest the effect of QLL and roughness on COF with respect to different lubrication regimes.

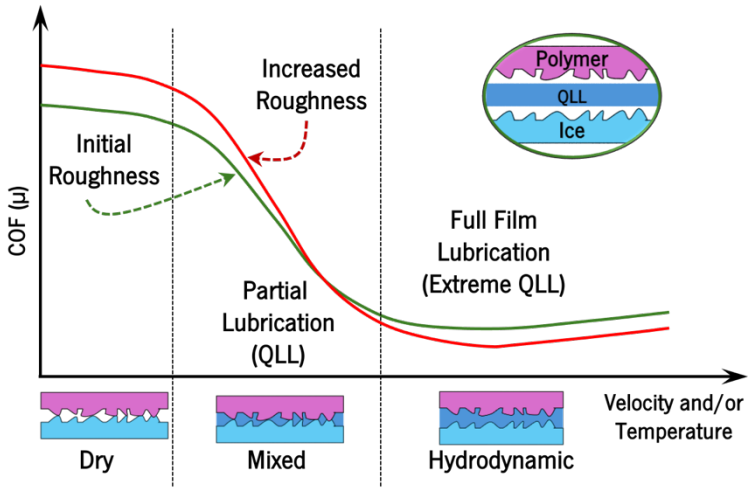


Figure 2.3 – A graphical representation of Stribeck curve depicting lubricating regimes and the effect of roughness for with the generation of quasi liquid layer [93].

Surface structures and textures are methods to design roughness in order to control COF on ice [20]. Polished surfaces with different orientations can significantly affect COF as random roughness decreases COF with increasing velocity following an inversely proportional relationship [94]. When roughness valleys are unable to contain excess liquid, it squirts out causing

interlocking and increased friction considering the normal load required to squeeze out the interfacial liquid [95]. Furthermore, textures or grooves aligned with the sliding direction reduce COF by allowing ice roughness to move freely within them, which is the reason skis often have diagonal, linear, or V-shaped patterns for smoother movement. Opposite to that, shoe-sole treads such as star-shaped, hexagonal, or V-shaped designs are never aligned in the direction of slip instead orthogonally to improve the ice adhesion [96], [97], [98].

2.3.3. Sliding speed and normal load

D.C.B. Evans' (1975) experimented with materials like perspex, copper, and mild steel sliding on ice at velocities of 0.2 m/s and 10 m/sec, temperatures of −11.5°C, and a normal load of 45 N, concluded that kinetic friction decreases for all temperature ranges with velocity following inverse velocity law. At higher speeds, the ice heats up more, producing QLL that takes lubrication from boundary/dry to mixed lubrication regime. However, the drop in COF become apparent only when liquid layer moves to hydrodynamic scenario where ice and surface separate [94], [99]. For a given speed and temperature, normal load also reduces COF, but this reduction has been observed in polymers like Polytetrafluoroethylene (PTFE) and polyethylene (PE) rather than metals like steel or aluminium alloys. For metals like steel, with speed the adhesion decreases but friction may rise again due to viscous effect of hydrodynamic regime. There is also a ploughing effect where metal slider can physically dig the ice by deforming the surface of ice. This ploughing effect is dependent on speed and temperature. Independence of high energy metals from COF is attributed to the dominance of hydrodynamic lubrication near melting point of ice, whereas COF change is observable in polymers' such as PTFE and PE credited to their hydrophobicity and surface roughness. Furthermore, COF reduction effect is also noticeable in ice-to-ice interfaces at very low temperatures (e.g., −15°C), where an increase in normal load from 10 N to 45 N leads to a significant drop in COF from 0.04 to 0.023. Nonetheless, as the temperature approaches −1°C (closer to the melting point) this reduction in COF becomes less prominent [51], [69], [100].

On the other hand, SCOF increases near melting point if the time of contact is more because both the surfaces freeze together below melting point, however, this effect was not recognisable. At higher loads, SCOF drops and is minimum near melting point due to QLL but can be increased with instantaneous local freezing [85]. Load Vs COF effect vanishes at higher temperatures. Once motion is set, kinetic friction becomes much lower and remains that way until very low speeds are approached, where COF increases. This effect is attached to stick-slip (capillary

bridges making and breaking) mechanism at lower speeds due to frictional heating rather than pressure melting i.e., the effect of normal load. Frictional heating is a major source of QLL generation at high speeds for impaired rubber-ice adhesion, nevertheless, due to conformability of rubber, normal load also become a parameter of interest. Ice adhesion is complex as at high loads rubber can deform, increase area of contact typically decreases COF due to lubrication, but increasing load near melting does not necessarily affect COF [101].

Figure 2.4 shows three regimes of lubrication for polymeric surfaces where adhesion/friction increase with sliding velocity up to a point where a substantial QLL is generated that starts lubricating the interface. This participates in dropping the COF in the mixed friction where liquid is enough but not enough to completely engulf the asperities. Furthermore, in hydrodynamic regime, capillary drag comes into play as the meltwater forms capillary bridges between the asperities on the sliding surface and the ice. These bridges create an additional force that resists the motion leading to higher friction. So, even though solid-to-solid contact is eliminated in the hydrodynamic regime, the combination of viscous resistance and capillary effects from the water layer contributes to the observed increase in friction at higher speeds in this regime. In this stage, substantial QLL supports the majority of the applied loads [90], [102].

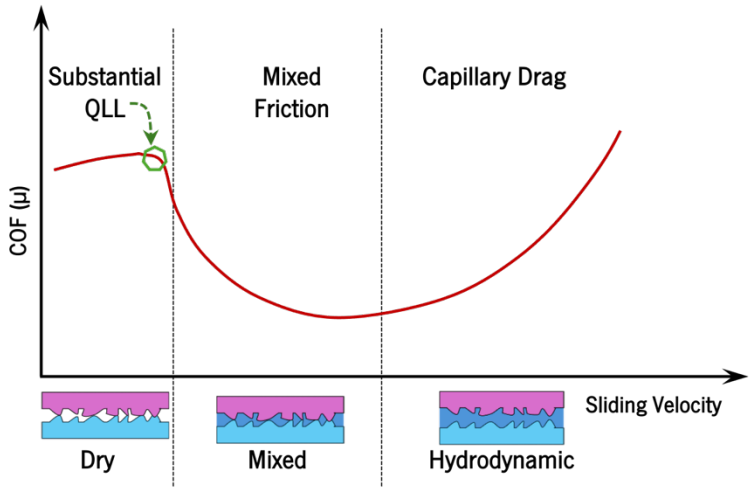


Figure 2.4 – Graphical representation of the effect of sliding velocity on coefficient of friction [102].

Unfortunately, walking on ice cannot take the advantage of this rise appearing in hydrodynamic regime because the occurrence generally occurs for higher QLL thickness (>500 nm) and the thickness of PGQLL while walking averages from angstroms to 100 nm that fall well within the mixed regime. Another predominant reason is the dynamics of human movement where

producing capillary drag by easy absorption of QLL is either possible by plenty of interfacial liquid that wets the shoe-sole or the material is too hydrophilic to absorb even the smallest of QLL [103], [104], [105].

The experiments on ice with elliptical/bell shape surface showed meagre adhesion during the approach of the contact, still provided higher resistive adhesion during the separation. On the other hand, speed of the walking and the elastic properties of the shoe-sole material (rubber) also vary amount of adhesion such as stiff rubber offers less contact area. Additionally, greater sliding speeds make the contact area dynamic and the values for dynamic contact area are less than static contact area under any temperature range or rubber, especially at moderate sliding speeds . Although adhesion is minimally affected by temperature, friction force is highly dependent on temperature regardless of the material's viscoelastic properties or sliding velocities. It was observed that COF increases up to 0.1 m/s for −10°C to −2.5°C and then sharply decreases. It was discovered that friction depends on surface roughness, particularly the peaks and shapes, while adhesion is governed by the peaks and the absorbed QLL. In addition, walking speed and mechanical properties of rubber also affect adhesion such as stiff material provides less area of contact. Moreover, higher sliding speeds cause the contact area to become dynamic, and the dynamic contact area is smaller than the static contact area at any temperature or with any type of rubber at moderate sliding speeds. Having described the importance of these dominant variable, water remains inseparable part of the discussion and therefore, wettability as a major factor when must be understood in the context of slipping or anti-slipping [52], [54], [99].

2.3.4. Wettability

Wettability is a measurement of ease of liquid to interact or spread with a solid surface governed by the interactions between liquid molecules and surface atoms [103]. Surface characteristics such as roughness, surface energy, porosity, capillarity, and structure are crucial to changing the wettability and can be determined using contact angle (CA, β) between hydrophilic and hydrophobic states. The contact angle is defined at the point where the solid, liquid, and air phases meet. Additionally, chemical properties of surfaces, which influence surface energy play a major role in altering wettability [96], [104]. Methods such as pre and post treatment via laser, ozone plasma, and UV irradiation are also methods to influence wetting behaviour. Chemical composition changes through these methods introduce or alter functional groups and adjust surface energy by adding hydrophilic groups (hydroxyl (-OH), carboxyl (-COOH), amine ($-NH_2$), carbonyl (>C=O), sulfhydryl (-SH), phosphate ($-PO_4^{2-}$), and ether (-O-)) increase wettability, while

incorporating hydrophobic groups (methyl (-CH_3), long alkyl chains (-C_nH_{2n+1}), fluorinated chains (-CF_3, -C_2F_5), silane) reduce surface energy and decrease wettability [97], [98]. These chemical modifications enable precise control over wettability and are crucial for applications ranging from creating self-cleaning surfaces, anti-icing, anti-fogging, and enhancing biomedical implant integration to optimise oil recovery processes and improving coating and printing technologies.

Surface topography by providing roughness to introduce the micro and nano structures is a physical way to tailor wettability because the coatings and chemical ways do not generally keep up with the material properties and eventually lose the effect especially in harsh applications like shoe-soles. Therefore, applications with intense wear, constant contact with fluids (wet ice contact), extreme heat and cold (condenser coils, heat exchangers, aeroplane wings) require more physical ways along with appropriate chemical alterations to serve the purpose [85]. Cassie-Baxter and Wenzel proposed theories to measure the wetness of a surface based on physical changes i.e., roughness using CA. Surface structures of micro or nano scale (tubes/rods/fibrillar wires etc.) increase surface free energy that results in directional dispersal of liquid as shown in Figure 2.5 [52], [103], [105].

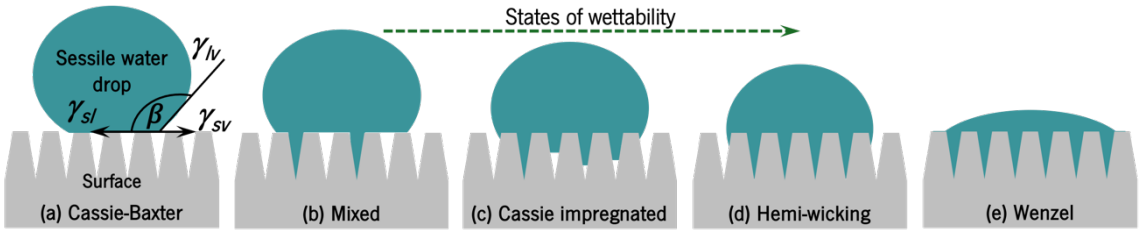


Figure 2.5 – Progression of wettability states shown on textured surfaces resembling micro roughness.

Thomas Young further conceptualised the equilibrium of three-phase at the contact of liquid with solid surface by contact angle in Equation 2.3 and describes theoretical basis of wettability states presented in Figure 2.5.

$$\gamma_{lv} \cos\beta = \gamma_{sv} - \gamma_{sl} \qquad \text{Equation 2.3}$$

Where γ_{lv}, γ_{sv}, and γ_{sl} express the surface tension of three phases i.e., solid, liquid, and vapour. Entrapped air inside the textured structures is the primary reason to restrict liquid infusion, otherwise all liquids have capacity to spread and wet the surface (β→0°) [108], [111]. Hence, the roughness factor ($r = actual\ surface/geometric\ surface$) defines the wettability index as a function of Young's angle, β and apparent contact angle, β^* by Wenzel's theory given by Equation 2.4 ;

$$\cos\beta^* = r\cos\beta \qquad \text{Equation 2.4}$$

Cassie-Baxter theory demonstrates in Figure 2.5(a) applies to the hydrophobicity where air filled cavities increase contact angle sometimes leading to partial wetting. However, this theory becomes insufficient while moving towards the capillary effect of liquid infusion from Figure 2.5(b) to Figure 2.5(d) [112]. On the other hand, Wenzel's theory holds true for hydrophilic ($\beta < 90°$) for and hydrophobic ($\beta > 90°$) states when increasing the surface roughness factor would respectively, increase or reduce wettability [33], [113]. In case of porous structures as proposed in this work, capillary imbibition takes effect and surface roughness becomes only a partial cause. Figure 2.5 shows a systematic movement of liquid inside the cavities where a highly hydrophobic structure full of air does not let liquid to penetrate due to the dominance of liquid-vapour surface tension. With the modification of surfaces by virtue of factors like roughness, charge, materials, capillarity, and porosity, liquid imbibition increases moving towards Figure 2.5(b) i.e., a mixed state where some liquid moves inside the cavities, nevertheless, others remain full of air without any absorption (almost alternative cavities). Figure 2.5(c) is a case of higher apparent contact angle due to air pockets where liquid penetrates partially in cavities along with full absorption but still having large liquid-vapour surface tension. Figure 2.5(d) is a closer state of fully hydrophilic surface where liquid sucks inside the cavities due to capillarity, but the spread remains close to the boundaries of droplet until the spread becomes fully overwhelming like Figure 2.5(e). Reactivity of the surface is a main factor as non-reactive surfaces attract more liquid whereas reactive liquid presents obstruction to capillarity by enhancing surface roughness/asperities [33], [114], [115]. The reactivity and polarity of the surface structures due to nanoparticles alter the wettability significantly like titania can modify chemical reactivity by increasing surface energy and introducing polar groups at the same time can also degrade the composite. Besides, inert zirconia particles can improve mechanical properties like strength, and hardness but not necessarily chemical reactivity [116], [117], [118].

It is extremely important to comprehend the size, shape, density of the structures and material chemistry on how and why liquid infuses in different states. As the properties like surface tension cannot be altered in environmental conditions for QLL or ice, therefore, the discussion is unsuitable here. Topographically sharp-edged pillars/roughness offer possibility of trapping air making surface hydrophobic, therefore, the generation of capillary adhesion by sucking up the liquid for conical cavities (conical pillars) must be tailored carefully to induce hydrophilicity in the present work [119], [120], [121], [122]. Surface chemistry affects wettability by altering surface

energy and introducing specific functional groups like materials with high surface energy and polar or charged groups (hydroxyl, carboxyl, or amino groups) enhance wettability by forming strong interactions like hydrogen bonds with polar liquids like water, leading to hydrophilicity. Conversely, surfaces with nonpolar groups (methyl or fluorinated chains) reduce wettability making them hydrophobic. Recent utilisation of nanopowders of metal oxides like titania, alumina, and zirconia or metalloids like silica are considered high surface energy materials due to their large surface area to volume ratio. The high surface energy arises from the unsaturated bonds at the surface of the nanoparticles, which makes them more reactive and prone to agglomeration. Metal oxides consist of metal-oxygen bonds in these compounds are mostly ionic with some covalent character, leading to polar surfaces. The oxygen atoms carry a partial negative charge, while the metal atoms (titanium or zirconium) carry a partial positive charge. This polarity contributes to their ability to interact with polar substances, such as water molecules, and affects their wettability and surface interactions [114], [123], [124]. Contrary to that, silicon-oxygen bonds of silica are polar covalent, and its surface often contains silanol (Si–OH) groups leading to polarity and hydrophilicity to cause strong interactions with other polar substances like water [125].

Tuning wettability alters the nature of a surface leading to its performance with adhesion. Adhesion of a surface by virtue of its physicochemical properties with liquid translates to the adhesion on wet surface. Thus, a fine tuning of wetting behaviour without compromising the favourable properties of the material is a matter of great import and is a key element of this PhD. After discussing the parameters for adhesion and friction on slippery ice, it is customary to discuss the previous works that used and explored these variables to synthesise a solution. Following section is an effort to elaborate on the work done so far in this complex field.

2.4. Existing shoe-sole solutions for anti-slipping

There have been efforts for decades to prevent SFs on wet ice and snow considering different aspects of adhesion ranging from surface structures (tread pattern variations), material alterations, and inclusion of external anti-slipping devices. Increasing friction on ice especially wet ice with QLL is a tedious task considering the variables involved. This thesis broadly classifies these solutions in three ways; anti-slipping devices, tread design-based, and material-based strategies. In these categorisations, we focus on most recent advancements in the field, their features, and drawbacks.

2.4.1. Anti-slipping devices

Reviews from places like Finland, Sweden, Canada etc established that no slip-resistant shoe provides grip on an extremely slippery ice and use of anti-slipping devices become inevitable. The basic idea of using anti-slipping/slip-resistant device is to offer mechanical interlocking by penetrating the ice/snow like ice trekkers. Externally or in-built fastening of interlocking media like crampons, chains, studs, cleats, and spikes to the shoe-sole produce friction on the ice or snow as shown Figure 2.6 [3], [126], [127]. Apparently, anti-skidding devices that use sharp penetration for interlocking are used at the heel and toe region rather than symmetrically distributed all over the sole. A Swedish study in 2020 conducted that on adults for 50+ years of age (23,168 subjects) provided that 28.5% people use anti-slip devices during winters covered with ice/snow. Increasing age of world population, pollution, and global warming have already pushed hot and warm temperatures to their extremes and this caused extreme cold in relevant places. These drastic developments push people in needing anti-slipping devices increasingly [128], [129], [130], [131]. However, study on an optimum location on sole where anti-slipping devices can offer maximum slipe resistant took place in Sweden, where devices were employed on whole foot, forefoot, and heel for slippery surfaces, gravel, ice, snow, and salts. It was established that the fixed heel anti-skidding device performed superior to whole foot followed by forefoot due to its stability, balance, and comfortability [132].

Walking on slippery surfaces follow specific gait pattern and varies person to person, nevertheless, heel strike is the first contact of the foot and is considered the most vulnerable section. The initial contact i.e., heel-strike when only small part of heel touches the slippery surface (Figure 2.7(a)) at the start of the movement makes instability and results SF, therefore, heel anti-slipping devices were found helpful. On the other hand, any walking scenario where the dynamic situation accompanied with least area of contact like heel-strike or pre-swing offer high probability of slips as shows Figure 2.7. For minimising the risk of SFs, ample balance is the priority and primarily the functions of gait speed and applied pressure more than Dynamic Coefficient of Friction (DCOF). Oily, greasy, muddy, extremely smooth surfaces also cause problems of SFs like wet ice, hence, carbide tipped studs were used inside British coal mines nearly 50 years ago. These studs also proved effective on ice as well [126], [133], [134]. In spite of their popularity, easy availability, ready to use and high resistance to slipping, pedestrians' perception is a vital factor when comes to anti-slipping devices. Given a choice, these devices would not be the first choice of an individual due to the lack of diversity and complications in usages because slip-resistance performance of

these devices is counterbalanced mostly by their balancing performance among comfort, normal gait cycle, ample foothold [132], [135].

The downside of anti-slipping devices is their unsuitability for long distances, instability, discomfort, and weight especially for elderlies and kids. Additionally, these devices must be put on and off before and after use or carry them as an accessary and have no possibility to be used by physically challenged people. Apart from that, these are only suitable for outdoors and damage indoor floors or tiles. As in case of crampons (Figure 2.6(a)), frontal pins do not play much role in normal walking among other reasons such as the loss of cleats, broken pins of crampons, trips, and severed chains requiring frequent replacement of entire devices add into their unpopularity as can be seen in Figure 2.7. Having discussed the details of anti-slipping devices, it is evident that they cannot be an appropriate choice for all and hence, shoe-sole tread designs can prove to be an alternate path to enhance the interfacial friction and reduce or prevent SFs [132], [136].



Figure 2.6 – Commonly used anti-slipping devices used for ice/snow; (a) crampons, (b) chains, (c) studs, (d) spikes, (e) cleats. (nomenclatures are interchangeable depending on places and applications).

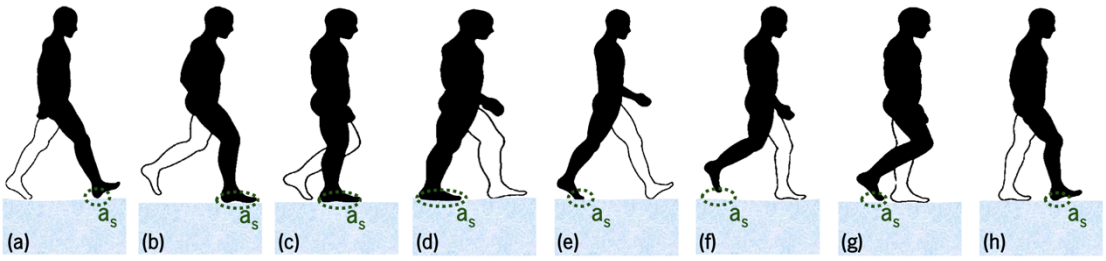


Figure 2.7 – Sequential gait cycle in a stroll over a surface; (a) initial contact (heel-strike), (b) loading (flatfoot), (c) midstance, (d) terminal stance, (e) pre-swing, (f) initial swing, (g) mid swing, and (h) terminal swing. Surface are of contact is represented by a_s [137]. (the foot sole represents the shoe-sole)

2.4.2. Tread design-based strategy

This strategy is based on the efficiency of different geometrical channels to deal with interfacial liquids and make contact. Generally, the tread designs of the channels for anti-slipping winter shoe-soles work on the principle of repelling the water from the interface by pressurising the sole over the surface that drives-out interfacial liquid/QLL with the help of hydrophobicity. Material hardness contacting the freezing surface is an important aspect of tread-based approach to enhance friction [138], [139], [140]. In addition, wettability in tread design can either be produced by altering the materials or surface structure. Tread designs are more complex than they appear because of their dimensions (width, depth, orientation), presence of interfacial liquid parameters (pressure, roughness, distribution), material properties, and wetting variables. Tread channels, texturing, or roughness on the shoe-sole are the similar variant of design concept and change wettability and their approach to deal with the liquid [141], [142]. Though shoe-sole material is pivotal to its nature, however, surface area of treads, heel shape, and hardness of the material encompass about 87% of the variations in available COF [143].

Treads compress the surface to disperse liquid from oil or wet surfaces is different from slippery ice where compression itself melts ice and produces liquid, nonetheless, the drainage phenomenon for interfacial liquid remains same except few material properties. Hydrodynamic pressure varies during slipping and treads are important to determine the fluid pressure and severity of the SF because of boundary and hydrodynamic lubrication regimes. Higher fluid pressures at the interface results in severe slip due to fluid build-up and untreaded soles were found to have 124 kPa pressure against 1.1 kPa for treaded ones [144], [145]. This suggests the fluid build-up more in untreaded soles offering a high rolling effect and chances to SF. The relationship between tread depth and fluid pressure is non-linear as pressure decreases with depth but stops decreasing with higher depths. On the other hand, viscosity of the fluid is another aspect that high viscous fluids result in high pressure. Treads must be wide and deep enough to produce low contact angles to absorb and disperse liquid like width of 0.9 cm to 1.2 cm and depth of 1.5 mm to 2 mm performed best on a surface with viscous fluids such as soybean/vegetable oil [146], [146], [147]. Analyses on non-slip resistant shoe-soles with high tread area showed COF reduction up to 40%, while slip-resistant soles with higher tread area, bevelled heels, and lower hardness improved COF up to 20%. Softer shoe-sole (Shore A = 40) provided more adhesion on water wet surface compared to 60 and 70 Shore A. Shoe tread wear impact on slip resistance is not

substantial until it reaches to certain threshold after which slip-resistance dramatically decreases [146], [148].

Research have established that among depth, width, and orientation, the latter has most impact and must be considered carefully. A comprehensive study on all three-variable found that tread orientation of grooves with 0° and 45° are better performing than 90°. Studies on rubber block with 2 mm height and 0° tread orientation (parallel to sliding) demonstrated SCOF of 1.39 ± 0.08 and a DCOF of 1.18 ± 0.08 compared to 90° tread orientation for glycerol [149], [150]. Having said that, draining capacity of treads cannot be optimised without attention to fluid as less viscous fluid behave different to high viscous ones. Orthogonal or diagonal tread grooves prove better than parallel in fluid handling and friction provided sufficient width in walking direction. Additionally, diagonal tread channels are capable to drain liquid and produce higher DCOF, whereas orthogonal grooves suffer proper drainage though offer motion resistance. This can be due to the running across length of the treads in transverse direction where fluid with foot pressure can be driven faster. Tread channels supposedly suppress the hydrodynamic pressure allowing the wet layer to escape. Variables as compressibility, viscoelastic properties, and elasticity also play a major role and decide the shape that contact surface takes. To decrease the contact angle, chemical surface modification using tri-chloro-iso-cyanuric acid of thermoplastic styrene butadiene rubber is common to increase roughness and work adhesion. However, at high concentrations mechanical properties such as tensile strength and abrasion resistance impair substantially [151], [152], [153].

Hardness, viscoelasticity, tread dimensions, fluid pressure, and surface roughness all lead to different wettability of the sole surface. Filling up tread channels completely by the virtue of hydrophilicity (high surface energy and low contact angles) can be helpful when amount of water/QLL is more at the interface operating at Wenzel state. The optimised design of tread grooves, their width and depth are important for liquid to rise otherwise narrow and deep grooves result in Cassie-Baxter effect where these cavities entrap air beforehand and deny entry to the liquid [154]. When higher liquid pressure makes a fluid film that spreads along the surface and does not let sole touch solid surface is a hemi wicking state, whereas the liquid partially filling some textures and avoiding others without interacting is a sign of mixed state or Cassie impregnation state. This capillarity can be the source of adhesion on freezing ice and for decades, shoe manufacturer from Frye to Nike gave importance to tread patterns and patented them [155], [156], [157].

Marketed slip-resistant shoes claim to have more available COF than required COF. A study confirms that slip-resistance of shoes decreases as tread wears out, initially increasing then decreasing as wear progresses. At the early wear stage (< 3 km), available COF increases slightly due to increased contact area, but once the tread reaches a certain wear threshold (between 1-11 km), fluid forces rise, and available COF declines drastically. The study also found that a worn-out tread area larger than 800 mm^2 leads to higher fluid pressures and an increased risk of slipping. Fluid forces become a key indicator for shoe replacement, suggesting shoes should be replaced once fluid forces exceed 10-20% of the vertical load. The progression of the tread wear is prominent in the heel region because first contact starts from heel-strike and terminal swing ends with heel as demonstrated in the gait cycle in Figure 2.7 [158], [159]. Heel also goes through prominent impact load during the gait cycle. Figure 2.8 organises a series of slip-resistant treads and their worn-out scenarios. Apart from height, width, and depth, fluid pressure, orientation, and maximum achievable inclination of the surface are the crucial factors especially on wet ice. A US study on ice with negative to positive temperature ranges for four anti-slip winter boots found that best performing treads can attain up to 17.5°±1.9° without slipping and worst performing reach only to 3.3°±0.8°. Tapered-wedged treads proved to be a favourite among others to study the SFs in worn-out shoe-soles. Wearing on ice is the sequence of macro phenomena of abrasion, crack propagation, rupture, temperature, interfacial fluid properties, and permanent damage, however micro-level wear goes through more severe changes [160], [161].

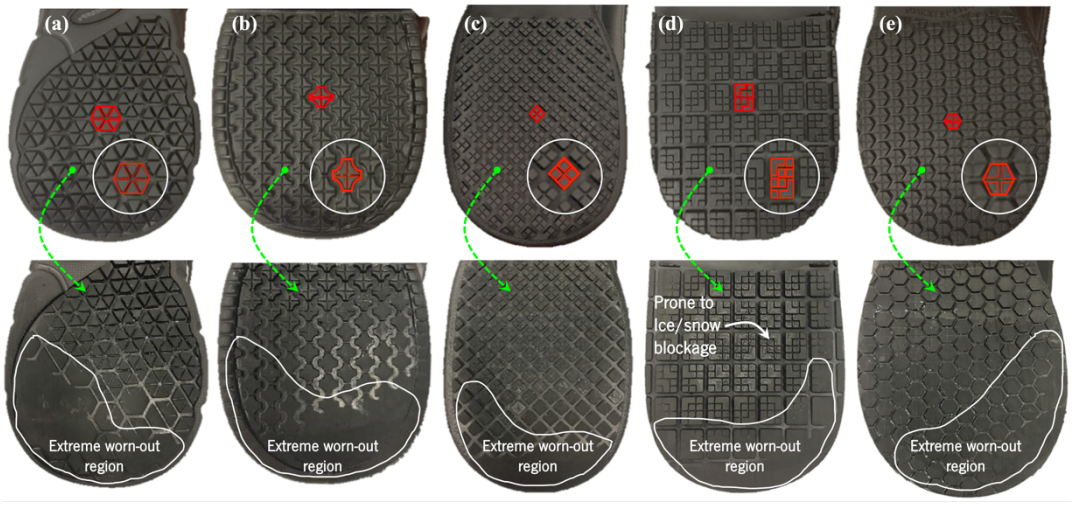


Figure 2.8 – Five tread designs (micro-embedded macro-treads) before and after the wear representing for; (a) Hexagonal-triangle (Brand – Keuka, Model - Galley 55014), (b) Star-shaped (Brand – SafeTstep , Model - Apollo 140060), (c) Square-square (Brand – Shoes for Crews, Model – Falcon 6007), (d) Rectangular-square (Brand – SR Max, Model – SRM 3500), (e) Hexagonal-trapezoidal (Brand – TredSafe, Model – M151044BU). Macro treads yield

deep and wide tread channels which carry maximum amount of liquid, whereas micro treads construct shallow and narrow channels. Micro treads do not specifically serve to drain out liquid instead provide initial pressure on the ice/snow to attain most area of contact [158], [162].

A soft shoe-sole material provides better friction, whereas harder material makes better solid-to-solid contact but produces thicker QLL. Thus, softer materials are suitable for higher COF, conformity, and comfort but lack in longevity, making them expensive as they worn out very quickly. On the other hand, hard materials offer more life but lack in comfort, conformability, and cause severe melting of ice. The micro-tread patterns of the shoe-sole do not contribute to drainage and can usually clogged with ice/snow due to their dimensions. Clogging along with constant contact with ice reduces the temperatures of sole tread to ice temperature and turns brittle in case of soft treads or harder for hard treads that melts more ice. Uneven wearing as depicted in Figure 2.8 occurrences make sole treads vulnerable to slips regardless of their design and pattern. Given the fact that shoe-sole treads are the combination of geometric and material variations and must be considered based on their applications. Hence, the following study of material-based approaches is put together as an approach to provide anti-slipping characteristics [163], [164], [164], [165].

2.4.3. Materials-based strategy

In any atmosphere, material of the shoe-sole contacts the surface and properties of material of sole decide the degree of adhesion, anti-slipping, wear, and life of the shoe. Customary outsole materials are polymers/elastomer such as rubber, Thermoplastic Rubber (TPR), Polyvinyl Chloride (PVC), Polyurethane (PU), Thermoplastic Polyurethane (TPU), Thermoplastic Elastomers (TPE), and Ethylene Vinyl Acetate (EVA). Rubbers like Natural Rubber (NR), Styrene Butadiene Rubber (SBR), Styrene Butadiene Styrene (SBS), Nitrile Butadiene Rubber (NBR), and Silicone Rubber (SR) are the most common materials covering 30% of global outsole production industry. Slip resistance, ease of availability, ease of moulding, durability, anti-icing/anti-frosting, and recycling ability makes rubber a universal favourite [166]. Table 2.2 compiles commonly used rubber variants from the shoe-sole manufacture.

Table 2.2 – Polymers, their ingredients, and deliverable properties for their selection.

Polymers	Ingredients of formulations	Properties
Rubber [166]	- fillers, vulcanisation additives and accelerators, activators, softeners, antioxidants, pore-forming agents, pigments, and dyes	- slip and frost resistant - durable - 30% of worldwide shoe-soles

	- fillers: soot, kaolin, chalk, lignin, magnesia carbonic acid, talc, diatomite	
Thermoplastic Rubber (TPR) [166]	- synthetic rubber	- more durability and retains elasticity better than natural rubber - median density and sp. gravity - non-slippery and lightweight - better cushioning
Polyvinyl Chloride (PVC) [166]	- polymerization of vinyl chloride at 20°C to 100°C with peroxide initiators, dyes - plasticizers: acid esters like phthalic, sebacic, and adipic - stabilizers: barium, cadmium, fatty acid salts	- high strength, heavy weight, frost and wear resistance from high density - highly flexible and elastic - elasticity loss from plasticizer depletion over time - cracks and loss of frost resistance
Polyurethane (PU) [167]	- silicone stabilizers - tertiary amine catalysts - organic-based foam property modifiers	- loss of elasticity below 0°C, good resistance to abrasion, deformation, oil/gas/acid, and wear - good mechanical memory, high density but low COF - poor ice/snow adhesion and frost resistance
Thermoplastic Polyurethane (TPU) [168]	- special purpose ingredients such as stabilisers, fillers, plasticisers - chloroprene rubber, acrylonitrile copolymers, vinyl chloride copolymers, phenol formaldehyde, and coumarone-indene resins	- excellent elasticity, rigidity, grip on ice/snow, and mechanical properties - porous and non-porous - higher density and resistance to wear, abrasion, deformation, punctures, and cut and heavy due to high density
Thermoplastic Elastomers (TPE) [72]	- TPR, polystyrene, butadiene-styrene copolymers, ethylene-vinyl acetate, chlorinated polyethylene, PVC - fillers: chalk, carbon black, minerals, kaolin; stabilisers: inaly, tinuvin, Agidol; plasticisers: naphthenic, industrial or transformer oils, petroleum jelly, dyes	- highly elastic, fluidic from thermoplastic properties, and deformable like rubber - medium frost resistant - non-corrosive by acids, alkalis, or organic matters - low weight and heat resistance, and good cushioning
PU+TPU [166]	- mixture of TPU and PU	- excellent thermal insulation due to porosity - brilliant adhesion to other surfaces, slip-resistant, good wear resistance, lightweight - expensive
Ethylene Vinyl Acetate (EVA) [166]	- polyolefins - copolymerisation of ethylene and vinyl acetate monomer	- high resistant to solvents, ozone, oils, and high temperatures - lightweight and good shock absorption but loses cushioning effect and elasticity - less slip-resistant
Special PU (SPU) [169], [170]	- specially manufactured PU having high density and viscosity of TPU	- medium weight, Cheaper than TPU - high strength, durability, resistance to frost, wear, and abrasion

Polymers like rubber can survive severe range of temperatures (–100°C to 300°C) and can retain their useful properties, which make them perfect choice for winter shoe-soles. Viscoelastic properties and shear of the area of contact are crucial for these applications as frequent melting and freezing occurs due to the contact with freezing temperatures. Ultimately, these properties are responsible for employing friction and slip resistance. At lower speeds than 1 m/sec (consider normal walking speed of 1.4 m/sec and approximately half for slippery surfaces), COF is affected as surface morphology of ice/snow significantly changes with rubber particles' viscoelasticity [171]. It was found that friction force reaches to 30 N against 50 N normal load (COF = 0.6) at –20°C [172], [173]. Through dynamic mechanical analysis, it was established that compounds respond differently under various temperatures and loading conditions such as more flexible with lower silica content rubber performs better in winter conditions emphasising temperature-dependent viscoelastic behaviour of the material. This comparison was also validated by rubber-ice traction (COF) due to the rise up to –5°C followed by a sharp reduction above –5°C, whereas rubber-mica, where COF remained constant at 0°C [167].

Selecting a polymeric material with good viscoelastic properties, density, hardness, wear resistance, vulcanisation, conductivity, toughness and stiffness, and T_g is an arduous task, hence, composites with wide spectrum of properties came into existence [174]. Introduction of carbon fibres, resins, natural fibres, fibre glass, minerals, aramid etc. in polymers induce desired strength, weight reduction, and life. In recent decades, polymer composites have revolutionised the shoe industry, making footwear significantly lighter, stronger, and more customisable especially in high-performance athletic shoes. Even with recent advancements, rubber and its composites remain the foundation of shoe-soles for winter anti-slipping footwear, thus, soft vulcanisable silicone rubber became the choice for this work as well. Surface modifications is one of the ways that can introduce properties on relevant areas keeping the bulk properties in the desired range. With better surface features and high viscoelasticity, formation of QLL can even be avoided at full contact and hefty normal loads [102].

A low Tg of rubber composite (peroxide cured) offer higher COF because rubber is less stiff and more resilient. At ultralow temperatures of –30°C, an SR compound though hydrophobic (Tg = –133°C) found to achieve a value of 2.2, whereas isoprene rubber (Tg = –67°C) gave 1.8, and nitrile rubber (Tg = –25°C) attained low values of 0.5 at –14°C. At 0°C, all these compounds fell within 0.1 to 0.2 of COF possibly resulting from QLL. A test on NR, where it was hardened by carbon black showed less COF compared to soft NR without the additive at –30°C. Despite being

harder than butadiene and styrene rubbers, TPU can still achieve high COF on dry ice and snow due to surface roughness characteristics. This high roughness of counter icy surface increases the deformation friction of TPU due to its low equivalent elastic modulus and high mean curvature of surface asperities. Contrary to that, TPU gains traction through adhesion by virtue of its low elasticity and high mechanical loss angle in case of smoother counter surface. Underperformance of softer shoe-sole materials are also reported by saturation effect near melting temperatures i.e., filling up of QLL in minute asperities at high speeds and large loads. Figure 2.9(a) is a combination of smooth and rough materials that establishes the effect of roughness as surface morphology. First smooth surface followed by rough surface produced SCOF as high as 0.37 to 0.45 and DCOF of 0.34 to 0.31 corresponding to 0°C to −10°C, respectively. Whereas Figure 2.9(b) exploits the hybridisation of soft and hard rubbers based on compounding rather than using them at separate locations. Inclusion of soft Poly-Phenylene-Benzobisoxazole (PBO) was mixed with hard carbon fibres (8% v/v) in TPU matrix. These sharp piercings of hard micro-fibres breach the ice/snow while soft fibres conform and reach DCOF up to 0.61±0.053. Comparative study associated TPU and SBS mixed with reinforcements like alumina, basalt, glass, carbon, and PBO showed that TPU+PBO offered maximum COF on ice of 0.375±0.031 friction against any combination of SBS or TPU itself. The wear resistance increased by 22% and COF by 57% in comparison to TPU without fillers. The combinations gathered in Figure 2.9 are the excellent illustrations of composites being used with their surface properties accompanied by the natural advantages provided by tread channel designs and location of the application [79], [170], [175], [176].

Not only synthetic fillers but fillers like silica taken from the incineration of the rice husk ash is also a good option to enhance COF on ice. The silica showed 300% rise in elasticity, less residual elongation, and higher loss angles at the melting point. In last two decades, use of 1D and 2D nanomaterials like graphene, carbon fibres, glass fibres in polymers increased several folds in footwear and tyre industry. Figure 2.9(c) shows a ski-boot sole with the inserts of rubber and glass fibre that increased its wear resistance, abrasion and, COF on ice. At −10°C, this composite increases COF by five folds (0.50) compared to plain rubber (0.1) while further decreases to 0.28 due to wettability increment of rubber at −1°C. Winter boots with glass nanofillers achieved as much as 0.57±0.19 that reduced to 0.45±0.13 with significant weight loss of 3.46±0.52 mg/cm^2 during ice traction tests. Due to roughening effect of glass fibre in rubber matrix, hydrophobic behaviour dominates that repels QLL and can meagrely increase friction [177], [178], [179], [180].

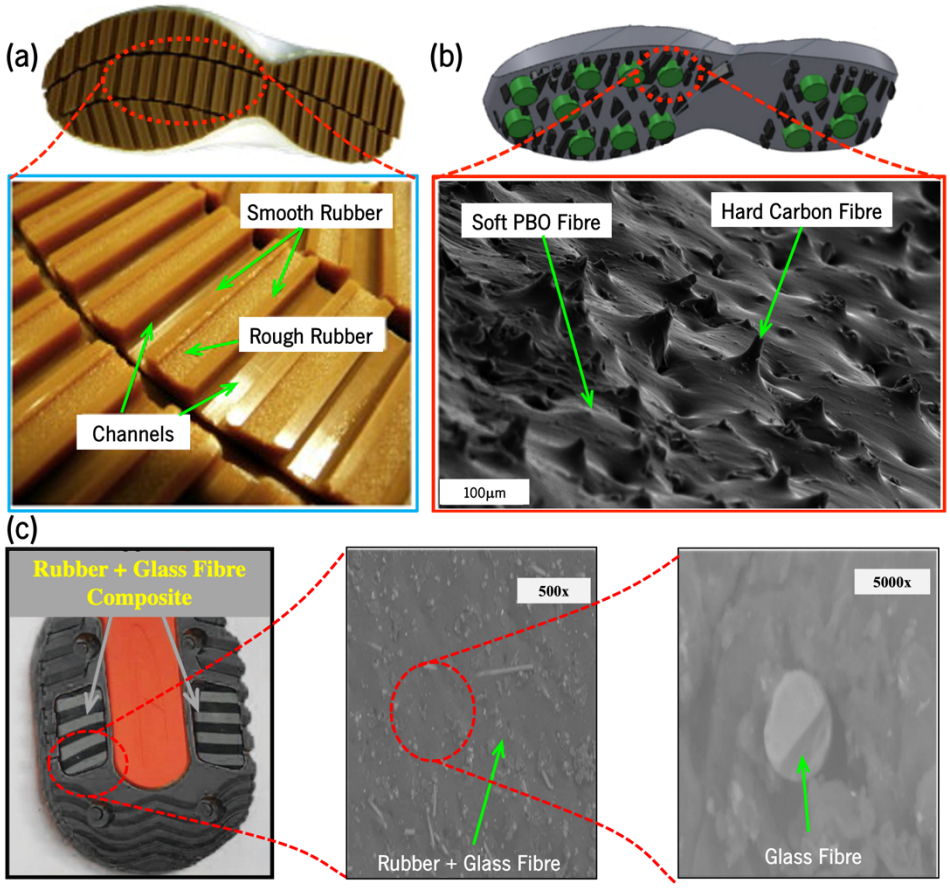


Figure 2.9 – Strategies to alter material of shoe-sole to exploit roughness, hardness compounding with fillers/reinforcements; (a) hybrid rubber patterned surface footwear outsole consisting smooth and rough rubber blocks to provide high SCOF and DCOF under wet and dry conditions both, and channels to help in dispersion of fluid from sole-floor interface, (b) SEM of composite of soft Poly-Phenylene-Benzobisoxazole (PBO) and protruding hard carbon fibres, protruded hard fibres, accommodated in shoe-sole, (c) SEM of rubber and glass fibre composite inserted at the heel of shoe-sole [176], [177], [178].

Invent of 1D and 2D nanomaterials is a big leap and Graphene nanoplatelets (GNPs) became an instantaneous favourite due to its excellent properties as it helps improve the COF and ice/snow adhesion significantly but tends to wear out from the surface. While 1D GNP composites enhance abrasion resistance, they are less durable with lower wear resistance and COF. Among the 1D fillers, Carbon Fiber (CF) and Carbon Nanofiber (CNF) showed initially high COF values of 0.58 and 0.72, respectively that decreased substantially after abrasion, though CNF exhibited less weight loss compared to CF. On the other hand, 2D GNP composites show excellent wear resistance and ice friction. After abrasion tests, recorded ice traction and surface weight loss for 2D GNP at 0.46±0.11 and 2.44±0.21 mg/cm^2 (more than before abrasion), respectively indicating superior performance compared to hexagonal Boron Nitride Nano-sheets (BNNS) and graphite. Figure 2.10(a) shows better morphology of GNP rubber composite (before in

Figure 2.10(a(i)) and after in Figure 2.10(a(iii))) compared to BNNS before and after abrasion before (before in Figure 2.10(a(ii)) and after in Figure 2.10(a(iv))) showing superior wear and drag resistance of GNP. Change in elastic properties noted for GNP compound was also less; hence, less impairment of longevity [181], [182], [183].

Instead of direct mixing, hierarchical structures inspired from natural icephobic surfaces can also use surface roughness and combination of soft-hard structures for frictional adhesion. Additionally, enhanced surface area, increment in hydrophobicity, adaptive rigidity and softness, and minimised ice adhesion are common aspects of these structures. Ice friction and wear with respect to hierarchical structures analysed in micro (Figure 2.10(b(i))), micro-micro (Figure 2.10(b(ii))), and protected micro-micro hierarchical textured (Figure 2.10(b(iii))) structures for propylene and rubber (hybrid of soft-hard). Among these three, soft textured micro-micro protected rubber offers COF of 0.145±0.006 compared to 0.114±0.003 at −10°C (drops for −3°C) under 20 N load on wet ice. Though propylene showed least COF, its performance is consistent and stable with abrasion-resistant and hardness during all the tests and wear is minimal among three. Moreover, unlike others hard rubber increases its COF by 28% at −10°C under load increment from (20 N to 40 N). Hydrophobicity resulting from hierarchical micro-micro protected structures of propylene made it least adherent to the ice and moderate stick-slip behaviour [180]. Quick abrasion, degradation of textures, and diminishing material properties of rubber at cold temperatures make it vulnerable to SFs on ice [184], [185], [186].

Material-based approaches brought a paradigm shift in the field of footwear industry by the introduction of nanomaterials, reinforcements and fillers, surface modifications along with patterns. The success of the change in material largely depends on specific structure, wettability, roughness, hardness, adopted manufacturing technique, and elastic properties, and is often accompanied with design variations. These solutions neither change the dynamics of human locomotion nor the fundamental nature of the shoe-sole, thus, are superior to anti-slipping devices or design-based strategies. Despite the merits, these approaches suffer in durability and effectiveness in long run. For example, CF, graphene, or GF protruding soles wear out very quickly either by breaking or by constant abrasion. Moreover, nanoparticle-based slip-resistant materials can be used indoors and by all ages, genders, and physical situations unlike the anti-slipping devices, nevertheless using them constantly on hard paver blocks or cemented floors severely limit their usages. Hierarchical structures, roughened, protrusion soles use hydrophobicity for their effectiveness and are fit for very limited amount of QLL, however, these surfaces do not consider PGQLL and are bound to fail

on dominantly melting ice. So far, no modern material solutions use the hydrophilic behaviour of nanotechnology and other substances in trend.

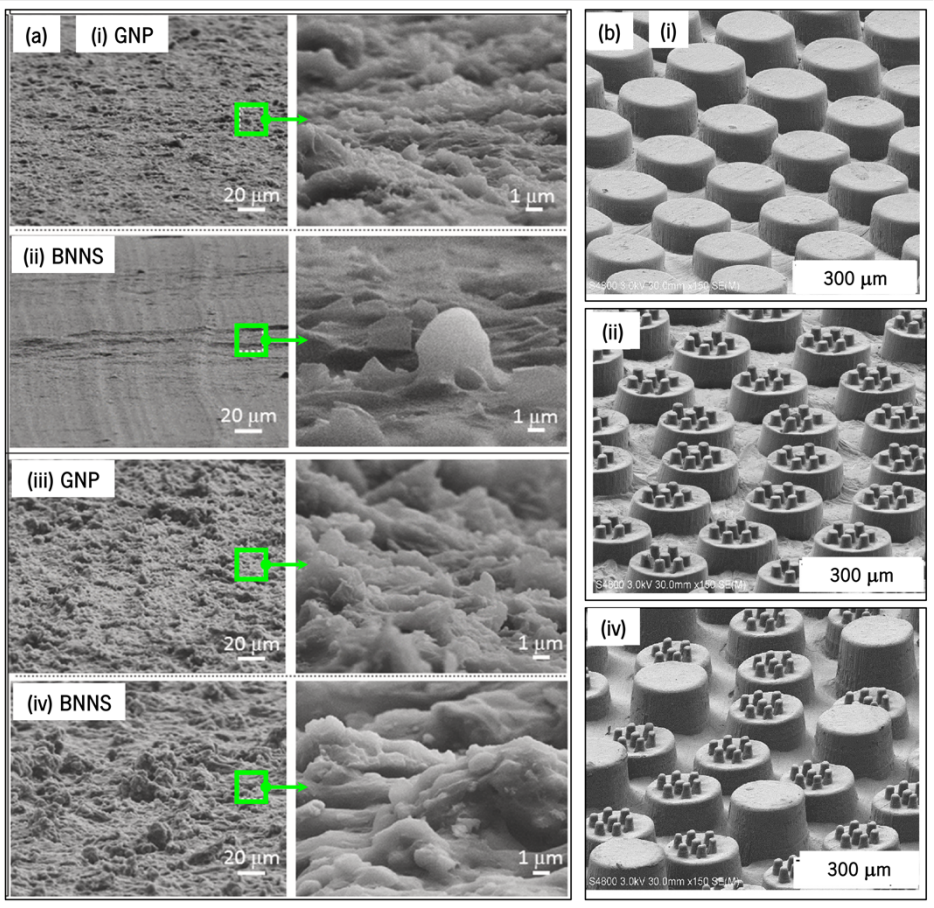


Figure 2.10 – SEM of Propylene (PP) and rubber textured surfaces; (a) SEM of 2D Graphene Nano-platelets (GNP) and hexagonal Boron Nitride Nano-sheets (BNNS) before and after the abrasion on ice; (i) GNP before abrasion, (ii) GNP after abrasion, (iii) BNNS before abrasion, (iv) BNNS after abrasion, (b) (i) only micro-textured PP, (ii) hierarchical micro-micro textured PP, (iii) protected micro-micro hierarchical PP textures [179], [187].

Having discussed the strategies of anti-slipping shoe-soles, a singular approach might not be sufficient and needs a combined one. The combination of material and design imbibing toepads characteristics of frog and gecko can provide a long-lasting solution. Therefore, following chapters of thesis focuses on achieving a right balance between material properties and surface variations.

CHAPTER 3

MATERIALS AND EXPERIMENTAL SECTION

This section compiles the materials' information, processing parameters, and properties in producing the composite. It also consists of compounding procedure of the polymer with nanoparticles to prepare compound, vulcanisation process, and post-processing via laser texturing for obtaining desirable surface effects. Furthermore, this section gathers techniques used in the characterisation of the produced material of multi-functional surface.

3.1. Materials

Three materials were used in the present work namely, SR, zirconium oxide/zirconia (ZrO_2), and titanium dioxide/titania (TiO_2). Zirconia was in the form of micro-agglomerates and titania was already in nanopowder form. The physical properties and process parameters of the materials used during experiments are listed in the following sections. SR was chosen due to its ease of processing, mouldability, and retention capacity of softness at very low temperatures as soft rubber favours the friction. However, soft SR suffers abrasion and wear and therefore reinforcement filler material must be highly resistant to wear and abrasion, and highly hydrophilic at the same time to turn inherent hydrophobic SR wettable. Selection of zirconia and titania nanoparticles is based on their wettable, wear-resistance, and anti-bacterial properties, so the composite produced can also be extended to other biomedical and health applications.

3.1.1. Silicone Rubber

The primary matrix SR was in the form of mouldable high consistency rubber and was procured from "MAFERM Machines & Tools" run by Albino Moutinho Laboratory group, Lda, Portugal. The silicone elastomer, SR is a gummy (little harder than peanut butter) consistent substance is in partially vulcanised sheets, doesn't require special processing/equipment and has straight chains with very high molecular weight. The properties and vulcanisation conditions for the SR are given in Table 3.1.

Table 3.1 – Standard characteristics of silicone rubber with working temperature range of –55°C to 200°C.

Physical properties			
Density ($\boldsymbol{kg/m^3}$)	1100-1500	Rebound resilience	52 – 60 %
Hardness (Shore A)	30 – 80	Typical curing condition	
Tensile strength (MPa)	7 – 12	Press-cure	5 min @ 160°C
Compressive strength (MPa)	2.5 – 4	Vulcanised	Room Temperature
Elongation at breaking (%)	350 – 820	Post-cure	4 hours @ 200°C
Tear strength (N/mm)	15 – 30	Catalyst	Platinum & Peroxide

3.1.2. Zirconium oxide and titanium dioxide

Zirconia used is commercial 3 mol% yttria-stabilized zirconia spray-dried powder purchased from TZ-3YSB-E, Tosoh Corporation, Tokyo, Japan. Titania anatase nanopowder was obtained from Sigma Aldrich (Millipore Sigma) under Merck KGaA group, Darmstadt, Germany. Table 3.2 and Table 3.3 consist of the physical and chemical properties of zirconia and titania, respectively. Selection of anatase over rutile phase is due to its higher surface area and a wider band gap (3.2 eV) that results in higher photoactivity playing an essential role in maintaining the hydrophilic nature of the surface over time.

Table 3.2 – Standard physical and chemical properties of TZ-3YSB-E yttria stabilised zirconia nanopowder.

Physical Properties		Chemical Properties	Weight %
Mass density ($\boldsymbol{kg/m^3}$).	6050	$\#ZrO_2 + H_fO_2 + Y_2O_3 + Al_2O_3$	> 99.9
Specific surface area ($\boldsymbol{m^2/gm}$)	7±2	Y_2O_3	5.15± 0.20
Agglomerate particle size (μm)	60	Al_2O_3	0.25± 0.10
Crystallite size (nm)	36	SiO_2	≤ 0.02
		Fe_2O_3	≤ 0.01
		Na_2O	≤ 0.04
#Calculated value = 100 – ($\boldsymbol{SiO_2}$ +$\boldsymbol{Fe_2O_3}$+ $\boldsymbol{Na_2O}$)			

Table 3.3 – Standard physical and chemical properties of titania nanopowder (Titanium(IV), Oxide, Anatase).

Physical Properties		Chemical Properties	Weight %
Mass density ($\boldsymbol{kg/m^3}$)	4000	TiO_2	> 99.7
Bulk density ($\boldsymbol{kg/m^3}$)	40-60	K	0.0055
Particle size (nm)	25-30	Na	0.0053
Specific surface area ($\boldsymbol{m^2/gm}$)	45-55	Fe	0.003
		Al	0.0022

3.2. Experimental section

3.2.1. Synthesis of zirconia/titania nanopowder reinforced silicone rubber

After obtaining the necessary material from different sources, the process of compounding to prepare the composite takes place. The compounding of composite occurs in four stages as shown in Figure 3.1: (i) initial mastication of the high consistency SR in a two roll-mill, (ii) removal of agglomerates from zirconia and moisture from titania, (iii) mechanical shear mixing of nanopowder and SR, and (iv) mixing in two roll-mill of premixed compound. SR specimens prepared (4 gm of SR) have five percentages of zirconia nanoparticles by weight (also loading) i.e., 1%, 3%, 5%, 7%, and 9% and 0.1%, 0.3%, 0.5%, 0.7%, and 0.9%. High and low percentages of zirconia nanoparticles are used to analyse the effect of loadings. It was established that zirconia-reinforced composite with SR can evidently be processed by compounding and vulcanisation for both high and low loadings, however, only later stages of experiments will prove the effects of loadings. On the other hand, high percentages of titania did not lead to proper compound and despite following the similar process, vulcanisation of high titania-reinforced SR failed to cross link and remained paste. This occurs due to huge volume of titania for weights of 1% to 9% and comparatively smaller size of nanoparticles. Despite the binder removal, zirconia can still be in small nano to few micro-agglomerates that does not hinder with cross linking of the rubber unlike titania that is in fine nano particles and dispersed. Titania-reinforced compound was prepared with 0.1%, 0.3%, 0.5%, 0.7%, and 0.9% loading percentages following the same procedure as zirconia-reinforced compound.

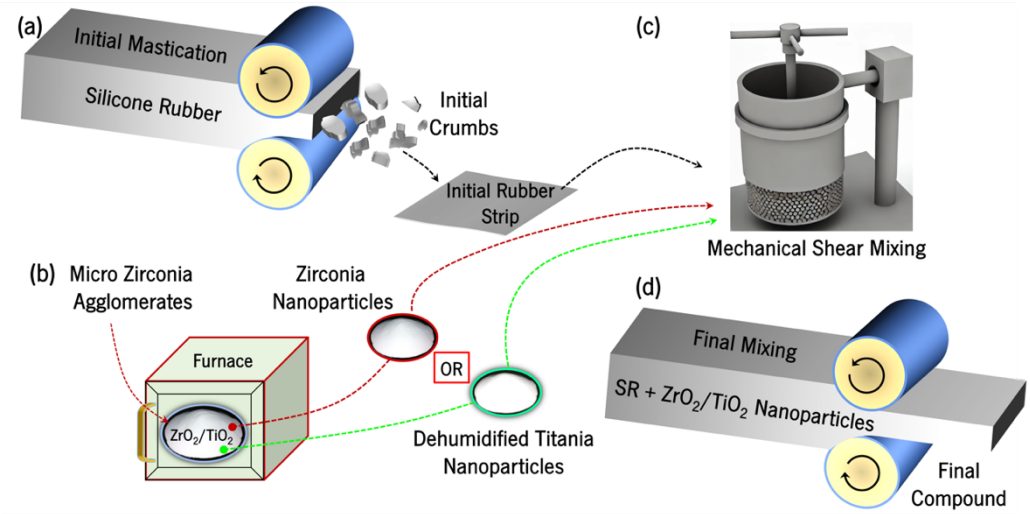


Figure 3.1 – Schematic representation of compounding method to fabricate nanoparticle-reinforced SR composite; (a) initial mastication of high consistency silicone rubber to small crumbs in two roll-mill and finally into a thin strip, (b) preparation of zirconia or titania nanopowder to mix with silicone rubber prepared after initial mastication. Zirconia is available in micro-agglomerates and needs to be binder removed followed by storage in vacuum vessel. Titania is already in nano form and just requires removing moisture contents before mixing, (c) mechanical shear mixing in mini extruder to initially blend nanopowder with silicone rubber to avoid material loss, (d) final mixing of silicone rubber with nanoparticles in two roll-mill.

3.2.1.1. Preparing silicone rubber

SR is semi-vulcanised high consistency thick paste and needs to masticate before mixing it with nanoparticles. Initial mastication of SR breaks it into small pieces due to the entanglement of molecular chains into smaller crumbs by virtue of yield stresses before re-agglomerating into another bulk. As mechanical force is applied, these chains are gradually broken down, aligned, and uniformly distributed. This process eventually leads to a smooth, soft strip as the internal stresses are reduced and the rubber becomes more homogeneous. The heat generated from mastication also contributes to softening the material. Initial mastication greatly helps in properly mixing nanoparticles, otherwise, immediate rolling of SR with nanopowder leads to material loss, improper and non-homogeneous dispersion along with other mixing and handling difficulties Dual speed two roll-mill (high and low) showed in Figure 3.2 is supplied by "Porfil Pereira Gomes & Sons Lda, Portugal" that supplies mechanical metalworking machines for jewellery industry and initially masticates the SR shown in Figure 3.1(a).



Figure 3.2 – An image of two roll-milling machine used for producing composite. Supplied by: Porfil – Mechanical Metalworking industry suppliers of machines for the jewellery industry from Pereira Gomes & Sons Lda, Portugal.

3.2.1.2. Obtaining dehumidified nanopowder of zirconia and titania

Smoothed and masticated SR is ready to be mixed with zirconia or titania nanopowder. However, zirconia is in micro-agglomerates and requires breaking down into nanoparticles through the binder removal as shown in Figure 3.1(b). The binder is removed inside a muffle chamber furnace as shown Figure 3.3, procured from "Thermolab Fornos Electricos Lda, Portugal". Zirconia powder was kept inside the furnace and maximum temperature was set to 400°C with heating rate of 5°C/minute. After attaining 400°C, stage cycle maintained for 30 minutes followed by cooling with the rate of 5°C/minute. The process takes approximately 4 hours to finish the whole cycle from room temperature to back at the same. Figure 3.4(a) shows Scanning Electron Microscopy (SEM) images of the zirconia nanoparticles after the removal of binder and titania nanoparticles. one can clearly see that zirconia is still in some agglomerates despite the binder removal. These agglomerates are smaller and less in number. Figure 3.4(b) shows titania nanoparticles that are

well dispersed and hardly have any agglomerates. Both the nanopowders are shown in Figure 3.4 after the moisture removal in the furnace



Figure 3.3 – An image of chamber muffle furnace (maximum temperature = 1380°C) used to deagglomerate zirconia micro-agglomerates to nanoparticles and dehumidify titania. Supplied by: Thermolab Fornos Electricos Lda, Portugal.

Unlike the zirconia, titania is already in nanoparticles, nevertheless removing moisture content from titania nanopowders before mixing with polymers is essential to improve dispersion, prevent defects, avoid unwanted chemical reactions, and enhance the interfacial interaction between the nanoparticles and the matrix. Moisture can lead to agglomeration, void formation, and unwanted side reactions, reducing the effectiveness of the composite. The process of binder removal takes care of moisture content for zirconia. Titania nanopowder was placed inside the muffle chamber furnace at 150°C for 30 minutes with heating and cooling rate of 5°C/minute. The whole process takes about 2 hours to complete whole cycle. Figure 3.1(b) also pictorially represent titania after removal of moisture and going for mixing with SR that comes out of rolling mill. Figure 3.4(b) exhibits SEM of the titania nanoparticles relative to their size.

3.2.1.3. Mechanical shear mixing

Mechanical shear mixing is a process to contain volatile nanoparticles inside the container and mixed it with SR obtained from initial mastication so nanoparticles can be contained and embedded in SR without any material loss. The hand operated mixer blender squeezes and shears rubber and nanoparticles continuously crushing any minute agglomerates especially for zirconia. Figure 3.1(c) shows a container fixed with rotating blender used for this purpose and based on the

experienced quality of mixture, it was concluded that proper mixing takes approximately 45 minutes to 60 minutes.

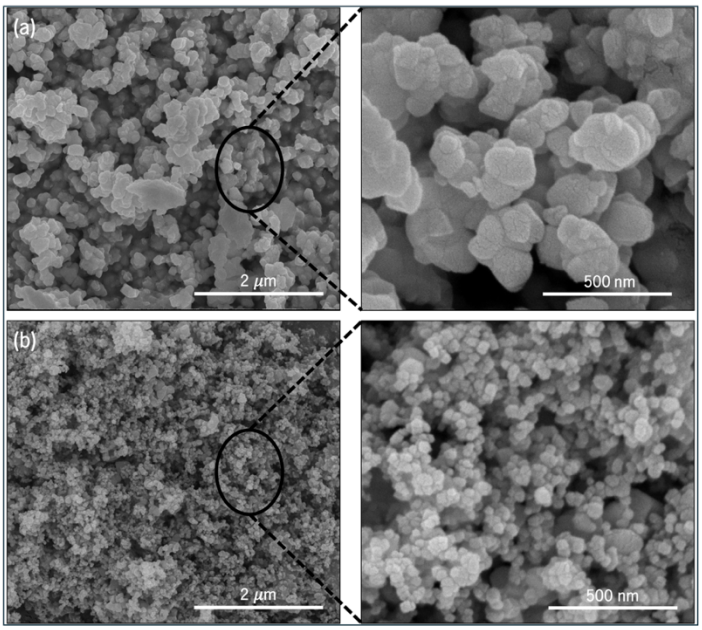


Figure 3.4 – SEM micrographs showing morphology and relative size of the nanoparticles; (a) zirconia micro-agglomerates and magnified version of the nanoparticles, (b) titania nanopowder and magnified version of nanoparticles.

3.2.1.4. Final mixing of pre-mixed compound

Compound obtained from the shear mixing goes through final round of high intensity roll milling as shows Figure 3.1(d). This mixing does not involve any crumbing of the compound rather a smooth SR strip with uniformly distributed nanoparticles. Throughout the roll milling operations, the rolling gap was decreased constantly to squeeze and integrate the compound furthermore to avoid any possible cracks or porosities in the later stages of the process. The nip gap (minimum achievable gap between the rolls) ranges between 200 μm to 500 μm for the equipment used in our experiments.

3.2.2. Vulcanisation of nanoparticle-reinforced silicone rubber compound

Vulcanisation is a chemical process that improves the mechanical properties of SR such as elasticity, durability, and thermal stability by crosslinking polymer chains. During the process, SR is heated and then crosslinking agents present in SR paste promote the formation of covalent bonds between polymer chains transforming it from a soft, sticky state to an elastic, resilient structure. At high temperature, the curing of the compound also occurred. Vulcanisation process takes place in a hot compression moulding machine placed inside an acrylic vacuum chamber

consisting of vacuum pump to deaerate it. Hot compression moulding is shown in Figure 3.5(a) used is a 2-phase, 220 volts machine supplied from “Hispana De Maquinaria, Barcelona, Spain” and has 250 mm × 250 mm counter moving plates. Maximum temperature reaches to 220°C and pressure up to 250 MPa without deforming plates. We used flame-resistant, anti-inflammatory fabric to contain the heat by wrapping it around the plates and because of that measured temperature can record a rise up to 250°C. This ready to vulcanise compound is placed inside an aluminium mould cavity of the size of specimens (15 mm) as shown in Figure 3.5(b). Moulding plate of 200 mm × 75 mm × 20 mm is a two-part aluminium plate held together by screws for easy removal of the specimen. The mould is large enough to conduct heat from the compressing machine plates when compound is placed inside the cavity and pressed until both the counter plates make complete contact with moulding plate. The punches are cylindrical two pieces of bottom 2 mm and top 12 mm, hence, the produced specimens are approximately 6 mm in height. We always made sure to utilise 20% more material than required to have desired size so to compress enough and flows outside in case of excess. This excess material of compound makes sure that porosities or pinholes are not present in the vulcanised specimens. After the preliminary vulcanisation tests for several specimens, it was concluded that 60 minutes is the optimum time for the complete cross linking and any time after that does not lead to any improvements in the quality of composite.

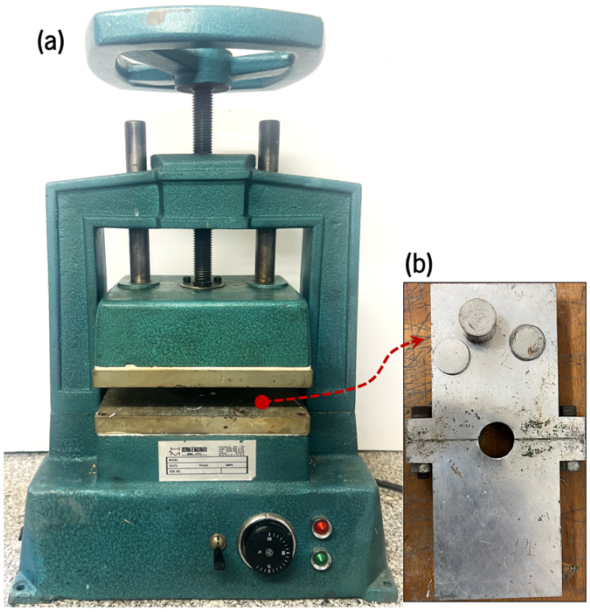


Figure 3.5 – Vulcanisation set-up and mould; (a) hot co pression moulding machine for vulcanisation, (b) aluminium moulding plate in assembled position with punches at the top.

3.2.3. Role of laser in optimisation and surface modification

Laser Surface Texturing (LST) was adopted for its merits over other surface texturing techniques because of localised treatment, non-contact application, high precision and control, ability to produce intricate and complex geometries, high speed, versatility in material compatibility etc. Apart from that, laser also modifies the composite surface to expose nanoparticles using selective ablation. This ablation is a continuous process of melting and evaporation of SR from the surface creating micro-roughness in the form of textures and micro-nano roughness on the surface of microstructures themselves. These micro and nano level roughness along with textures alter the wettability of the surface without compromising bulk properties of the composite. As the motive of the study lies in the capacity to absorb water through capillarity, it is essential to explore best geometries and sizes of the cavities among textures that will help to simulate a range of dimensional geometries for the optimum capillarity. Wettability is a function of physical geometry as much as chemical composition. Hence, laser photolithography used to explore optimum dimensions of the texturing geometry before going through LST to predict the best possible dimensions and geometries.

3.2.3.1. Laser photolithography

Laser photolithography is a precision technique used in microelectronics to create intricate patterns on substrates like silicone wafers or Polydimethylsiloxane (PDMS) by utilising laser light to expose a light-sensitive material called photoresist. The process begins by coating the substrate with the photoresist, which is then selectively exposed to a laser through a mask that contains the desired pattern. After development, the patterned areas are either etched or deposited, transferring the design onto the substrate. PDMS photolithography was done for cylindrical and conical cavities. Despite that the PDMS is hydrophobic in nature and will not absorb water inside the lithographed cavities, holes were made through so water rises inside the cavities. Jean-Baptiste Gorce et al. examined the capillary imbibition into tubes where the radius decreases in the direction of flow (conical shape) compared to traditional cylindrical tubes of constant radius described by Washburn's law. The simulation and experimental findings concluded that in tubes with a radius changing according to a power-law relationship, liquid imbibition occurs more quickly (almost half) compared to constant-radius tubes. Experiments of capillary rise confirmed that circular conical holes possess least water suction timings depending on the inlet radius to height against uniform cylindrical hole. Based on extensive geometrical trials with diameters ranging from 1 mm to 100 µm and heights between 1 mm to 2 mm, it was concluded that diameter below 500 µm yield the

best suction timings irrespective of height. Specifically, diameters of 250 µm, 200 µm, and 150 µm were chosen as inlet diameters for generating capillary action in a conical cavity due to their optimal performance in capillarity. Cylindrical cavity was found to be most effective in 500 µm diameter and 2 mm height as the capillarity observed in other cylindrical dimensions was not substantial. Nevertheless, conical shaped geometries outperformed uniform section cylindrical cavities and hence considered for the fabrication. Figure 3.6 is a visual manifestation of different conical shapes with entrance diameters and one optimum cylindrical entity.

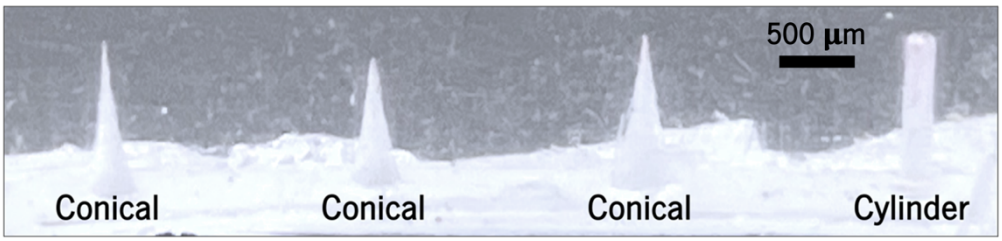


Figure 3.6 – A visual reference that resembles the concept of conical and cylindrical cavities formed using laser photolithography.

3.2.3.2. Laser surface texturing

After the selection of optimum geometrical shape and size of the capillary cavities, LST was used to deliver desired entities. Conical structures by removing the material from the surface of the vulcanised nanocomposite were obtained. Laser used in the experiments is an Nd: YV04 fibre laser (Model: XM-30D Fibre Laser Marking Machine) of 30 watts maximum power, 10 µm spot size, 10 µs pulse width, 1064 nm wavelength, and focal distance of 160 mm as shown in Figure 3.7.

The experimental set up consists of a laser, exhaust system (suction unit) to extract removed vapourised debris, argon atmosphere around the specimen to create inert surroundings as shown in Figure 3.7. Continuous stream of argon not only blows away molten material, creates inert atmosphere but also reduces the heat affected zone that can lead to brittleness of the rubber compound. During LST, microsecond pulsed laser waves break the nanocomposite's bonds by photo-chemical effect, increase the temperature by photo-thermal effect, and propel of molten material from the surface by the shock waves by photo-physical effect. Figure 3.8 shows comprehensive strategic method to produce conical cavities on the surface of specimens with desired dimension. Figure 3.8(a) shows interaction of laser with nanocomposite following the instructions given by EzCAD laser operative software. Parallel lines 10 µm apart were drawn to

cover the cut dimension (such as 26 lines for 250 µm, 21 lines for 200 µm, and 16 lines for 150 µm) due to the 10 µm spot size of the laser.

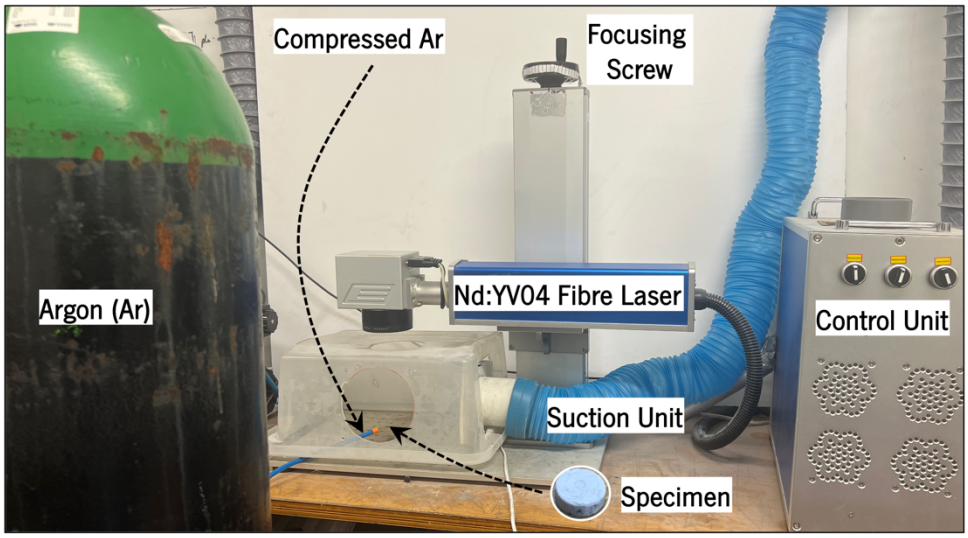


Figure 3.7 – Experimental set up of laser surface texturing for nanopowder-reinforced silicone rubber composite.

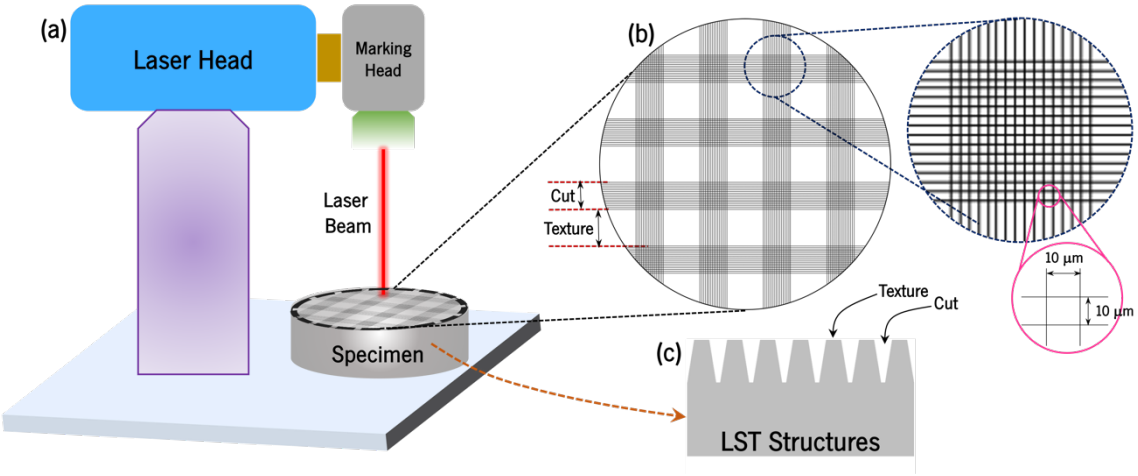


Figure 3.8 – LST of vulcanised composite; (a) laser machine setup, (b) cutting strategy i.e., parallel lines at 10 µm apart to attain desired cut (capillary cavity), (c) LST structures produced showing conical cavities.

The laser beam converges as it enters the bulk material, creating a conical shape with nearly linear tapering, while simultaneously exposing the nanoparticles embedded within the rubber compound. The interspacing between cuts is maintained at approximately 500 µm to ensure the structural integrity necessary to withstand adhesion forces without damage. This interspacing represents the width of the micro-pillar/texture at the top. To prevent excessive heat buildup, each line of cuts was made in a staggered sequence like starting with the first line of each

groove, then moving on to the second instead continuously cutting adjacent lines. This staggered approach allowed the nanocomposite material to cool down, dissipate heat, and release residual stresses effectively. Without these precautions, continuous cutting would have led to significant melting, remelting, debris formation, and vaporisation, resulting in poor quality cuts and considerable thermal stress [169],[170],[171]. The process parameters used to optimise LST are power, scanning speed, and number of passages by keeping frequency and other parameters unaltered for the whole experimentation. Extensive study was done to optimise laser process parameters on pure vulcanised SR and nanocomposite for both quantitative and qualitative until best possible values were obtained as records Table 3.4. Additionally, Table 3.5 gathers number of specimens for each condition i.e., percentage of nanopowders per textures along with control specimens.

Table 3.4 – Optimised preliminary and finalised laser process parameters for textures.

LST Conditions	Preliminary Parameters	Final Parameters
500 × 150 500 × 200 500 × 250	Power = 15 W for first 50 passages followed by 12 W for next 50 passages. Scanning speed = 1000 mm/second, Frequency = 20 kHz	Power = 15 W, Scanning speed = 1000 mm/second, Passages = 100, Frequency = 20 kHz

Table 3.5 – Number of specimens for each percentage of nanopowder and LST.

Percentage of Nanopowder by weight (No. of specimens)	500 × 150	500 × 200	500 × 250	No Texture
1wt% (15)	4	4	4	3
3wt% (15)	4	4	4	3
5wt% (15)	4	4	4	3
7wt% (15)	4	4	4	3
9wt% (15)	4	4	4	3
Control specimens (Pure SR) = 5				
**Equal number of specimens for 0.1wt%, 0.3wt%, 0.5wt%, 0.7wt%, and 0.9wt% for zirconia and titania*				

3.3. Advanced characterisation and friction tests

The material characterisation techniques used for the morphological, physical, mechanical, and chemical characteristics of produced nanocomposites and MFSs. The advanced characterisation techniques encapsulate surface analysis, composition observations, and hydrophilic properties. Additionally, a large section is dedicated to the frictional analysis of the MFS against wet ice. Information of equipment, dimensions of the specimens, parameters adopted for tests are the key elements of this section.

3.3.1. Morphological and dimensional, analyses of surface

SEM is a distinctive and advanced imaging technique used to examine the surface topography and composition of materials at the micro and nanoscale. It works by focusing a beam of high-energy electrons onto the specimens' surface. When these electrons interact with the atoms in the specimen, they produce various signals including secondary electrons and backscattered electrons which are collected to generate highly detailed images of the surface. The SEM used here was JSM-6010 LV, JEOL, Japan equipped with an Energy Dispersive Spectroscope (EDS) (INCAx-Act, Penta FET Precision, Oxford Instruments). Secondary electron and back scattered electron both modes were used to perform the investigation. Being a non-conductive material, SR has very poor imaging characteristics. Thus, a sputtering coating of gold-palladium alloy was required to prevent surface charging stimulating secondary electrons and yielding a homogeneous conductive surface. SEM used additional settings such as low vacuum mode (accelerating voltage = 10 kV and spot size = 50 nm) and high vacuum mode (accelerating voltage = 15 kV and spot size = 40 nm). By performing EDS analyses, the dispersion and presence of nanoparticles were also confirmed that were exposed due to laser surface ablation. To further analyse the surface roughness, a Profilm 3D Optical Profiler (2592×1944, 5 MP, 4X) with anti-vibratory table was used. ImageJ's Fiji was used as an image processing software to determine the dimensions of laser textured pillars.

3.3.2. Strength and elasticity analyses

Elasticity (Young's modulus) testing is a method used to evaluate strength of the material against the mechanical stresses, specifically measuring their ability to deform and return to their original shape. During the tests, a controlled force, and the resulting deformation is recorded to determine its elastic modulus or stiffness. This is also vital to understand integrity, material's resilience, and suitability for shoe-sole applications as repeated contact of sole with ice/wet surface occurs. Young's modulus was obtained by the compression test using an Instron-8874, USA universal servo-hydraulic testing Universal Testing Machine (UTM). The tests (three tests per specimen and three specimens for each condition) were performed at the 5 mm/minute movement speed at room temperature as per the ISO:13314 standards. Furthermore, tensile tests were also performed using Hounsfield H100KS precision UTM at 5 N preload, gauge length of 20 mm, and speed of 50 mm/minute. Figure 3.10 shows the preparation of nanocomposite specimens and mounting in the machine followed by failed specimen after the test. The neck area of the dog bone specimen is 8 mm × 3 mm and original length of the curved section is 20 mm. Obtained load vs deflection values were converted appropriately using the dimension of the

specimen and changed o stress vs stain to plot and finding the elasticity as slope of the curve. For compression tests, the cylindrical diameter of 15 mm was converted to the area 176.71 mm^2 and initial length was 5.5 mm.

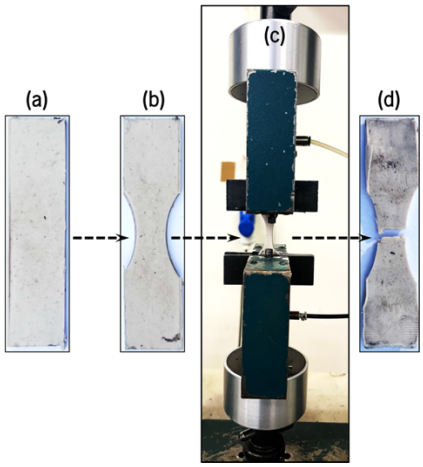


Figure 3.9 – Schematic set up of UTM for elasticity tests; (a) silicone rubber composite, (b) silicone rubber composite in dog-bone shape, (c) fixture of the specimen in the UTM machine, (d) fractured silicone rubber composite specimen after reaching its ultimate tensile strength.

3.3.3. Surface hardness

Hardness of the soft polymers is measured by Shore hardness durometer. It measures the resistance of a material to indentation, specifically for materials like rubber, elastomers, and some plastics. Durometer, which applies a specific force to the material's surface and measures the depth of indentation. Shore A hardness durometer from SAUTER HDA 100-1, Germany (SAUTER HD Version 2.3 Serial: IA1400001) measured hardness. The resolution was 0.1 resolution, range was 0~100 hardness scale, and accuracy level was $\leq \pm 1\%$. Five measurements were done per specimen, and three specimens were selected for each condition. The specimens were placed carefully at the centre of the probe and in 2 to 5 seconds, the durometer readings were stabilised and recorded.

3.3.4. Fourier Transform Infrared Spectroscopy

Attenuated Total Reflectance - Fourier Transform Infrared Spectroscopy (ATR - FTIR) is an analytical technique used to identify and study the molecular composition based on the interaction of electromagnetic radiation with the material to reveal the structure, chemical compounds, and changes that take place at the time of chemical reaction. In an FTIR setup, a beam of infrared light is passed through the specimen, and the system measures which wavelengths are absorbed/transmitted by the sample. This absorption/transmittance occurs because

specific chemical bonds within the molecules vibrate at characteristic frequencies. Hooke's law defines vibrational frequencies of molecular bonds and frequency of vibrations are given by Equation 3.1.

$$\mathfrak{f} = \frac{1}{2\pi}\sqrt{\frac{F}{\mu_m}} \qquad \text{Equation 3.1}$$

Where; $\mathfrak{f}$ is the vibrational frequency, F is the force constant of the bond (depends on bond strength), μ_m is the reduced mass of the atoms involved in the bond. The peaks of absorbance or dip in transmittance recorded against wavenumber (cm^{-1}). The Beer-Lambert law governs absorbance ($A = -\log(T)$), on the other hand, transmittance is measured in arbitrary units (a.u.) and is expressed as the ratio of the transmitted intensity (I) to the incident intensity (I_0). Equation 3.2 gives transmittance (T);

$$T = \frac{I}{I_0} \times 100 \qquad \text{Equation 3.2}$$

The FTIR spectra of the specimens were performed on a Shimadzu IRAffinity-1S single beam Michelson Interferometer, Kyoto-Japan. The ATR-FTIR spectra were analysed between 400 cm^{-1} to 4000 cm^{-1} with 100 scans and a resolution of 8 cm^{-1}.

In order to analyse the crystalline phases of zirconia and titania in the SR matrix, an XRD analysis was also performed using X-Ray Diffraction - Bruker D8 Discover equipment that is a high angle diffraction and high-resolution machine. The peaks of the diffraction curve were carefully analysed and represented with their crystallographic lattice structures.

3.3.5. Wettability and capillarity

Wettability of the textured composite surface was measured using contact angle (β) by "Sessile Drop Method" with an optical tensiometer/goniometer (OCA 15 plus, DataPhysics, Germany) at room temperature (≈ 23 °C). A drop of 5 μL volume of tap water was dispensed on the textured composite surface by a micrometric syringe. As the water on the molten ice/snow is natural liquid with impurities, salt and other substances, therefore, always used tap water to establish effects as close as to the real-life scenario. Before the measurement, specimens were properly cleaned and dried with ethanol for 120 seconds ultrasonically. The contact angles were confirmed and displayed using Fiji image graphic software after analysing through DataPhysics SCA software that uses Laplace-Young model creating an outline of the droplet. Additionally, quantitative analysis of ultrafast water absorption due to wettability converting into capillarity is important to determine the time of suction. The high-resolution videos were captured by a high-

speed camera (OLYMPUS i-SPEEDLT) and further converted to the smallest frames possible i.e. approximately 0.5 millisecond per frame. The specimens were glued upside down on a frame, and a pipette filled with water was brought closer until it reached the point where the liquid drop emerging from it touched the specimen's surface. These tests are dependent on human factor like closeness of the pipette and the time of absorption, nevertheless, the margin of error does contradict the proof of the concept.

3.3.6. Bacterial adhesion

Prior to conducting in vitro tests, the specimens were first immersed in absolute ethanol for 2 minutes. They were then rinsed with distilled water and placed in an ultrasonic bath (250 W, 50 kHz, J.P. Selecta, Barcelona, Spain) for 30 minutes. Following this, the specimens were rinsed three times with distilled water. After rinsing, they were immersed in ultra-pure water for 20 minutes and subsequently transferred to an open Petri dish. The specimens were then exposed to UV-C radiation for 20 minutes inside a biological safety level 2 airflow chamber. After UV exposure, the specimens were transferred under sterile conditions to a 2 mL Eppendorf tube containing 1.5 mL of absolute ethanol for 48 hours. Finally, the specimens were left to air-dry for 24 hours at room temperature inside an airflow chamber.

For the preparation of the bacterial pre-inoculum, a single colony P. aeruginosa (CIP 76.110) was isolated from an agar plate and cultured overnight in Tryptic Soy Broth (TSB) at 37°C under dynamic conditions with shaking at 120 rpm. The bacteria concentration was adjusted to an optical density of 0.125 at 600 nm using a spectrophotometer equivalent to approximately 1.25×10^7 CFU/mL. After adjusting the concentration, 1 mL of bacteria suspension was inoculated onto the zirconia specimens placed in 24 - well plates. The bacteria culture was incubated for 24 hours at 37°C under dynamic conditions again with shaking at 120 rpm.

For the quantification of adhered bacteria, the supernatant in the wells containing specimens' discs was discarded, and each disc was transferred to an individual Falcon tube with 6 mL of Phosphate Buffered Saline (PBS). Subsequently, the microtubes, each containing a single specimen, underwent ultrasonication for 10 minutes (50/60 Hz, J.P. Selecta, Spain) and vortexing for 1 minute to detach bacteria adhered to the disc's surface. Serial dilutions were then carried out in PBS, and the bacterial concentration was determined by plating on Tryptic Soy Agar (TSA) medium (Merck, Darmastadt, Germany), followed by incubation at 37 °C overnight. Subsequently, the viable colonogenic cell numbers, measured in Colony Forming Units (CFU) per millilitre

(CFU/mL) were enumerated. These units represent the quantity of cells capable of sustaining viability, proliferation, and the formation of small colonies.

3.3.7. Sliding friction test

A friction enhancement test for the vulcanized, textured, nanopowder-reinforced SR was performed on a modified friction tribometer, which was placed over a Peltier-based refrigerator. The Peltier-cooled device was used to freeze domestic water to simulate real streets or pavements in cold climates, where ice can be several centimetres to meters thick. The COF was determined by calculating the friction force required to break the capillary pillars frozen inside the textured surface. A composite specimen of 15 mm was glued with superglue onto a specimen fixation (a cylindrical brass piece) that could freely reciprocate inside a tight-fitting glass tube, as glass offers minimal frictional resistance with brass. The acrylic block accommodating the specimen assembly extends to an acrylic tube to guide the weights. The weights were molten and cast from lead due to their low volume-to-weight ratio.

Figure 3.9 shows a fully functional tribometer setup that was used to perform drag tests on ice. The portable tribometer was placed over the temperature-monitored icing device and moved in a horizontal direction, with the specimen connected by a rigid rod to the load cell. Parameters such as speed, number of cycles, and test duration could be adjusted via tribometer's guided user interface. When the specimen touches QLL on wet ice, it instantly freezes followed by the movement of lead screw to break the micro-frozen pillars. The forces required to overcome the initial interlocking followed by dragging were recorded by the load cell's guided user interface. The free movement of the specimen fixation inside the glass tube was crucial to ensure that the normal load applied to the specimen remained unaffected by any other force component except in the normal direction.

Modified friction device tested the drag in the form of frictional/tangential force over wet glistening ice (–5°C to 0°C) under normal atmospheric conditions. The tests can be affected by the atmospheric temperatures given exposed ice can be just wet to flooded. All the tests were performed at approximately 15°C and 65% to 75% relative humidity (atmospheric conditions). Under these conditions, ice was maintained wet at its surface.

Ideally, a 70 kg (687 N) human body with a foot area of 0.01 m^2 (EU 41/UK 7/USA 8) walks at a speed of 1.35 to 1.40 m/s for brisk movement or 1 to 1.2 m/s for a normal pace. However, on slippery ice, the walking speed decreases between 0.5 to 0.7 m/s, with an average of 0.6 m/s. Under these conditions, an individual exerts approximately 68.7 kPa of pressure while

walking. Tribological tests were conducted in the laboratory using a 12 N normal load on a 15 mm cylindrical specimen, resulting in approximately 68 kPa of surface pressure to calculate the SCOF and DCOF.

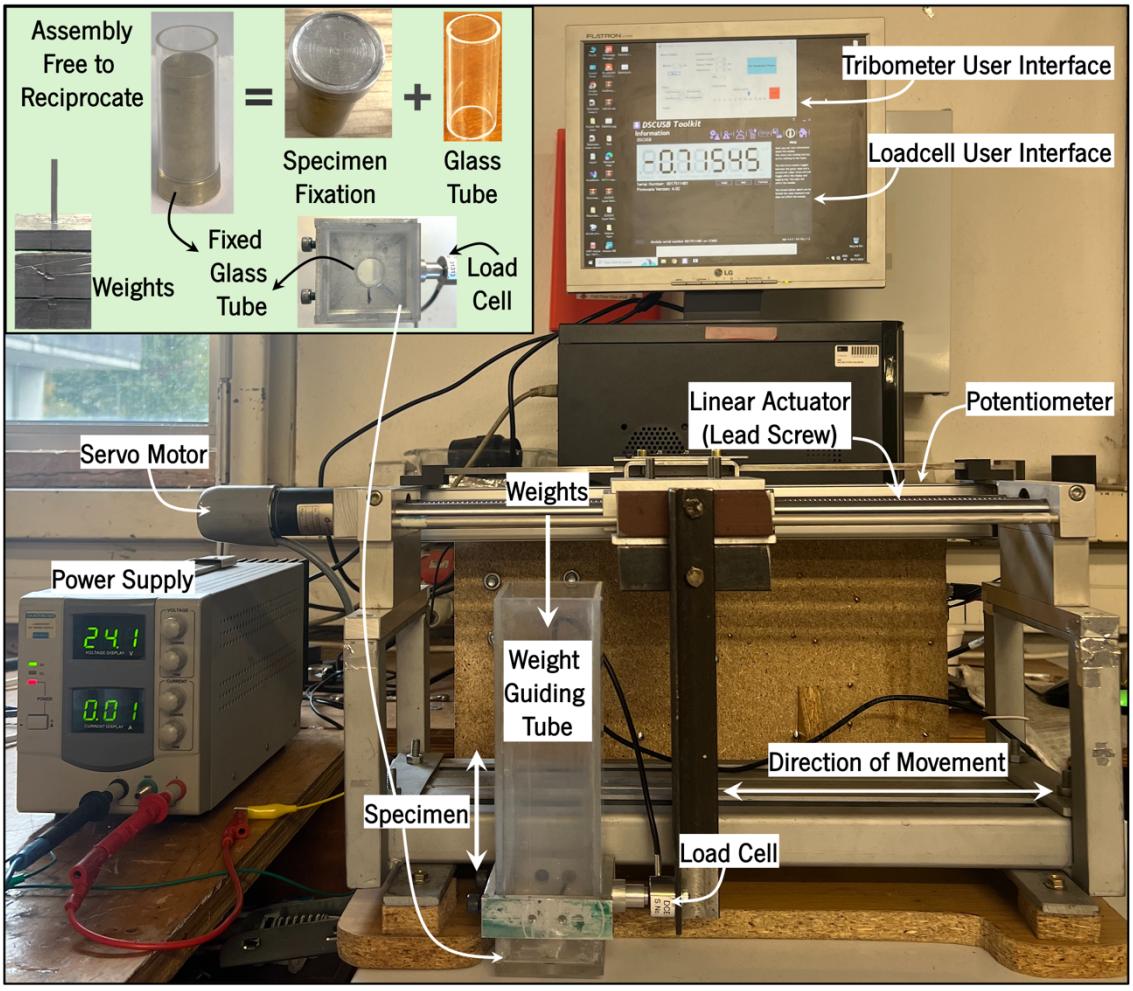


Figure 3.10 – Schematic set up of a functional friction tribometer modified for the purpose of sliding test on ice.

Test were performed at two frequencies 0.05 Hz (5 mm/sec) and 0.1 Hz (10 mm/sec), with a total stroke length of 100 mm. Two speeds will demonstrate the change in COF with respect to walking speed, which is typically considered negligible in the classical law of friction. Additionally, performing some tests with different loads resulted in equal COF as frictional force varies proportionally to normal load, maintaining the ratio approximately constant. Changes in body weight due to acceleration were neglected since the tests were conducted at the lowest possible speeds, leading to similar pressure variations during weight shifts. The DSUSB interface from the load cell converts signals from load cell to force that was further used to determine the COF.

CHAPTER 4

RESULTS & DISCUSSIONS

This chapter is the core evaluation of the PhD work and consists of results followed by in-depth discussions on the obtained outcomes. It records performance of the nanocomposites produced during friction and capillary/wettability analyses alongside advanced materials and surface characterisations. The section will simultaneously compare the effect of loading through zirconia nanocomposites and material variation through zirconia and titania nanocomposites.

4.1. Morphology and topology

The roughness, existence of hydrophilic substance in the form of nanoparticles, and dimensional analyses are vital to understand the surface characteristics of the fabricated MFS and its interaction with water and ice. Hence, surface characterisations using advanced analytical techniques are discussed to determine the functional properties of the MFS.

4.1.1. Surface morphology and roughness analyses

The surface morphology and composition of materials are fundamental characteristics that determine their overall behaviour, performance, and life in surface encountering applications such as shoe-soles, where a constant adhesion and de-adhesion takes place frequently yielding severe cyclic stresses. Morphological analysis provides insights into the surface structure, roughness, particle shape, size, and distribution, while compositional analysis reveals the elemental or chemical makeup of the material. A systematic morphological and topographical analyses were performed for the zirconia and titania nanocomposites. SEM observed the surface characteristics with the help of EDS like presence of nanoparticles and their dispersion as size and shape of the nanoparticles are already known from their properties. On the other hand, topological analysis determines the geometries and dimensions of textures produced using laser. These characteristics together influence properties such as mechanical strength, thermal stability, wettability, and friction on wet icy surface making them critical for optimising material composition. An overall understanding of the material composition and the modified surface of the nanocomposite will establish as how the microstructural and compositional features contribute to the desired functional properties.

This thesis discusses the performance and characterisation beginning with high amounts of zirconia nanocomposites at weight percentages of 1wt%, 3wt%, 5wt%, 7wt%, and 9wt% while simultaneously comparing zirconia small percentage loadings of 0.1wt%, 0.3wt%, 0.5wt%, 0.7wt%, and 0.9wt%. The comparison between high and low loadings will determine the effect of nanoparticles in a compound, whereas comparison between low loading of zirconia and titania will establish the effects of nanoparticles in a similar matrix material.

Introduction of hydrophilic nanoparticles in SR matrix is a way to introduce hydrophilic substance in the hydrophobic matrix and then make them active by uncovering through laser treatment. Because pure SR does not respond well to laser treatment due to its poor thermal conductivity, low laser energy absorption, mechanical stability, and elasticity. Stable and highly temperature resistant zirconia and titania that are affine to lasers used as reinforcements. The

reinforcements do not only introduce polar groups but also participate in improving the mechanical strength, stiffness, and toughness. Zirconia's hydrophilic characteristic arises from hydroxyl groups (-OH) and the ability to undergo surface adsorption. The efficacy of zirconia that is inherently polar forms hydrogen bonds with water molecules establishing strong dipole-dipole interactions and has been exploited in this work along with titania. The surface micro-structures shown in Figure 4.1 clearly demonstrate that addition of zirconia favours the machinability of the material in addition to the changes in its morphology i.e. roughness. The locations of nanoparticles provide the active sites for laser beam to heat, melt, and evaporate SR giving it more depth of cut. These locations of zirconia crystals on the surface can be active sites for multiple bonds to facilitate water adhesion for filling-freezing effect or various biomedical applications like tissue integration with biological fluids, enhancing cellular adhesion [188], [189], [190], [191].

Laser energy interacts with zirconia nanopowders embedded in SR composite and triggers a combination of thermal, optical, and structural effects. Zirconia nanoparticles have excellent thermal stability, optical properties, and efficiently absorb laser energy resulting localised heating of the composite sites. Thus, with increase in zirconia loading, more laser energy gets absorbed leading to rougher, deeper cuts and can be compared from 0wt% to 9wt% nanocomposite from Figure 4.1. SEM micrographs also depict increment in surface roughness and fragility of the micro-pillars. It can be observed from Figure 4.1(a) that pure SR has a smoother smooth surface and as percentage of zirconia increase, roughness increases. Figure 4.1 also demonstrates the presence of zirconia by surrounding them with white circles. As roughness increases with higher amount of zirconia, the visibility of the nanoparticles goes down because of high machinability originating from higher loadings increase engulfing of nanoparticles in large irregularities. Absorbed heat through laser machining can also enhance interfacial bonding between the polymer matrix and the nanoparticles by promoting adhesion and potentially changing the polymer's cross-linking density. However, this adhesion will not be a favourable aspect for the wettable behaviour as it also leads to engulfing of nanoparticles which are the major player in interacting with QLL [122], [192], [193].

On the other hand, the nanometre size and large surface area provide titania a sizeable volume fraction inside the SR matrix and thus, despite being in small quantities it can impart distinct properties from the bulk polymer. The dispersion of zirconia and titania nanoparticles can be observed from Figure 4.2(a) and 4.2(b) at smaller loadings, respectively. The micrographs exhibit the presence of both the nanoparticles, and it can be observed that titania nanocomposites exhibit more surface roughness than zirconia nanocomposites. This comparative rise in roughness

can be attributed to the dispersion and specific volume of the titania inside the SR matrix. As titania's dispersion is better than zirconia, it has more homogeneous locations to interact with laser energy and laser removes more material and creates larger roughness dispersed all over the surface. Titania's photocatalytic activity especially in the anatase phase is activated by the laser generating reactive oxygen species that clean the surface by breaking down organic contaminants and introducing polar functional groups like hydroxyl (-OH). These changes increase the surface energy, improving water spreading and adhesion. The surface roughness at high and low loading appears to be approximately in equilibrium based on visual observations [194], [195], [196], [197], [198].

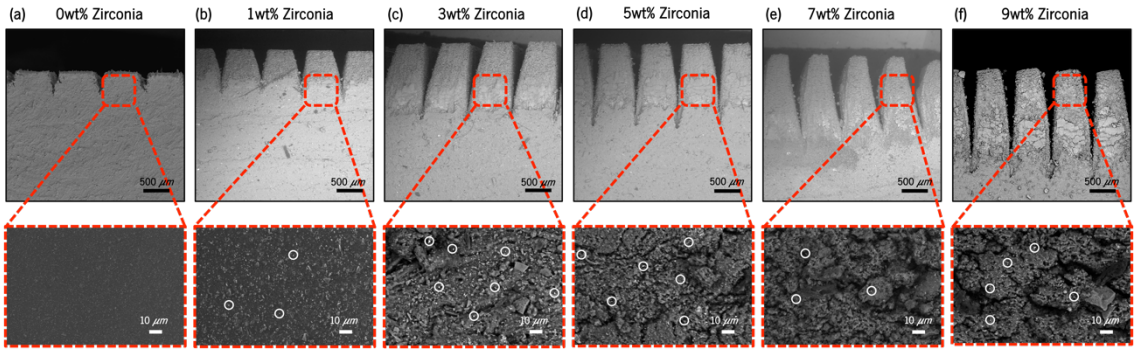


Figure 4.1 – SEM micrographs to show the geometry obtained for zirconia specimens for different weight percentages with optimum texturing geometry of 500×200; (a) 0wt% zirconia, (b) 1wt% zirconia, (c) 3wt% zirconia, (d) 5wt% zirconia, (e) 7wt% zirconia, (f) 9wt% zirconia. White circles show the location of nanoparticles visible from the images.

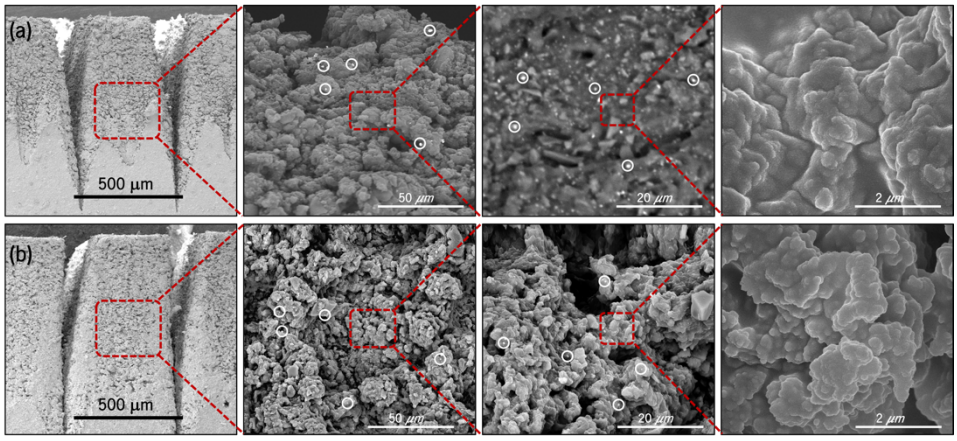


Figure 4.2 – SEM micrographs magnifying microfibrillar pillar surface of nanoparticle-reinforced composite of 0.3wt% 500×200; (a) morphology of zirconia-reinforced SR composite, (b) morphology of titania-reinforced SR composite.

Proper compounding process ensures a homogeneous and uniform composite with almost no porosities confirmed by SEM images are shown in successive micrographs of high loadings of zirconia in Figure 4.1 and with increasing magnifications for zirconia and titania in Figure 4.2. The

voids that are visible in SEM images are the results of surface roughness originating from laser interactions not internal porosities. Further in the advanced surface characterisations, EDS graphs also confirm existence of nanoparticles. The test of surface quality and role of roughness in nanocomposites can only be addressed based on their performance of wettability and sliding friction tests. For that reason, SEM micrographs for highly damaged specimens have been chosen to analyse aftereffect of adhesion on ice. Despite serving good SCOF and DCOF, these specimens could not survive the quality mark of the performance by virtue of their high roughness and fragile structures [199], [200]. Figure 4.3 shows the conditions of the specimens' surfaces before and after the ice friction test. Making the surface hydrophilic comes with a compromise in strength and longevity of an MFS. The image in Figure 4.3(a) is the top view of micropillar obtained after the LST and approximately all the top surfaces of pillars look in good condition before the sliding friction test. Figure 4.3(b) is a post-frictional image of nanocomposite for 5wt% zirconia showing its condition. As SEM image suggests there is no substantial damage to the specimen's pillars. Top surface is the first contact with ice and remains in contact for longest time as it makes contact first and leaves the surface last, therefore, there can be severe changes in the top of micro-pillars for any loading condition. In contrast, high surface roughness, deeper cuts, and fragile micropillars of 7wt% and 9wt% suffer heavily as shown in Figure 4.3(c) and 4.3(d). All the specimens are supposed to go through 45 minutes and 30 cycles of ice friction tests for each stroke of 100 mm (total cycle of 200 mm). However, 7wt% and 9wt% specimens destroyed within three to five tests including 9wt% that lost micropillars over the ice due to micropillars' high adhesion to ice and low strength [198], [201]. The dysfunctionality of the specimen in this work is related to their performance for repeated number of cycles with reasonable wettable characteristics, however, complete dislodging and removal are the end of their lifecycles. Moreover, introduction of nanoparticles is a tricky preposition because micro-roughness of the pillars can be a good sign for the enhanced wettability and adhesion, but nanoparticles make soft SR brittle as well. The T_g of SR is very low and at –5°C or –10°C, normally, it does not lose softness, however, mixing the nanopowders of zirconia/titania exposes special locations where freezing effect can take place [202], [203]. An already weaker cross-linking in polymer chain near the proximity of nanoparticles is more vulnerable to the freezing temperatures [204], [205].

Lower loading surfaces perform satisfactorily for all respective geometries during sliding friction tests. Lower loadings found to be favourable because SR can retain its cross-linking properties, mechanical strength and elasticity. The 0.1wt% to 0.9wt% of zirconia/titania

nanoparticles induce on par wettability with higher loadings and at the same time do not lose the integrity of the material by dislodging or damaging during the rigorous friction tests [206]. Not all specimens exhibit excellent material properties and durability; however, those with lower loadings remain within the working range across all percentages [206], [207], [208].

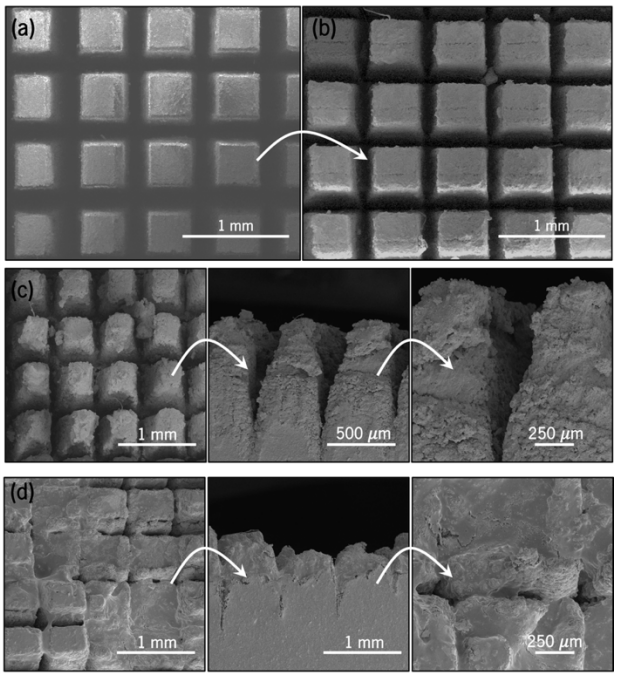


Figure 4.3 – SEM micrographs for the textured hydrophilic SR composite with their successive operations (textured specimen before and after the ice adhesion friction tests; (a) top view of the textured microfibrillar structures (approximately remains similar for all loadings before friction tests), (b) representative top view of the textured microfibrillar structures after the ice friction test for 0wt% to 5wt% of zirconia and all lower loadings for both zirconia and titania, (c) condition of surface after sliding friction tests on ice for 7wt%, and (d) condition of surface after sliding friction test on ice for 9wt%.

4.1.2. Topographical analysis

Having discussed the importance of surface roughness visually, it becomes customary to analyse the roughness with the help of more modern techniques and therefore, Figure 4.4 presents 3D topographical optical profilometer images of the surfaces and their roughness with relevant scales. We specifically chose 0.1wt%, 0.3wt%, and 0.9wt% of 500×200 LST for zirconia and titania to visualise the clear differentiation in surface roughness. A comparison between plain SR surface or 0wt% nanoparticle (Figure 4.4(a)) and textured surface without any nanoparticles (Figure 4.4(b)) resulted an approximate increase in average roughness of 35% from plain to textured surface.

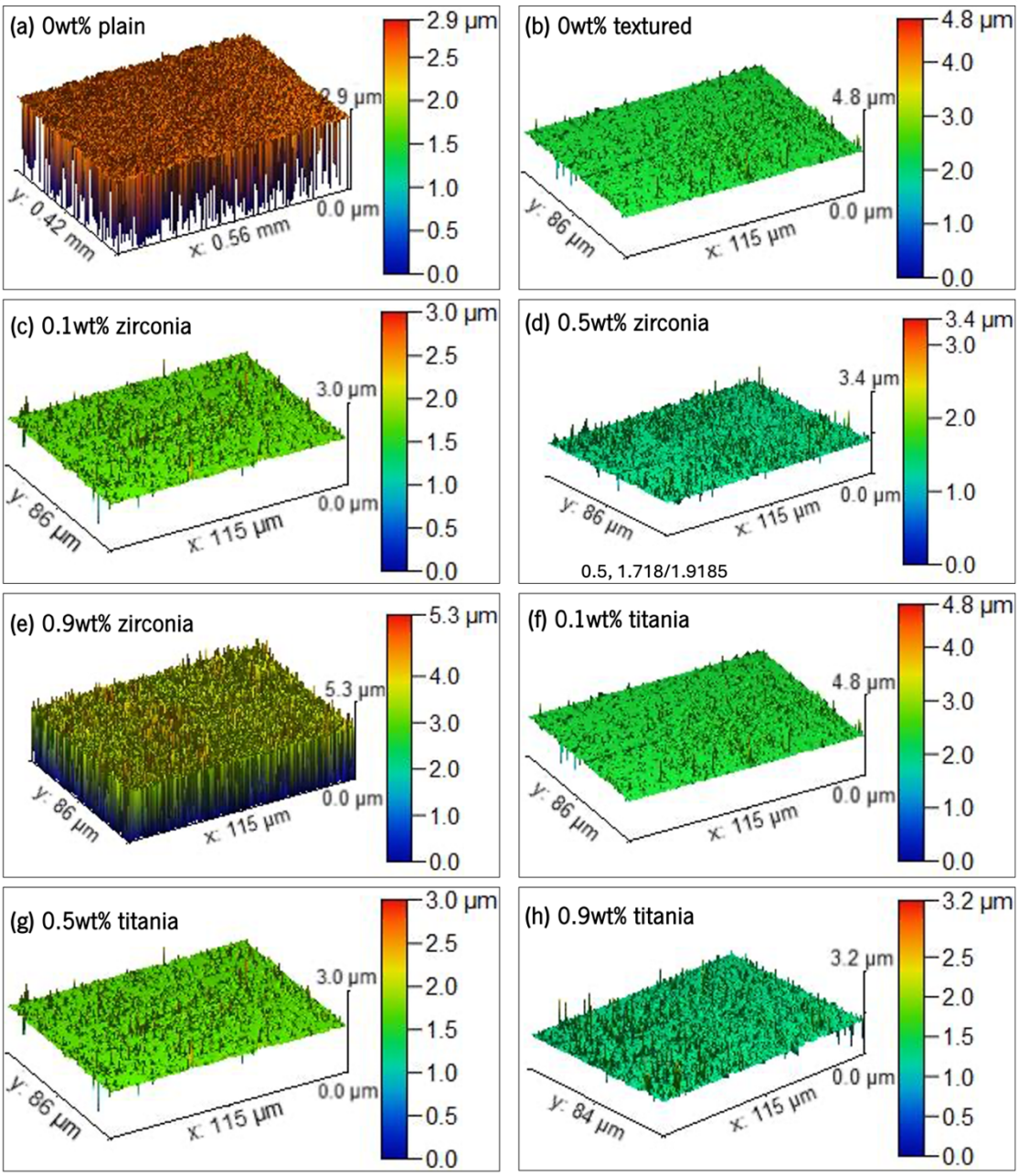


Figure 4.4 – Optical profilometer 3D images of the surface of composites; (a) 0wt% reinforcement vulcanised plain SR surface with average roughness of 0.09 µm and maximum roughness of 0.17 µm, (b) 0wt% reinforcement vulcanised textured SR surface with average roughness of 0.23 µm and maximum roughness of 0.40 µm, (c) 0.1wt% zirconia reinforced vulcanised textured SR composite surface with average roughness of 1.32 µm and maximum roughness of 1.5 µm, (d) 0.5wt% zirconia reinforced vulcanised textured SR composite surface with average roughness of 2.06 µm and maximum roughness of 2.45 µm, (e) 0.9wt% zirconia reinforced vulcanised textured SR composite surface with average roughness of 3.75 µm and maximum roughness of 4.86 µm, (f) 0.1wt% titania reinforced vulcanised textured SR composite surface with average roughness of 1.36 µm and maximum roughness of 1.48 µm, (g) 0.5wt% titania reinforced vulcanised textured SR composite surface with average roughness of 1.72 µm and maximum roughness of 1.92 µm, (h) 0.9wt% titania reinforced vulcanised textured SR composite surface with average roughness of 2.07 µm and maximum roughness of 2.23 µm.

These average roughness values increased almost 5 times for 0.1wt% of zirconia and titania for the textured pillars as shown by Figure 4.4(c) and 4.4(f). Roughness increases more prominently for zirconia percentages (8 times and 15 times for 0.5wt% and 0.9wt%) than titania (6.5 time and 8 times for 0.5wt% and 0.9wt%) as evident from Figures 4.4 [105], [209], [210]. The average roughness values remain in a close range but the roughness peaks for some indicated dispersion of the nanoparticles and represents the effect of LST on the surface. 3D optical images faced substantial limitation capturing the images due to the nature of polymer and extremely small micropillars. The images are taken from the top of the micro-pillars and laser only affects a small portion of the pillar (near the corners) that are visible from top, other regions remain untouched and untextured. Since these are images from the top, there is a possibility of downplaying the roughness, instead roughness can be higher. Nonetheless, the comparison and relative values of the irregularities can be strikingly proportionate [211].

4.1.3. Dimensional analyses

Developed MFS is the result of the combination of two phenomena that deliver the desired effect, that are physical and chemical material modifications. While the composite does not chemically alter the fundamental structure of the SR, it changes the overall chemical behaviour by affecting cross-linking, bulk surface energy, and water absorption capacity through the incorporation of nanopowders. Both modifications are closely associated with the laser texturing of the nanocomposite. Physical modification performed by LST is a direct action of the laser engraving and revealing the nanoparticles, oxidising the micropillars, roughening, whereas making MFS active is an indirect effect of laser interaction. When laser beam impinges on material's surface, it generates huge energy due to its highly focused beam and hence, determination of laser fluence or energy becomes crucial for laser engraving. These laser values remain same for all the experiments.

Laser fluence can be calculated based on Table 3.4 for average laser power (P) used of 15 watts, spot size/diameter (d) of 10 μm, and frequency (ν) of 20 kHz. The laser used is a pulse microseconds fibre laser and energy applied in the pulses is focused on the area of the spot [199], [212], [213]. Therefore, by calculating the fluence and energy density of the laser, one can predict the ablation, physical, or chemical changes of the surface. Following steps calculate numerical values of fluence and density;

$$Laser\ pulse\ energy\ (E) = \frac{Average\ power\ (P)}{Frequency\ (\nu)} = \frac{15\ W}{20000\ Hz} = 0.00075\ J$$

$$Spot\ area\ \ (A) = \frac{\pi}{4}d^2 = \frac{\pi}{4}(0.001^2) = 7.854 \times 10^{-7} cm^2$$

$$Laser\ fluence\ (F) = \frac{E}{A} = \frac{0.00075\ J}{7.854 \times 10^{-7} cm^2} = 954.93\ J/cm^2$$

$$Power\ density\ (P_d) = \frac{Average\ power\ (P)}{Spot\ area\ (A)} = \frac{15\ W}{7.854 \times 10^{-7} cm^2} = 1.91 \times 10^{-7} W/cm^2$$

The generated energy yields microfibrillar structures in LST operation of three selected cut sizes or configurations i.e. 500×150, 500×200, and 500×250 with five nanoparticles' loadings. With the morphological and topographical analyses, the presence of nanoparticles and roughness have already been proven. The limitations on the roughness and quantity of nanoparticles indicate the importance of textured dimensions that requires thorough investigation of the size of the cut or cavities, dimensions of the micro-pillars, depth of cut, and material removal. The quantity and speed of water absorption depend on the optimal dimensions and depth of the cavity. Later analyses confirm that deeper cavities do not necessarily improve absorption. An increase in zirconia content leads to greater depths of cut and higher volumes of material removal, ranging from 1wt% to 9wt%. This variation is demonstrated qualitatively in Figure 4.1, where increment in thinning, roughening, and deepening of the cavities can be seen. Additionally, Table 4.1 consists of complete set of relevant values that combinedly define the MFS. Among these values, depth of the cavity due to the capillary effect and volume of material removed are separately drawn in graphical forms to notice their variations in Figure 4.5. Depth of cavity and volume of material removed command the absorption quantity of QLL and features like roughness and size of the micro-pillars as more removed material leads to thinner and deeper cut majorly affecting wettable phenomenon as well.

Table 4.1 – Dimensions of pillars and cut/cavities for zirconia weight percentages (higher loadings).

Zirconia (500×200)	Top width of pillar (μm)	Bottom width of pillar (μm)	Volume of textured pillar/unit width (μm³)	Perimeter of textured pillar (μm)	Volume of material removed/unit width (μm³)	Perimeter of removed material (μm)	Depth of the cut/groove (μm)
(a) 0%	420	510	257320	1967	25600	650	250
(b) 1%	398	635	346956	2390	63060	1334	595
(c) 3%	406	648	555273	3171	93389	2201	976
(d) 5%	438	660	615923	3310	112411	2249	1055
(e) 7%	332	608	647857	3586	142644	2468	1224
(f) 9%	352	586	878587	4322	196047	3152	1401

Though SR is not completely resistant to laser cutting, LST only removes a limited material from pure SR as is noticeable from Figure 4.1. Laser density per square area penetrate the surface if beam can be absorbed by the material; however, in absence of laser affine substance unlike

nanoparticle-reinforced compounds, the progress of the cut hinders, and beam entirely reflects without heating and melting the impact zone. Laser removes substantial material from the surface but stops once the cuts reach a certain depth. Addition of 1wt% of zirconia more than doubles the depth and volume removed compared to pure SR due to more sites for laser beam to interact. Figure 4.5 shows approximate linear trend for depth and volume of removed material; however, the rise does not occur multiple folds after 3wt% loading and rises slowly. The saturation in depth and material removal are the outcomes of decreasing the width of the cavity as beams penetrate deeper as top and bottom width of the micro-pillars suggest. As the laser penetrates deeper into the bulk material, reflections from the cavity walls result in conical shapes rather than rectangular holes. Decreasing top width is the indication of high laser beam energy absorption due to rising amount of zirconia, nevertheless, moving into deep conical cavities, beam reflects more, and bottom width decreases substantially.

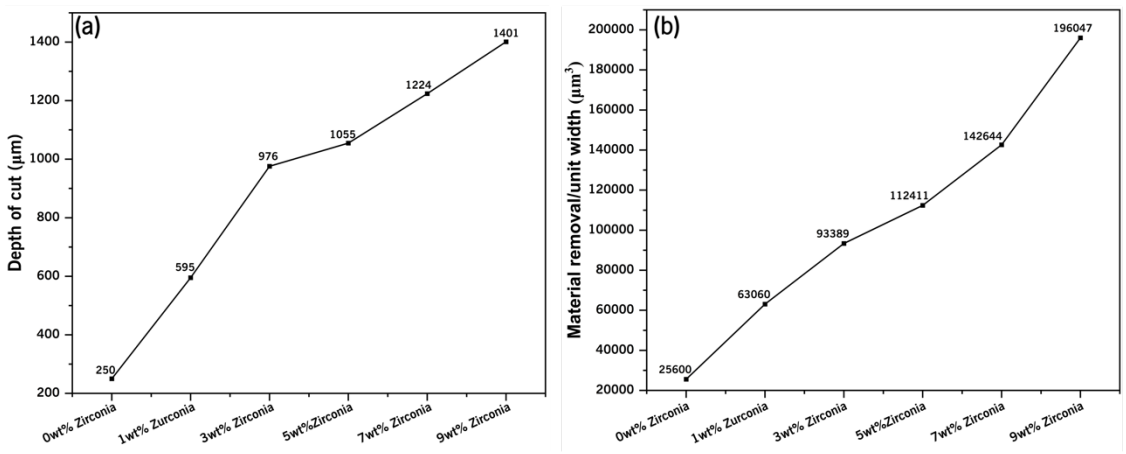


Figure 4.5 – Variations of depth of the cut of cavities and volume of material removed obtained through LST for higher loadings of zirconia; (a) depth of cut/cavity, (b) material removal/unit width.

There is significant drop in top and bottom thickness for 7wt% and 9wt% nanocomposites as higher zirconia ceramic loadings and plenty of laser energy absorption sites cause substantial material removal. The deeper bulk material removal results in pointy pillars with higher conicity as shown in Figure 4.1(e) and (f). These pillars are flexible, conforming, rough, and expose more nanoparticles but are fragile, prone to adhere to ice due to filling-freezing effect and can have compromised wettability by virtue of air entrapment. Therefore, size or volume of micropillar and its perimeter are calculated to observe the overall strength of the structures. Higher loadings yield benefits for a limited extent of reinforcements, but their qualities are influenced by numerous variables due to the interplay between the properties of SR, zirconia, and laser interactions, leading

to a complex and challenging-to-control outcome. Hence, lower zirconia loadings combined with alternative hydrophilic nanoparticles like titania, are explored in the subsequent discussion.

Figures 4.6 and 4.7 depict SEM micrographs showing the progression of micro-pillars for five loading percentages (0.1wt%, 0.3wt%, 0.5wt%, 0.7wt%, and 0.9wt%) of zirconia and titania, respectively with three textured configurations (500×150, 500×200, and 500×250). SEM images represent post-laser micro-pillars' quality and dimensions that are the basis of the quantitative calculations to determine pillar dimensions, cavity depths, and volume of material removal. It is evident that initially small addition range of 0.1wt%, 0.3wt%, and 0.5wt% of zirconia for 500×150 as shown in Figures 4.6(a(i)), 4.6(b(i)), and 4.6(c(i)) results comparatively more material volume removed and depth of cavity than its counterpart titania as shown in Figures 4.7(a(i)), 4.7(b(i)), and 4.7(c(i)). However, for all combinations except 0.1wt% for 500×250, affinity of titania is on par with zirconia as titania loadings produce deep and clean cavity cuts. This can be attributed to specific locations encountered by the laser as better machinable performance is not consistent throughout all the compositions. On the other hand, titania is generally more responsive to laser due to its high thermal absorption rates and thus, smaller cut size for 500×150 is responsible for its less material removal volume rather than interaction with laser beam. Observing the micropillars from Figures 4.6 and 4.7 one can visualise that cavity cuts are sharper and deeper for titania nanocomposites especially at the highest quantity of 0.9wt% regardless textured dimensions with some exceptions. Because the dispersion of titania nanoparticles is found to be better and that provides uniform and homogeneous location for laser to impinge, and moreover, titania does not agglomerate during the compounding process [214], [215], [216].

Tables 4.2 and 4.3 are the tabular records of output parameters for the zirconia and titania reinforced nanocomposites, respectively. From the analysis of the data, it can be concluded that for zirconia, the top width of the micro-pillars remains consistently around 400 μm, except for the 0.9wt% sample with the 500×250 configuration (highest loading and largest cavity size). The bottom width of the micro-structures within the micro-textures stays well above 600 μm, indicating the sustainable strength of the micropillars across all specimens. Slightly reduced bottom width values for the 500×150 configuration at 0.1wt%, along with narrower top widths at 0.3wt% and 0.5wt%, suggest localised zirconia deposition that removed significant material volumes, as previously discussed.

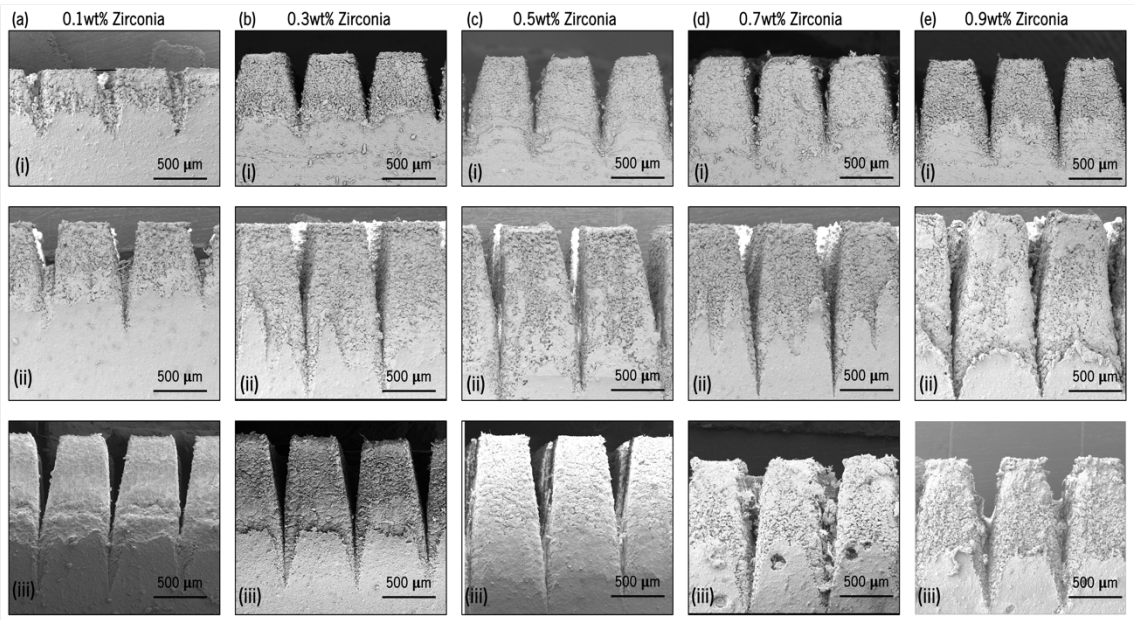


Figure 4.6 – SEM micrographs to show the geometry obtained for zirconia specimens for different weight percentages and textured dimension. Three textured dimensions 500×150, 500×200, 500×250 are shown with numbers (i), (ii), and (iii), respectively below the zirconia weight percentages; (a) 0.1wt% zirconia, (b) 0.3wt% zirconia, (c) 0.5wt% zirconia, (d) 0.7wt% zirconia, and (e) 0.9wt% zirconia.

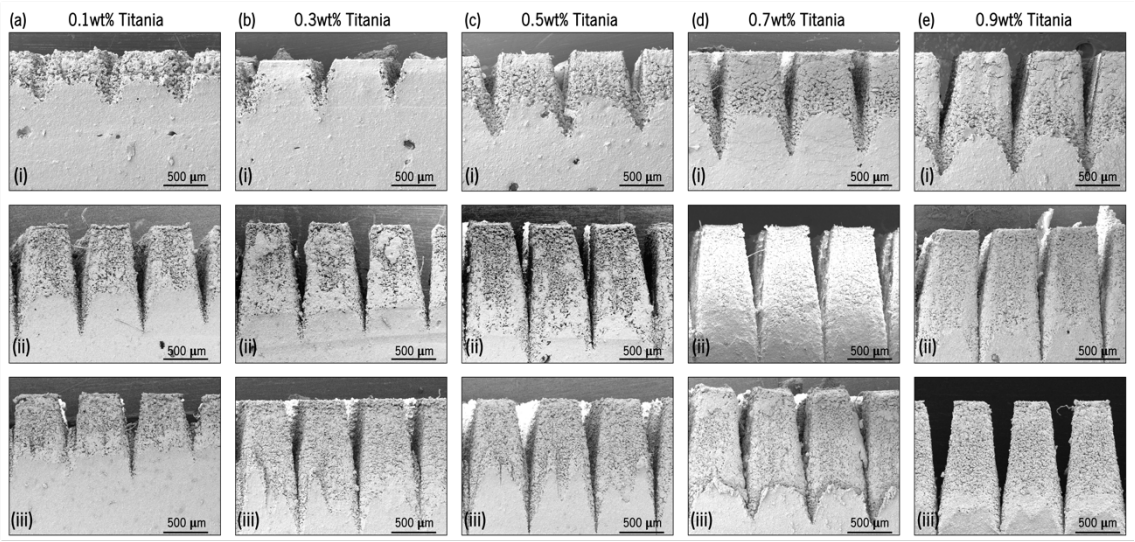


Figure 4.7 – SEM micrographs to show the geometry obtained for titania specimens for different weight percentages and textured dimension. Three textured dimensions 500×150, 500×200, 500×250 are shown with numbers (i), (ii), and (iii), respectively below the zirconia weight percentages; (a) 0.1wt% titania, (b) 0.3wt% titania, (c) 0.5wt% titania, (d) 0.7wt% titania, and (e) 0.9wt% titania.

Titania-reinforced nanocomposites show more consistent values for top width above 400 µm and bottom width above 600 µm without any exceptions. Since titania demonstrates superior mixing and distribution tendencies within the SR matrix, emphasis has been consistently placed on

ensuring uniform and homogeneous mixing and compounding to achieve optimal dimensions throughout the spectrum of the experimentation. Similar to high loadings nanocomposites, depth of cavity and volume removed are crucial to lower loadings as well [217].

Table 4.2 – Dimensions of pillars and cut/cavities for zirconia weight percentages (small loadings).

Zirconia (500×150)	Top width of pillar (μm)	Bottom width of pillar (μm)	Volume of textured pillar/unit width (μm³)	Perimeter of textured pillar (μm)	Volume of material removed/unit width (μm³)	Perimeter of removed material (μm)	Depth of the cut/groove (μm)
(a(i)) 0.1%	461	567	216123	1879	57360	1135	377
(b(i)) 0.3%	380	643	301180	2219	79456	1461	547
(c(i)) 0.5%	367	632	350363	2421	84843	1681	665
(d(i)) 0.7%	415	665	409094	2604	75859	1757	729
(e(i)) 0.9%	401	653	433019	4322	79058	1830	784
Zirconia (500×200)							
(a(ii)) 0.1%	459	719	511665	2919	136376	2171	899
(b(ii)) 0.3%	459	703	757703	3770	139297	2721	1307
(c(ii)) 0.5%	463	763	829964	3979	155716	2986	1327
(d(ii)) 0.7%	419	724	843341	3980	164546	3151	1402
(e(ii)) 0.9%	397	705	913142	4105	174959	3270	1417
Zirconia (500×250)							
(a(iii)) 0.1%	403	637	598343	3249	104792	2254	1093
(b(iii)) 0.3%	421	670	731537	3603	97942	2479	1197
(c(iii)) 0.5%	420	702	789325	3847	167569	3069	1410
(d(iii)) 0.7%	412	733	715067	3697	226403	2973	1262
(e(iii)) 0.9%	369	699	630487	3401	162437	2591	1151

Figure 4.8 is a graphical representation to compare geometric dimensions of zirconia and titania nanocomposites with respect to their depth of cut and volume of material removed. Comparing the material removal volumes for zirconia at both loadings reveals that lower zirconia loadings, combined with high-cut geometries such as 500×200 and 500×250 achieve similar removal volumes from the compound. Interestingly, the depth of cut reaches its maximum for the 500×200 LST, regardless of higher or lower loading reinforcements (zirconia or titania). This strongly indicates the dominance of the physical structure on which the process relies on to achieve the capillary filling-freezing effect. Figures 4.8(a) and 4.8(b) illustrate a consistent increase in material removal for titania nanocomposites with the 500×150 configuration, an approximately linear increase for 500×200, and a drop to a minimum after peaking at 0.5wt%. In contrast, material removal for configurations other than 500×200 does not exhibit a discernible trend.

The interaction of laser beam for evenly dispersed titania exposes controlled quantity of nanoparticles with small LST dimensions of 500×150 that yields uniform rise in depth and material

removed with increment in titania percentages, whereas zirconia agglomerates deprive zirconia composites of uniform and homogeneous dispersion even though the binders were removed beforehand [193], [218], [219].

Examining the depth of the cavity will enhance the investigation into wettability. Both zirconia and titania exhibit an increasing trend for 500×150 and 500×200, reaching their maximum depths. Additionally, for 500×250, the depth peaks and then sharply declines at 0.9wt% for zirconia, while the decrease for titania is negligible. Highly rough surfaces are evident in Figures 4.6(d(iii)) and 4.6(e(iii)) for the 500×250 configuration at 0.7wt% and 0.9wt% on the pillars of zirconia nanocomposites. This roughness, generated during LST, may contribute to the decrease in material removal and cavity depth, as it interferes with the laser beam, leading to uneven melting and solidification.

Table 4.3 – Dimensions of pillars and cut/cavities for titania weight percentages (lower loadings).

Titania (500×150)	Top width of pillar (μm)	Bottom width of pillar (μm)	Volume of textured pillar/unit width (μm³)	Perimeter of textured pillar (μm)	Volume of material removed/unit width (μm³)	Perimeter of removed material (μm)	Depth of the cut/groove (μm)
(a(i)) 0.1%	500	653	255862	2084	48632	951	332
(b(i)) 0.3%	555	761	324737	2345	57849	1138	433
(c(i)) 0.5%	570	783	505555	2873	93651	1638	722
(d(i)) 0.7%	551	768	662480	3328	112745	2133	949
(e(i)) 0.9%	529	790	694492	3456	148575	2303	963
Zirconia (500×200)							
(a(i)) 0.1%	412	700	598334	3241	130418	2347	1050
(b(i)) 0.3%	439	717	685629	3537	164500	2595	1164
(c(i)) 0.5%	457	720	786462	3796	164227	2938	1307
(d(i)) 0.7%	460	738	850603	3921	170264	3041	1375
(e(i)) 0.9%	465	715	851794	3994	175790	3056	1391
Zirconia (500×250)							
(a(i)) 0.1%	437	671	458748	2771	114551	1981	859
(b(i)) 0.3%	445	683	763494	3828	138000	2798	1328
(c(i)) 0.5%	408	680	847585	3922	166410	3007	1333
(d(i)) 0.7%	410	721	826668	4004	128493	2911	1290
(e(i)) 0.9%	400	710	743550	3857	150329	2955	1356

Moreover, the presence of zirconia agglomerates could be a likely cause, resulting in areas where the SR melts excessively while other regions melt minimally, creating an inconsistent MFS. The high roughness can hinder the flow of QLL inside the cavities, decrease wettability and capillary adhesion, or can get damaged losing surface integrity. Therefore, it is crucial to ensure that surface roughness is adjusted for hydrophilic behaviour. Nevertheless, zirconia nanocomposites show

overall high material removal volume and depth of cut for 500×200 and 500×250 unlike 500×150. The behaviour can be attached to size of the cavities, as at small cavity cuts of 500×150, removal remains less, whereas at higher dimensional cuts, higher amount of nanopowder compensates the loss caused by agglomerates [119], [193], [218], [219], [220], [221], [222].

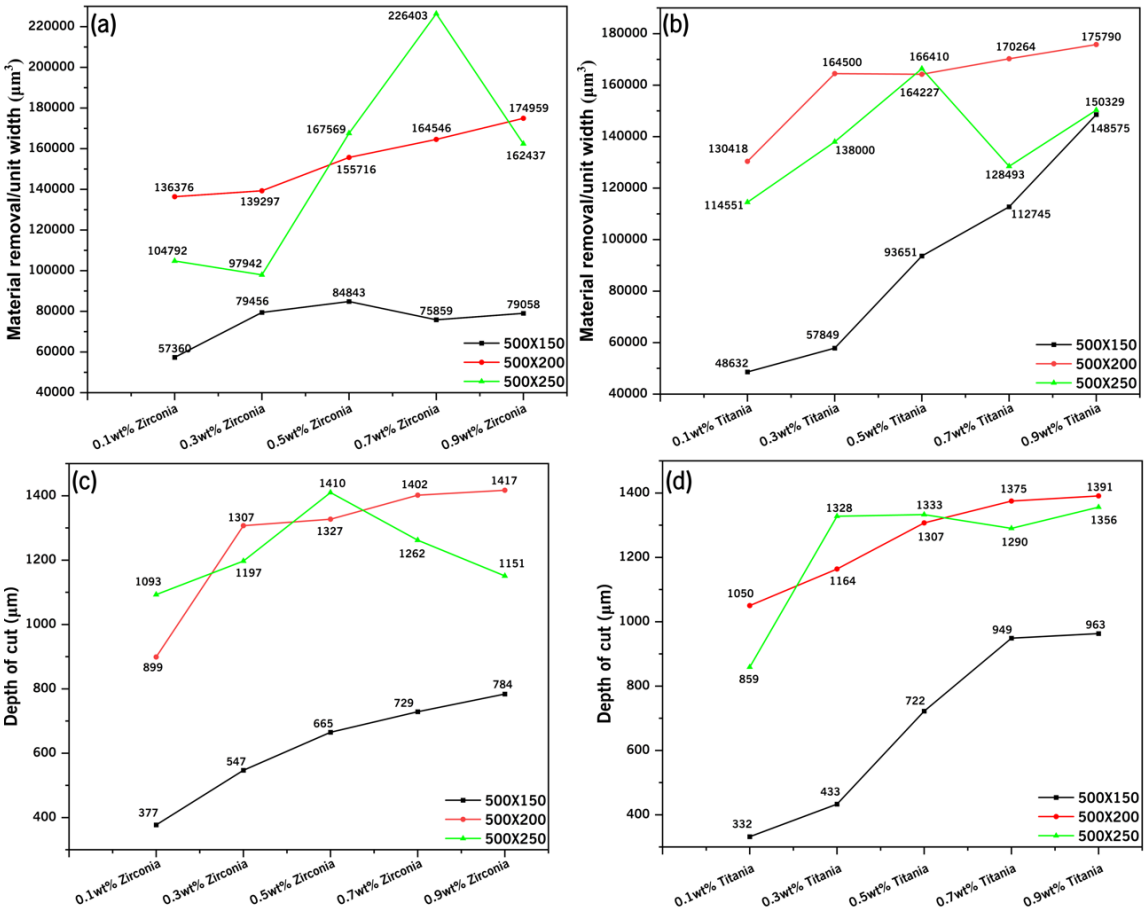


Figure 4.8 – Variations of depth of the cut of cavities and volume of material removed obtained through LST for zirconia and titania; (a) material removal/unit width for zirconia weight percentages, (b) material removal/unit width for titania weight percentages, (c) depth of cut for zirconia loadings, (d) depth of cut for titania loadings.

The PhD thesis utilises the principle of mimicking frog and gecko toepads, which rely on absorbing surface fluid rather than repelling it. The morphological and dimensional analyses of the produced micro-pillars for two loading conditions and two reinforced nanocomposites must possess the properties within the biomimicking range of frog and gecko footpads. Detailed SEM and 3D optical profile images already established the dimensions and surface characteristics. Therefore, before going into the details of mechanical properties and wettable behaviour, information on gecko and frog toepads must be revised to understand the target range of properties [223], [224].

Each gecko toepad contains around 20 lamellae measuring 400–600 μm, each with thousands of setae of 3–5 μm in length branching into hundreds to thousands of spatulae about 200 nm in size. The spatulae tips adhere to a dry surface via van der Waals forces, and their high adhesion strength is due to their vast numbers. On moist surfaces, these lamellae absorb humidity to create a dry contact that forms molecular bonds. Meanwhile, frog toepads feature polygonal structures, mostly hexagonal, approximately 10 μm in size and separated by a distance of 1 μm, creating a channelled distribution. Each polygon contains nanopillars 300–400 nm in diameter and 200–300 nm in height, whose concave tips arguably form suction adhesion. The large channels in frog toepads can absorb significant amounts of liquid, while the mucous gland produces mucus that keeps the surface wet, attracting additional liquid via capillary bridges [225]. Initial wetting or direct moisture content on the produced MFS can help and induce better capillary adhesion. Despite variations in the arrangement and sizes of these hierarchical structures, they serve the same function to provide slip-resistant movement on wet or dry surfaces. The nanostructures are proportioned to each animal's bodyweight, but they can support many times their own weight on vertical slippery surfaces through capillary bridges formed by interfacial liquids. The morphological study presented here involves fabricating surface structures in the form of micropillars made of reinforced SR, aiming to produce capillarity in proportion to human weight rather than at the nanoscale. The presence of hydrophilic nanoparticles with capillary rise aims to compensate the absence of mucous glands or other biological components [226], [227], [228], [229], [230], [231], [232]. Beyond the biomimicked hydrophilic structures, it is essential for the pillar hardness to match the range of gecko or frog toepads to maximize their effectiveness. Therefore, the next section focuses on scratch or wear resistance, i.e. hardness.

4.2. Wear resistance and hardness

Hardness serves as a fundamental measure of scratch resistance and plays a significant role in determining wear resistance making it essential for evaluating a material's durability under mechanical stresses. A shoe-sole undergoes numerous adhesion-deadhesion cycles, and an effective, durable sole must balance wear resistance with optimal hardness. Particularly in biomimicking, a balance of the mechanical properties is of utmost important like too soft material can offer excellent initial traction but wears down quickly and loses its grip under repeated cycles of locomotion. On the other hand, a hard sole last long but has poor flexibility and conformity over the slippery surface. Surface hardness for gecko/frog toepads can range from 5 to 40 on the Shore A scale, while normal anti-slip shoe-soles typically range from 40 to 60. Accordingly, the vulcanised

reinforced SR material must remain within the bioinspired toepad range. Figure 4.9 shows the variation of Shore A hardness for titania and both higher and lower loadings of zirconia. As Figure 4.9(a) shows the hardness variations for higher loadings of zirconia-reinforced nanocomposite against unaltered SR. Pure SR demonstrates the hardness of approximately 42.91 after vulcanisation, but when zirconia is added up to 3wt%, the Shore A hardness drops sharply (36.9 for 1wt% and 33.67 for 3wt%) before rising again. Although no visible porosities appear in the compound's morphology, there may still be some hindrance to cross-linking in the polymer matrix, potentially explaining the drop in hardness. Another likely explanation can be that the hardness tester's stylus contacts the boundary of a zirconia agglomerate and the polymer, causing a significant loss of hardness. Furthermore, nano-porosities could exist in specific locations. As the powder loading increases, the hardness rises again, likely due to more nanoparticles (even if agglomerated) being distributed across multiple locations. A higher zirconia content dispersed in the bulk polymer matrix interacts with the stylus yielding greater hardness values that reach 38.85 for 9wt%. Though there is a notable drop in hardness from pure vulcanised SR, composite's hardness consistently remains within an acceptable biomimicking range. Despite the broad range of frog/gecko toepad hardness, our composite should not have very low hardness since biological toepads feature sophisticated movements such as adhesion, conformity, peeling off, natural skin replenishment, and biomechanics of movement that are absent in the fabricated nanocomposite. Hence, maintaining hardness comparable to winter slip-resistant soles ensures both longevity and a level of biomimicry. Observing the damages of produced composite structures after the experimental cycles from Figure 4.3(c) and (d), it can be established that though hardness values at 7wt% (37.4) and 9wt% (38.85) are satisfactory but the durability impaired severely by high roughness and huge zirconia content that make the material extremely fragile. Therefore, striking a compromise among mechanical properties, durability, and the intended purpose of the material is essential [222], [225], [233], [234].

For 0.1wt% to 0.9wt% of zirconia and titania, the Shore A hardness gradually increases especially for zirconia nanocomposites that have approximately linear rise and attains to the highest value of 39.5. On the other hand, after a dip at 0.3wt% titania nanocomposite (possibly due to measuring a soft spot on the surface or localised porosity), the hardness rises and obtains equals to pure SR reaching 43 as shown in Figure 4.9(b). The average hardness of titania compounds is higher than that of zirconia due to the better dispersion on the surface. Homogeneous surfaces offer favourable combination of softness of SR and hardness of nanoparticles supporting each other

to maintain uniform hardness values. In contrast, zirconia, despite being added in the same proportion forms agglomerates during blending, slightly reducing overall average hardness. Nevertheless, individual hardness values for zirconia nanocomposites in some cases were found to be more than titania nanocomposites [198], [222], [235], [236].

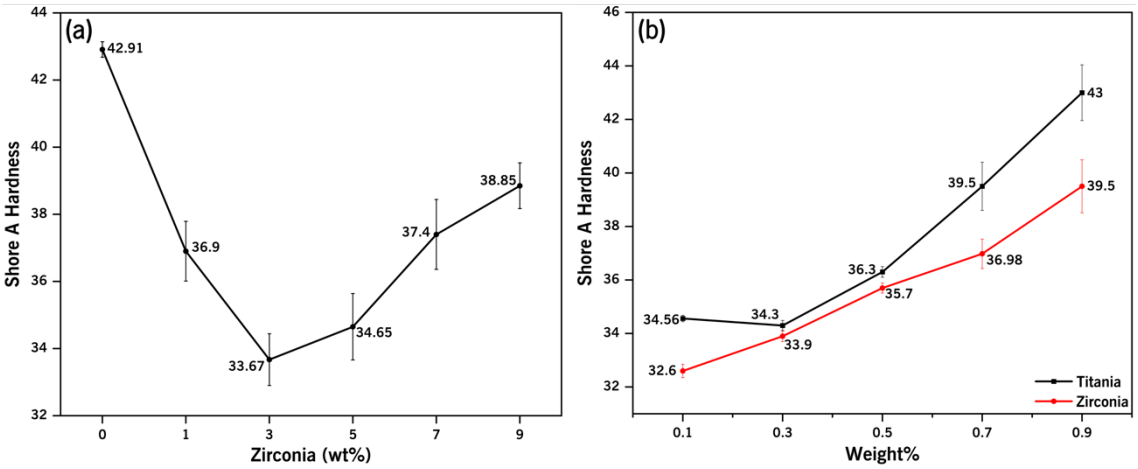


Figure 4.9 – Variations of Shore A hardness measured through durometer for nanoparticle-reinforced untextured composites; (a) Shore A hardness for zirconia composite for 0%, 1%, 3%, 5%, 7%, and 9% weight percentages, (b) Shore A hardness for zirconia and titania composite for 0.1%, 0.3%, 0.5%, 0.7%, and 0.9%.

Again, particle size and mixing method influence mechanical surface hardness as mixing methodology ensures proper mixing of the nanoparticles for both nanopowders, nevertheless, titania nanocomposites exhibit superior hardness characteristics due to their lower particle size along with less average roughness after laser engraving than that of zirconia nanocomposite. The concept to improve the hardness for this study is driven by the importance of mechanical strength that should complement the required wettability, capillarity adhesion, longevity, and biomimicking. The complete destruction (dislodging) in case of 7wt% and 9wt% zirconia-reinforced SR can be avoided with the help of enough mechanical hardness. Observations indicate that lower nanoparticle loadings provide a uniform increase in hardness and remain within a biomimicking range. Despite the 0.9wt% titania values closely matching those of plain vulcanised SR with 0wt%, is unsuitable for anti-slipping due to lack of hydrophilicity. If the MFSs with the hardness values close to 40 offer optimum wettability and considerable friction, then can be selected as a favourable choice. Hardness is the first measure of mechanical endurance of the fabricated compound and affect its life cycle. In addition to the absolute values of hardness, maintaining consistent hardness is crucial for the success of the nanocomposite. If the compound becomes too stiff, it may slide and lose its wettability. Contrary to that, if it becomes excessively hard, it will lose its ability to

conform. Therefore, achieving a balance between hardness and conformability is essential for the nanocomposite's effectiveness. Since elastic strength of the material must also be determined as shoe-sole goes through repeated cycles of contact with cold surface, next section is dedicated to elaborating on strength and elasticity [237], [238], [239].

4.3. Strength and elasticity analyses

Compressive and tensile elasticity moduli were determined through two separate Universal Testing Machines. Observed elasticity values of 2.50 MPa to 2.80 MPa under compression tests fall in a close range for all the nanocomposites regardless of loadings (whether higher or lower) and nanoparticles (whether zirconia or titania). Thus, Figure 4.10 is presented as a representative graph for zirconia with higher loadings to show the behaviour of the specimens. The compression tests repeated three time for three specimens and attained graphs were smoothed by Fast Fourier Transform. Furthermore, the elasticity modulus from each graph was calculated by fitting a straight-line segment and by determining the slope of the curve as demonstrated by Figure 4.10(b). It was established that elasticity in compression tests of the composite drops with loading and noted 2.18 MPa for 5wt% zirconia nanocomposite, however for all other loading proportions remains comparatively higher [194], [240]. This reduction can be attributed to the hindrance in cross-linking of the polymeric matrix and nano level porosities, if any present. Another common reason is the formation of agglomerates that exists with zirconia nanoparticles resulting in poor dispersion of nanoparticles. Poor dispersion creates stress concentration zones and reduces the material's ability to deform elastically. Additionally, hindrance to polymer chain mobility caused by excessive filler content or strong filler-polymer interactions can lead to a stiffer and less elastic material. Because the composite will be in contact with freezing water and the stiffness of the rubber can increase, thus, elasticity of the substance is a crucial characteristic. If the composite loses elasticity by loading it with nanoparticles, then this scenario also becomes the limiting factor for the addition of nanoparticles. Depending on the species, elastic modulus of the frog and gecko toepad inspired artificial adhesive vary in a large range. The values mentioned in the earlier works mentioned values like 1 MPa, 3.7 MPa, 4.2 MPa, and 5.7 MPa. Most of these values are tested for good wet adhesion. Therefore, a range of 1 MPa to 6 MPa can be considered an optimised including a quick deformation recovery [208], [236], [241], [242], [243].

All the obtained values fall within the safe range of elasticity confirming the material's suitability. While compressive strength has an important role in capillary-enhanced adhesion by supporting the micro-pillars against impact loads and maintaining structural integrity. During

compression, the larger surface area of the shoe sole prevents material failure, and compressive strength helps absorb impact without compromising elasticity. However, shoe-sole failures rarely occur due to compressive stresses alone. Instead, continuous bending (a combination of compression and tension), rubbing, and peeling are the main causes of failure. In capillary adhesion scenarios, compressive strength provides stability against forces but is unlikely to dislodge or damage the structure. The greater risk comes from peeling or pulling off forces making tensile strength analysis far more crucial [239], [244], [245], [246].

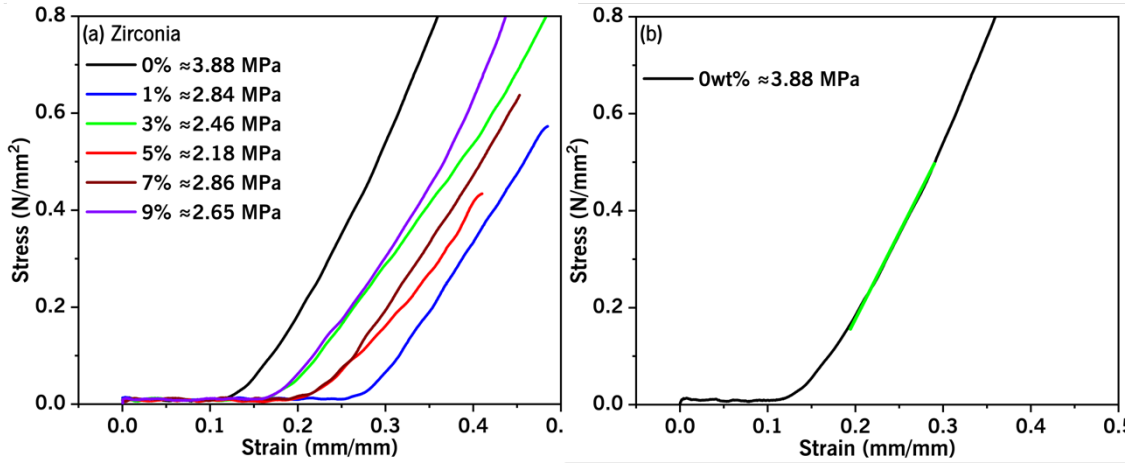


Figure 4.10 – Stress vs strain plots to obtain elasticity modulus via compression tests; (a) curves for 1wt% to 9wt% reinforced zirconia nanocomposites, (b) illustration to measure the slope of the curve by fitting a line segment at the linearity zone.

Figure 4.11 illustrates the stress vs strain curves for zirconia and titania nanocomposites alongside pure SR, respectively. Elasticity obtained during tensile tests is significantly lower than in compression because the material resists deformation more effectively due to the bulk resistance of the polymer matrix in compression. Nanovoids, internal deformities, agglomerates, and poor dispersion of the reinforcement have a greater influence during tensile tests. Dog bone shaped specimens (gauge length = 20 mm, gauge width = 8 mm, thickness = 3 mm) were used to perform conventional tensile tests, and the recorded values were converted to stress and strain under all loading conditions to produce final stress-strain curves. Figure 4.11(a) and 4.11(b) display respective Young's modulus values for zirconia and titania, respectively. Figure 4.12 is an elaborative display of elasticity curves for various loading conditions for both the composites. The graphs show the nature of the stress-strain curve, respective elasticity values, breaking strength, and elongation before permanent failure. SR has a non-linear elastic behaviour after initial

deformation; thus, it is customary to use the initial segment of the curve to determine Young's modulus as shown in Figure 4.12 [247], [248], [249].

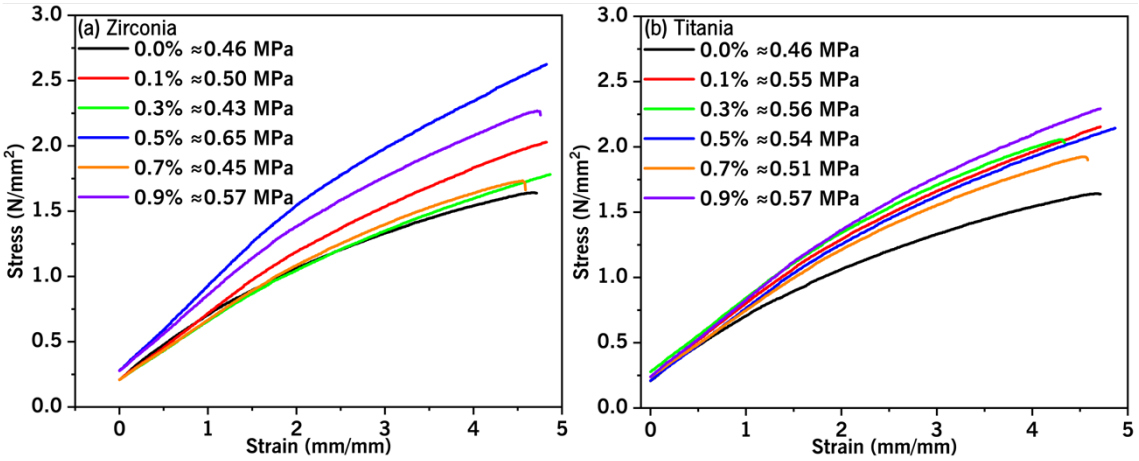


Figure 4.11 – Stress vs strain plots to obtain elasticity modulus via tensile tests; (a) curves for 0.1wt% to 0.9wt% reinforced zirconia nanocomposites, (b) curves for 0.1wt% to 0.9wt% reinforced titania nanocomposites.

The Young's moduli obtained represent the increase in tensile strength of the composite material with the addition of nanoparticles, with titania showing slightly superior effects. Capillary adhesion occurs at the microscale, and the frozen peaks at this level require the material's microstructures to be as robust as possible. Thus, it is important to consider both the breaking strength and the elongation of the material before failure. Greater elongation allows the material to withstand higher peeling forces under tension during deadhesion, while breaking strength determines the ultimate durability of the nanocomposite. Elongation reaches 590% for zirconia reinforcement at 0.3wt% and 599% for titania reinforcement at 0.5wt%, compared to 465% for unreinforced SR. Breaking strength peaks at 50.50 N for zirconia reinforcement at 0.1wt% and 56.70 N for titania reinforcement at 0.5wt%, compared to 39.40 N for unreinforced SR. The incorporation of nanoparticles results in a Young's modulus of 0.65 MPa for 0.5wt% zirconia and 0.57 MPa for 0.9wt% titania, compared to 0.46 MPa for unreinforced SR. Higher nanoparticle loadings improve the elastic modulus, but the combination of elongation before failure, breaking strength, and elasticity is optimum at 0.5wt% for both materials. This indicates that while higher amounts of zirconia can enhance certain properties, the overall optimised tensile characteristics are achieved with moderate nanoparticle loadings [238], [246], [249], [250], [251].

The incorporation of nanoparticles enhances the stiffness and load-bearing capacity of the SR matrix by improving the distribution of stress across the material. It can be attributed to enhancement of the strength of the interface. The elastic properties are most influenced by the

interfacial bonding between the polymer chains and nanoparticles because the matrix must transfer the load to the nanoparticles through the interfaces. If the interface is not strong enough then instead of transferring the load to the nanoparticles, it releases loads making the compound fail quickly.

On the other hand, a strong interfacial bonding between the polymer chains and the nanoparticles helps in better load transfer. In addition, the nanoparticles also act as fillers that restrict polymer chain mobility, thereby increasing the material's resistance to deformation while maintaining flexibility under tensile stress. The homogeneous dispersion of nanoparticles, especially for titania reduces stress concentration points and improves the material's uniformity further enhancing its elastic response [252], [253]. Moderate nanoparticle loadings ensure a balance between reinforcement and flexibility preventing the brittleness that could occur with excessive filler content. These factors collectively contribute to the observed improvement in elasticity with nanoparticle reinforcements [196], [208], [244], [254], [255].

The application discussed in this thesis is based on the viability of the developed structures to perform under rapid cycles of adhesion and deadhesion during walk. The developed nanocomposites show substantial improvement under tensile forces and remain in the range of adaptation for compression. The selection of a good shoe-sole material is a combination of overall optimised properties rather than hardness, elasticity, or roughness alone. After performing mechanical characterisations, some advanced material characterisations to decipher the chemical properties of the nanocomposites were performed to understand the surface behaviour of the developed MFS. These advanced characterisations will lead to the comprehension of wettability and capillarity of the surfaces.

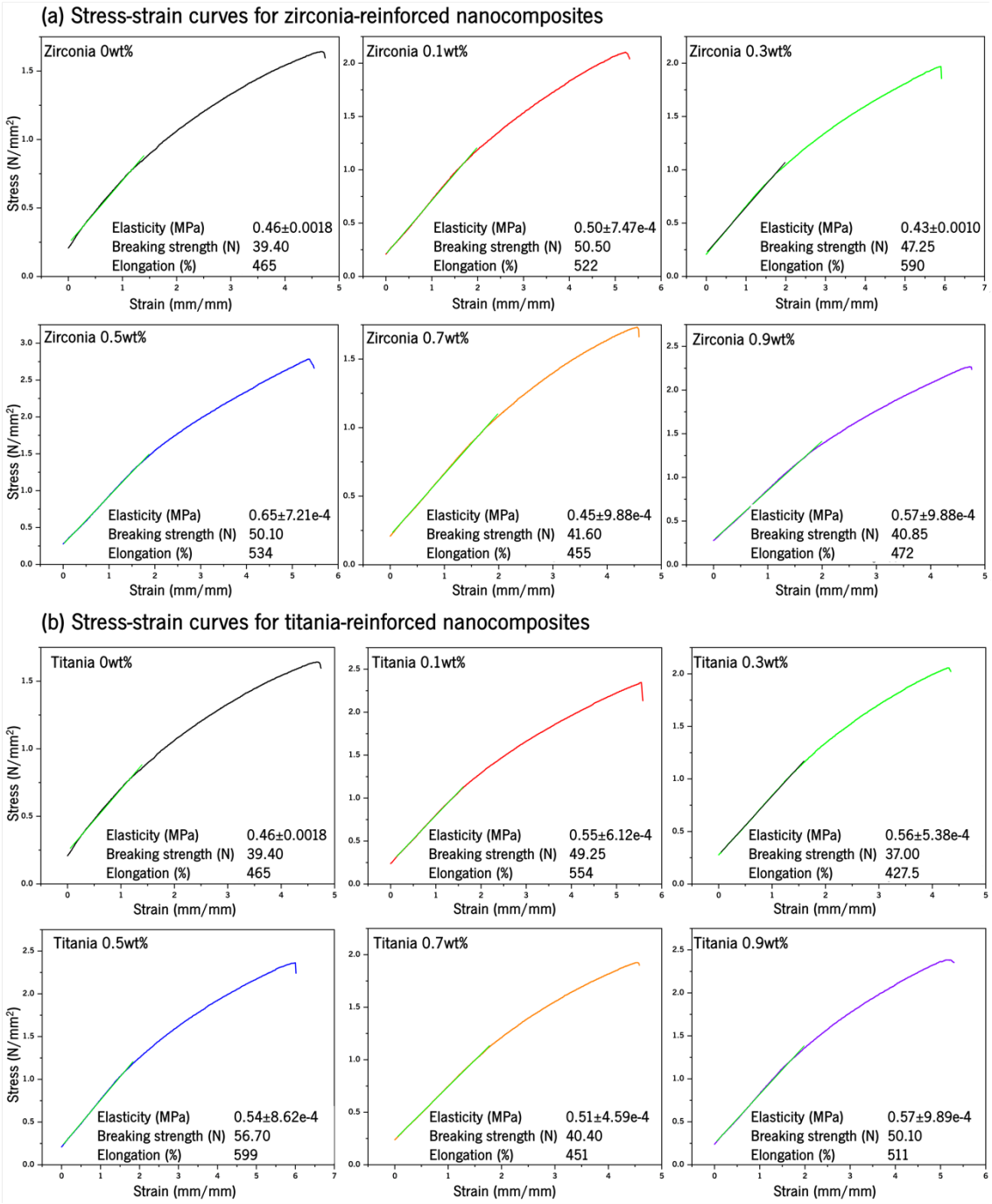


Figure 4.12 – Individual stress vs strain curves obtained from tensile tests for; (a) zirconia-reinforced nanocomposites, (b) titania-reinforced nanocomposites.

4.4. Advanced material characterisations

The chemical analyses of fabricated nanocomposites are important to observe the changes in the basic nature of the compound as they define the overall behaviour of the compound. Furthermore, the phases and chemical linkages present in the substance also help us understand its dealings with the other substances like water at micro-level.

4.4.1. Chemical analyses through FTIR and EDS

ATR-FTIR spectrogram of vulcanised SR with and without the reinforcement reveals chemical structure and the presence of key functional groups responsible for its properties. These peaks can be analysed by the transmittance curves with respect to wavenumber from Figures 4.13(a), and 4.14. Figure 4.13(a) shows the FTIR curves for higher loading of zirconia and can be analysed for the presence of zirconia nanoparticles. The strong peaks corresponding to the siloxane backbone (Si-O-Si) occur about 1000 to 1150 cm^{-1} in the spectrum due to the stretching vibrations of silicone-oxygen bonds. The methyl groups (-CH_3) attached to silicone generate peaks due to their deformation or bending vibrations near 1260 to 1270 cm^{-1}. Silicone-carbon bonds (Si-C) also produce bending vibrations near 800 to 850 cm^{-1} at characteristic regions because of the relative rigidity of the silicone-carbon linkage compared to the more flexible siloxane bonds. Carbon-hydrogen bonds show peaks about 2900 to 2960 cm^{-1} by virtue of symmetric and asymmetric stretching vibrations due to the presence of methyl groups [256], [257].

The presence of non-polar methyl groups (-CH3) on the surface leads to a higher prevalence of Si-C bonds compared to Si-O bonds in SR resulting in a hydrophobic surface. Being a polar substance water lacks attraction to the non-polar methyl groups, which have no ionic or hydrogen bonding sites. Thus, the addition of zirconia changes the surface chemistry, charge distribution, and energy to make it more water affine. Zirconia nanoparticles contain polar hydroxyl groups (-OH) that are absent in SR. These -OH groups not only stabilise the interface between nanoparticles and water but also act as nucleation points for forming hydrate shells. The dissociation of -OH and other functional groups imparts a negative charge to nanoparticles, which attracts the positively charged hydrogen atoms of water molecules enhancing the water-zirconia interface for hydrophilicity. Additionally, crystal lattice defects, such as oxygen vacancies and unsaturated coordination sites increase the surface energy of the compound promoting the adsorption of water molecules. The adsorption of water molecules enhances the capacity of textured nanocomposite to absorb liquid making it hydrophilic [258], [259], [260], [261], [262].

A wide absorption band between 3200 and 3750 cm^{-1}, with a peak around 3338 cm^{-1} corresponds to the stretching vibrational mode associated with the physical absorption of moisture by zirconia nanoparticles on the surface. The intensity of these peaks increases with higher zirconia loading due to the rise in moisture absorption capacity. Figures 4.13(a), 4.14(a), and 4.14(b) clearly demonstrate that pure rubber (0wt%) lacks this spectral intensity in both nanocomposites

(zirconia and titania). For zirconia composites, the Zr-OH group becomes prominent at higher loading levels, whereas for lower loadings, these peaks are only visible at the highest concentrations such as 0.7wt% and 0.9wt% as shown in Figure 4.14(a). These peaks are also present in titania nanocomposites but appear at shorter wavenumbers between 3250 and 3600 cm^{-1} with a peak around 3370 cm^{-1} as depicted in Figure 4.14(b). Another hydroxyl group in zirconia nanocomposites is observed near 1650 to 1700 cm^{-1}, suggesting hydrosilylation that indicates cross-linking and an increase in hydrophilicity. This phenomenon could also be attributed to the oxidation of the rubber matrix following the addition of zirconia nanoparticles (oxidation can also result from LST). Unlike zirconia, titania-reinforced SR shows a peak around 650 cm^{-1}, attributed to O-Ti-O flexural vibrations. Furthermore, at higher loadings of titania, a peak appears near 2850 cm^{-1} adjacent to C-H methyl group approximately 2900 cm^{-1} and might be related to symmetric and asymmetric stretching vibrations in the presence of nanoparticles. In addition to FTIR analysis, an EDS study was performed, confirming the presence of zirconia and titania nanoparticles, as shown in Figures 4.13(b) and 4.13(c), respectively [118], [196], [263], [264], [265].

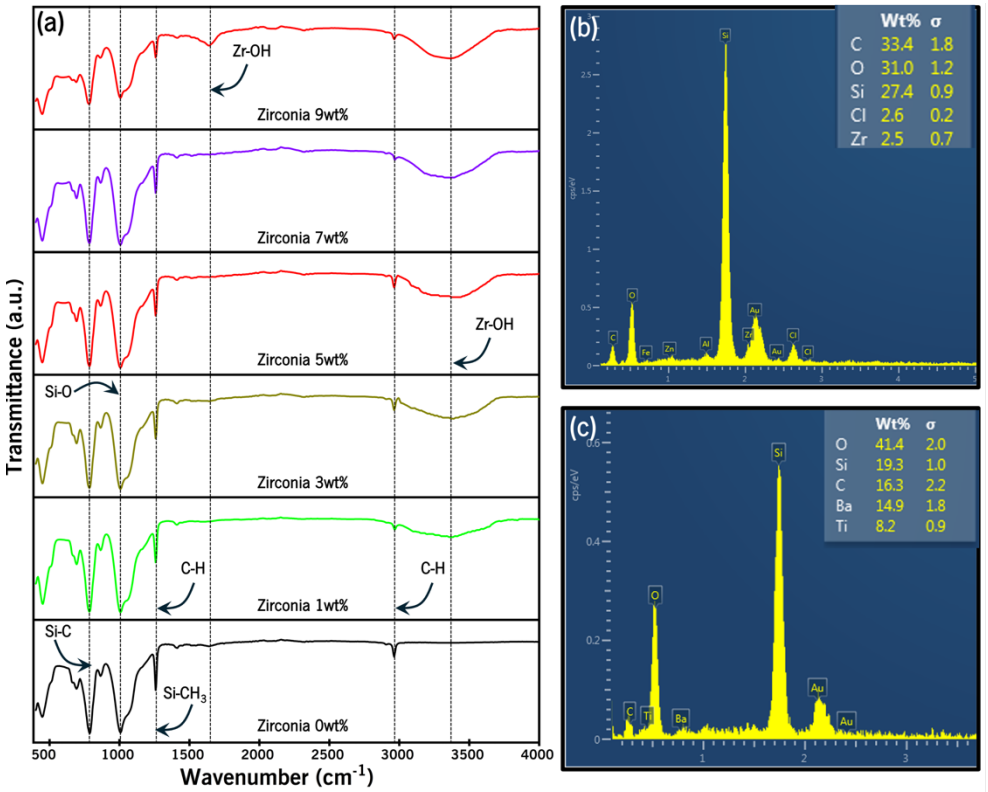


Figure 4.13 – Chemical composition analyses to gather the presence of zirconia nanoparticles in SR under loading conditions; (a) FTIR plots of zirconia-reinforced nanocomposite for high amount zirconia loading, (b) EDS of zirconia-reinforced nanocomposite (c) EDS of titania-reinforced nanocomposite.

The visibility of titania is enhanced due to the homogeneous dispersion and absence of agglomerates making it easier to detect. However, being somewhat in agglomerated state, zirconia appears in smaller percentages. Despite the improved dispersion, occasional engulfing of nanoparticles by the SR matrix caused by melting and solidification during high-energy laser engraving poses challenges to visualise the nanoparticles in the dispersion.

Chemical analyses via FTIR and EDS play a crucial role in assessing the cross-linking and surface behaviour of nanocomposites. The observations presented here indicate favourable development and cross-linking between the two substances, which enhance surface chemistry and increase surface energy to attract and absorb water. Proper cross-linking of the SR matrix and the presence of effective sites provided by hydrophilic nanoparticles establish the foundation for improved wettability.

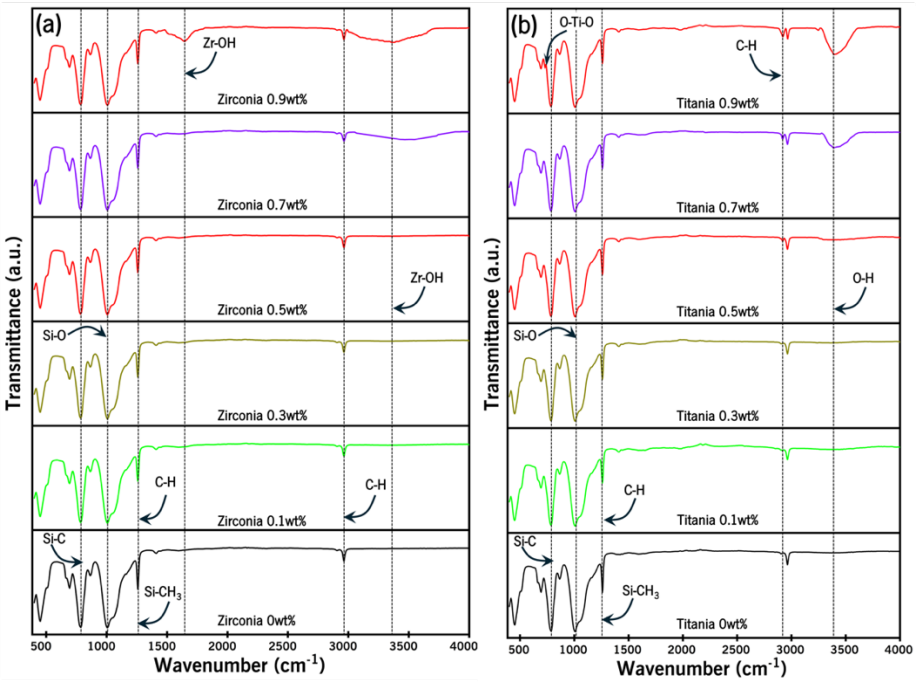


Figure 4.14 – Chemical composition analyses to gather the presence of nanoparticles in SR nanocomposites under different loading conditions for; (a) zirconia, (b) titania.

4.4.2. X-Ray diffraction analysis

The crystallographic phases of zirconia and titania nanoparticles were obtained by XRD analysis after laser texturing as laser textured nanocomposites define the wettability of the prepared compound. The vulcanisation temperature reaches maximum up to 220°C and may not result any crystalline changes in lattice structure of the nanopowders due to the stability of zirconia/titania under moderate temperature such as 220°C. However, phase change is possible due to LST as

temperature reaches to intensely high by the focused laser beam. Therefore, phase analysis after high temperature laser engraving ensures the thorough nature of compound along with wettable and capillary behaviour. Patterns were recorded in the range of 2θ = 20° to 80° and intensity peaks were observed. Miller indices (hkl) for all the peaks obtained are shown in Figure 4.15 for both the nanopowders. The peaks observed from titania specimens were 20.96° (010), 26.72° (101), 36.60° (110), 39.52° (102), 40.73° (111), 42.50° (111), 45.88° (201), 50.20° (112), 55.40° (013), 59.85° (121), 67.74° (122), and 68.34° (031). The strongest peak at 26.72° suggests the presence of tetragonal titania anatase phase followed by other intense peaks at 36.60°, 50.20°, 55.40°, and 68.34°. Peaks at 39.52° and 42.50° suggest some phase transformation to rutile from anatase of titania and can be attributed to laser's high temperature. Anatase can transit to more thermodynamically stable phase rutile in the temperature range of 600°C to 700°C for pure anatase and about 400°C to 600°C for nanoparticles. There are other mixed peaks where the phases coexist and structures also change, nevertheless, dominance of anatase is a positive sign for wettability. High temperature of laser cutting, titania can transform its tetragonal crystal lattice structure leading to metastable hexagonal state and can coexists with other phase whether anatase, brookite, or rutile [123], [266], [267].

Zirconia, on the other hand peaks at 20.85° (010), 26.54° (101), 28.04° (–111), 30.07° (011), 31.83° (110), 34.50° (002), 35.40° (110), 36.54° (110), 39.45° (102), 40.73° (111), 42.46° (200), 45.81° (201), 50.60° (112), 59.15° (013), 59.85° (121), 62.59° (022), and 68.31° (122). Most intense peaks at 30.07°, and 50.60° along with less intense peaks such as 31.83°, 34.50°, 35.40°, 42.46°, 45.81°, 50.60°, 59.15° , 62.59° are the evidence of tetragonal lattice crystal structures of zirconia, however, tetragonal and cubic crystal lattice structures can coexist at 30.07°. A strong peak at 26.54° followed by weaker intensities at 28.04°, 36.54° and 39.45° illustrate the existence of monoclinic phases as well. The transition of tetragonal to monoclinic occurs in the temperature range of 950°C to 1100°C. SR is an amorphous or semi-crystalline substance and lacks long-range crystalline structure [118], [268], [269]. Nonetheless, intense common peaks at 20.96° (titania)/20.85° (zirconia) and others at 40.73° and 59.85° are consistent in both the nanocomposites and can be the evidence of the presence of SR. The transformation of tetragonal zirconia to monoclinic or cubic phases is strongly influenced by temperature or dopants like yttria (Y_2O_3). At temperatures more than 2370°C, zirconia adopts a stable cubic structure due to the high thermal energy then transitions to the tetragonal phase while cooling and eventually attains monoclinic phase at room temperature [256], [270], [271].

Depending on the laser fluence, there can also be modifications such as phase transitions in zirconia or titania and micro-structuring of the composite surface which can improve mechanical properties and wear resistance. However, yttria-stabilised zirconia needs large laser fluence to obtain these changes. Therefore, heat dissipation characteristics of yttria-stabilised zirconia can be a favourable shielding for SR polymer from excessive thermal damage while facilitating precise control over the production of texturing and limited roughness. Titania anatase can also change its phase to rutile at high laser interaction temperatures (600°C to 1200°C) because of rutile's thermal stability, however, anatase is more hydrophilic and presents favourable aspects of wettability. Since the selection of nanopowders was based on their mechanical, hydrophilic, and anti-bacterial properties (zirconia, being bacterial-aversive, and titania, anti-bacterial), next section sheds light on the bacterial adhesion behaviour of the developed nanocomposites [118], [206], [262], [272].

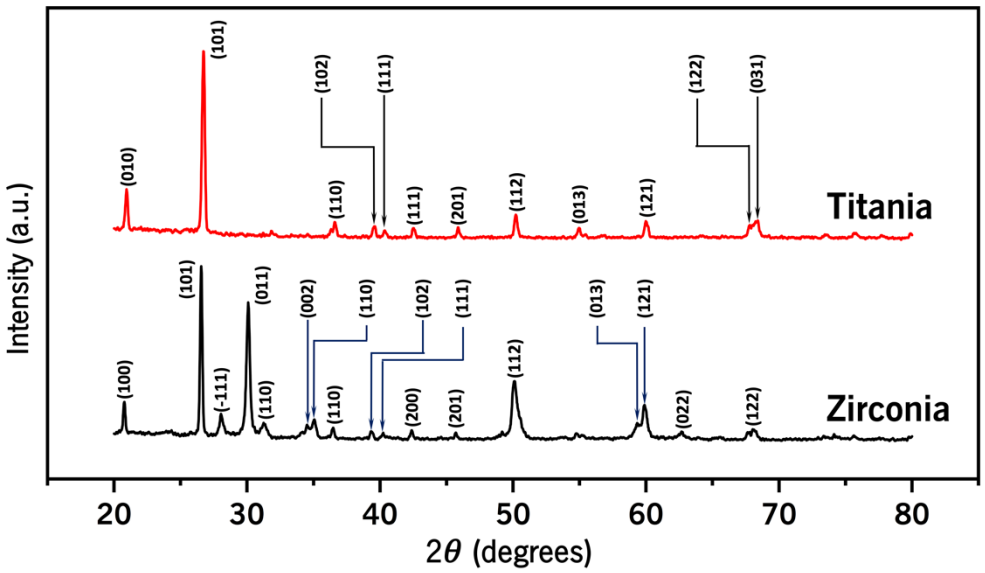


Figure 4.15 – X-Ray Diffraction spectrum plot of Intensity vs 2θ depicting Miller indices for crystallographic lattice structures for zirconia and titania.

4.5. Anti-bacterial evaluation

The application of the developed compound is not limited to shoe-soles as it can also be extended to gloves, wearable skin patches for biosensors, skin drug delivery systems, and wound healing, where handling liquids is a key factor. Furthermore, this concept can also be applied in environments requiring sterile or bacteria-resistant footwear, such as medical device manufacturing, vaccine manufacturing, and pharmaceutical industries, where surfaces may be slippery, and anti-bacterial conditions are essential. In these fields, it is crucial that the compounds

exhibit bacterial resistance, if not outright antibacterial properties. Non-slippery shoe-soles with bacterial-resistant properties are the optimal choice for such environments. This consideration was one of the reasons for adopting zirconia and titania nanoparticles: firstly, because nanoparticles often exhibit bacterial resistance, and secondly, because they impart hydrophilicity to intrinsically hydrophobic SR. Consequently, bacterial tests were performed on both nanocomposites in their untextured and textured states. In general, higher loadings with surface modification provide better bacterial resistance than lower loadings [273], [274].

Since most bacteria are negatively charged, a common negatively charged bacterium P. aeruginosa was chosen for the bacterial adhesion tests. Figures 4.16(a) and 4.16(b) demonstrate a reduction in bacterial adhesion after an incubation period of 24 hours at 37°C for zirconia and titania, respectively. Laser textured surfaces largely perform better due to the micro-roughness of the generated topography, which disrupts bacterial adhesion. Many bacteria prefer smooth, flat surfaces for colonisation and are less likely to adhere to rough surfaces. The compounds fabricated in this study exhibit surface roughness (after texturing) that can penetrate bacterial cells while simultaneously exposing nanoparticles with bacteria repellent properties. These nanoparticles increase the active surface area of the textured surface by inducing roughness, thereby creating an environment that discourages bacterial growth. Furthermore, high-energy laser engraving can induce chemical changes, such as oxidation or the formation of functional groups on the surface that enhance antibacterial activity by disrupting bacterial attachment or metabolism. As shown in Figure 4.16(a), pure vulcanised SR without additives supports nearly a million CFU/mL, while the textured counterpart reduces this to approximately 0.7 million. Additionally, it is evident that increasing the amount of zirconia in textured surfaces significantly reduces the number of bacterial colonies. However, the remaining bacterial colonies can be attributed to the fact that zirconia is not inherently antibacterial and the reduction in bacterial adhesion is primarily due to the physical effects of the textured surface combined with the limited bacteria repellent properties of zirconia [275], [276], [277], [278], [279]. Additionally, as higher loadings can also produce hydrophobic effect at high LST configurations and can also repel adhesion.

Titania anatase is inherently antibacterial due to its photocatalytic properties and high surface energy, thus, bacterial adhesion decreases exponentially with increasing titania content as shown in Figure 4.16(b). The combination of physical roughness and changes in surface chemistry due to the addition of titania reduce bacterial adhesion to minimum levels especially for textured surfaces with the highest loading, though complete elimination is not achieved. This significant

reduction in bacterial colonies highlights the advantage of incorporating titania nanoparticles to enhance hydrophilicity [280], [281], [282].

However, there are instances where textured surfaces suffer performance compared to their non-textured counterparts such as at 0.5wt% (for both zirconia and titania) and 0.3wt% (zirconia). This could be endorsed to the limited number of tests, and further rigorous bacterial adhesion studies are recommended to fully understand the effects of textured nanoparticle-reinforced vulcanised SR. These initial experiments underscore the positive impact of nanoparticle inclusion and demonstrate the potential of the developed material for applications in several medical fields.

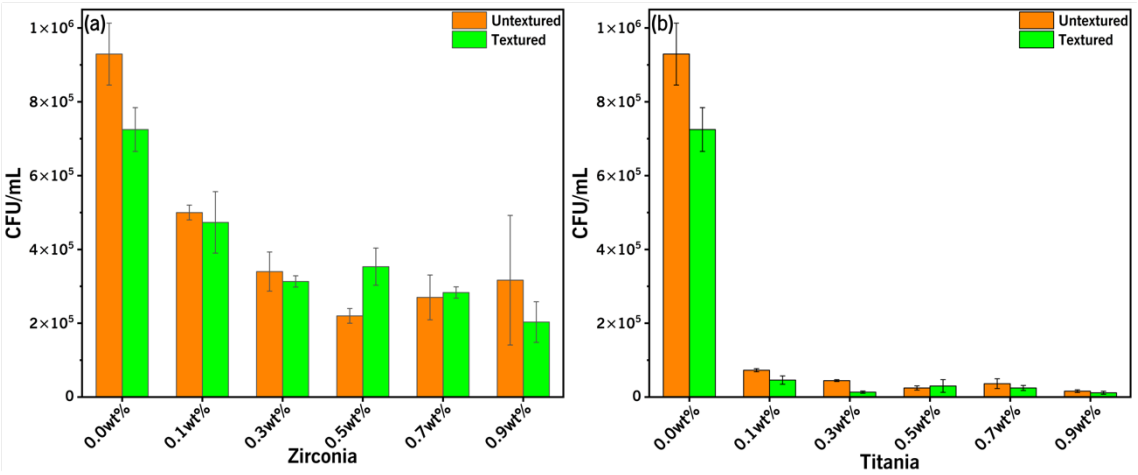


Figure 4.16 – Graphical representation of the performance of nanoparticle-reinforced composites with and without laser texturing in terms of Colony Forming Unit/millilitre (CFU/mL); (a) zirconia untextured and textured bacterial adhesion, (b) titania untextured and textured bacterial adhesion. The textured surface is with 500×200 configuration.

4.6. Significance of water imbibition

Ultrafast suction of QLL followed by instantaneous freezing proves the effectiveness of the developed MFS using nanocomposite. The wettability dictates the frictional performance of the MFS and needs to be quantified in terms of wettability angles based on the material and their structural properties. Furthermore, wettability transforming into capillarity for the time of filling is also discussed.

4.6.1. Wettability

Wettability as the affinity to water is a surface characteristic that reflects surface's ability to interact with water and is the centre of attention of this work. The degree of water interaction is determined by the Contact Angle (CA). CAs greater than 90° indicate hydrophobic behaviour, with

very high CAs (e.g., 135° or more) signifying superhydrophobicity, while CAs below 90° represent hydrophilicity. A complete spread of water (zero CA) over a surface signifies superhydrophilicity, however, the concepts of water absorption and spreading are distinct. Spreading occurs when a water droplet reaches an equilibrium state of minimal energy on the surface, whereas absorption or suction into cavities or pores is governed by the surface's capillarity. Importantly, spreading does not necessarily imply wetting as water can form a spread-out thin film without wetting the surface. These cavities can exist at micropores or surface roughness. Surfaces can be made hydrophilic by depositing a more hydrophilic material or modifying the surface chemistry [283], [284]. Coating deposition is a common method for imparting hydrophilicity to polymers, however, its application is immensely limited in the cases involving surfaces with high wear rates, extreme wetness, or hardness such as shoe soles. Winter shoe-soles, which encounter constant slippery wet and dry icy conditions are particularly unsuitable for hydrophilic coatings due to their lack of durability and inability to sustain harsh interactions including their permanence in wetting. These coatings are not ideal for creating capillary bridges that enhance adhesion and friction under such demanding conditions [122], [285], [286], [287].

Having said that, this thesis work puts forward a way to induce permanent hydrophilicity using simultaneous physical and chemical alterations on the SR polymer. Chemical modification is by changing the chemistry with the introduction of inherently hydrophilic nanoparticles into the SR followed by production of surface roughness in the form of microcavities using LST that simultaneously reveals nanoparticles as well. Either one of these modifications does not guarantee permanent hydrophilicity and wet capillary-adhesion bridges by keeping the mechanical properties intact. Most solids are naturally rough, but their surface roughness is often insufficient to sustain a hydrophilic state especially where roughness makes polymeric surface more hydrophobic because polymers are inherently hydrophobic. Besides small roughness cannot be enough to offer the mechanical interlocking mentioned in this PhD concept. Thus, hydrophilic surfaces can be achieved through chemical treatments combined with mechanical roughening. Titania, silica (SiO_2) and zinc oxide (ZnO) have been widely studied for their photoinduced self-cleaning properties, affordability and hydrophilicity. Nevertheless, polymers often require oxidation combined with surface roughening through treatments such as plasma, electron beams, and ion irradiation to impart hydrophilicity. Zirconia and titania as polar materials are inherently hydrophilic, bacteria aversive, and have superior material properties, therefore were chosen to fabricate multifunctional surface.

At the same time, LST can oxidise the exposed nanoparticles and polymeric surface, over the produced micropillars and cavities, in addition to material-based hydrophilicity.

The transition of wettable effect into capillarity has been comprehensively studied for different loadings of nanoparticles in SR. The focus is on converting hydrophilicity into capillarity is to achieve the suction of QLL entirely in its cavities. Ultrafast capillary rise and immediate freezing inside the microcavities (filling-freezing effect) define the gravity and intensity of the mechanical interlocking. Figure 4.17 highlights wettability and capillary tests against gravity, for higher zirconia loadings, with similar tests conducted for zirconia and titania at lower loadings presented in Figure 4.18. Replicating naturally occurring capillary adhesion in frog and gecko toepads, requires the rapid absorption of QLL. The CA and capillary effects against gravity illustrate the initial water affinity of the produced textures. Textures with 0wt% nanoparticle or pure SR created using lasers, exhibit a superhydrophobic nature (CA = 135°) that immediately repel water droplets. Since physical structures also alter the surface free energy, pure SR untextured and textured with all three dimensions were tested for wetting. It was observed that all SR specimens show superhydrophobic features though 500×250 shows a little improvement providing CA < 80°, nevertheless, it will not help in improving mechanical interlocking if it does not absorb enough quantity of water from molten ice (Figure 4.17(a)). This implies the significance of altering the material composition of the polymer. Furthermore, this little hydrophilicity shows water droplet hanging on the textured surface as shown in 0wt% zirconia of Figure 4.17(b) but immediately departs leaving the surface completely dry during antigravity capillary suction tests. Pure SR textured or plain zirconia/titania surfaces have low surface energies, which is the energy required to form and maintain the interface between two phases, regulates the CA and indicates the degree of hydrophilicity of substances [117], [288], [289].

LST of pure SR creates roughness and can increase the contact area but fails to sufficiently increase the surface energy to overcome the adhesive forces between the liquid and the surface, preventing the liquid from spreading over it. The law of wettability dictates, “hydrophobic surfaces become more hydrophobic and hydrophilic surfaces become more hydrophilic by the introduction of surface roughness”. Therefore, wettability cannot be induced just by creating the roughness in the form of micro-pillars on hydrophobic SR. Adding zirconia/titania nanoparticles into the SR matrix followed by laser texturing not only increases the machinability of the material but also imparts wettability [290]. Exposed nanoparticles attract water and drastically decreases the contact

angle from 135° for plain SR to the superhydrophilic range of 33° for 1wt% zirconia nanocomposite, leading to the wet Wenzel state as shown in Figure 4.17(b). Similar kind of behaviour can be observed in Figure 4.18(a), where addition of zirconia and titania produce positive but different effects on wetting behaviour. Increasing the zirconia to 3wt% enhanced the wetting effect from hydrophilicity to capillarity, where the water droplet was sucked in immediately upon contact. Despite this rapid absorption, the effect remains unverified without capillary suction against gravity. Therefore, all specimens were tested for capillary suction against gravity, although gravitational pull may not be available in real application like capillary tests here, as body weight will provide the necessary push on the textured surface to force liquid inside the microcavity. Figures 4.17(b) shows that 3wt% and 5wt% zirconia achieve optimum capillarity taking approximately 1.5 milliseconds to completely absorb the liquid droplet as every frame is approximately 0.5 millisecond. Beyond this optimum level, introducing more zirconia does not guarantee further improvement in capillarity, instead, wettability regresses from the Wenzel to Cassie impregnated state due to the wider and deeper cavities formed by higher percentages (7wt% and 9wt%) of laser-machinable zirconia nanopowder. These deeper cavities trap air and resist water penetration, making the textures less wettable. However, these higher percentage specimens still absorb water to some extent due to the presence of water-attracting zirconia on sites of the rough surfaces of micropillars. The Cassie impregnated state is a mixed state where some liquid penetrates the cavity while some remains on the surface, balanced by air pockets. Figure 4.17(b) shows empty space underneath the water droplet in the case of 7wt% and 9wt% compositions, with 9wt% trapping more air and repelling penetration, while 7wt% quickly displaces air pockets, allowing water to occupy the space. For 9wt% zirconia, the textured MFS become hydrophobic again illustrating CA of 120°. In Figure 4.17(b), evolution of hydrophilicity can be seen simply by observing as how different states of wettability generate with physicochemical modifications.

Hence, an optimum limit has been established to loading quantity of nanoparticles i.e. 5wt% for best water absorption after which the capillary effect declines. While higher percentages increase the depth of cut and accommodate more water, they also make the SR composite stiff, brittle, and harder as evidenced by their destruction after sliding friction tests on ice. In addition, QLL is a nanometre layer with a limited quantity to be absorbed within the depths and limited depth of the cavities are sufficient without compromising the integrity of the material. Figure 4.17 demonstrates all three geometric configurations for mechanically best performing specimens of LST 500×200 configuration.

On the other hand, Figure 4.18 illustrates the CAs and anti-gravity capillary rise phenomena for zirconia and titania nanoparticle loadings ranging from 0.1wt% to 0.9wt%, respectively. LST with dimensions of 500×150 and increasing loading percentages led to the reduction of CAs. However, the zirconia-reinforced specimens did not achieve as effective wetting as titania. Because for 500×150, the wettability increased with loadings and always remain in hydrophilic range (well below 90°). Homogeneous dispersion of nanoparticles leaves most significant effect on wettability as titania performs better in wetting effect for small cavity cut sizes i.e., 500×150. Despite binder removal, zirconia tends to coagulate during processing, making its dispersion challenging. Consequently, zirconia nanocomposites with lower cavity textured sizes exhibit limited wettability, particularly at loadings up to 0.3wt%, compared to titania nanocomposites, which consistently achieve lower CAs and hydrophilic properties. At 0.9wt% loading, both zirconia and titania attain hydrophilic limits, characterized by thorough suction shown in Figure 4.18(a). Textured dimensions of 500×200 and 500×250 for all loading conditions attain good hydrophilic characteristics for both the nanocomposite until the higher loading meets larger texturing dimensions of 500×250 where nanocomposites' surfaces become hydrophobic again. Generated hydrophobicity is the evidence of dominant effect of physical structure over the composition of hydrophilic material. Though high loading percentages of zirconia/titania should ideally attract more and faster water, larger cavities accommodate enough air to prevent the entrance of water molecules. A balance between percentage of nanoparticles and textured dimensions can lead to good filling-freezing effect. Larger dimensions are also not desirable due to the limitation on the strength of the micropillars and resistance to slip. A slight superiority of titania while testing for wettability is attributed to the homogeneous and uniform distribution without agglomerated in SR matrix [33], [141], [291], [292].

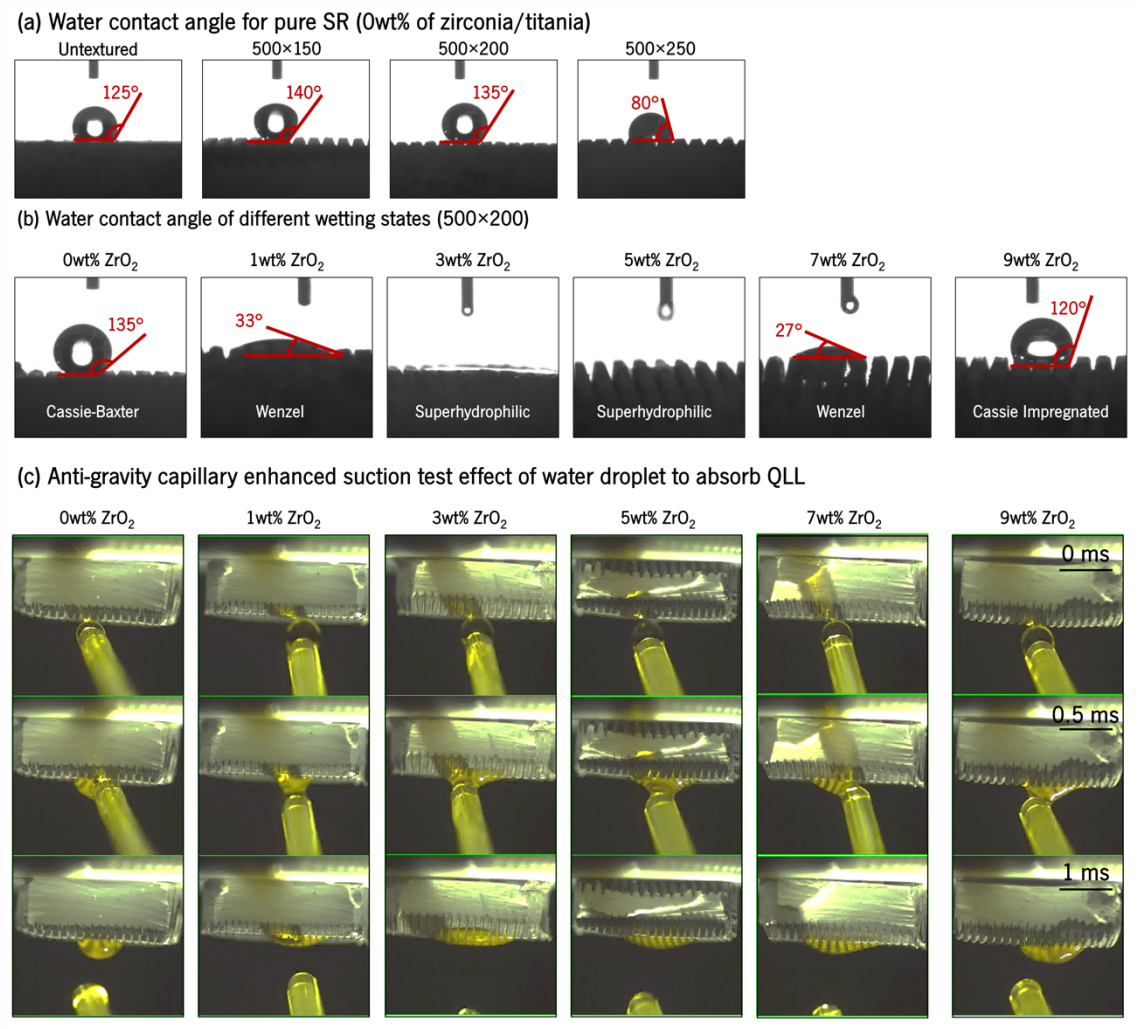


Figure 4.17 – Contact angle measurement using the sessile drop method with a goniometer and capillary suction tests for pure SR (plain and textured) and SR with five different weight percentages of zirconia nanoparticles for 500 µm × 200 µm samples; (a) water CAs for plain SR without any loading to comprehend the importance of physical structures, individually, (b) CAs measured and classified into different wettability states: Cassie-Baxter, Wenzel, Cassie impregnated, and superhydrophilic, (c) capillary suction experiments conducted against gravity. The specimens were glued with superglue on a flat surface with the textured side facing down. A pipette with water (resembling QLL) was then brought close to the surface until an appropriate distance was achieved to establish contact between the squeezed-out water and the textured surface. The droplet's behaviour upon contact—whether it wets, does not wet, or is completely suctioned was observed. Three frames, each approximately 0.5 milliseconds apart, were used to demonstrate the capillary effect. (All tests involving water and ice were conducted using normal tap water to simulate natural conditions, as natural molten ice typically contains impurities such as mineral salts, organic matter, dissolved gases, particulate matter, chemical pollutants, and biological contaminants).

Biomimicked adhesion of produced MFSs on wet ice becomes especially challenging due to different natures of the produced surfaces accompanied with their mechanical properties in the absence of biological elements like generation of mucus in frog toes or self-cleaning properties of

gecko footpads. Thus, MFS must be an equilibrium between wettability and mechanical properties of the nanocomposite. Specimens with CAs exceeding 90° exhibit a non-wetting nature, referred as the Cassie-Baxter state. This state indicates reduced surface energy in the roughened specimens, preventing the liquid from penetrating the surface roughness to increase surface-to-surface contact. However, the Cassie-Baxter state is unsuitable for anti-slip applications in this application for two basic reasons: (i) the inability to absorb water in the form of a QLL to enable mechanical interlocking, and (ii) the rolling effect caused by hydrophobic or superhydrophobic shoe-sole surfaces in the presence of PGQLL (Figure 1.2). Therefore, favourable specimens must exhibit at least the Wenzel state of wetting or, ideally superhydrophilicity. The Wenzel state with the lowest possible CAs is preferred as inadequate absorption of water into surface cavities can impede the solid-to-solid contact required for effective capillary enhanced adhesion. This adhesion is achieved by forming capillary bridges of frozen pillars between the shoe-sole and the icy surface. The water entering these cavities must freeze immediately, a process influenced by the dimensions of the microcavities. While larger cavities can hold more interfacial liquid, they also require a higher energy release and more time to freeze. Thus, an optimal cavity size that balances sufficient wettability and rapid freezing is the ideal choice. Besides, the Cassie impregnated state, where water/QLL seeps inside the cavities slowly by replacing the entrapped air can also offer favourable CAs, however, time required to absorb and freeze interfacial water/QLL will not be sufficient while walking. Filling and freezing effect is essential for the concept to work, therefore next section explains the capillary rise inside the cut cavities.

4.6.2. Capillarity

The capillary ability of the produced specimens was recorded using a high-speed camera, with a pipette positioned close to the upside-down specimen glued to a flat plate. When the pipette squirted water onto the specimen, hydrophilic surfaces instantly absorbed the droplet. Plain specimens without any textures whether pure SR reinforced nanocomposites could not retain any water droplets during the capillary tests against gravity. Flat surfaces lack physicochemical elements of wettability and therefore they do not retain water droplet even for milliseconds. This underscores the critical role of physical roughness, as altering the chemical composition of the silicone rubber does not create visible hydrophilic properties unless nanoparticles are exposed through LST. Similarly, textured surfaces with high contact angles or pure textured SR also failed to retain water droplets. Nevertheless, a droplet of water can momentarily be seen hanging in Figure 4.17(b) for 0wt% or pure SR. Thus, hanging droplet does not necessarily represent wettability

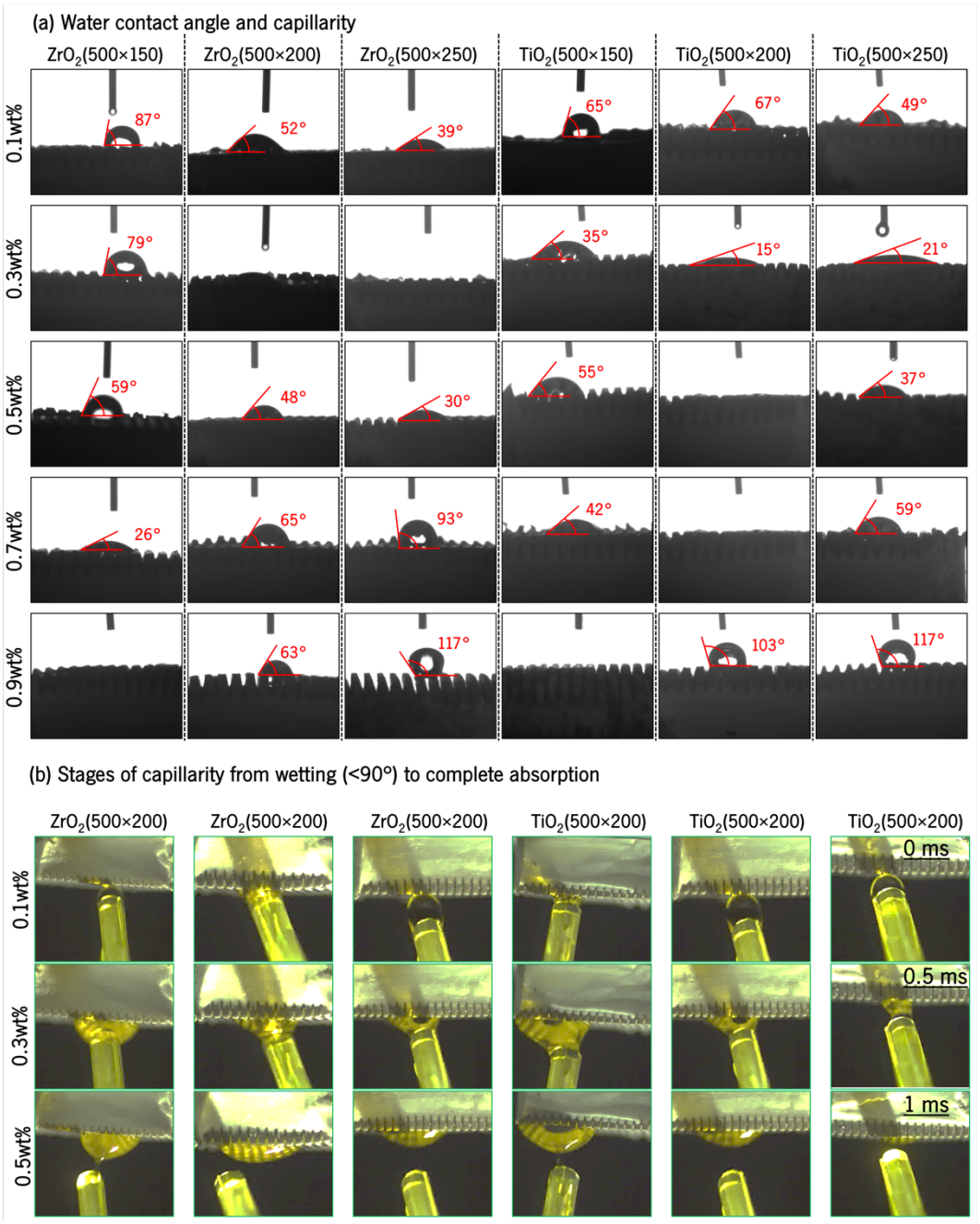


Figure 4.18 – Contact angle measurement using the sessile drop method with a goniometer and capillary suction tests for zirconia and titania for five different weight percentages; (a) CAs measured and classified into with their numerical values, (b) capillary suction experiments conducted against gravity. The specimens were glued with superglue on a flat surface with the textured side facing down. A pipette with water (resembling QLL) was then brought close to the surface until an appropriate distance was achieved to establish contact between the squeezed-out water and the textured surface. The droplet's behaviour upon contact—whether it wets, does not wet, or is completely suctioned was observed. Three frames, each approximately 0.5 milliseconds apart, were used to demonstrate the capillary effect. (All tests involving water and ice were conducted using normal tap water to simulate natural conditions, as natural molten ice typically contains impurities such as mineral salts, organic matter, dissolved gases, particulate matter, chemical pollutants, and biological contaminants).

of the MFS until it is absorbed inside the micro-textures. Figure 4.17(b) shows the agreement of CA tests with capillarity, where 3wt% and 5wt% zirconia absorb water completely and spread all over the surface. The visible part of the water hanging is visible due to the gravitational pull. Two consecutive frames considered are 0.5 milliseconds apart the absorption of complete water can be considered within three frames i.e., 1.5 milliseconds [33], [293], [294].

Figure 4.18(b) demonstrate capillary rise tests performed similar way and found in agreement with CA measurements for lower loading of zirconia and titania. Here, characteristic wettable behaviour of zirconia and titania reinforced nanocomposite can be observed. Figure 4.18(b) was organised to consider wettable states only i.e., Wenzel or superhydrophilic as the importance of wettable state was explained earlier in the section of wettability. For both nanocomposites, liquid rises and fills the cavities quickly and remains inside the cavities whole time. Furthermore, the suction of titania reinforced nanocomposite is more prevalent than zirconia-reinforcement as the spread is quick. This agrees with the explanation on zirconia agglomerates where less homogeneous dispersion in the polymer matrix results in impaired absorption effect with other weakening properties. Titania nanoparticles always disperse better, remain evenly distributed and produce consistent wetting. Homogeneous and uniform distribution of nanoparticles in polymer matrix came out as an essential element to retain favourable mechanical properties and permanent wetting effect by the virtue of increasing the surface energy.

Transformation of wettability into capillarity progresses through the diffusion of the fluid due to interaction with the hydrophilic substance simultaneously by the capillary action. Once the diffusion phase is over and fluid steadily and gradually rises inside the porosity with the help of adhesion between the fluid and substrate (here nanoparticles on the rough micro-pillars), reaches to a saturation. After the saturation phase, rise is almost invisible because of the dominance of viscous forces and gravitational pull in the last phase. Therefore, it is necessary to study diffusion theory based on chemical interaction and its validity for this work leading to further investigation of dynamics of capillary rise. The dynamics presented in this work is specific to capillary phenomenon obtained in experiments considering the assumptions. The mathematical explanation does not claim to produce a versatile and universal model for the capillary rise for all the cases, nevertheless, is a surrogate measure for the study of the phenomenon.

4.6.2.1. Diffusion theory

A surface with textures infiltrating fluid without any visible sign of contact angle or partial wetting represents transformation of wettability to capillarity. How fast liquid diffuses inside defines the degree of hydrophilicity. Initial spread, rise/fall of the fluid is initially defined by concentration gradient (diffusion) of the substances. Size, shape, geometry of the capillary cavity, pressure, and temperature, fluid viscosity, and concentration are the basic parameters to be considered while studying capillarity. Fick's second law defines the time for instantaneous diffusion due to concentration gradient of fluid in a porous media like water entering microcavities.

Fick's second law of diffusion;

$$Time\ of\ diffusion\ (t) = \frac{h^2}{2D} \qquad \text{Equation 4.1}$$

Where t, h, and D are the time of diffusion, length of the diffusion path, and diffusion constant, respectively. Considering capillary height/rise of 1 mm or 1000 microns (as majority of specimens nears to 1 mm or maximum up to 1.4 mm) and diffusion coefficient of water as 2.3×10^{-5} cm^2/sec (at 27°C), determined diffusion time from Equation 4.1 is approximately 430 seconds i.e., 7.17 minutes. For an instantaneous wetting, the time is too large. This impractical timespan denotes the limitation of diffusion law in case of micro-cavities fabricated here, because it only holds true only for nano to few microns. Therefore, a more complex expression must be established for the current work [295], [296], [297].

4.6.2.2. Dynamics of capillarity

Cohesion and adhesion are responsible for capillarity and categorised in wetting (initial diffusion), filling, and saturation phases. The time required to complete all three phases is the time of capillarity. Cavity's geometry, viscosity, surface tension, and gravitational force are factors that affect the capillary rise. Liquid rises and occupies the spaces between the cavity walls by virtue of zirconia/titania nanoparticles and fluid-air interface results in a meniscus. In the present work, CA of meniscus with the conical cavity wall can be considered 0° considering complete wetting that is required for absorption and spreading. Moreover, there is no fluid air interface because cavity is not open at the other end, instead ends inside the bulk material and therefore, it can be considered without meniscus angle. Once the fluid rises to the utmost height, the situation is known as saturation phase. There is no further movement of the capillary columns after it reached the end of the microcavities [298], [299], [300]. Current capillary enhanced suction adhesion concept is a

special case where the last phase of capillarity where gravity balances liquids weight does not effectively become effective i.e., saturation phase does not necessarily occur. Absence of saturation phase is again due to the end of cavity and there is stabilisation rather just filling and freezing. It is vital to determine and establish a relationship among governing forces in action. These forces are responsible for different regimes of the capillary rise [220], [301]. Conservation of momentum yields early and late inertial, and viscous regimes considering the mass added due to rise.

$$\frac{d}{dt}\{m(t).\dot{z}(t)\} = F_{Total} + \oiint \rho vv.n\, dA \qquad \text{Equation 4.2}$$

Where $\oiint \rho vv.n\, dA$ is the total momentum flux and evaluates to $\rho(\pi a^2 \dot{z}^2) = \dot{m}\dot{z}$. Henceforth,

$$(m + m_a)\ddot{z} = 2\pi a\sigma \cos\beta - \pi a^2 z\rho g - \frac{1}{2}\rho \dot{z}^2 \pi a^2 - 2\pi az.\tau_v \qquad \text{Equation 4.3}$$

Where $(m + m_a)\ddot{z}$ is the "**Inertial Force**" and m_a is the mass added in the presence of a reservoir. Term $2\pi a\sigma \cos\beta$ is "**Surface Tension Force**", term $\pi a^2 z\rho g$ is "**Gravitational Force**" consisting $\pi a^2 z\rho$ as mass in the capillary cavity, term $\frac{1}{2}\rho \dot{z}^2 \pi a^2$ is "**Dynamic Pressure Force**" where term $\frac{1}{2}\rho \dot{z}^2$ represents "**Bernoulli's pressure**", and the term $2\pi az.\tau_v$ is "**Viscous Force**" consisting shear area of $2\pi az$ and τ_v as viscous shear stress. Being the main driving force, the surface tension is omnipresent throughout the capillary [302], [303].

The microcavity deals with limited fluid quantity in case of QLL, therefore, added mass m_a due to reservoir is neglected in the Equations 4.2 and 4.3 assuming unchanging angle of contact (Young's angle or CA, β) due to the constant velocity movement of the meniscus, fluid's surface tension and viscosity. Though Young's angle represents theoretical CA under ideal conditions, hydrophilic nature of the cavity and absorbance of total quantity of water leads to zero value, and assumption of Young's angle representing real CA can be made [300], [304]. Considering the generation of boundary layer by diffusion as initial stage, timespan to develop the fully developed boundary layer after the diffusion is governed by Jurin's law;

$$t_\mu = \frac{a^2}{\nu} \qquad \text{Equation 4.4}$$

Where t_μ = time taken to develop a fully developed flow, a = radius of the capillary tube/characteristic length. The varying conical section of the texture proved to be helpful for the capillary imbibition. To keep the realistic view of the analysis, the size of the cut at the entry or top width of the cut/cavity was taken 250 μm and the bottom width of cut/cavity 50 μm (refer Figure 4.20(b), though these values change significantly with loadings and LST configurations).

Furthermore, the same calculations can be performed for other cut geometries as well [305]. For further simplification of the mathematics, characteristic length is used and given as;

$$d_{eq} = \frac{d_1+d_2}{2} = \frac{250+50}{2} = 150\ \mu m \implies a = 75\ \mu m$$

Applying Jurin's law from Equation 4.4, the time for the diffusion;

$$t_\mu = \frac{a^2}{\nu} = \frac{(75\times10^{-6})^2}{0.89\times10^{-6}} = 0.006333\ second = 6.333\ milliseconds$$

After 6.333 milliseconds and Equation 4.3 becomes active for different stages. A fully developed Hagen-Poiseuille's laminar flow establishes immediately after this negligible diffusion timespan throughout the capillary. For laminar flow, velocity profile is $u(r) = 2\dot{z}\ (1 - \frac{r^2}{a^2})$, the flux along the tube is $F = \pi a^2 \dot{z}$, the shear stress (τ_v) along the outer walls of the capillary cavity is $\mu . \frac{du}{dr}|_{r=a} = \frac{4\mu}{a}\dot{z}$.

Equation 4.3 yields the dynamic equation for the capillary;

$$z\ddot{z} = \frac{2\sigma\cos\beta}{\rho a} - zg - \frac{\dot{z}^2}{2} - \frac{8\mu}{\rho a^3} z\dot{z} \qquad \text{Equation 4.5}$$

Where z = capillary rise, $\dot{z}$ = velocity of the rise, $\ddot{z}$ = acceleration along z-axis, σ = surface tension of the fluid, ρ = density of the fluid, β = contact angle, a = capillary radius, μ = dynamic viscosity, and g = gravitational acceleration. Equation 4.5 is a second order non-linear differential equations where capillary rise (z) is the function of time (t). Due to the dominance of inertial force, velocity is considered zero and hence the capillary rise as a function of time gives $z = \frac{6}{7}\frac{\sigma\cos\beta}{\rho a^2}t^2$. This early pure inertial regime will provide the time to rise of fluid with polynomial trend. As the column accelerates from the initial velocity $\dot{z} = 0$, $\dot{z}^2$ becomes important in this regime and dynamic pressure term dominates the inertial as $\ddot{z} \to 0$ and a late inertial regime sets up resulting $z = \sqrt{\frac{4\sigma\cos\beta}{\rho a}}t$. During this regime, gravity and viscosity become irrelevant. Zero inertial effect ($\ddot{z} = 0$) and dynamic pressure lead to the viscous regime i.e., $z = \sqrt{\frac{\sigma a\cos\beta}{2\mu}}\sqrt{t}$ where fully viscous regime is approached. Subsequently the static regime approaches to exponential decay ($z = 1 - e^{t/\tau}$) and stabilises until fluid reaches to final height. Figure 4.19 summarise the nature of the curve and timespans for each stage of capillarity excluding the time of diffusion. From Figure 4.19, time to overcome the three stages can be added to 1.56 ms for 1 mm and 2.02 ms for 1.4

mm. The durations obtained in this study align with the results of the capillary tests and can be verified by analysing the frames captured within 1.5 milliseconds. The time required to fill the cavity is a critical parameter, as it indicates optimised material removal to hold just enough water in the shortest possible duration, allowing it to freeze rapidly. The freezing of the filled cavity depends on several factors, including the amount of energy dissipated (energy is also a function of quantity of liquid), the temperature of the contacting ice and the surrounding environment, the thickness of the QLL, and the walking speed of the individual [261], [306], [307].

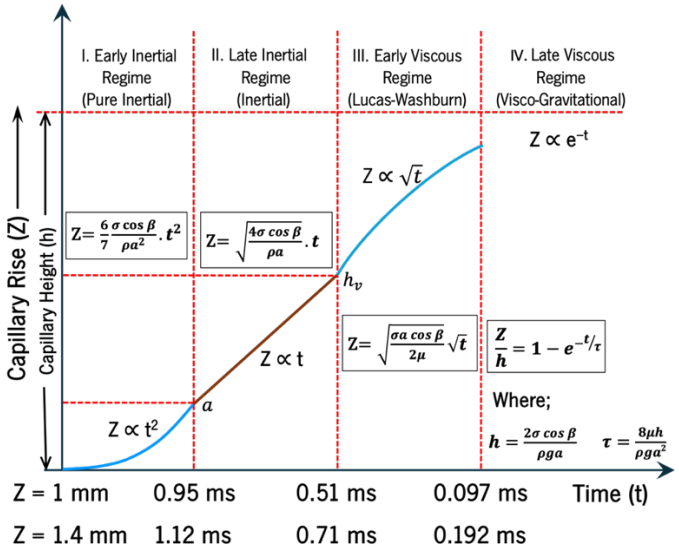


Figure 4.19 – Capillary regimes covered during the rise of water and the nature of their variations. The summation of all the regimes determines the time for suction of fluid in capillary tube of a micrometre to mm size.

Calculating the time to fill the micro-cavity, while incorporating assumptions, is a basic approach and does not claim to provide exact values due to the numerous factors involved. Capillarity itself is a complex phenomenon, and factors like the initial diffusion time of 6.33 ms may contribute to achieving wettability but are not conserved in the total time taken to fill the cavity. This and other simplifications result in the determined values being a simplified representation of capillary rise for water. Additionally, it is possible for the liquid to freeze before the cavity is fully filled, as is often observed in hydrophilic states where the entire droplet is not absorbed. In such cases, the capillary time would naturally differ. The recorded frames also offer an approximation, as high-resolution videos capture thousands of frames per second, and even over several frames, observable changes can be minimal. Having said that, the capillary dynamics demonstrate that, even in the worst-case scenario, the cavity filling time remains well below 100 ms (10% of a second). This rapid filling is sufficient to generate the capillary-enhanced adhesion phenomenon,

ensuring that quick filling and freezing will consistently benefit the walker. Another essential element of the produced MFS is to test it against the QLL and determine the SCOF and DCOF, and next section presents a thorough account of the sliding friction tests on ice.

4.7. Sliding friction test

Tribological tests to understand the friction characteristics of the produced geometries on nanocomposite is a major part of the development in this work. Therefore, following section will compile the significance of the friction generated on wet ice with respect to nanocomposites' dimensional and mechanical properties.

4.7.1. Relevance of tribological test for friction on ice

The friction tests were performed by a modified tribometer shown in Figure 3.9 placed on a Peltier-based freezing refrigerator. Before starting on the results and discussions over SCOF and DCOF obtained from sliding friction tests, the background of the tribological friction test must be discussed with respect to the ice friction as shown in Figure 4.20(a). Figure 4.20(a) is a pictorial representation to simulate the evolution of walking describing the requirement of friction. Following steps are the comprehensive description of the process and the factors during stepping on wet ice.

(i) At the start of the walk, when the heel strikes and first contact occurs on wet ice, the QLL (–1.5°C to 0°C) is absorbed by the textured surface, causing the capillary rise. The moment water enters the cavities (within milliseconds), a freezing front moves from an icy interface to liquid inside. Faster dissipation of heat helps freezing front to move upward leading to a stage of solidification of liquid inside the cavity to attain maximum hardness. As water enters the cavity, the freezing front loses its ability to dissipate heat due to the distance from the frozen surface and the relatively higher temperature of the substrate. Conical structures offer a favourable configuration because the conicity gradually decreases the area, allowing the cavity to absorb water more quickly and freeze faster, as smaller volumes require less energy dissipation. While a polynomial conical wall is arguably the best performer, the limitations of fabrication via LST result in the linear wall shaped conical microcavities [293]. For the given cavity size, linearly varying conicity performs exceptionally well. The meagre amount of water and an optimised shape for capillarity make inside liquid freeze instantaneously, creating mechanical interlocking. The force required to overcome this interlocking is the SCOF, which leaves micro-structured pillars on the ice. This primary interlocking is crucial to prevent SFs when the heel contacts the slippery ice. The SCOF must be as high as possible to achieve enough friction at the start of the walk to prevent SF [140], [257].

(ii) Once the SCOF phase passes and the specimen starts slipping on ice, the friction force decreases and remains within a small range of variation, keeping it constant. This behaviour is typical of sliding tribological tests and represents the minimum friction force i.e. the DCOF. DCOF region occurs when the full shoe-sole meets the ice, and QLL suction spreads across the surface. During the tests as the contact area increases at full sole contact, impact and time required for interlocking reduce, resulting in lower DCOF values compared to real-life walking, where a greater number of frozen peaks can create more friction. Initial impact of foot sole helps creating suction force and melts more ice that might enhance interlocking. During the ice drag tests, DCOF can also be raised by high conformity of soft micro-structures or quick successions of suction and freezing inside the cavities, although limited due to the speed of tests. DCOF can resist slips but cannot avoid fall once slip takes place. DCOF is a an important factor and needs attention with the context of QLL, therefore a separate section details its importance in further reading [308], [309].

(iii) High SCOF is required to prevent initial slip, as slipping during the heel strike (the most prone moment of slipping) cannot be avoided even with good DCOF values. Therefore, high SCOF and a safe range of DCOF are essential to prevent SF on icy surfaces.

(iv) While peeling off from the surface, the foot sole bends forward, gradually releasing the frozen peaks. Figure 4.20(a) illustrates this mechanism, where the toe sole contacts the surface as the heel lifts (toe sole produce the force to release heel), creating space for the peaks to detach. The elasticity, hardness, and ice adhesion due to roughness of the MFS micro-cavities are crucial during this process, as these prevent damage to the micro-pillars, which must balance flexibility and strength for effective deadhesion.

Inspired by the toepads of frogs and geckos, the developed microstructures generate capillary-enhanced adhesion through a filling-freezing effect. Figure 4.20(b) illustrates this phenomenon, achieved by designing micro-textures with ultrafast capillary rise. In Figure 4.20(b), frozen ice peaks are depicted both with and without colour. The whitish-grey peaks represent the actual broken remnants of frozen capillary-risen water left inside the cavities. To measure the SCOF, these peaks, which create mechanical interlocking must be broken. As a result, the remaining ice micro-pillars are very short, with only visible patterns. In contrast, the coloured peaks are created by pushing the specimen over ice containing a QLL and immediately removing it to observe the filling and freezing effect. These pillars are shown by vertically removing the specimen to preserve the peaks, unlike during real friction testing, where the peaks are broken [310].

It can happen that after several steps or even after few steps, ice pillars can lodge inside and block the cavity i.e., clogging, but this can be an added advantage to promote friction as already ice inside the cavity will contact the ice in following repetition, while QLL will be absorbed by other unblocked cavities. That gives the chance to already blocked cavities to adhere to ice by the virtue of low temperatures (ice-to-ice adhesion is more prominent). This way ice and broken ice pillar can weld with each other better than newly filled cavities to promote friction. Besides, number of blocked cavities must not be in plenty, otherwise newly molten water will have no place to get absorbed due to lack in capacity of capillary cavities to execute the real idea of friction generation. Figure 4.20(a) shows a real-time image (adjacent to the leftover pillars) of a specimen (9wt% zirconia) after the first test. The surface appears stiffened by the cold and completely clogged with ice peaks, unable to detach due to insufficient elasticity and softness of the microstructures. This is one of the reasons why higher loading zirconia 7wt% and 9wt% got destroyed during the tests.

4.7.2. Static and dynamic coefficient of friction

Based on the discussion from the relevance of friction coefficients, extensive sliding friction tests were performed, and friction curves were obtained for higher loading of zirconia and small loadings of zirconia and titania. Looking at the importance of COF tests, we analyse the findings in separate sections i.e. first the higher zirconia loading followed by small loadings for zirconia and titania both nanoparticles in comparative manner.

4.7.2.1. Static and dynamic coefficient of friction for higher zirconia loadings

Figure 4.21(a) compiles COF data for 1wt% to 9wt% of zirconia-reinforced specimens along with pure SR with and without textures. Experiments consistently showed that micro-patterned surfaces significantly alter the SCOF and DCOF as shown in Figures 4.21(b) and 4.21(c). A plain SR specimen without zirconia addition exhibited an average SCOF of 1.19 (Figure 4.21(a)) and a DCOF of 0.732 (Figure 4.21(c)) during tribological performance. Initially, the plain vulcanised SR produced substantial traction due to its softness and adhesion to the surface. However, once the force required to overcome this initial sticking was surpassed, the COF becomes negligible, resulting in a simple slip over the wet surface. Furthermore, under freezing temperatures, the pure SR specimen becomes extremely hard and slid over the QLL without any grip [143], [308].

Micro-structures on the surface increase roughness, surface area, and surface energy. LST can create micro-patterns that act as capillary sites by absorbing the QLL to enhance adhesion. Textured pure SR achieved a maximum SCOF of 1.44 and a DCOF of 1.26. The slight rise in friction

from plain SR can be attributed to initial sticking at the first contact point as happens at heel strike, which pushes out entrapped air from the textured pockets and allows a small amount of liquid to form capillary interlocks. The textured micro-pillars increase surface area and SR used here is appropriately conforming/soft, hence, the DCOF increases due to high conformability and surface area like frog toepads that conform by increasing their surface area. The inefficiency of the physical structure in providing capillary suction for prominent interlocking directs us towards altering the surface chemistry of SR. Physicochemical changes through laser patterning produce different ranges of wettability. The 1wt% composite achieves a Wenzel state of wetting by increasing surface energy and positioning zirconia at capillary sites. The rise in hydrophilicity enhances the capillary suction of the QLL inside the micro-cavities, immediately forming bridges by freezing water in the cavities [311], [312].

Capillary suction adhesion yields a maximum SCOF and DCOF of 1.70 and 1.32, respectively, for 500×200 dimensions, compared to 1.54 and 1.21 for 500×150. Further changes in texture to 500×250 reduce the COF to 1.46 and 1.17. Specimens with 1wt% exhibit considerably higher friction values sufficient to prevent SFs. However, as the substrate temperature drops, the freezing effect becomes more dominant, causing cold stiffening and clogging completely, thus preventing the peeling-off effect and due to these effects, detachment becomes extremely difficult.

Further increment in zirconia enhances the capillary effect, thereby increasing friction on wet ice until a critical point of 5wt% is reached. Beyond this point, the fragility and stiffness become so prominent that they either dislodge during adhesion or conform excessively, causing the capillary suction adhesion to diminish. The 3wt% composite offers the best grip and smooth peeling off on wet ice, thanks to the quick suction of the QLL, freezing, and favourable elasticity and flexibility resembling the toepads. This combination achieves an excellent SCOF of 3.46 and DCOF of 1.88. The flexibility, elasticity, and ultrafast suction remained intact across all geometries for 3wt%, with 500×200 performing extraordinarily due to its highest wetting effect. While the 500×150 and 500×250 specimens also showed satisfactory effects. As 500×150 geometry produced a slightly lower SCOF of 2.7 and DCOF of 1.48, which can be attributed to the smaller depth of the cavities. This trend of lower COF for 500×150 is consistent across all zirconia-reinforced SR combinations. It establishes that 500×200 patterns are the best-performing textures, producing optimum results, while 500×250 offers better friction compared to 500×150. For instance, 500× 200 with 5wt% yields an impressive SCOF of 2.94 and DCOF of 1.55, comparable to the 3wt% specimens.

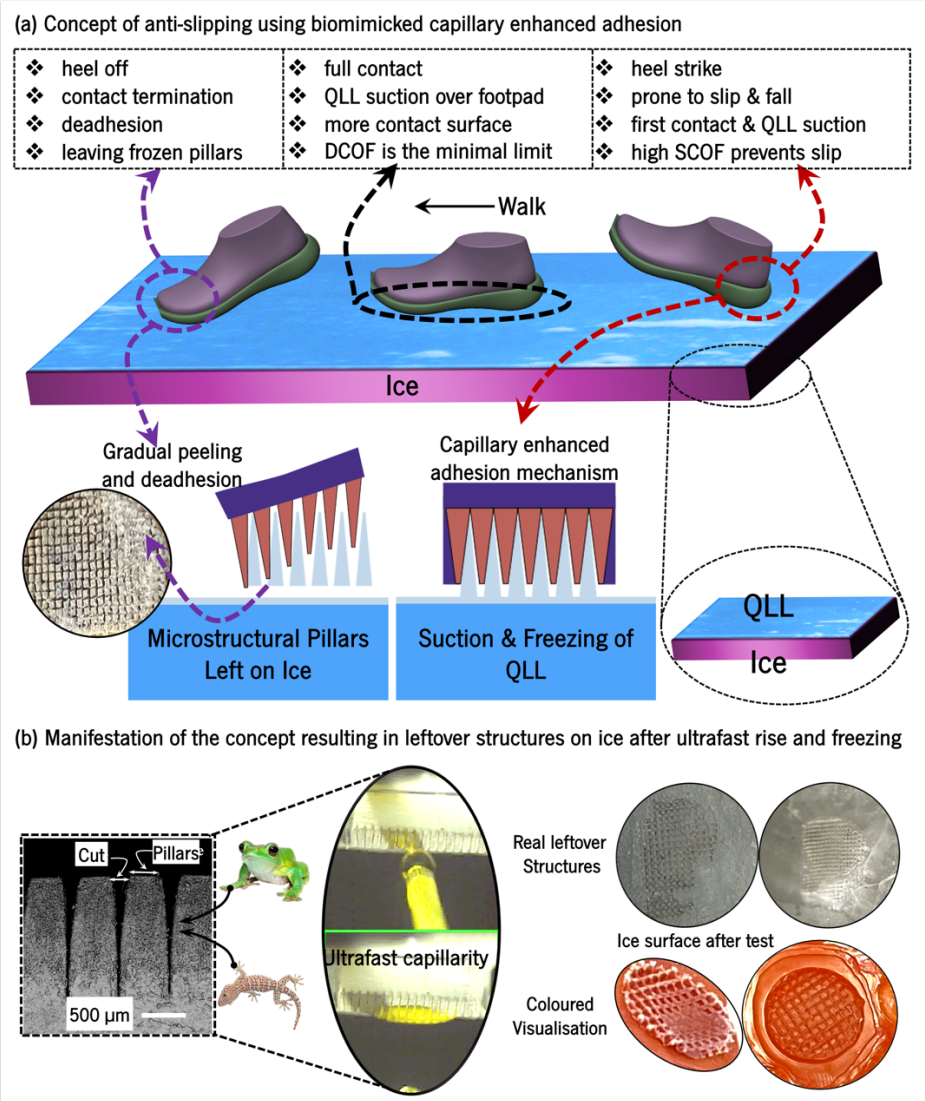


Figure 4.20 – Imagery of the concept; (a) the concept of anti-slipping using biomimicked enhanced adhesion during the process of movement illustrating heel strike, full contact, and peeling off or termination of contact. This shows the suction of QLL into the cavities at the start of contact, leading to full contact, and then the release of ice peaks during termination, (b) the manifestation of adapted concept in terms of micro-structures produced incorporating frog and gecko toepads' properties to perform capillarity followed by the representation of leftover pillars on wet ice. The colour was introduced to visualise the presence of micropillars of ice. Coloured images are the images taken after vertical impact of specimen on the QLL and then removing it vertically to see frozen pillars.

Although 7wt% zirconia can be considered slip-resistant, it performs poorly when compared to 3wt% and 5wt%. Additionally, increasing zirconia in the SR matrix to achieve faster suction and freezing does not enhance wettability further but saturates the matrix, weakens the pillars, and impairs detachment. This is evident from the friction outcomes of 9wt%, where the SCOF of 1.68 and DCOF of 0.908 indicate slip resistance. However, most of the pillars dislodged due to brittleness from the specimen and remained on the ice, demonstrating the detrimental effects of

excessive zirconia content. The damaged surface brittle, inelastic, and stiff micropillars can be observed in Figure 4.2(b) and 4.2(c).

The microstructures can be considered like tread patterns, where the loss of treads results in increased pressure at the interface, making surface SFs inevitable. Shoe-sole designs must prevent the accumulation of interfacial fluid and the buildup of pressure to prevent slip. If the micro-textures are too soft and conform entirely to the surface, they behave like a flat surface, offering no slip resistance and building up interfacial fluid pressure, resulting in creating a rolling effect. This phenomenon is not in agreement with natural toepads, which are both flexible and strong. After extensive ice friction tests, it has been observed that geometry and nanoparticle, both have a saturation point beyond which no further improvements are seen. Because a normal person walks about 10,000 steps a day and shoe-sole material and design must sustain its quality and effectiveness for the expected life of shoe. Figure 4.21(b) and 4.21(c) shows the SCOF and DCOF for all the specimens and can be observed for their performances [313].

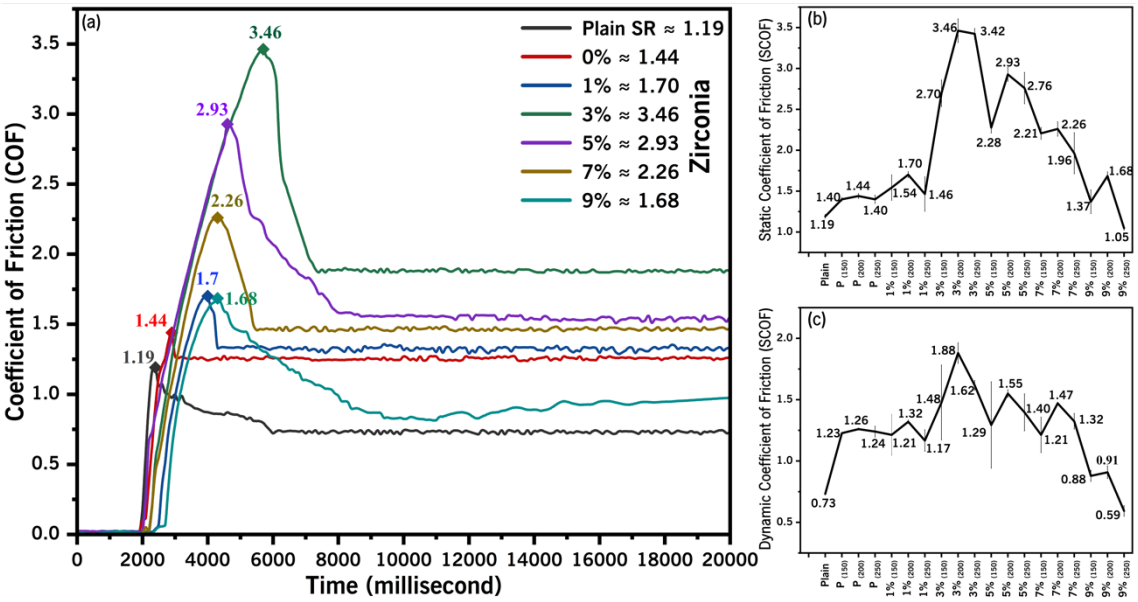


Figure 4.21 – Experimental results for sliding friction tests performed on higher zirconia loading (from plain SR, textured SR, and 1wt% to 9wt%) specimens; (a) COF curves obtained for the optimised zirconia-reinforced nanocomposites i.e., 500×200 LST, (b) SCOF for all specimens i.e., plain SR, plain textured SR, and reinforced textured specimens with 500×150, 500×200, and 500×250, (c) DCOF for all specimens i.e., plain SR, plain textured SR, and reinforced textured specimens with 500×150, 500×200, and 500×250. Sliding tests were performed at the speed of 5 mm/sec for 100 mm span.

4.7.2.2. Static and dynamic coefficient of friction for lower loadings

Using higher quantity of nanoparticles for zirconia is a way to understand the effect of number of nanoparticles in SR matrix. However, high quantity also poses a challenge during preparation of the compound, can hinder the cross-linking of the SR matrix, and can make specimens porous and fragile as was observed. Despite no visible porosities for higher loadings due to agglomerating nature of zirconia, it is evident that hardness decreases for almost all percentages of zirconia nanocomposites except 9wt% where zirconia becomes so prevalent that it directly participates on superficial surface and increases hardness. Apart from that, compression strength of these specimens also suffers significantly, though remains in working range due to good elongation properties and elasticity like lower zirconia loadings. Under compressive loads, pores can lead to localised collapse or deformation unlike tension, where fibres can align to resist the stretch and bulk material can carry the tensile load. Furthermore, the production cost of the shoe-sole is a major factor as well as a higher concentration of nanoparticles would result in more expensive footwear. Incorporating nanoparticles into the shoe-sole can significantly increase the overall price. Therefore, the study furthers towards tribological performances of 0.1wt% to 0.9wt% of zirconia and titania nanocomposites. Unlike the higher loading tests, the effect of sliding speed replicating the speed of locomotion is also considered. According to classical theory of friction, weight and speed do not leave any effect on COF, however, slipping on ice is different as walking at high speeds lead to a quicker fall with the same pair of shoes. Performed tests with increment in load yielded the similar results and were omitted, however, the trend of DCOF for higher speeds found excessively different to lower speeds. The graphs shown in Figures 4.22 and 2.23 were created by averaging the values obtained from three specimens, with five tests conducted for each specimen. The tests were conducted for all compositions and LST configurations in similar way and at 0.05 Hz and 0.1 Hz speeds (5 mm/sec and 10mm/sec). This approach ensures that the data represents consistent and reliable measurements by accounting for variability across multiple tests and samples.

Unlike scenarios with higher nanoparticle loadings, specimens with lower zirconia particles showed minimal damage over similar cycles. Furthermore, both SCOF and DCOF remained significantly better. For instance, at 0.1wt% zirconia and titania, SCOF values were slightly higher (1.29 and 1.21, respectively) compared to plain silicone rubber (1.19), highlighting the insufficiency of nanoparticles in the matrix. For 1wt% addition, the values were substantially higher i.e., SCOF 1.70 and DCOF of 1.32. for 500×200 configuration of LST. Increasing zirconia content

in lower loading led to a substantial improvement, with SCOF reaching 3.29 and DCOF 1.45 at 0.7wt% for 500×200 textured geometry. Unlike scenarios with higher nanoparticle loadings, specimens with lower zirconia particles showed minimal damage over similar cycles.

Furthermore, both SCOF and DCOF remained significantly better. For instance, at 0.1wt% zirconia and titania, SCOF values were slightly higher (1.29 and 1.21, respectively) compared to plain silicone rubber (1.19), highlighting the insufficiency of nanoparticles in the matrix. For 1wt% addition, the values were substantially higher i.e., SCOF 1.70 and DCOF of 1.32. for 500×200 configuration of LST. Increasing zirconia content in lower loading led to a substantial improvement, with SCOF reaching 3.29 and DCOF 1.45 at 0.7wt% for 500×200 textured geometry. Titania nanocomposites outperformed zirconia, achieving a maximum SCOF of 3.43 and DCOF of 1.85 at 0.3wt% for 500×250. Additionally, titania at 0.9wt% for 500×150 achieved an SCOF comparable to the highest zirconia values i.e., 3.24, with a much higher DCOF of 1.87.

The higher CA of zirconia nanocomposites at 0.7wt% for 500×200 compared to 0.3wt% for 500×250 indicates stronger capillary bridges and better mechanical interlocking. However, the Cassie impregnated state hinders friction performance, as slow water absorption reduces adhesion within the cavities. This issue is exacerbated with lower cut dimensions (500×150), as seen in titania COF curves, where SCOF drops to 1.32 and 1.72 at 0.3wt% and 0.5wt%, respectively. Wider cut geometries can mitigate the effect of the impregnated state, as demonstrated by zirconia at 0.5wt% for 500×200, which offers maximum COF. However, this does not hold true for 0.9wt% zirconia specimens with 500×250 geometry, where SCOF drops to 1.70 despite the impregnated state. This decline is due to high nanoparticle concentrations, which lead to increased material removal, thinning of the micropillars, greater interspacing, and reduced structural strength. These weaker pillars result in three typical outcomes: (i) excessive deformation under load, preventing cavity filling, (ii) bending during sliding, even if the cavities are initially filled, offering minimal resistance to movement, and (iii) hydrophobic behaviour in larger cut geometries as trapped air prevents water penetration. All these results can be observed together from the Figures 4.24 (a), 4.24(b), 4.24(c), and 4.24(d) [314], [315].

Titania nanocomposites, on the other hand, exhibit better adhesion and friction with consistent performance across lower cut-higher loading and higher cut-lower loading combinations (Figure 4.22). As previously discussed, the superior dispersion of titania compared to zirconia contributes to its overall better performance, even at higher loadings. However, for both additives,

at 0.9wt% loading with 500×200 and 500×250 geometries, COF values drop due to the onset of hydrophobicity. Nevertheless, zirconia SCOF values of 1.70 (0.9wt% for 500×200) and 1.60 (0.9wt% for 500×250), along with titania values of 1.70 (0.9wt% for 500×200) and 1.29 (0.9wt% for 500×250), remain relatively high.

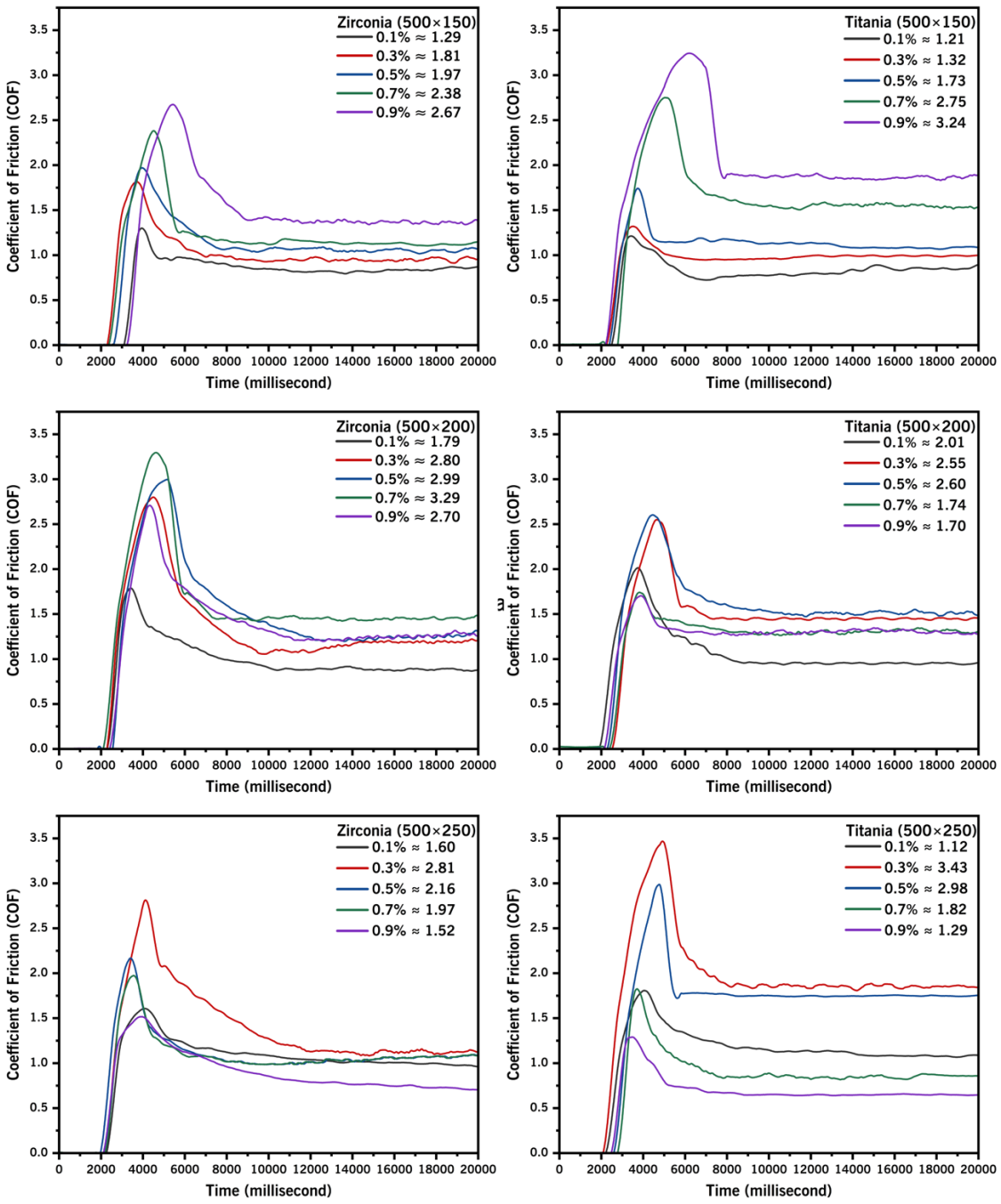


Figure 4.22 – COF curves with their corresponding SCOF values created by averaging the values obtained from three specimens, with five tests conducted for each specimen obtained after averaging five repetitions of each for three specimens under similar experimental conditions at 0.05 Hz (5 mm/sec for 100 mm stroke length).

These results are primarily attributed to the soft, thin pillars, which adhere and stick to surfaces due to the polymer's inherent properties. While these pillars bend and rub against the icy surface increasing surface contact and friction, the DCOF values fall below the desired range due to the absence of effective cavity filling and freezing. Figure 4.22 demonstrates that titania consistently exhibits better DCOF across all graphs compared to both small and large zirconia loadings. The drop in DCOF observed with zirconia is attributed to the behaviour of its agglomerates, which occupy specific localised areas. If these areas are exposed through LST, the filling and freezing effect occurs consistently. However, without this exposure, zirconia fails to attract water after the initial impact. In contrast, titania's superior dispersal ensures homogeneous and uniformly distributed sites and though rare under these sliding speeds, occasional filling-freezing effect can occur in sliding motion, otherwise, consistent higher DCOF can be attributed to the good material properties that offer comparatively better surface adhesion and friction by conforming and increasing contact area without any damage [316], [317].

These sliding traction tests were also performed by doubling the speed (0.1 Hz from 0.05 Hz) of the sliding to understand the behaviour of the produced nanocomposites. The sliding takes half the time to complete a full cycle, and the data recorded were for smaller time interval. There is a stability in SCOF values, however, DCOF falls at much faster and much prominently for all specimens whether zirconia or titania. SCOF for zirconia nanocomposite attains approximate maximum value of 3.30 at 0.7wt% for 500×200 at higher speed when compared to 3.30 for the same specimen at the lower speed, nonetheless. all other values decreased by 5% to 10%. Despite the decrease, values that were more than 2.00 for SCOF remained above this threshold value. On the other hand, for titania nanocomposites, maximum value achieved was 3.30 for 0.3wt% for 500×250 and 0.9wt% for 500×150 keeping all other values above the threshold of 2.00 with a slight decrease. Figure 4.23 compiles the nature of the friction curves obtained while experimenting with nanocomposites. These graphs show a sharp rise and drop after attaining followed by slightly noisy stabilisation compared to lower speeds. These irregularities during the stabilisation state are due to the little vibrations occurring at relatively higher speeds. Titania nanocomposites still offer superior SCOF, cumulatively, however, overall DCOF for titania drops substantially, whereas zirconia specimens do not show that drastic change as their DCOFs were already lower compared to titania. All these results can be observed together from the Figures 4.24 (e), 4.24(f), 4.24(g), and 4.24(h) [318].

That establishes that SCOF remains unaltered but drop occurs in DCOF for the micro-textures with changing speeds. The total scenario can be explained by following reasons.

(i) As SCOF represents the mechanical interlocking created at the first impact and is primarily associated with the performance of the specimen contacting wet ice rather than sliding speed, it remains remarkably consistent. This reflects a typical walking scenario, where the first impact occurs as the heel touches the surface, and mechanical interlocking happens immediately. Breaking the frozen capillary bridges requires roughly the same tangential force (friction needed to overcome adhesion resistance) regardless of speed. While forward movement at higher speeds can influence the breaking of adhesive bonds, in a real walking situation, unlike controlled friction sliding tests, where the adhesive force needs only be sufficient to prevent slipping rather than causing the bond to break entirely, resulting in a fall.

When slipping progresses to falling, DCOF becomes the critical parameter for safety. The extremely high SCOF values observed here primarily contribute to slip prevention rather than mitigating the risk of sliding into a fall. An SCOF of 2.00 can be considered a practical threshold, based on previous anti-slipping footwear studies where an SCOF of 2.3 was achieved and remained effective. This contrasts with other findings where shoe soles with a COF of 1.45 or lower became ineffective after repeated use, or experienced a significant drop in friction coefficient [319].

(ii) From Figures 4.22 and 4.23, it is evident that the variations in DCOF for all specimens at higher speeds are minimal and fall within a narrow range of values. This indicates insufficient time for additional capillary bridges to form or for the filling-freezing effect to occur at higher speeds, leading to a further decline in DCOF. However, in this kind of sliding tests, there are very rare situations for filling-freezing affect. Because once the initial breaking of the bridges occurs, the specimen starts sliding without any real resistance in the absence of vertical movement or impact. Walking speed is, therefore, a critical factor in winter locomotion on ice (no wonder speed almost halves during walking on ice) and this can allow time for capillary-based adhesion within micro-cavities to develop through filling and freezing. A significant increase in walking speed not only impacts DCOF but also SCOF, as the micro-structured capillarity relies on time to produce capillary adhesion and function effectively. This also highlights the unsuitability of the Cassie impregnated state of wettability, as the cavities require time to fill, which is not achievable with faster walking. Figure 4.24 summarises the overall COFs at two speeds for zirconia and titania, providing a clear view of the effects of speed, composition, and textured geometry. A critical focus of this thesis is

achieving hydrophilicity, extending to capillarity, to enable ultrafast filling and immediate freezing. The validity of this concept is confirmed by the COF values of the hydrophilic specimens, which fully absorb the water and deliver some of the excellent SCOF and DCOF values [7], [88], [233].

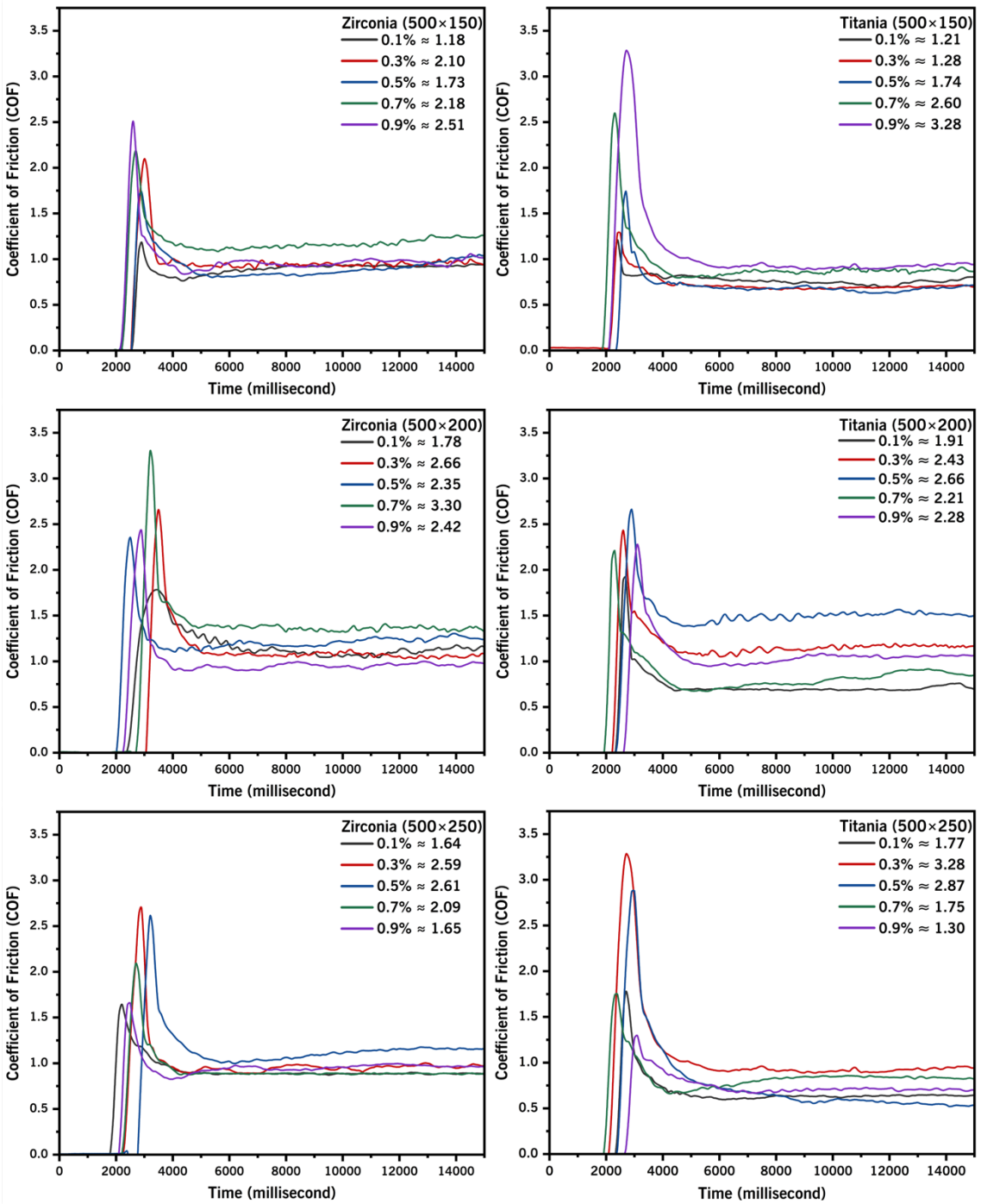


Figure 4.23 – COF curves with their corresponding SCOF values created by averaging the values obtained from three specimens, with five tests conducted for each specimen obtained after averaging five repetitions of each for three specimens under similar experimental conditions at 0.1 Hz (10 mm/sec for 100 mm stroke length).

(iii) The results here simulate a single step where initial impact happens followed by overcoming or breaking the capillary bridges to observe the strength of the adhesion. In practical case, insufficient SCOF means a slip and inevitability of a fall. In addition, DCOF plays an important role during the sliding tests and can be a measure of extreme situation where slip already took place but fall still can be prevented with the help of right balance. Better mechanical interlocking while slipping can help gaining right balance even during slip and DCOF is relevant to this aspect. Thus, it is safe to say that the minimum adhesion force (COF) is DCOF and if this value is sizeable, it can be a positive signal towards preventing a disastrous fall [78], [320].

(iv) Since the specimen touches the cold surface and then it takes approximately 2 seconds to start recording the data, hence, during this time freezing inside the cavities takes place (Figure 4.21, 4.22, and 4.23 all start rising approximately at 2000 ms). However, this does not estimate the real freezing time because freezing time must be much smaller while walking.

4.7.2.3. Significance of dynamic coefficient of friction

The significance of DCOF in the context of SFs is often misunderstood, as the common assumption is that losing balance on wet ice inevitably leads to a fall. However, the body's inherent biomechanics, coupled with instinctive responses, play a critical role in resisting and mitigating falls after slipping. A shoe-sole with higher DCOF can provide essential resistance, utilising mechanisms such as hydrophilic capillary bridges forming through the filling and freezing effect or leveraging the material’s properties. Additionally, microfibrillar hierarchical structures, like those found in gecko footpads, can stabilise momentary disbalance, giving the body the time needed to restore balance. While high DCOF values cannot fully prevent slipping, they serve as a crucial layer of protection during locomotion [321].

The DCOF values observed in the experiments primarily arise during sliding over wet ice after the initial impact, where capillary bridging may occur. Two primary factors contribute to these values: (i) the filling and freezing effect within micro-cavities, resulting in increased resistance, or (ii) drag resistance produced by the interaction of soft, micro-pillared surfaces with nanoparticles.

Although the likelihood of filling and freezing during sliding is minimal, the material properties of the soft micropillars are significant. These micropillars conform to the ice surface, increasing contact area, while nanoparticles deform irregularly to enhance traction. Furthermore, the wet surface itself may contribute partially to the filling and freezing effect. Experimental results

from Figure 4.24 show that while DCOF decreases with speed, it remains within an excellent range, likely due to one or the combination of these factors.

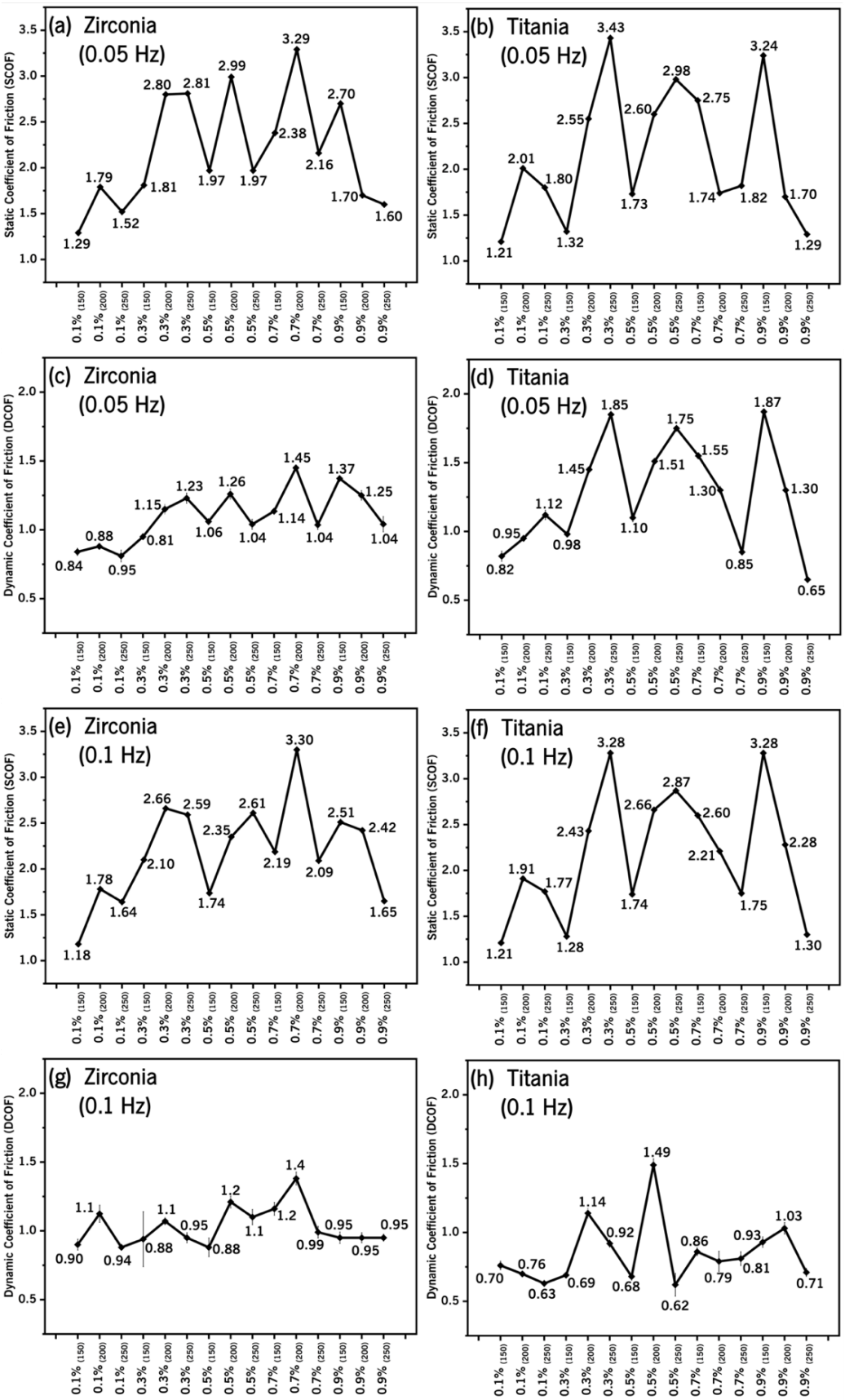


Figure 4.24 – Graphical representation of overall obtained values for SCOF and DCOF for the visualisation of comparison (zirconia is on the left, titania is on the right); (a) SCOF for zirconia-reinforced nanocomposite at 0.05 Hz (5 mm/sec), (b) SCOF for titania-reinforced nanocomposite at 0.05 Hz (5 mm/sec), (c) DCOF for zirconia-reinforced nanocomposite at 0.05 Hz (5 mm/sec), (d) DCOF for titania-reinforced nanocomposite at 0.05 Hz (5 mm/sec), (e) SCOF for zirconia-reinforced nanocomposite at 0.1 Hz (10 mm/sec), (f) SCOF for titania-reinforced nanocomposite at 0.1 Hz (10 mm/sec), (g) DCOF for zirconia-reinforced nanocomposite at 0.1 Hz (10 mm/sec), (h) DCOF for titania-reinforced nanocomposite at 0.1 Hz (10 mm/sec). Sliding tests were performed at the speed of 5 mm/sec and 10 mm/sec for 100 mm stroke length.

A thesis on the study of SFs on dry and wet ice for three shoes-sole material (PU, TPU, and vulcanised rubber) analysed that among three shoe-sole, average SCOF topped for PU (~ 0.8 to 1 at 0°C), SCOF values remain high, below this temperature. Additionally, vulcanised rubber showed maximum DCOF of 0.4 at −10°C at the speed of 0.3 m/sec. DCOF drops to 0.15 at the speed of 5 m/sec at the same temperature. Moreover, DCOF suffers heavily at 0°C (wet ice) and regardless of material or speed, it reduces to 0.05 after consistent drop with nearing zero temperature. Regardless of SCOF, an improvement in DCOF either by materials or by designs or by combining them can have positive response to SFs [98], [322], [323]

.

CHAPTER 5

RECOMMENDATIONS AND PERSPECTIVES ON FUTURE WORKS

This chapter consists of further optimisation to make it useful for the possible extensions of the PhD work. It also describes how the biomimicking can help in providing solution to the critical societal issues like slips and falls. Furthermore, the conclusions are put together for the work produced during the span of the work.

5.1. Limitations and further optimisation of the work

The presented work is a proof of a concept that uses biomimicked enhanced adhesion with experiments performed at the laboratory scale (15 mm specimens). The nanocomposites produced enhanced the wettability of the inherently hydrophobic silicone rubber by introducing hydrophilic nanoparticles of zirconia/titania with simultaneous adapting the material properties and structures from frog/gecko toepads. Obtained wettability is also not without limitations and depends on the material properties, shape and size of the structures, and design of the surface. The habitat of torrent treefrogs in humid environments, combined with their mucous gland secretions, facilitates prewetting of the interface. Similarly, the synthesised nanocomposites exhibit superior performance in the presence of wet environment as this enhances their affinity for the QLL. Furthermore, inherently hydrophobic polymers are not easily tuneable to permanent hydrophilicity, therefore, it needs more in-depth and fine-tuned augmentation of materials and methodologies. Optimisation will focus on enhancing material properties, process efficiency, and application-specific performance. This includes refining nanoparticle dispersion and loading percentages to balance mechanical strength, frictional properties, and antibacterial efficacy. Optimisation can also ensure reproducibility, cost-effectiveness, alternative compounds, and environmental sustainability for industrial applications. In due course, there remains scope for analysing viscoelastic, thermal properties, and anti-bacterial characteristics. These properties can provide valuable insights into the nanocomposites' interactions and the changes that may occur upon encountering a cold surface and wetness due to thicker fluids like oil or other chemically active fluids.

5.2. Towards the extension of the work

The whole shoe-sole does not need to be made of the nanocomposite to provide effective slip resistance, as these materials are soft and are best used to produce capillary adhesion. Therefore, prepared palettes will be accommodated by gluing into the cylindrical cavities produced on the shoe-sole at the toe and heel region because these are the regions mainly participating in slip resistance (heel at the time of first contact and toe during the termination or peeling off). These specimens can be incorporated into the toe and heel areas of the hydrophobic, harder shoe sole (50 to 70 Shore A), where maximum contact occurs. A detailed representation of the method to accommodate nanocomposite MFS is shown in Figure 5.1. The hard sole material serves three key purposes: (i) driving out the interfacial QLL left on ice after the specimens absorb water, (ii) melting hard ice through pressure melting from impact to generate QLL for capillary bridging, and (iii) protecting the softer specimens from permanent damage. The specimens positioned a few

millimetres inside the hard sole will shield the micropillars from direct impact forces. The hard sole first contacts the ice, followed by slight compression, allowing the microstructures to interact with the QLL. Additionally, the hard sole can feature hexagonal tread patterns similar to frog toepads to drain excess interfacial water (Figure 5.1(b)). The produced shoe-sole must be tested for different inclinations and temperatures of the ice to understand total scenario. The force required for pressure or friction melting is generated by body weight, which also helps prewetting the specimens, aiding water absorption. These small palettes can be changed once worn out.

The concept is equally applicable to normal wet floors or flooded environments, where water or other less viscous fluids can enter the cavities, while the remaining fluid is expelled from the interface by the hard hydrophobic shoe sole. This hybrid system presents opportunities for specific applications, including medical devices and footwear designed for sterile environments, leveraging the anti-bacterial properties of the compounds to enhance functionality. This patented work (protected under Portuguese patent (EU): Polymeric structures and its applications (119649 PP 2024.08.09) also holds potential for use in drug delivery and wound healing patches, where it can contain and deliver controlled quantities of liquid. Additionally, in biosensing wearables where, it can absorb and channel out bodily exudations like sweat, which could otherwise interfere with sensory equipment.

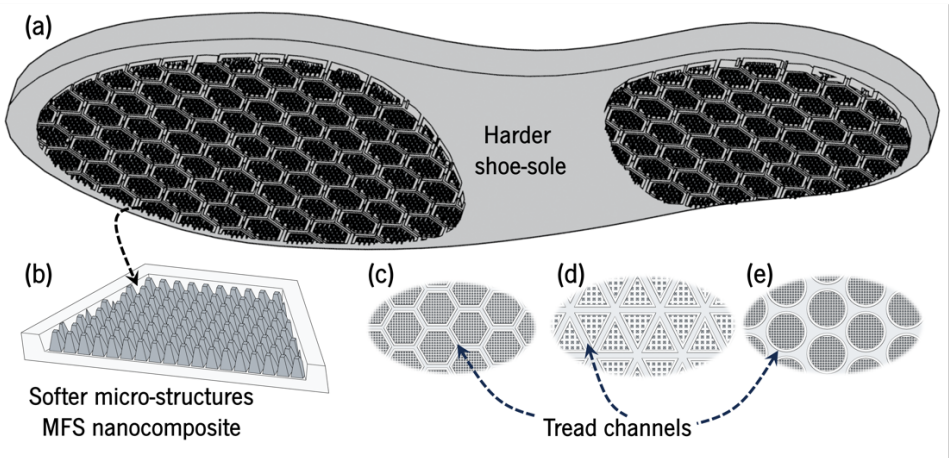


Figure 5.1 – Imagery of the concept employed in real application; (a) accommodation of softer nanocomposite micro-structures as an MFS to place on shoe-sole with tread channels, (b) hexagonal tread channels (mainly resembling frog toepad structures) designed on harder shoe-sole. The harder shoe-sole tread patterns cut in shoe-sole protect the softer MFS by keeping them few mm inside, (c) hexagonal tread channels, (d) triangular tread channels, (c) circular/cylindrical tread channels. Several tread channels can be implemented in the shoe-sole for appropriate drainage of access interfacial liquid. The produced palettes can also be accommodated inside the cavities of any kind of tread channels without changing the cylindrical shape of the produced specimens.

5.3. Bridging nature with science and safety

This doctoral research focuses on the issue of SFs that is a widespread problem. Despite causing significant injuries and fatalities, SFs remain underestimated and overlooked. According to the World Health Organization (WHO), approximately 6,84,000 deaths occur annually due to SFs, alongside nearly 37.3 million injuries worldwide. Of these, nearly half are attributed to harsh winters across approximately 60 countries, including Nordic and European nations, Canada, the United States of America (USA), the United Kingdom (UK), and Russia. However, SFs are not confined to icy or snowy conditions; they also occur on other slippery surfaces, such as those contaminated with fluids, making the problem even more pervasive.

Imagine the devastating impact when a breadwinner loses his/her balance on slippery ice, resulting in incapacitation, disability, traumatic injuries, or even death. In their absence, who assumes responsibility for the family? Similarly, a company may lose a highly skilled worker it has trained for years, or worse, an SF incident may incapacitate a healthcare worker, compounding the challenges of an already overstretched system. Public perception towards SFs has been largely negligent, often viewing such incidents as comical rather than recognising their gravity. Unfortunately, society fails to understand the serious consequences of SFs until one becomes a victim. While attitudes cannot be changed overnight, the inevitability of human movement demands a practical solution.

Nature-inspired solutions have gained significant attention over the past two decades, offering innovative approaches to long-standing challenges. It is time to adapt such strategies to address overlooked problems like SFs. This research contributes to a practical solution by introducing targeted modifications to shoe-sole materials through physical and chemical enhancements. These methods utilise widely available fabrication techniques, ensuring scalability, replication, and optimisation for future applications. The research adopts systematic four steps approach; (i) synthesis of a nanoparticle-reinforced polymer compound, (ii) surface modification of the prepared compound using LST, (iii) proof of enhanced wettability and capillary to obtain hydrophilicity, and (iv) sliding traction experiments to obtain SCOF and DCOF. This research serves as a proof of concept, achieving promising friction coefficients under laboratory conditions. The top-performing compound demonstrated an SCOF of 3.46 and a DCOF of 1.88, along with satisfactory mechanical properties and traction performance, that is a positive note, if not the whole resolve.

The findings of this research not only highlight feasibility but also offer a scalable and cost-effective solution to mitigate SFs. By addressing this long-overlooked issue with a nature-inspired and pragmatic approach, this work lays the foundation for advancements in footwear technology and public safety. The work represents an initial step and a conceptual approach to addressing the problem, without claiming to provide a complete or definitive solution.

5.4. Conclusions

This thesis investigated the optimisation of nanoparticle-reinforced silicone rubber composites for enhanced mechanical, frictional, and antibacterial properties. The findings consisted of the effect of loading percentages of zirconia and influence of zirconia and titania nanoparticles accompanied with physical textures produced via laser on surface characteristics, hydrophilicity, friction on wet ice offering a balance between durability and functionality. Advanced characterisation and processing techniques highlighted critical parameters for achieving uniform dispersion and improved performance. The study contributes valuable insights into the development of materials for applications in winter shoe-soles and can be extended to wearable sensing devices, drug delivery, and wound healing applications. The PhD thesis invokes following key outcomes encompassing original contributions, critical analyses, and practical implications of the research findings.

- Addition of nanoparticles in silicone rubber polymer matrix result in enhanced mechanical and material properties.
- To study the effect of loading (weight percentages) of nanoparticles, zirconia higher loadings (1wt% to 9wt%) and lower loadings (0.1wt% to 0.9wt%) were compared. Comparison based on different characterisations show almost no significant difference in wettability, strength, or frictional characteristics within a range. High loadings of titania nanoparticles do not allow cross-linking of polymer chains due to large quantity and surface area of nanoparticles. On the other hand, zirconia being heavier for the given weight percentages allow cross-linking of polymer during vulcanisation. Agglomeration of zirconia is also an aspect for its occupying lesser sites in matrix despite the removal of binder.
- High zirconia loadings yield in lower Shore A hardness compared to small zirconia/titania loadings where hardness improves significantly.
- Inclusion of nanoparticles enhance the machinability of the silicone rubber via laser engraving while producing micro-structures, however, there is a saturation point after

which the material removal do not increase in the same proportions albeit increment in nanoparticles.

- Elasticity during tensile tests improves with the inclusion of zirconia/titania nanoparticles, however, compressive strength approximately remains in a common range for all nanocomposites. The elasticity in tension is a significant variable as friction on shoe-sole and constant adhesion-deadhesion can destroy the micropillars if material do not possess sufficient tensile strength.
- Values of the elasticity and hardness of nanocomposites fall well within the range of desired working range similar to frog/gecko toepads.
- Wettable behaviour of all compositions and laser textured dimensions boosted several folds with the physicochemical modification of the inherently hydrophobic silicone rubber except some higher loading-higher cut geometries where potent deeper engraved surface become hydrophobic. Furthermore, wettability transforms into capillary enhanced hydrophilicity for optimum compositions especially for 500×200 laser textured dimensions and medium percentages of nanoparticles. Dimensions of the textures and quantity of nanoparticles have an optimum value and limit the hydrophilic performance of the compound.
- The dispersion of titania is uniform and homogeneous compared to zirconia that eventually agglomerates at certain locations; therefore, hydrophilicity of titania-reinforced nanocomposite is more consistent to zirconia.
- Titania-reinforced nanocomposites demonstrated profound superiority over zirconia-reinforced nanocomposites in anti-bacterial adhesion tests.
- For textured dimensions of 500×200, 3wt% zirconia provides a static coefficient of friction of 3.46 and a dynamic coefficient of friction of 1.88. Comparatively, lower zirconia concentrations, such as 0.7wt%, yield static and dynamic coefficients of 3.29 and 1.45, respectively. Similarly, 0.3wt% titania under the same textured dimensions exhibits static and dynamic coefficients of 3.43 and 1.85, respectively. Thus, LST configuration of 500×200 exhibits an optimum micro-structural dimension.
- Effect of the speed was also covered in the PhD project and significant loss of dynamic coefficient of friction was noticed throughout the compositions. Nevertheless, overall performance of titania has upper hand over zirconia nanocomposites in producing dynamic coefficient friction at both speeds, anti-bacterial effect, hardness, and wettability.

- Thesis invokes a thoughtful discussion on the relevance of dynamic coefficient of friction and its importance on wet ice.
- In conclusion, thesis might be considered as a proof of concept on physical plus chemical alterations to fabricate a multi-functional surface of silicone rubber with improved properties especially wettability and capillarity to enhance adhesion on wet ice based on the adaptation from gecko and frog toepads.

THESIS BASED PUBLICATIONS, CONFERENCES, AND PATENTS

This thesis presented has resulted in three journal articles (excluding co-authorship from contemporary wors), six conferences, and one patent.

- Vipin Richhariya; Ashis Tripathy; Oscar Carvalho; Md Julker Nine; Dusan Losic; F. S. Silva. "Unravelling the physics and mechanisms behind slips and falls on icy surfaces: A comprehensive review and nature-inspired solutions". Materials & Design(2023).
- Vipin Richhariya; Ashis Tripathy; Oscar Carvalho; Jose Gomes; Md Julker Nine; F. S. Silva. " Capillary-enhanced biomimetic adhesion on icy surfaces for high-performance anti-slip shoe-soles". ACS Applied Materials & Interfaces (2024).
- Vipin Richhariya, Georgina Miranda, and Filipe Samuel Silva. "An Experimental Parametric Optimisation for Laser Engraving and Texturing to Integrate Zirconia Ceramic Blocks into Stainless Steel Cutlery: A State-of-the-Art Aesthetically Improved Perspective." Materials, MDPI (2023).
- Vipin Richhariya, Oscar Carvalho, Ashis Tripathy, and F. S. Silva, "A nature-inspired slip-resistant shoe-sole". [IMFAHE Foundation - 2022, Boston, USA].
- Vipin Richhariya, Oscar Carvalho, Ashis Tripathy, and F. S. Silva, "Anti-slipping winter shoe-soles: A nature inspired solution". [Junior Euromat-2022, University of Coimbra, Portugal]
- Vipin Richhariya, Ashis Tripathy, O. Carvalho, and F.S. Silva, "A bio-inspired Anti-slipping Winter Shoe-sole". [DCE-21, University of Porto, Portugal]
- Vipin Richhariya, O. Carvalho, A Tripathy, F.S. Silva, "An innovative moulding method for anti-slipping shoe-soles". [EM-2022, University of Porto, Portugal].
- Vipin Richhariya, O. Carvalho, A Tripathy, F.S. Silva, "A Nature-Inspired Superhydrophilic Nano-Powder based Silicone Rubber Composite". [PowderMet2023/AMPM2023 Conference, Las Vegas, USA].
- Vipin Richhariya, O. Carvalho, A Tripathy, F.S. Silva, "A Superhydrophilic Biomimicked Ceramic-Reinforced-Polymer Nanocomposite for Enhanced Slip Resistance and Adhesion". [EMRS - 2024, European Conference, Warsaw, Poland].
- Vipin Richhariya, F.S. Silva, "Polymeric structure and its applications" (Patented Under Portuguese Patent (EU)119649 PP 2024.08.09).

REFERENCES

[1] QEB, 'Slips, trips and falls on the level', *Caualty Risk Solution*, 2016, [Online]. Available: http://www.hsa.ie/eng/Topics/Slips_Trips_Falls/Slips_Trips_Falls_Info/

[2] W. R. Chang, S. Leclercq, T. E. Lockhart, and R. Haslam, 'State of science: occupational slips, trips and falls on the same level*', *Ergonomics*, vol. 59, no. 7, pp. 861–883, 2016, doi: 10.1080/00140139.2016.1157214.

[3] O. C. Jensen and L. H. Laursen, 'Reduction of slips, trips and falls and better comfort by using new anti-slipping boots in fishing', *International Journal of Injury Control and Safety Promotion*, vol. 18, no. 1, pp. 85–87, 2011, doi: 10.1080/17457300.2010.487156.

[4] A. Tarcea, M. Vergouwen, E. C. Sayre, and N. J. White, 'The Slip and Fall Index: Assessing the risk of slipping and falling on ice', *Can J Public Health*, vol. 115, no. 2, pp. 296–304, Apr. 2024, doi: 10.17269/s41997-024-00855-z.

[5] C. Gao, I. Holmér, and J. Abeysekera, 'Slips and falls in a cold climate: Underfoot surface, footwear design and worker preferences for preventive measures', *Applied Ergonomics*, vol. 39, no. 3, pp. 385–391, 2008, doi: 10.1016/j.apergo.2007.08.001.

[6] Health and Safety Executive (HSE), 'Kinds of accident in Great Britain (Annual Statistics)', no. 04/11/2020, pp. 1–7, 2020.

[7] C. Gao, J. Abeysekera, M. Hirvonen, and C. Aschan, 'The effect of footwear sole abrasion on the coefficient of friction on melting and hard ice', *International Journal of Industrial Ergonomics*, vol. 31, no. 5, pp. 323–330, 2003, doi: 10.1016/S0169-8141(02)00234-2.

[8] É. Lépy, S. Rantala, A. Huusko, P. Nieminen, M. Hippi, and A. Rautio, 'Role of winter weather conditions and slipperiness on tourists' accidents in Finland', *International Journal of Environmental Research and Public Health*, vol. 13, no. 8, 2016, doi: 10.3390/ijerph13080822.

[9] M. Hippi and M. Kangas, 'Impact of Weather on Pedestrians' Slip Risk', *International Journal of Environmental Research and Public Health*, vol. 19, no. 5, 2022, doi: 10.3390/ijerph19053007.

[10] M. Hippi and S. Hartonen, 'Statistical data of slipping injuries happened in the winter time', *SIRWEC*, no. May, pp. 23–25, 2012.

[11] M. Hippi, M. Kangas, R. Ruuhela, J. Ruotsalainen, and S. Hartonen, 'RoadSurf-Pedestrian: a sidewalk condition model to predict risk for wintertime slipping injuries', *Meteorological Applications*, vol. 27, no. 5, 2020, doi: 10.1002/met.1955.

[12] C. S. Florence, G. Bergen, A. Atherly, E. Burns, J. Stevens, and C. Drake, 'Medical Costs of Fatal and Nonfatal Falls in Older Adults', *Journal of the American Geriatrics Society*, vol. 66, no. 4, pp. 693–698, 2018, doi: 10.1111/jgs.15304.

[13] Y. K. Haddad, G. Bergen, and C. S. Florence, 'Estimating the Economic Burden Related to Older Adult Falls by State', *Journal of Public Health Management and Practice*, vol. 25, no. 2, pp. E17–E24, 2019, doi: 10.1097/PHH.0000000000000816.

[14] S. Chen, J. Jin, and E. Lou, 'Toward slip and fall prevention: Exploring the guidance and challenges of anti-slip footwear', *Procedia Engineering*, vol. 43, no. January, pp. 364–368, 2012, doi: 10.1016/j.proeng.2012.08.063.

[15] C. Beynon *et al.*, 'The cost of emergency hospital admissions for falls on snow and ice in England during winter 2009/10: A cross sectional analysis', *Environmental Health: A Global Access Science Source*, vol. 10, no. 1, pp. 1–7, 2011, doi: 10.1186/1476-069X-10-60.

[16] T. N. Unguryanu, A. M. Grjibovski, T. A. Trovik, B. Ytterstad, and A. V. Kudryavtsev, 'Weather conditions and outdoor fall injuries in Northwestern Russia', *International Journal of*

Environmental Research and Public Health, vol. 17, no. 17, pp. 1–16, 2020, doi: 10.3390/ijerph17176096.

[17] A. R. Fekr *et al.*, 'Evaluation of winter footwear: Comparison of test methods to determine footwear slip resistance on ice surfaces', *International Journal of Environmental Research and Public Health*, vol. 18, no. 2, pp. 1–22, 2021, doi: 10.3390/ijerph18020405.

[18] J. Hsu *et al.*, 'Slip resistance of winter footwear on snow and ice measured using maximum achievable incline', *Ergonomics*, vol. 59, no. 5, pp. 717–728, 2016, doi: 10.1080/00140139.2015.1084051.

[19] M. Kandeva and N. Dishovsky, 'Friction behavior produced in the course of a contact enabled between composite materials and eco-friendly soles prototypes made of elastomeric material with regard to ice-covered surface', *Tribology in Industry*, vol. 41, no. 1, pp. 90–99, 2019, doi: 10.24874/ti.2019.41.01.10.

[20] L. Bäurle, T. U. Kaempfer, D. Szabó, and N. D. Spencer, 'Sliding friction of polyethylene on snow and ice: Contact area and modeling', *Cold Regions Science and Technology*, vol. 47, no. 3, pp. 276–289, 2007, doi: 10.1016/j.coldregions.2006.10.005.

[21] C. Gao, J. Abeysekera, M. Hirvonen, and R. Grönqvist, 'Slip resistant properties of footwear on ice', *Ergonomics*, vol. 47, no. 6, pp. 710–716, 2004, doi: 10.1080/00140130410001658673.

[22] H. Asakawa, G. Sazaki, K. Nagashima, S. Nakatsubo, and Y. Furukawa, 'Two types of quasi-liquid layers on ice crystals are formed kinetically', *Proceedings of the National Academy of Sciences of the United States of America*, vol. 113, no. 7, pp. 1749–1753, 2016, doi: 10.1073/pnas.1521607113.

[23] S. Zhang, J. Huang, Y. Cheng, H. Yang, Z. Chen, and Y. Lai, 'Bioinspired Surfaces with Superwettability for Anti-Icing and Ice-Phobic Application: Concept, Mechanism, and Design', *Small*, vol. 13, no. 48, pp. 1–20, 2017, doi: 10.1002/smll.201701867.

[24] A. V. Khomenko, K. P. Khomenko, and V. V. Falko, 'Nonlinear model of ice surface softening during friction', *Condensed Matter Physics*, vol. 19, no. 3, pp. 1–10, 2016, doi: 10.5488/CMP.19.33002.

[25] M. Alejandra Sánchez *et al.*, 'Experimental and theoretical evidence for bilayer-bybilayer surface melting of crystalline ice', *Proceedings of the National Academy of Sciences of the United States of America*, vol. 114, no. 2, pp. 227–232, 2017, doi: 10.1073/pnas.1612893114.

[26] A. M. Kietzig, S. G. Hatzikiriakos, and P. Englezos, 'Physics of ice friction', *Journal of Applied Physics*, vol. 107, no. 8, pp. 1–15, 2010, doi: 10.1063/1.3340792.

[27] V. Richhariya, A. Tripathy, O. Carvalho, J. Nine, and D. Losic, 'Unravelling the physics and mechanisms behind slips and falls on icy surfaces : A comprehensive review and nature-inspired solutions', *Materials & Design*, vol. 234, no. Sep 2023, p. 112335, Oct. 2023, doi: 10.1016/j.matdes.2023.112335.

[28] X. Wu and Z. Chen, 'A mechanically robust transparent coating for anti-icing and self-cleaning applications', *Journal of Materials Chemistry A*, vol. 6, no. 33, pp. 16043–16052, 2018, doi: 10.1039/c8ta05692g.

[29] D. N. Soulas, M. Sanopoulou, and K. G. Papadokostaki, 'Hydrophilic modification of silicone elastomer films: Thermal, mechanical and theophylline permeability properties', *Materials Science and Engineering C*, vol. 33, no. 4, pp. 2122–2130, 2013, doi: 10.1016/j.msec.2013.01.031.

[30] C. Yun, J. W. Choi, H. Kim, D. Kim, and H. Y. Kim, 'Sliding on ice: Real contact area, melted film thickness, and friction force', *International Journal of Heat and Mass Transfer*, vol. 160, 2020, doi: 10.1016/j.ijheatmasstransfer.2020.120166.

[31] L. B. Boinovich, K. A. Emelyanenko, and A. M. Emelyanenko, 'Superhydrophobic versus SLIPS: Temperature dependence and the stability of ice adhesion strength', *Journal of Colloid and Interface Science*, vol. 606, no. January, pp. 556–566, 2022, doi: 10.1016/j.jcis.2021.08.030.

[32] B. Weber *et al.*, 'Molecular Insight into the Slipperiness of Ice', *Journal of Physical Chemistry Letters*, vol. 9, no. 11, pp. 2838–2842, 2018, doi: 10.1021/acs.jpclett.8b01188.

[33] S. C. Colbeck, 'Capillary bonding of wet surfaces - the effects of contact angle and surface roughness', *Journal of Adhesion Science and Technology*, vol. 11, no. 3, pp. 359–371, 1997, doi: 10.1163/156856197X00750.

[34] F. W. Delrio, M. P. De Boer, L. M. Phinney, C. J. Bourdon, and M. L. Dunn, 'Van der Waals and capillary adhesion of microelectromechanical systems', *American Society of Mechanical Engineers, Micro-Electro Mechanical Systems Division, (Publications) MEMS*, pp. 1–6, 2006, doi: 10.1115/IMECE2006-15169.

[35] P. Flammang and R. Santos, 'Biological adhesives: from biology to biomimetics', *Interface Focus*, vol. 5, no. 1, pp. 1–3, 2014, doi: 10.1098/rsfs.2014.0086.

[36] W. M. Kier and A. M. Smith, 'The structure and adhesive mechanism of octopus suckers', *Integrative and Comparative Biology*, vol. 42, no. 6, pp. 1146–1153, 2002, doi: 10.1093/icb/42.6.1146.

[37] R. I. Pocock, 'On the Feet and other External Features of the Canidae and Urside', pp. 913–941, 1914.

[38] D. P. Manning, J. E. Cooper, I. Stirling, C. M. Jones, M. Bruce, and P. C. McCausland, 'Studies on the footpads of the polar bear (ursus maritimus) and their possible relevance to accident prevention', *Journal of Hand Surgery*, vol. 10, no. 3, pp. 303–307, 1985, doi: 10.1016/S0266-7681(85)80049-8.

[39] G. Hanna and W. J. P. Barnes, 'Adhesion and detachment of the toe pads of tree frogs', *Journal of Experimental Biology*, vol. 155, no. January 1991, pp. 103–125, 1991, doi: 10.1242/jeb.155.1.103.

[40] R. Bogue, 'Biomimetic adhesives: A review of recent developments', *Assembly Automation*, vol. 28, no. 4, pp. 282–288, 2008, doi: 10.1108/01445150810904422.

[41] J. H. Lever, S. Taylor, G. R. Hoch, and C. Daghlian, 'Evidence that abrasion can govern snow kinetic friction', *Journal of Glaciology*, vol. 65, no. 249, pp. 68–84, 2019, doi: 10.1017/jog.2018.97.

[42] J. H. Lever, A. P. Lines, S. Taylor, G. R. Hoch, E. Asenath-Smith, and D. S. Sodhi, 'Revisiting mechanics of ice-skate friction: From experiments at a skating rink to a unified hypothesis', *Journal of Glaciology*, 2021, doi: 10.1017/jog.2021.97.

[43] F. Formenti, 'A review of the physics of ice surface friction and the development of ice skating', *Research in Sports Medicine*, vol. 22, no. 3, pp. 276–293, 2014, doi: 10.1080/15438627.2014.915833.

[44] B. N. J. Persson, 'Ice friction: Role of non-uniform frictional heating and ice premelting', *Journal of Chemical Physics*, vol. 143, no. 22, pp. 1–9, 2015, doi: 10.1063/1.4936299.

[45] K. Sotthewes, P. Bampoulis, H. J. W. Zandvliet, D. Lohse, and B. Poelsema, 'Pressure-Induced Melting of Confined Ice', *ACS Nano*, vol. 11, no. 12, pp. 12723–12731, 2017, doi: 10.1021/acsnano.7b07472.

[46] Luz Yolanda Toro Suarez, 'Unified analysis of pressure melting of ice around horizontal columns', *Progress in Natural Science*, vol. 17, no. 3, pp. 1–27, 2015.

[47] F. Base, A. Bejan, and P. A. Tyvand, 'The Pressure Melting of Ice Under a Body With Flat Base', *Journal of Heat Transfer*, vol. 114, no. May 1992, pp. 529–531, 2017.

[48] K. I. Murata, H. Asakawa, K. Nagashima, Y. Furukawa, and G. Sazaki, 'Thermodynamic origin of surface melting on ice crystals', *Proceedings of the National Academy of Sciences of the United States of America*, vol. 113, no. 44, pp. E6741–E6748, 2016, doi: 10.1073/pnas.1608888113.

[49] J. R. Blackford, 'Sintering and microstructure of ice: a review', *J. Phys. D: Appl. Phys.*, vol. 40, no. 21, pp. R355–R385, Nov. 2007, doi: 10.1088/0022-3727/40/21/R02.

[50] C. T. Calderon and P. Mohazzabi, 'Premelting, Pressure Melting, and Regelation of Ice Revisited', *Journal of Applied Mathematics and Physics*, vol. 06, no. 11, pp. 2181–2191, 2018, doi: 10.4236/jamp.2018.611183.

[51] P. Oksanen and J. Keinonen, 'The mechanism of friction of ice', *Wear*, vol. 78, no. 3, pp. 315–324, 1982, doi: 10.1016/0043-1648(82)90242-3.

[52] S. Rønneberg, S. Xiao, J. He, and Z. Zhang, 'Nanoscale correlations of ice adhesion strength and water contact angle', *Coatings*, vol. 10, no. 4, pp. 1–17, 2020, doi: 10.3390/coatings10040379.

[53] J. K. A. Langowski, D. Dodou, M. Kamperman, and J. L. van Leeuwen, 'Tree frog attachment: Mechanisms, challenges, and perspectives', *Frontiers in Zoology*, vol. 15, no. 1, pp. 1–21, 2018, doi: 10.1186/s12983-018-0273-x.

[54] J. Iturri *et al.*, 'Torrent frog-inspired adhesives: Attachment to flooded surfaces', *Advanced Functional Materials*, vol. 25, no. 10, pp. 1499–1505, 2015, doi: 10.1002/adfm.201403751.

[55] G. Huber *et al.*, 'Evidence for capillarity contributions to gecko adhesion from single spatula nanomechanical measurements', *Proceedings of the National Academy of Sciences of the United States of America*, vol. 102, no. 45, pp. 16293–16296, 2005, doi: 10.1073/pnas.0506328102.

[56] K. Autumn and J. Puthoff, 'Properties, Principles, and Parameters of the Gecko Adhesive System', in *Biological Adhesives*, A. M. Smith, Ed., Cham: Springer International Publishing, 2016, pp. 245–280. doi: 10.1007/978-3-319-46082-6_11.

[57] S. Gernay, W. Federle, P. Lambert, and T. Gilet, 'Elasto-capillarity in insect fibrillar adhesion', *Journal of the Royal Society Interface*, vol. 13, no. 121, 2016, doi: 10.1098/rsif.2016.0371.

[58] R. Yue and S. Wang, 'A survey of technologies for climbing robots', *Applied Mechanics and Materials*, vol. 236–237, pp. 556–562, 2012, doi: 10.4028/www.scientific.net/AMM.236-237.556.

[59] K. W. Allen, *Adhesion and Adhesives.*, vol. 22, no. 5. 1986. doi: 10.1201/9781482269741-24.

[60] J. A. Von Fraunhofer, 'Adhesion and cohesion', *International Journal of Dentistry*, vol. 2012, no. November, pp. 1–8, 2012, doi: 10.1155/2012/951324.

[61] L. Heepe and S. N. Gorb, 'Biologically inspired mushroom-shaped adhesive microstructures', *Annual Review of Materials Research*, vol. 44, no. July, pp. 173–203, 2014, doi: 10.1146/annurev-matsci-062910-100458.

[62] M. Jamali and H. V. Tafreshi, 'Studying droplet adhesion to fibers using the magnetic field: a review paper', *Experiments in Fluids*, vol. 62, no. 8, pp. 1–15, 2021, doi: 10.1007/s00348-021-03258-9.

[63] X. Zhao *et al.*, 'Effect of surface characteristics of asphalt pavement on ice-pavement adhesion', vol. 0123456789, 2022.

[64] Y. Shen, Y. Lv, H. Yang, W. Ma, L. Zhang, and J. Pan, 'Effect of different ice contents on heat transfer and mechanical properties of concrete', *Cold Regions Science and Technology*, vol. 199, no. December 2021, p. 103570, 2022, doi: 10.1016/j.coldregions.2022.103570.

[65] A. T. A. Dhyani, W. Choi, K. Golovin, 'Surface design strategies for mitigating ice and snow accretion', *Matter, CellPress*, vol. 5, no. 5, pp. 1423–1454, 2022.

[66] H. H. G. Jellinek, 'Ice Adhesion', *Canadian Journal of Physics*, vol. 40, no. 10, pp. 1294–1309, 2020, doi: 10.1139/p62-138.

[67] S. Ella, P. Y. Formagne, V. Koutsos, and J. R. Blackford, 'Investigation of rubber friction on snow for tyres', *Tribology International*, vol. 59, no. March, pp. 292–301, 2013, doi: 10.1016/j.triboint.2012.01.017.

[68] M. Moncalero, S. Signetti, B. Mazzanti, P. Bruzzi, N. M. Pugno, and M. Colonna, 'Effect of material elastic properties and surface roughness on grip performances of ski boot soles under wet and icy conditions', *International Journal of Industrial Ergonomics*, vol. 61, pp. 62–70, 2017, doi: 10.1016/j.ergon.2017.04.004.

[69] A. M. Kietzig, S. G. Hatzikiriakos, and P. Englezos, 'Ice friction: The effect of thermal conductivity', *Journal of Glaciology*, vol. 56, no. 197, pp. 473–479, 2010, doi: 10.3189/002214310792447752.

[70] J. Abeysekera and C. Gao, 'The identification of factors in the systematic evaluation of slip prevention on icy surfaces', *International Journal of Industrial Ergonomics*, vol. 28, no. 5, pp. 303–313, 2001, doi: 10.1016/S0169-8141(01)00027-0.

[71] S. A. Suresh, A. Hajj-Ahmad, E. W. Hawkes, and M. R. Cutkosky, 'Forcing the issue: Testing gecko-inspired adhesives: Forcing the issue: Testing gecko-inspired adhesives', *Journal of the Royal Society Interface*, vol. 18, no. 174, pp. 1–10, 2021, doi: 10.1098/rsif.2020.0730rsif20200730.

[72] S. Srewaradachpisal, C. Dechwayukul, S. Chatpun, R. J. Spontak, and W. Thongruang, 'Optimization of the rubber formulation for footwear applications from the response surface method', *Polymers*, vol. 12, no. 9, pp. 7–11, 2020, doi: 10.3390/POLYM12092032.

[73] V. L. Popov, *Contact Mechanics and Friction :Physical Principles and Applications*, vol. 55. 1977.

[74] Z. A. Janjua, 'The influence of freezing and ambient temperature on the adhesion strength of ice', *Cold Regions Science and Technology*, vol. 140, pp. 14–19, Aug. 2017, doi: 10.1016/j.coldregions.2017.05.001.

[75] D. Buhl, M. Fauve, and H. Rhyner, 'The kinetic friction of polyethylen on snow: The influence of the snow temperature and the load', *Cold Regions Science and Technology*, vol. 33, no. 2–3, pp. 133–140, 2001, doi: 10.1016/S0165-232X(01)00034-9.

[76] K. A. Emelyanenko, A. M. Emelyanenko, and L. B. Boinovich, 'Water and ice adhesion to solid surfaces: Common and specific, the impact of temperature and surface wettability', *Coatings*, vol. 10, no. 7, pp. 1–23, 2020, doi: 10.3390/coatings10070648.

[77] D. D. Higgins, B. A. Marmo, C. E. Jeffree, V. Koutsos, and J. R. Blackford, 'Morphology of ice wear from rubber – ice friction tests and its dependence on temperature and sliding velocity', vol. 265, pp. 634–644, 2008, doi: 10.1016/j.wear.2007.12.015.

[78] R. W. Liefferink, F. C. Hsia, B. Weber, and D. Bonn, 'Friction on Ice : How Temperature , Pressure , and Speed Control the Slipperiness of Ice', *American Physical Society (Physics Review)*, vol. 011025, no. 1, pp. 1–13, 2021, doi: 10.1103/PhysRevX.11.011025.

[79] C. Klapproth, T. M. Kessel, K. Wiese, and B. Wies, 'An advanced viscous model for rubber-ice-friction', *Tribology International*, vol. 99, pp. 169–181, 2016, doi: 10.1016/j.triboint.2015.09.012.

[80] A. D. Roberts, 'Rubbe Contact Phenomena', *Rubber Chemistry and Technology*, vol. 87, no. 3, pp. 383–416, Sep. 2014, doi: 10.5254/rct.14.85982.

[81] A. D. Roberts, 'Adhesion of Rubber Against Ice', *Tribology Series*, vol. 7, no. C, pp. 311–320, 1981, doi: 10.1016/S0167-8922(08)70890-3.

[82] E. Ringoot, T. Roch, J.-F. Molinari, T. J. Massart, and T. Cohen, 'Stick–slip phenomena and Schallamach waves captured using reversible cohesive elements', *Journal of the Mechanics and Physics of Solids*, vol. 155, p. 104528, Oct. 2021, doi: 10.1016/j.jmps.2021.104528.

[83] R. A. Schapery, 'The effect of global viscoelasticity on rubber friction with Schallamach waves', *Tribology International*, vol. 148, p. 106306, Aug. 2020, doi: 10.1016/j.triboint.2020.106306.

[84] B. Raeesi and M. Piri, 'The effects of wettability and trapping on relationships between interfacial area , capillary pressure and saturation in porous media : A pore-scale network modeling approach', *Journal of Hydrology*, vol. 376, no. 3–4, pp. 337–352, 2009, doi: 10.1016/j.jhydrol.2009.07.060.

[85] F. P. Bowden and T. P. Hughes, 'The mechanism of sliding on ice and snow', *Proceedings of the Royal Society of London. Series A. Mathematical and Physical Sciences*, vol. 172, no. 949, pp. 280–298, 2022, doi: 10.1098/rspa.1939.0104.

[86] H. N. G. Nguyen, C.-F. Zhao, O. Millet, and A. P. S. Selvadurai, 'Effects of surface roughness on liquid bridge capillarity and droplet wetting', *Powder Technology*, vol. 378, pp. 487–496, Jan. 2021, doi: 10.1016/j.powtec.2020.10.016.

[87] A. M. Palecek *et al.*, 'An investigation of gecko attachment on wet and rough substrates leads to the application of surface roughness power spectral density analysis', *Scientific Reports*, vol. 12, no. 1, pp. 1–12, 2022, doi: 10.1038/s41598-022-15698-2.

[88] N. Mizukami and N. Maeno, 'Normal stress dependence of ice-ice friction coefficients', *Institute of Low Temperature Science*, vol. 11, no. 62/6, pp. 515–521, 2000.

[89] N. Orndorf, A. M. Garner, and A. Dhinojwala, 'Polar bear paw pad surface roughness and its relevance to contact mechanics on snow', *Journal of the Royal Society Interface*, vol. 19, no. 196, pp. 1–11, 2022.

[90] P. B. Louden and J. D. Gezelter, 'Why is Ice Slippery? Simulations of Shear Viscosity of the Quasi-Liquid Layer on Ice', *J. Phys. Chem. Lett.*, vol. 9, no. 13, pp. 3686–3691, Jul. 2018, doi: 10.1021/acs.jpclett.8b01339.

[91] R. Robert, 'Why is ice slippery?', *New Scientist*, vol. 227, no. 3037, p. 38, 2015, doi: 10.1016/S0262-4079(15)31136-2.

[92] S. Ducret, H. Zahouani, A. Midol, P. Lanteri, and T. G. Mathia, 'Friction and abrasive wear of UHWMPE sliding on ice', *Wear*, vol. 258, no. 1-4 SPEC. ISS., pp. 26–31, 2005, doi: 10.1016/j.wear.2004.09.026.

[93] I. Velkavrh, J. Lungevičs, E. Jansons, S. Klien, J. Voyer, and F. Ausserer, 'The influence of isotropic surface roughness of steel sliders on ice friction under different testing conditions', *Lubricants*, vol. 7, no. 12, 2019, doi: 10.3390/LUBRICANTS7120106.

[94] D. C. B. Evans, J. F. Nye, and K. J. Cheeseman, 'The kinetic friction of ice', *Proceedings of the Royal Society of London. A. Mathematical and Physical Sciences*, vol. 347, no. 1651, pp. 493–512, 1976, doi: 10.1098/rspa.1976.0013.

[95] S. C. Colbeck, 'The kinetic friction of snow', *Journal of Glaciology*, vol. 34, no. 116, pp. 78–86, 1988, doi: 10.1017/S0022143000009096.

[96] A. Iraqi, N. S. Vidic, M. S. Redfern, and K. E. Beschorner, 'Prediction of coefficient of friction based on footwear outsole features', *Applied Ergonomics*, vol. 82, no. January 2019, p. 102963, 2020, doi: 10.1016/j.apergo.2019.102963.

[97] S. R. M. Moghaddam, S. L. Hemler, M. S. Redfern, T. D. B. Jacobs, and K. E. Beschorner, 'Computational model of shoe wear progression: Comparison with experimental results', *Wear*, vol. 422–423, no. August 2018, pp. 235–241, 2019, doi: 10.1016/j.wear.2019.01.070.

[98] A. Banik and K. T. Tan, 'Dynamic Friction Performance of Hierarchical Biomimetic Surface Pattern Inspired by Frog Toe-Pad', *Advanced Materials Interfaces*, vol. 7, no. 18, pp. 1–12, 2020, doi: 10.1002/admi.202000987.

[99] E. Jansons, J. Lungevics, K. Stiprais, L. Pluduma, and K. A. Gross, 'Measurement of sliding velocity on ice, as a function of temperature, runner load and roughness, in a skeleton push-start facility', *Cold Regions Science and Technology*, vol. 151, no. March, pp. 260–266, 2018, doi: 10.1016/j.coldregions.2018.03.015.

[100] A. M. Kietzig, S. G. Hatzikiriakos, and P. Englezos, 'Ice friction: The effects of surface roughness, structure, and hydrophobicity', *Journal of Applied Physics*, vol. 106, no. 2, pp. 1–7, 2009, doi: 10.1063/1.3173346.

[101] M. Scherge, R. Böttcher, A. Spagni, and D. Marchetto, 'High-speed measurements of steel-ice friction: Experiment vs. calculation', *Lubricants*, vol. 6, no. 1, pp. 2–9, 2018, doi: 10.3390/lubricants6010026.

[102] C. Stamboulides, P. Englezos, and S. G. Hatzikiriakos, 'The ice friction of polymeric substrates', *Tribology International*, vol. 55, no. Nivember, pp. 59–67, 2012, doi: 10.1016/j.triboint.2012.05.001.

[103] X. Zhang, H. Liu, and L. Jiang, 'Wettability and Applications of Nanochannels', *Advanced Materials*, vol. 31, no. 5, p. 1804508, 2019, doi: 10.1002/adma.201804508.

[104] S. Wang, K. Liu, X. Yao, and L. Jiang, 'Bioinspired Surfaces with Superwettability: New Insight on Theory, Design, and Applications', *Chem. Rev.*, vol. 115, no. 16, pp. 8230–8293, Aug. 2015, doi: 10.1021/cr400083y.

[105] X. B. Zhou and J. Th. M. De Hosson, 'Influence of surface roughness on the wetting angle', *Journal of Materials Research*, vol. 10, no. 8, pp. 1984–1992, Aug. 1995, doi: 10.1557/JMR.1995.1984.

[106] M. Laurenti *et al.*, 'Wettability Control on ZnO Nanowires Driven by Seed Layer Properties', *European Journal of Inorganic Chemistry*, vol. 2013, no. 14, pp. 2520–2527, 2013, doi: 10.1002/ejic.201201420.

[107] A. B. D. Cassie and S. Baxter, 'Wettability of porous surfaces', *Trans. Faraday Soc.*, vol. 40, p. 546, 1944, doi: 10.1039/tf9444000546.

[108] R. N. Wenzel, 'RESISTANCE OF SOLID SURFACES TO WETTING BY WATER', ACS Publications. Accessed: Nov. 11, 2024. [Online]. Available: https://pubs.acs.org/doi/pdf/10.1021/ie50320a024

[109] E. Balaur, J. M. Macak, L. Taveira, and P. Schmuki, 'Tailoring the wettability of TiO2 nanotube layers', *Electrochemistry Communications*, vol. 7, no. 10, pp. 1066–1070, Oct. 2005, doi: 10.1016/j.elecom.2005.07.014.

[110] J. Lv, J. Zhu, K. Huang, F. Meng, X. Song, and Z. Sun, 'Tunable surface wettability of ZnO nanorods prepared by two-step method', *Applied Surface Science*, vol. 257, no. 17, pp. 7534–7538, Jun. 2011, doi: 10.1016/j.apsusc.2011.03.113.

[111] A. Aziz *et al.*, 'The Effect of Porosity and Contact Angle on the Fluid Capillary Rise for Bone Scaffold Wettability and Absorption', *Malaysian Journal of Medicine and Health Sciences*, vol. 18, no. April, pp. 6–11, 2022.

[112] L. Makkonen, 'Ice Adhesion —Theory, Measurements and Countermeasures', *Journal of Adhesion Science and Technology*, vol. 26, no. 4–5, pp. 413–445, Mar. 2012, doi: 10.1163/016942411X574583.

[113] C. H. Kung, P. K. Sow, B. Zahiri, and W. Mérida, 'Assessment and Interpretation of Surface Wettability Based on Sessile Droplet Contact Angle Measurement: Challenges and Opportunities', *Advanced Materials Interfaces*, vol. 6, no. 18, pp. 1–27, 2019, doi: 10.1002/admi.201900839.

[114] J. S. Cho, Y.-W. Beag, S. Han, K.-H. Kim, J. Cho, and S.-K. Koh, 'Hydrophilic surface formation on materials and its applications', *Surface and Coatings Technology*, vol. 128–129, pp. 66–70, Jun. 2000, doi: 10.1016/S0257-8972(00)00658-7.

[115] D. Quéré, 'Wetting and Roughness', *Annual Review of Materials Research*, vol. 38, no. Volume 38, 2008, pp. 71–99, Aug. 2008, doi: 10.1146/annurev.matsci.38.060407.132434.

[116] P. N. Manoudis and I. Karapanagiotis, 'Modification of the wettability of polymer surfaces using nanoparticles', *Progress in Organic Coatings*, vol. 77, no. 2, pp. 331–338, Feb. 2014, doi: 10.1016/j.porgcoat.2013.10.007.

[117] H. Eltoum, Y.-L. Yang, and J.-R. Hou, 'The effect of nanoparticles on reservoir wettability alteration: a critical review', *Pet. Sci.*, vol. 18, no. 1, pp. 136–153, Feb. 2021, doi: 10.1007/s12182-020-00496-0.

[118] K. Siwińska-Ciesielczyk, A. Andrzejczak, T. Jesionowski, Ł. Gierz, A. Marcinkowska, and M. Robakowska, 'New Insights into the Application of Biocompatible (Un)Modified TiO2 and TiO2-ZrO2 Oxide Fillers in Light-Curing Materials', *Materials*, vol. 17, no. 12, Art. no. 12, Jan. 2024, doi: 10.3390/ma17122908.

[119] C. Ishino, M. Reyssat, E. Reyssat, K. Okumura, and D. Quéré, 'Wicking within forests of micropillars', *Europhys. Lett.*, vol. 79, no. 5, p. 56005, Sep. 2007, doi: 10.1209/0295-5075/79/56005.

[120] D. Ahmad, I. van den Boogaert, J. Miller, R. Presswell, and H. Jouhara, 'Hydrophilic and hydrophobic materials and their applications', *Energy Sources, Part A: Recovery, Utilization, and Environmental Effects*, vol. 40, no. 22, pp. 2686–2725, Nov. 2018, doi: 10.1080/15567036.2018.1511642.

[121] E. Arzt, H. Quan, R. M. McMeeking, and R. Hensel, 'Functional surface microstructures inspired by nature – From adhesion and wetting principles to sustainable new devices', *Progress in Materials Science*, vol. 120, p. 100823, Jul. 2021, doi: 10.1016/j.pmatsci.2021.100823.

[122] A. O. Ijaola *et al.*, 'Wettability Transition for Laser Textured Surfaces: A Comprehensive Review', *Surfaces and Interfaces*, vol. 21, p. 100802, Dec. 2020, doi: 10.1016/j.surfin.2020.100802.

[123] L. Sikong, M. Masae, K. Kooptarnond, W. Taweepreda, and F. Saito, 'Improvement of hydrophilic property of rubber dipping former surface with Ni/B/TiO 2 nano-composite film', *Applied Surface Science*, vol. 258, no. 10, pp. 4436–4443, 2012, doi: 10.1016/j.apsusc.2012.01.002.

[124] C. I. Park, H. E. Jeong, S. H. Lee, H. S. Cho, and K. Y. Suh, 'Wetting transition and optimal design for microstructured surfaces with hydrophobic and hydrophilic materials', *Journal of Colloid and Interface Science*, vol. 336, no. 1, pp. 298–303, 2009, doi: 10.1016/j.jcis.2009.04.022.

[125] A. Maestro *et al.*, 'Wettability of silica nanoparticle – surfactant nanocomposite interfacial layers', *Soft Matter*, vol. 8, no. 3, pp. 837–843, 2012, doi: 10.1039/C1SM06421E.

[126] G. Berggård and C. Johansson, 'Pedestrians in wintertime - Effects of using anti-slip devices', *Accident Analysis and Prevention*, vol. 42, no. 4, pp. 1199–1204, 2010, doi: 10.1016/j.aap.2010.01.011.

[127] M. Bruce, C. Jones, and D. P. Manning, 'Slip-Resistance on Icy Surfaces of Shoes, Crampons and Chains - A New Machine', *Journal of Occupational Accidents, Elsevier*, vol. 7, pp. 273–283, 1986.

[128] J. Gustavsson, F. Nilson, and C. Bonander, 'Individual and contextual factors associated with the use of anti-slip devices according to a Swedish national survey', *Journal of Transport and Health*, vol. 17, no. August 2019, p. 100865, 2020, doi: 10.1016/j.jth.2020.100865.

[129] G. Gard and G. Lundborg, 'Test of Swedish anti-skid devices on five different slippery surfaces', *Accident Analysis and Prevention*, vol. 33, no. 1, pp. 1–8, 2001, doi: 10.1016/S0001-4575(00)00002-6.

[130] G. Gard and G. Berggård, 'Assessment of anti-slip devices from healthy individuals in different ages walking on slippery surfaces', *Applied Ergonomics*, vol. 37, no. 2, pp. 177–186, 2006, doi: 10.1016/j.apergo.2005.04.004.

[131] F. E. McKiernan, 'A simple gait-stabilizing device reduces outdoor falls and nonserious injurious falls in fall-prone older people during the winter', *Journal of the American Geriatrics Society*, vol. 53, no. 6, pp. 943–947, 2005, doi: 10.1111/j.1532-5415.2005.53302.x.

[132] A. Larsson, G. Berggård, P. Rosander, and G. Gard, 'Gait speed with anti-slip devices on icy pedestrian crossings relate to perceived fall-risk and balance', *International Journal of Environmental Research and Public Health*, vol. 16, no. 14, 2019, doi: 10.3390/ijerph16142451.

[133] C. Bonander and R. Holmberg, 'Estimating the effects of a studded footwear subsidy program on pedestrian falls among older adults in Gothenburg, Sweden', *Accident Analysis and Prevention*, vol. 132, no. August, p. 105282, 2019, doi: 10.1016/j.aap.2019.105282.

[134] G. Gard and G. Lundborg, 'Pedestrians on slippery surfaces during winter - Methods to describe the problems and practical tests of anti-skid devices', *Accident Analysis and Prevention*, vol. 32, no. 3, pp. 455–460, 2000, doi: 10.1016/S0001-4575(99)00070-6.

[135] H. T. Ramsay and C. R. Senneck, 'Anti-slip studs for safety footwear', *Applied Ergonomics*, vol. 3, no. 4, pp. 219–223, 1972, doi: 10.1016/0003-6870(72)90104-4.

[136] K. Shah, M. Solan, and E. Dawe, 'The gait cycle and its variations with disease and injury', *Orthopaedics and Trauma*, vol. 34, no. 3, pp. 153–160, 2020, doi: 10.1016/j.mporth.2020.03.009.

[137] T. E. Lockhart, *Biomechanics of Human Gait - Slip and Fall Analysis*. Elsevier Ltd., 2013. doi: 10.1016/B978-0-12-382165-2.00151-3.

[138] C. Aschan, M. Hirvonen, E. Rajamäki, T. Mannelin, J. Ruotsalainen, and R. Ruuhela, 'Performance of slippery and slip-resistant footwear in different wintry weather conditions measured in situ', *Safety Science*, vol. 47, no. 8, pp. 1195–1200, 2009, doi: 10.1016/j.ssci.2009.01.006.

[139] Y. Lin *et al.*, 'Durable and robust transparent superhydrophobic glass surfaces fabricated by a femtosecond laser with exceptional water repellency and thermostability', *Journal of Materials Chemistry A*, vol. 6, no. 19, pp. 9049–9056, 2018, doi: 10.1039/c8ta01965g.

[140] L. Chen *et al.*, 'Icing performance of superhydrophobic silicone rubber surfaces by laser texturing', *Materials Research Express*, vol. 6, no. 12, 2019, doi: 10.1088/2053-1591/ab6542.

[141] D. I. Yu *et al.*, 'Wetting state on hydrophilic and hydrophobic micro-textured surfaces: Thermodynamic analysis and X-ray visualization', *Applied Physics Letters*, vol. 106, no. 17, pp. 1–6, 2015, doi: 10.1063/1.4919136.

[142] B. C. Grieser and J. Frantz, 'Slip resistance assessment of common shoe sole materials on selected floor surfaces', *Proceedings of the Human Factors and Ergonomics Society*, vol. 1, pp. 435–439, 2018, doi: 10.1177/1541931218621099.

[143] R. Grönqvist, 'Mechanisms of friction and assessment of slip resistance of new and used footwear soles on contaminated floors', *Ergonomics*, vol. 38, no. 2, pp. 224–241, 1995, doi: 10.1080/00140139508925100.

[144] G. Singh and K. E. Beschorner, 'A Method for Measuring Fluid Pressures in the Shoe–Floor–Fluid Interface: Application to Shoe Tread Evaluation', *IIE Transactions on Occupational Ergonomics and Human Factors*, vol. 2, no. 2, pp. 53–59, Apr. 2014, doi: 10.1080/21577323.2014.919367.

[145] K. E. Beschorner, D. L. Albert, A. J. Chambers, and M. S. Redfern, 'Fluid pressures at the shoe-floor-contaminant interface during slips: Effects of tread & implications on slip severity', *Journal of Biomechanics*, vol. 47, no. 2, pp. 458–463, 2014, doi: 10.1016/j.jbiomech.2013.10.046.

[146] K. W. Li and C. J. Chen, 'The effect of shoe soling tread groove width on the coefficient of friction with different sole materials, floors, and contaminants', *Applied Ergonomics*, vol. 35, no. 6, pp. 499–507, Nov. 2004, doi: 10.1016/j.apergo.2004.06.010.

[147] K. E. Beschorner, E. E. Meehan, A. Iraqi, and S. L. Hemler, 'Designing shoe tread for friction performance: a hierarchical approach', *Footwear Science*, vol. 13, no. sup1, pp. S97–S99, Jul. 2021, doi: 10.1080/19424280.2021.1917701.

[148] C. M. Strobel, P. L. Menezes, M. R. Lovell, and K. E. Beschorner, 'Analysis of the Contribution of Adhesion and Hysteresis to Shoe–Floor Lubricated Friction in the Boundary Lubrication Regime', *Tribol Lett*, vol. 47, no. 3, pp. 341–347, Sep. 2012, doi: 10.1007/s11249-012-9989-5.

[149] T. Yamaguchi, Y. Katsurashima, and K. Hokkirigawa, 'Effect of rubber block height and orientation on the coefficients of friction against smooth steel surface lubricated with glycerol solution', *Tribology International*, vol. 110, pp. 96–102, Jun. 2017, doi: 10.1016/j.triboint.2017.02.015.

[150] M. G. Blanchette and C. M. Powers, 'The influence of footwear tread groove parameters on available friction', *Applied Ergonomics*, vol. 50, pp. 237–241, Sep. 2015, doi: 10.1016/j.apergo.2015.03.018.

[151] K. W. Li and C. J. Chen, 'Effects of tread groove orientation and width of the footwear pads on measured friction coefficients', *Safety Science*, vol. 43, no. 7, pp. 391–405, Aug. 2005, doi: 10.1016/j.ssci.2005.08.006.

[152] J. Hale, A. O'Connell, R. Lewis, M. J. Carré, and J. A. Rongong, 'An Evaluation of Shoe Tread Parameters using FEM', *Tribology International*, vol. 153, no. March 2020, 2021, doi: 10.1016/j.triboint.2020.106570.

[153] R. Mohan, S. Raja, G. Saraswathy, and B. N. Das, 'Surface Modification of TPR Sole: An Approach to Improve Slip Resistance on Quarry and Ceramic Tiles', *Rubber Chemistry and Technology*, vol. 88, no. 1, pp. 163–175, Mar. 2015, doi: 10.5254/rct.14.85965.

[154] J. Bico, U. Thiele, and D. Quéré, 'Wetting of textured surfaces', *Colloids and Surfaces A: Physicochemical and Engineering Aspects*, vol. 206, no. 1–3, pp. 41–46, 2002, doi: 10.1016/S0927-7757(02)00061-4.

[155] C. Ishino and K. Okumura, 'Wetting transitions on textured hydrophilic surfaces', *European Physical Journal E*, vol. 25, no. 4, pp. 415–424, 2008, doi: 10.1140/epje/i2007-10308-y.

[156] S. Pechook and B. Pokroy, 'Self-assembling, bioinspired wax crystalline surfaces with time-dependent wettability', *Advanced Functional Materials*, vol. 22, no. 4, pp. 745–750, 2012, doi: 10.1002/adfm.201101721.

[157] S. Baik *et al.*, 'Bioinspired Microsphere-Embedded Adhesive Architectures for an Electrothermally Actuating Transport Device of Dry/Wet Pliable Surfaces', *ACS Applied Materials and Interfaces*, vol. 13, no. 5, pp. 6930–6940, 2021, doi: 10.1021/acsami.0c21847.

[158] S. L. Hemler *et al.*, 'Changes in under-shoe traction and fluid drainage for progressively worn shoe tread', *Applied Ergonomics*, vol. 80, no. February, pp. 35–42, 2019, doi: 10.1016/j.apergo.2019.04.014.

[159] J. Hsu, Y. Li, T. Dutta, and G. Fernie, 'Assessing the performance of winter footwear using a new maximum achievable incline method', *Applied Ergonomics*, vol. 50, pp. 218–225, 2015, doi: 10.1016/j.apergo.2015.03.016.

[160] S. L. Hemler, D. N. Charbonneau, and K. E. Beschorner, 'Predicting hydrodynamic conditions under worn shoes using the tapered-wedge solution of Reynolds equation', *Tribology International*, vol. 145, no. October 2019, p. 106161, 2020, doi: 10.1016/j.triboint.2020.106161.

[161] I. J. Kim, 'Identifying shoe wear mechanisms and associated tribological characteristics: Importance for slip resistance evaluation', *Wear*, vol. 360–361, pp. 77–86, 2016, doi: 10.1016/j.wear.2016.04.020.

[162] R. Grönqvist and M. Hirvonen, 'Slipperiness of footwear and mechanisms of walking friction on icy surfaces', *International Journal of Industrial Ergonomics*, vol. 16, no. 3, pp. 191–200, 1995, doi: 10.1016/0169-8141(94)00095-K.

[163] V. H. Sundaram, S. L. Hemler, A. Chanda, J. M. Haight, M. S. Redfern, and K. E. Beschorner, 'Worn region size of shoe outsole impacts human slips: Testing a mechanistic model', *Journal of Biomechanics*, vol. 105, p. 109797, 2020, doi: 10.1016/j.jbiomech.2020.109797.

[164] Y. J. Tsai and C. M. Powers, 'The influence of footwear sole hardness on slip initiation in young adults', *Journal of Forensic Sciences*, vol. 53, no. 4, pp. 884–888, 2008, doi: 10.1111/j.1556-4029.2008.00739.x.

[165] K. E. Beschorner *et al.*, 'An observational ergonomic tool for assessing the worn condition of slip-resistant shoes', *Applied Ergonomics*, vol. 88, no. April, p. 103140, 2020, doi: 10.1016/j.apergo.2020.103140.

[166] O. Golubeva and A. Pogorelova, 'Analysis of the quality of modern polymer materials of sole', in *E3S Web of Conferences*, 2021, pp. 1–7. doi: 10.1051/e3sconf/202127305002.

[167] F. Lecadre, M. Kasuya, S. Hemette, A. Harano, Y. Kanno, and K. Kurihara, 'Ice premelting layer of ice-rubber friction studied using resonance shear measurement', *Soft Matter*, vol. 16, no. 37, pp. 8677–8682, 2020, doi: 10.1039/d0sm00478b.

[168] Z. Shaghayegh Bagheri, A. Anwer, G. Fernie, H. E. Naguib, and T. Dutta, 'Effects of multi-functional surface-texturing on the ice friction and abrasion characteristics of hybrid composite materials for footwear', *Wear*, vol. 418–419, no. May 2018, pp. 253–264, 2019, doi: 10.1016/j.wear.2018.11.030.

[169] E. Orgilés-Calpena, F. Arán-Ais, A. M. Torró-Palau, and C. Orgilés-Barceló, 'Novel polyurethane reactive hot melt adhesives based on polycarbonate polyols derived from CO2 for the footwear industry', *International Journal of Adhesion and Adhesives*, vol. 70, pp. 218–224, 2016, doi: 10.1016/j.ijadhadh.2016.07.009.

[170] S. Sato *et al.*, 'Dry sliding friction and Wear behavior of thermoplastic polyurethane against abrasive paper', *Biotribology*, vol. 23, no. May, p. 100130, 2020, doi: 10.1016/j.biotri.2020.100130.

[171] A. J. Tuononen, A. Kriston, and B. Persson, 'Multiscale physics of rubber-ice friction', *Journal of Chemical Physics*, vol. 145, no. 11, 2016, doi: 10.1063/1.4962576.

[172] J. M. Isomaa, A. J. Tuononen, and S. Bossuyt, 'Onset of frictional sliding in rubber-ice contact', *Cold Regions Science and Technology*, vol. 115, pp. 1–8, 2015, doi: 10.1016/j.coldregions.2015.03.003.

[173] S. Hemette, J. Cayer-Barrioz, and D. Mazuyer, 'Friction setup and real-time insights of the contact under controlled cold environment: The KŌRI tribometer for rubber-ice contact

application', *Review of Scientific Instruments*, vol. 89, no. 12, 2018, doi: 10.1063/1.5048844.

[174] M. Colonna, M. Nicotra, and M. Moncalero, 'Materials, designs and standards used in ski-boots for alpine skiing', *Sports*, vol. 1, no. 4, pp. 78–113, 2013, doi: 10.3390/sports1040078.

[175] G. Skouvaklis, J. R. Blackford, and V. Koutsos, 'Friction of rubber on ice: A new machine, influence of rubber properties and sliding parameters', *Tribology International*, vol. 49, pp. 44–52, 2012, doi: 10.1016/j.triboint.2011.12.015.

[176] T. Yamaguchi, J. Hsu, Y. Li, and B. E. Maki, 'Efficacy of a rubber outsole with a hybrid surface pattern for preventing slips on icy surfaces', *Applied Ergonomics*, vol. 51, pp. 9–17, 2015, doi: 10.1016/j.apergo.2015.04.001.

[177] Z. S. Bagheri, A. A. Anwer, G. Fernie, H. E. Naguib, and T. Dutta, *Improving Slip Resistance on Ice: Surface-Textured Composite Materials for Slip-Resistant Footwear*, vol. 819. Springer International Publishing, 2019. doi: 10.1007/978-3-319-96089-0_83.

[178] M. Colonna *et al.*, 'Ski Boot Soles Based on a Glass Fiber/Rubber Composite with Improved Grip on Icy Surfaces', *Procedia Engineering*, vol. 147, no. June 2017, pp. 372–377, 2016, doi: 10.1016/j.proeng.2016.06.316.

[179] N. Namdari, G. Joseph, G. Guo, H. Sojoudi, and R. Rizvi, 'Nanotextured surfaces with enhanced ice-traction and wear-resistance', *Composites Part B*, vol. 238, no. January, p. 109916, 2022, doi: 10.1016/j.compositesb.2022.109916.

[180] P. Hong and X. Xinqiao, 'Application of graphene and aerogel in winter running shoes products', *IOP Conference Series: Materials Science and Engineering*, vol. 573, no. 1, 2019, doi: 10.1088/1757-899X/573/1/012044.

[181] M. Dishovsky, Filis Mitkova, Yordan Angelov, 'From Renewable Resources With Improved Adhesion To Icy Surfaces', *Journal of Chemical Technology and Metallurgy*, vol. 53, no. 3, pp. 399–407, 2018.

[182] J. M. Baydal-Bertomeu, S. A. Puigcerver, J. C. González, J. Gomez, M. Perez-Fernandez, and J. R. Sempere-Tortosa, 'Nanotechnology can provide a real breakthrough in the anti-slip properties of safety footwear soles', *Footwear Science*, vol. 7, no. June 2015, pp. S58–S60, 2015, doi: 10.1080/19424280.2015.1038607.

[183] R. Rizvi, H. Naguib, G. Fernie, and T. Dutta, 'High friction on ice provided by elastomeric fiber composites with textured surfaces', *Applied Physics Letters*, vol. 106, no. 11, 2015, doi: 10.1063/1.4913676.

[184] L. Valentini, S. Bittolo Bon, N. M. Pugno, M. Hernandez Santana, M. A. Lopez-Manchado, and G. Giorgi, 'Synergistic icephobic behaviour of swollen nitrile butadiene rubber graphene and/or carbon nanotube composites', *Composites Part B: Engineering*, vol. 166, no. June, pp. 352–360, 2019, doi: 10.1016/j.compositesb.2018.11.095.

[185] L. Valentini, S. Bittolo Bon, M. Hernández, M. A. Lopez-Manchado, and N. M. Pugno, 'Nitrile butadiene rubber composites reinforced with reduced graphene oxide and carbon nanotubes show superior mechanical, electrical and icephobic properties', *Composites Science and Technology*, vol. 166, pp. 109–114, 2018, doi: 10.1016/j.compscitech.2018.01.050.

[186] G. Momen, R. Jafari, and M. Farzaneh, 'Ice repellency behaviour of superhydrophobic surfaces: Effects of atmospheric icing conditions and surface roughness', *Applied Surface Science*, vol. 349, pp. 211–218, 2015, doi: 10.1016/j.apsusc.2015.04.180.

[187] K. Mielonen *et al.*, 'Sliding friction of hierarchically micro–micro textured polymer surfaces on ice', *Cold Regions Science and Technology*, vol. 163, no. November 2018, pp. 8–18, 2019, doi: 10.1016/j.coldregions.2019.04.002.

[188] F. Melo-Fonseca, B. Guimarães, M. Gasik, F. S. Silva, and G. Miranda, 'Experimental analysis and predictive modelling of Ti6Al4V laser surface texturing for biomedical applications', *Surfaces and Interfaces*, vol. 35, no. November, p. 102466, 2022, doi: 10.1016/j.surfin.2022.102466.

[189] A. De Zanet, V. Casalegno, and M. Salvo, 'Laser surface texturing of ceramics and ceramic composite materials – A review', *Ceramics International*, vol. 47, no. 6, pp. 7307–7320, 2021, doi: 10.1016/j.ceramint.2020.11.146.

[190] N. Ackerl and K. Wegener, 'Ablation characteristics of alumina and zirconia ceramics on ultra-short pulsed laser machining', *Journal of Laser Micro Nanoengineering*, vol. 14, no. 2, pp. 168–172, 2019, doi: 10.2961/jlmn.2019.02.0009.

[191] V. Richhariya, G. Miranda, and F. S. Silva, 'An Experimental Parametric Optimisation for Laser Engraving and Texturing to Integrate Zirconia Ceramic Blocks into Stainless Steel Cutlery: A State-of-the-Art Aesthetically Improved Perspective', *Materials*, vol. 17, no. 10, Art. no. 10, Jan. 2024, doi: 10.3390/ma17102452.

[192] O. F. Biswas, A. Sen, G. Kibria, B. Doloi, and B. Bhattacharyya, 'Experimental analysis of fiber laser milling process for generating microchannel on zirconia (ZrO2)', *Materials Today: Proceedings*, vol. 18, pp. 3566–3574, 2019, doi: 10.1016/j.matpr.2019.07.287.

[193] Z. Ma, Z. Wang, X. Wang, and T. Yu, 'Effects of laser-assisted grinding on surface integrity of zirconia ceramic', *Ceramics International*, vol. 46, no. 1, pp. 921–929, 2020, doi: 10.1016/j.ceramint.2019.09.051.

[194] O. O. Daramola, I. O. Oladele, B. Omotayo, J. L. Olajide, A. S. Ogunbadejo, and P. Adeyemi, 'Tensile and hydrophilic properties of low-density polyethylene/titania composites', vol. 29, no. July, pp. 125–147, 2016.

[195] M. S. M. Rigolin *et al.*, 'Effect of the aging of titanium and zirconia abutment surfaces on the viability, adhesion, and proliferation of cells and the adhesion of microorganisms', *The Journal of Prosthetic Dentistry*, vol. 122, no. 6, p. 564.e1-564.e10, Dec. 2019, doi: 10.1016/j.prosdent.2019.08.027.

[196] J. Datta, P. Kasprzyk, and M. Włoch, 'Effect of high loading of titanium dioxide particles on the morphology, mechanical and thermo-mechanical properties of the natural rubber-based composites', *Iranian Polymer Journal*, vol. 25, Nov. 2016, doi: 10.1007/s13726-016-0488-7.

[197] N. F. Amat, A. Muchtar, H. Z. Yew, M. S. Amril, and R. L. Muhamud, 'Machinability of a newly developed pre-sintered zirconia block for dental crown applications', *Materials Letters*, vol. 261, p. 126996, 2020, doi: 10.1016/j.matlet.2019.126996.

[198] H. Huang, Z. C. Guo, W. Zhu, and F. C. Li, 'Preparation and characterization of conductive polyaniline/zirconia nanoparticles composites', *Advanced Materials Research*, vol. 221, pp. 302–307, 2011, doi: 10.4028/www.scientific.net/AMR.221.302.

[199] S. L. Sing, F. E. Wiria, and W. Y. Yeong, 'Selective laser melting of titanium alloy with 50 wt% tantalum: Effect of laser process parameters on part quality', *International Journal of Refractory Metals and Hard Materials*, vol. 77, no. July, pp. 120–127, 2018, doi: 10.1016/j.ijrmhm.2018.08.006.

[200] B. Makurat-Kasprolewicz and A. Ossowska, 'Recent advances in electrochemically surface treated titanium and its alloys for biomedical applications: A review of anodic and plasma electrolytic oxidation methods', *Materials Today Communications*, vol. 34, p. 105425, Mar. 2023, doi: 10.1016/j.mtcomm.2023.105425.

[201] L. Tiainen *et al.*, 'Novel laser surface texturing for improved primary stability of titanium implants', *Journal of the Mechanical Behavior of Biomedical Materials*, vol. 98, no. May, pp. 26–39, 2019, doi: 10.1016/j.jmbbm.2019.04.052.

[202] B. Li, K. P. Baxevanakis, and V. V. Silberschmidt, 'Water Diffusion in Additively Manufactured Polymers: Analysis of the Capillary Effect', *Micro*, vol. 4, no. 2, Art. no. 2, Jun. 2024, doi: 10.3390/micro4020017.

[203] S. C. Ambilkar *et al.*, 'Precise role of zirconia to boost up the mechanical, thermal, viscoelastic, dielectric, and chemical resistance properties of natural rubber-nitrile rubber blend', *European Polymer Journal*, vol. 194, p. 112163, Jul. 2023, doi: 10.1016/j.eurpolymj.2023.112163.

[204] D. Faria, B. Henriques, F. Silva, and O. Carvalho, 'Laser - assisted manufacturing of 45S5 Bioglass - coated zirconia structured surfaces targeting medical implants : adhesive , wettability , mechanical , and bioactivity evaluation', *The International Journal of Advanced Manufacturing Technology*, vol. 119(3), no. December, pp. 1595–1612, 2021.

[205] V. Prakash, S. Pradhan, S. K. Acharya, S. K. Pal, and S. Majhi, 'Effect of Drying Route and Sintering Temperature on Zirconia Nanoparticle Synthesis for Filler Application in Polymer Composites', *Transactions of the Indian Institute of Metals*, no. 0123456789, 2023, doi: 10.1007/s12666-022-02836-7.

[206] P. Bargavi, S. Chitra, D. Durgalakshmi, G. Radha, and S. Balakumar, 'Zirconia reinforced bio-active glass coating by spray pyrolysis: Structure, surface topography, in-vitro biological evaluation and antibacterial activities', *Materials Today Communications*, vol. 25, no. May, p. 101253, 2020, doi: 10.1016/j.mtcomm.2020.101253.

[207] J. Fröhlich, W. Niedermeier, and H. D. Luginsland, 'The effect of filler-filler and filler-elastomer interaction on rubber reinforcement', *Composites Part A: Applied Science and Manufacturing*, vol. 36, no. 4, pp. 449–460, 2005, doi: 10.1016/j.compositesa.2004.10.004.

[208] M. R. B. Mermet-Guyennet *et al.*, 'Size-dependent reinforcement of composite rubbers', *Polymer*, vol. 73, pp. 170–173, 2015, doi: 10.1016/j.polymer.2015.07.041.

[209] 'Fabrication of robust superhydrophobic surface on silicone rubber - ScienceDirect'. Accessed: Jan. 10, 2025. [Online]. Available: https://www.sciencedirect.com/science/article/pii/S0266353823004955

[210] T. Bharathidasan, S. V. Kumar, M. S. Bobji, R. P. S. Chakradhar, and B. J. Basu, 'Effect of wettability and surface roughness on ice-adhesion strength of hydrophilic, hydrophobic and superhydrophobic surfaces', *Applied Surface Science*, vol. 314, no. September, pp. 241–250, 2014, doi: 10.1016/j.apsusc.2014.06.101.

[211] B. Zhang, K. Rane, M. Piri, and L. Goual, 'Impact of surface roughness, surface charge, and temperature on sandstone wettability alteration by nanoparticles', *Petroleum Science*, vol. 20, no. 5, pp. 2852–2863, Oct. 2023, doi: 10.1016/j.petsci.2023.04.004.

[212] C. G. Jothi Prakash and R. Prasanth, 'Approaches to design a surface with tunable wettability: a review on surface properties', *J Mater Sci*, vol. 56, no. 1, pp. 108–135, Jan. 2021, doi: 10.1007/s10853-020-05116-1.

[213] G. Zhang, X. Hua, F. Li, Y. Zhang, C. Shen, and J. Cheng, 'Effect of laser cleaning process parameters on the surface roughness of 5754-grade aluminum alloy', *International Journal of Advanced Manufacturing Technology*, vol. 105, no. 5–6, pp. 2481–2490, 2019, doi: 10.1007/s00170-019-04395-6.

[214] M. Manninen, M. Hirvimäki, V. P. Matilainen, and A. Salminen, 'Comparison of laser-engraved hole properties between cold-rolled and laser additive manufactured stainless steel sheets', *Applied Sciences (Switzerland)*, vol. 7, no. 9, 2017, doi: 10.3390/app7090913.

[215] S. D. Dondieu *et al.*, 'Process Optimization for 100 W Nanosecond Pulsed Fiber Laser Engraving of 316L Grade Stainless Steel', *Journal of Manufacturing and Materials Processing*, vol. 4, no. 4, p. 110, 2020, doi: 10.3390/jmmp4040110.

[216] M. N. F. B. Haron and F. R. B. M. Romlay, 'Parametric study of laser engraving process of AISI 304 Stainless Steel by utilizing fiber laser system', *IOP Conference Series: Materials Science and Engineering*, vol. 469, no. 1, 2019, doi: 10.1088/1757-899X/469/1/012124.

[217] Y. He, C. Jiang, X. Cao, J. Chen, W. Tian, and W. Yuan, 'Reducing ice adhesion by hierarchical micro-nano-pillars', *Applied Surface Science*, vol. 305, pp. 589–595, 2014, doi: 10.1016/j.apsusc.2014.03.139.

[218] E. Nikolidakis, I. Choreftakis, and A. Antoniadis, 'Experimental investigation of stainless steel SAE304 laser engraving cutting conditions', *Machines*, vol. 6, no. 3, pp. 1–8, 2018, doi: 10.3390/MACHINES6030040.

[219] S. Pattanayak and S. Kumar Sahoo, 'Micro engraving on 316L stainless steel orthopedic implant using fiber laser', *Optical Fiber Technology*, vol. 63, no. November 2020, p. 102479, 2021, doi: 10.1016/j.yofte.2021.102479.

[220] J. Kim, M.-W. Moon, and H.-Y. Kim, 'Capillary rise in superhydrophilic rough channels', *Physics of Fluids*, vol. 32, no. 3, p. 032105, Mar. 2020, doi: 10.1063/1.5133826.

[221] J. Metelkova, Y. Kinds, K. Kempen, C. de Formanoir, A. Witvrouw, and B. Van Hooreweder, 'On the influence of laser defocusing in Selective Laser Melting of 316L', *Additive Manufacturing*, vol. 23, no. April, pp. 161–169, 2018, doi: 10.1016/j.addma.2018.08.006.

[222] M. Li, J. Xie, Q. Dai, W. Huang, and X. Wang, 'Effect of wetting case and softness on adhesion of bioinspired micropatterned surfaces', *Journal of the Mechanical Behavior of Biomedical Materials*, vol. 78, no. November 2017, pp. 266–272, 2018, doi: 10.1016/j.jmbbm.2017.11.036.

[223] K. Autumn, A. Dittmore, D. Santos, M. Spenko, and M. Cutkosky, 'Frictional adhesion: A new angle on gecko attachment', *Journal of Experimental Biology*, vol. 209, no. 18, pp. 3569–3579, 2006, doi: 10.1242/jeb.02486.

[224] S. B. EMERSON and D. DIEHL, 'Toe pad morphology and mechanisms of sticking in frogs', *Biological Journal of the Linnean Society*, vol. 13, no. 3, pp. 199–216, 1980, doi: 10.1111/j.1095-8312.1980.tb00082.x.

[225] I. Scholz, W. Barnes, J. Smith, and W. Baumgartner, 'Ultrastructure and physical properties of an adhesive surface, the toe pad epithelium of the tree frog, Litoria caerulea White', *The Journal of experimental biology*, vol. 212, pp. 155–62, Feb. 2009, doi: 10.1242/jeb.019232.

[226] K. Autumn *et al.*, 'Evidence for van der Waals adhesion in gecko setae', *Proceedings of the National Academy of Sciences of the United States of America*, vol. 99, no. 19, pp. 12252–12256, 2002, doi: 10.1073/pnas.192252799.

[227] S. Terashima, A. Ochi, J. Sato, M. Suzuki, T. Takahashi, and S. Aoyagi, 'Proposal of a three-stage hair structure imitating the sole of gecko foot and its fabrication by UV nanoimprinting', *Precision Engineering*, vol. 67, pp. 359–369, 2021, doi: 10.1016/j.precisioneng.2020.10.005.

[228] T. Gamble, 'Duplications in Corneous Beta Protein Genes and the Evolution of Gecko Adhesion', *Integrative and Comparative Biology*, vol. 59, no. 1, pp. 193–202, 2019, doi: 10.1093/icb/icz010.

[229] Y. Tian, J. Wan, N. Pesika, and M. Zhou, 'Bridging nanocontacts to macroscale gecko adhesion by sliding soft lamellar skin supported setal array', *Scientific Reports*, vol. 3, no. 1382, pp. 1–6, 2013, doi: 10.1038/srep01382.

[230] N. S. Pesika *et al.*, 'The crowding model as a tool to understand and fabricate gecko-inspired dry adhesives', *Journal of Adhesion*, vol. 85, no. 8, pp. 512–525, 2009, doi: 10.1080/00218460902996390.

[231] W. J. P. Barnes, M. Baum, H. Peisker, and S. N. Gorb, 'Comparative Cryo-SEM and AFM studies of hylid and rhacophorid tree frog toe pads', *Journal of Morphology*, vol. 274, no. 12, pp. 1384–1396, 2013, doi: 10.1002/jmor.20186.

[232] L. Alibardi, 'Review: mapping proteins localized in adhesive setae of the tokay gecko and their possible influence on the mechanism of adhesion', *Protoplasma*, vol. 255, no. 6, pp. 1785–1797, 2018, doi: 10.1007/s00709-018-1270-9.

[233] A. Anwer, Z. S. Bagheri, G. Fernie, T. Dutta, and H. E. Naguib, 'Evolution of the Coefficient of Friction with Surface Wear for Advanced Surface Textured Composites', *Advanced Materials Interfaces*, vol. 4, no. 6, pp. 1–11, 2017, doi: 10.1002/admi.201600983.

[234] G. Wen, Z. Guo, and W. Liu, 'Biomimetic polymeric superhydrophobic surfaces and nanostructures: From fabrication to applications', *Nanoscale*, vol. 9, no. 10, pp. 3338–3366, 2017, doi: 10.1039/c7nr00096k.

[235] N. Wang, J. Y. H. Fuh, S. T. Dheen, and A. Senthil Kumar, 'Functions and applications of metallic and metallic oxide nanoparticles in orthopedic implants and scaffolds', *Journal of Biomedical Materials Research Part B: Applied Biomaterials*, vol. 109, no. 2, pp. 160–179, 2021, doi: 10.1002/jbm.b.34688.

[236] J. Chen, J. Liu, Y. Yao, and S. Chen, 'Effect of microstructural damage on the mechanical properties of silica nanoparticle-reinforced silicone rubber composites', *Engineering Fracture Mechanics*, vol. 235, no. March, p. 107195, 2020, doi: 10.1016/j.engfracmech.2020.107195.

[237] S. Punj, J. Singh, and K. Singh, 'Ceramic biomaterials: Properties, state of the art and future prospectives', *Ceramics International*, vol. 47, no. 20, pp. 28059–28074, Oct. 2021, doi: 10.1016/j.ceramint.2021.06.238.

[238] A. L. Nikolaeva *et al.*, 'Metal Oxide Nanoparticles: An Effective Tool to Modify the Functional Properties of Thermally Stable Polyimide Films', *Polymers*, vol. 14, no. 13, Art. no. 13, Jan. 2022, doi: 10.3390/polym14132580.

[239] S. Mathew Simon *et al.*, 'Recent advancements in multifunctional applications of sol-gel derived polymer incorporated TiO2-ZrO2 composite coatings: A comprehensive review', *Applied Surface Science Advances*, vol. 6, p. 100173, Dec. 2021, doi: 10.1016/j.apsadv.2021.100173.

[240] A. S. Nobrega, A. M. Andreotti, A. Moreno, M. A. C. Sinhoreti, D. M. dos Santos, and M. C. Goiato, 'Influence of adding nanoparticles on the hardness, tear strength, and permanent deformation of facial silicone subjected to accelerated aging', *The Journal of Prosthetic Dentistry*, vol. 116, no. 4, pp. 623-629.e1, Oct. 2016, doi: 10.1016/j.prosdent.2016.03.004.

[241] P. F. Ibáñez-Ibáñez, F. J. Montes Ruiz-Cabello, M. A. Cabrerizo-Vílchez, and M. A. Rodríguez-Valverde, 'Ice adhesion of PDMS surfaces with balanced elastic and water-repellent properties', *Journal of Colloid and Interface Science*, vol. 608, pp. 792–799, 2022, doi: 10.1016/j.jcis.2021.10.005.

[242] X. Zhu and W. Li, 'Research on Dynamic Compression Testing of Silicone Rubber under Different Temperatures', *Journal of Physics: Conference Series*, vol. 2002, no. 1, 2021, doi: 10.1088/1742-6596/2002/1/012047.

[243] X. Zhu, Y. Zhou, Y. Zhang, L. Zhou, and X. Huang, 'The Effects of Nano-ZrO_2 on the Mechanical and Electrical Properties of Silicone Rubber and a Corresponding Mechanism Analysis', *IEEE Transactions on Dielectrics and Electrical Insulation*, vol. 29, no. 6, pp. 2218–2226, 2022, doi: 10.1109/TDEI.2022.3203373.

[244] J. Srinivas, K. R. Karthikeyan, T. S. Senthil, K. Yesuraj, K. S. J. Aultrin, and T. S. Senthil, 'Characterization of Mechanical and Viscoelastic Properties of Ceramic Nanoparticle-Reinforced Polymer Composites', *jopc*, vol. 13, no. 01, p. 71} – 82, Oct. 2024.

[245] N. Mohamad *et al.*, 'Mechanical and morphological properties of polypropylene/epoxidized natural rubber blends at various mixing ratio', *Procedia Engineering*, vol. 68, pp. 439–445, 2013, doi: 10.1016/j.proeng.2013.12.204.

[246] C. Cazan, A. Enesca, and L. Andronic, 'Synergic Effect of TiO2 Filler on the Mechanical Properties of Polymer Nanocomposites', *Polymers*, vol. 13, no. 12, Art. no. 12, Jan. 2021, doi: 10.3390/polym13122017.

[247] K. Li, H. Kou, J. Rao, C. Liu, and C. Ning, 'Fabrication of enamel-like structure on polymer-infiltrated zirconia ceramics', *Dental Materials*, vol. 37, no. 4, pp. e245–e255, Apr. 2021, doi: 10.1016/j.dental.2021.01.002.

[248] R. B. Heimann, 'Bioceramics: An Overview', in *Silicon Nitride Bioceramics*, B. S. Bal, B. J. McEntire, and G. Pezzotti, Eds., Cham: Springer International Publishing, 2024, pp. 1–25. doi: 10.1007/978-3-031-67047-3_1.

[249] E. w. Awin, K. c. h. Kumar, S. Bernard, and R. Kumar, 'Mechanical characterization of spark plasma sintered titania-silicon oxycarbide (TiO2/SiOC) nanocomposites', *Materialwissenschaft und Werkstofftechnik*, vol. 53, no. 2, pp. 235–243, 2022, doi: 10.1002/mawe.202100010.

[250] S. Tang, J. Zhang, P. Ma, and Z. Zhang, 'Effect of ultraviolet treatment on soft tissue healing and bacterial attachment to titania-coated zirconia', *Biomed. Mater.*, vol. 20, no. 1, p. 015003, Nov. 2024, doi: 10.1088/1748-605X/ad8827.

[251] M. Wu, L. Chang, L. Zhang, X. He, and X. Qu, 'Effects of roughness on the wettability of high temperature wetting system', *Surface and Coatings Technology*, vol. 287, pp. 145–152, Feb. 2016, doi: 10.1016/j.surfcoat.2015.12.092.

[252] S. Hemette, J. Cayer-Barrioz, and D. Mazuyer, 'Thermal effects versus viscoelasticity in ice-rubber friction mechanisms', *Tribology International*, vol. 162, no. February, p. 107129, 2021, doi: 10.1016/j.triboint.2021.107129.

[253] C. Zhan *et al.*, 'Thermal conductivity and compressive strength of silicone rubber composites enhanced by aligned carbon nanofiber scaffold', *Polymer Composites*, vol. 43, no. 8, pp. 5291–5300, 2022, doi: 10.1002/pc.26827.

[254] Z. X. Zhang, X. R. Dai, L. Zou, S. B. Wen, T. K. Sinha, and H. Li, 'A developed, eco-friendly, and flexible thermoplastic elastomeric foam from sebs for footwear application', *Express Polymer Letters*, vol. 13, no. 11, pp. 948–958, 2019, doi: 10.3144/expresspolymlett.2019.83.

[255] K. Parvathi, M. A. Al-Maghrabi, M. Subburaj, and M. T. Ramesan, 'Natural rubber and copper alumina nanocomposite-based flexible elastomer-inorganic hybrid systems', *Polymer Composites*, vol. 42, no. 9, pp. 4586–4595, 2021, doi: 10.1002/pc.26170.

[256] X. Zhou, Y. Zhang, X. Shi, and D. Fan, 'Preparation, Characterization, and Preliminary Biocompatibility Evaluation of Carbon Ion-Implanted Silicone Rubber', 2017. doi: 10.5772/intechopen.69251.

[257] M. Zhao, Y. Yin, Q. He, and X. Zhao, 'Anti-icing capability of textured silicone rubber surfaces via laser processing', *Materials and Manufacturing Processes*, vol. 36, no. 8, pp. 979–986, Jun. 2021, doi: 10.1080/10426914.2021.1885697.

[258] O. S. Dahham *et al.*, 'The Influences of Zirconium Dioxide on ENR-25/ZrO2 Composites: FTIR and TGA Analysis', *Journal of Physics: Conference Series*, vol. 1019, no. 1, 2018, doi: 10.1088/1742-6596/1019/1/012055.

[259] S. Liu, F. Fang, J. Wu, and K. Zhang, 'The anti-biofouling properties of thin-film composite nanofiltration membranes grafted with biogenic silver nanoparticles', *Desalination*, vol. 375, pp. 121–128, 2015, doi: 10.1016/j.desal.2015.08.007.

[260] H. Guo *et al.*, 'Universal Intraductal Surface Antifouling Coating Based on an Amphiphilic Copolymer', *ACS Applied Materials and Interfaces*, vol. 13, no. 18, pp. 21051–21059, 2021, doi: 10.1021/acsami.1c04579.

[261] V. Richhariya, A. Tripathy, O. Carvalho, J. Gomes, M. J. Nine, and F. S. Silva, 'Capillary-Enhanced Biomimetic Adhesion on Icy Surfaces for High-Performance Antislip Shoe-Soles', *ACS Appl. Mater. Interfaces*, vol. 17, no. 1, pp. 1–12, Dec. 2024, doi: 10.1021/acsami.4c14496.

[262] I. Sanaullah *et al.*, 'Tangerine mediated synthesis of zirconia as potential protective dental coatings', *Materials Science and Engineering C*, no. February 2018, p. 111653, 2020, doi: 10.1016/j.msec.2020.111653.

[263] Y. Zeng *et al.*, 'Structural, dielectric and mechanical behaviors of (La, Nb) Co-doped TiO2/Silicone rubber composites', *Ceramics International*, vol. 47, no. 16, pp. 22365–22372, 2021, doi: 10.1016/j.ceramint.2021.04.245.

[264] X. Bai, Y. Zhang, H. Wang, H. Zhang, and J. Liu, 'Study on the modification of positively charged composite nanofiltration membrane by TiO2 nanoparticles', *Desalination*, vol. 313, pp. 57–65, Mar. 2013, doi: 10.1016/j.desal.2012.12.006.

[265] W. Zhang, X. Lu, Z. Xin, and C. Zhou, 'Development of a superhydrophobic polybenzoxazine surface with self-cleaning and reversible water adhesion properties', *RSC Advances*, vol. 6, no. 108, pp. 106054–106063, 2016, doi: 10.1039/C6RA22524A.

[266] L. Velardi, L. Scrimieri, A. Serra, D. Manno, and L. Calcagnile, 'Effect of temperature on the physical, optical and photocatalytic properties of TiO2 nanoparticles', *SN Appl. Sci.*, vol. 2, no. 4, p. 707, Mar. 2020, doi: 10.1007/s42452-020-2544-3.

[267] Z. N. Jameel, A. Haider, and Y. Taha, *Synthesis of TiO2 Nanoparticles by Using Sol-Gel Method and its Applications as Antibacterial Agents*. 2013.

[268] G. Zhou, P. Jin, Y. Wang, G. Pei, J. Wu, and Z. Wang, 'X-ray diffraction analysis of the yttria stabilized zirconia powder by mechanical alloying and sintering', *Ceramics International*, vol. 46, no. 7, pp. 9691–9697, May 2020, doi: 10.1016/j.ceramint.2019.12.236.

[269] D. Manoharan, A. Loganathan, k Vishista, and V. Nesamony, 'Unique sharp photoluminescence of size-controlled sonochemically synthesized zirconia nanoparticles', *Ultrasonics sonochemistry*, vol. 23, pp. 174–84, Mar. 2015, doi: 10.1016/j.ultsonch.2014.10.004.

[270] A. Zolriasatein, S. Navazani, M. R. Abadchi, and N. R. Noori, 'Two-component room temperature vulcanized silicone-rubber (RTV2) properties modification: effect of aluminum three hydrate and nanosilica additions on the microstructure, electrical, and mechanical properties', *Journal of Materials Science: Materials in Electronics*, vol. 32, no. 7, pp. 8903–8915, 2021, doi: 10.1007/s10854-021-05562-w.

[271] X. Shi, P.-A. Albouy, and P. Launois, 'Strain-induced changes of the X-ray diffraction patterns of cross-linked Poly(dimethylsiloxane): The texture hypothesis', *Polymer*, vol. 247, p. 124760, Apr. 2022, doi: 10.1016/j.polymer.2022.124760.

[272] M. Kumaresan, K. Vijai Anand, K. Govindaraju, S. Tamilselvan, and V. Ganesh Kumar, 'Seaweed Sargassum wightii mediated preparation of zirconia (ZrO 2) nanoparticles and their antibacterial activity against gram positive and gram negative bacteria', *Microbial Pathogenesis*, vol. 124, no. August, pp. 311–315, 2018, doi: 10.1016/j.micpath.2018.08.060.

[273] A. Zore *et al.*, 'Antibacterial Effect of Polymethyl Methacrylate Resin Base Containing TiO2 Nanoparticles', *Coatings*, vol. 12, no. 11, Art. no. 11, Nov. 2022, doi: 10.3390/coatings12111757.

[274] W. Ahmed, Z. Zhai, and C. Gao, 'Adaptive antibacterial biomaterial surfaces and their applications', *Materials Today Bio*, vol. 2, p. 100017, Mar. 2019, doi: 10.1016/j.mtbio.2019.100017.

[275] Y. Chen, Y. Gao, Y. Chen, L. Liu, A. Mo, and Q. Peng, 'Nanomaterials-based photothermal therapy and its potentials in antibacterial treatment', *Journal of Controlled Release*, vol. 328, pp. 251–262, Dec. 2020, doi: 10.1016/j.jconrel.2020.08.055.

[276] A. Mostafaei and F. Nasirpouri, 'Preparation and characterization of a novel conducting nanocomposite blended with epoxy coating for antifouling and antibacterial applications', *J Coat Technol Res*, vol. 10, no. 5, pp. 679–694, Sep. 2013, doi: 10.1007/s11998-013-9487-1.

[277] V. K. Truong, M. Al Kobaisi, K. Vasilev, D. Cozzolino, and J. Chapman, 'Current perspectives for engineering antimicrobial nanostructured materials', *Current Opinion in Biomedical Engineering*, vol. 23, p. 100399, Sep. 2022, doi: 10.1016/j.cobme.2022.100399.

[278] K. Schwibbert, A. M. Richter, J. Krüger, and J. Bonse, 'Laser-Textured Surfaces: A Way to Control Biofilm Formation?', *Laser & Photonics Reviews*, vol. 18, no. 1, p. 2300753, 2024, doi: 10.1002/lpor.202300753.

[279] F. Rodrigues *et al.*, 'Zirconia Dental Implants Surface Electric Stimulation Impact on Staphylococcus aureus', *International Journal of Molecular Sciences*, vol. 25, p. 5719, May 2024, doi: 10.3390/ijms25115719.

[280] Y. F. Makableh, N. F. Momani, T. Athamneh, R. Al-Abed, and I. Alshorman, 'Enhanced synergic effect of the antibacterial activity and hydrophobicity of polydimethylsiloxane polymer loaded with titanium dioxide nanoparticles and ciprofloxacin', *Polym. Bull.*, vol. 80, no. 4, pp. 3703–3715, Apr. 2023, doi: 10.1007/s00289-022-04226-x.

[281] 'Antibacterial Properties and Biocompatibility of Multicomponent Titanium Oxides: A Review - PMC'. Accessed: Jan. 10, 2025. [Online]. Available: https://pmc.ncbi.nlm.nih.gov/articles/PMC11642476/

[282] 'Influence of TiO2 and ZrO2 Nanoparticles on Adhesive Bond Strength and Viscosity of Dentin Polymer: A Physical and Chemical Evaluation'. Accessed: Jan. 10, 2025. [Online]. Available: https://www.mdpi.com/2073-4360/13/21/3794

[283] 'An overview of surface with controllable wettability for microfluidic system, intelligent cleaning, water harvesting, and surface protection | Advanced Composites and Hybrid Materials'. Accessed: Jan. 10, 2025. [Online]. Available: https://link.springer.com/article/10.1007/s42114-022-00603-2

[284] Y. Jiao *et al.*, 'Femtosecond laser-induced shape memory polymer micropillar with tunable wettability and reversible adhesion for underwater oil droplet lossless transfer', *Applied Physics Letters*, vol. 118, no. 3, p. 033701, Jan. 2021, doi: 10.1063/5.0040990.

[285] M. Aliofkhazraei, *Wetting and Wettability*. BoD – Books on Demand, 2015.

[286] S. Al-Amshawee, M. Y. B. M. Yunus, J. G. Lynam, W. H. Lee, F. Dai, and I. H. Dakhil, 'Roughness and wettability of biofilm carriers: A systematic review', *Environmental Technology & Innovation*, vol. 21, p. 101233, Feb. 2021, doi: 10.1016/j.eti.2020.101233.

[287] M. I. Jamil, A. Ali, F. Haq, Q. Zhang, X. Zhan, and F. Chen, 'Icephobic Strategies and Materials with Superwettability: Design Principles and Mechanism', *Langmuir*, vol. 34, no. 50, pp. 15425–15444, 2018, doi: 10.1021/acs.langmuir.8b03276.

[288] T. Aziz, M. Waters, and R. Jagger, 'Surface modification of an experimental silicone rubber maxillofacial material to improve wettability', *Journal of Dentistry*, vol. 31, no. 3, pp. 213–216, 2003, doi: 10.1016/S03005712(02)00131-8.

[289] 'The Influence of Surface Modification on Bacterial Adhesion to Titanium-Based Substrates | ACS Applied Materials & Interfaces'. Accessed: Jun. 03, 2024. [Online]. Available: https://pubs.acs.org/doi/full/10.1021/am507148n

[290] A. Keykhosravi, M. B. Vanani, and C. Aghayari, 'TiO2 nanoparticle-induced Xanthan Gum Polymer for EOR: Assessing the underlying mechanisms in oil-wet carbonates', *Journal of Petroleum Science and Engineering*, vol. 204, p. 108756, Sep. 2021, doi: 10.1016/j.petrol.2021.108756.

[291] K. L. Mittal, *Advances in contact angle, wettability and adhesion*. 2015.

[292] R. Artikboeva, M. Yang, Y. Wu, C. Jie, and Q. Heng, 'Preparation and Application of the Hydrophilic Amino-Silicone Softener by Emulsion Polymerization', *Advances in Chemical Engineering and Science*, vol. 10, no. 01, pp. 1–23, 2020, doi: 10.4236/aces.2020.101001.

[293] F. Xie, J. Yang, and C. V. Ngo, 'The effect of femtosecond laser fluence and pitches between V-shaped microgrooves on the dynamics of capillary flow', *Results in Physics*, vol. 19, no. November, p. 103606, 2020, doi: 10.1016/j.rinp.2020.103606.

[294] J. Cai, Y. Chen, Y. Liu, S. Li, and C. Sun, 'Capillary imbibition and flow of wetting liquid in irregular capillaries: A 100-year review', *Advances in Colloid and Interface Science*, vol. 304, no. March, p. 102654, 2022, doi: 10.1016/j.cis.2022.102654.

[295] 'Knudsen diffusion differs from Fickian diffusion | Physics of Fluids | AIP Publishing'. Accessed: Jan. 10, 2025. [Online]. Available: https://pubs.aip.org/aip/pof/article/33/4/042009/1064181

[296] 'Fick's Law Algorithm: A physical law-based algorithm for numerical optimization - ScienceDirect'. Accessed: Jan. 10, 2025. [Online]. Available: https://www.sciencedirect.com/science/article/pii/S0950705122012424

[297] K. M. Graczyk, D. Strzelczyk, and M. Matyka, 'Deep learning for diffusion in porous media | Scientific Reports', *Scientific Reports, Nature*, vol. 9769, no. 13, Jun. 2023, doi: 0.1038/s41598-023-36466-w.

[298] 'Dynamic Effects during the Capillary Rise of Fluids in Cylindrical Tubes | Langmuir'. Accessed: Jan. 10, 2025. [Online]. Available: https://pubs.acs.org/doi/full/10.1021/acs.langmuir.1c02680

[299] Y. Shiri and S. M. J. Seyed Sabour, 'Analytical, experimental, and numerical study of capillary rise dynamics from inertial to viscous flow', *Physics of Fluids*, vol. 34, no. 10, p. 102105, Oct. 2022, doi: 10.1063/5.0111688.

[300] A. Chaudhuri, V. Arya, C. Bakli, and S. Chakraborty, 'Capillary filling dynamics in closed-end carbon nanotubes—Defying the classical Lucas–Washburn paradigm', *The Journal of Chemical Physics*, vol. 161, no. 18, p. 184702, Nov. 2024, doi: 10.1063/5.0237885.

[301] P. Renvoisé, J. W. M. Bush, M. Prakash, and D. Quéré, 'Drop propulsion in tapered tubes', *EPL*, vol. 86, no. 6, p. 64003, Jul. 2009, doi: 10.1209/0295-5075/86/64003.

[302] D. Langbein, and K. Ruschak, *Capillary Surfaces: Shape, Stability, Dynamics, in Particular Under Weightlessness. Tracts in Modern Physics, Vol 178*, vol. 56, no. 1. 2003. doi: 10.1115/1.1523364.

[303] 'Lucas–Washburn Equation-Based Modeling of Capillary-Driven Flow in Porous Systems | Langmuir'. Accessed: Jan. 10, 2025. [Online]. Available: https://pubs.acs.org/doi/full/10.1021/acs.langmuir.0c03134

[304] J. Berthier and K. A. Brakke, *The Physics of Microdroplets*. 2012. doi: 10.1002/9781118401323.

[305] J. B. Gorce, I. J. Hewitt, and D. Vella, 'Capillary Imbibition into Converging Tubes: Beating Washburn's Law and the Optimal Imbibition of Liquids', *Langmuir*, vol. 32, no. 6, pp. 1560–1567, 2016, doi: 10.1021/acs.langmuir.5b04495.

[306] N. Fries and M. Dreyer, 'The transition from inertial to viscous flow in capillary rise', *Journal of Colloid and Interface Science*, vol. 327, no. 1, pp. 125–128, 2008, doi: 10.1016/j.jcis.2008.08.018.

[307] A. Salama, J. Kou, A. Alyan, and M. M. Husein, 'Capillary-Driven Ejection of a Droplet from a Micropore into a Channel: A Theoretical Model and a Computational Fluid Dynamics Verification', *Langmuir*, vol. 38, no. 14, pp. 4461–4472, 2022, doi: 10.1021/acs.langmuir.2c00426.

[308] D. P. Manning, C. Jones, F. J. Rowland, and M. Roff, 'The Surface Roughness of a Rubber Soling Material Determines the Coefficient of Friction on Water-Lubricated Surfaces', *Journal of Safety Research*, vol. 29, no. 4, pp. 275–283, Dec. 1998, doi: 10.1016/S0022-4375(98)00053-X.

[309] s Xu, S. De, M. Khaleghian, and A. Emami, 'Comparative tribological and drainage performance of additively manufactured outsoles tread designs', *Friction*, Oct. 2024, doi: 10.26599/FRICT.2025.9441024.

[310] K. Shibata, A. Ohnishi, S. Asahina, and T. Yamaguchi, 'Slip-resistance of rubbers and polymer fibers as shoe sole on dry and wet ice surfaces - ScienceDirect', *Tribology International*, vol. 198, no. October 2024, pp. 1–10, doi: 10.1016/j.triboint.2024.109867.

[311] A. Ishizako, T. Nishi, and T. Yamaguchi, 'Effect of orientation and hardness of rubber tread block on the friction coefficient under glycerol lubrication and its underlying mechanisms', *Tribology International*, vol. 198, p. 109904, Oct. 2024, doi: 10.1016/j.triboint.2024.109904.

[312] R. J. Elkington, J. L. Armitage, T. Khan, and M. G. Bryant, 'Sticky feet: a tribological study of climbing shoe rubber', *Sports Eng*, vol. 27, no. 2, p. 30, Sep. 2024, doi: 10.1007/s12283-024-00474-4.

[313] S. Gupta, D. Sharma, Rohan Singla, and Arnab Chanda, 'Frictional Performance of Geometrically Modified Footwear Outsoles with Obliquely Oriented Tread Patterns', *IISE Transactions on Occupational Ergonomics and Human Factors*, vol. 12, no. 4, Nov. 2024, Accessed: Jan. 10, 2025. [Online]. Available: 10.1080/24725838.2024.2430199

[314] L. Jakobsen, T. Bagehorn, I. M. Sivebaek, and F. G. Lysdal, 'Comparison of mechanical friction evaluations from occupational footwear certified as slip resistant', *Proceedings of the Institution of Mechanical Engineers, Part J: Journal of Engineering Tribology*, vol. 238, no. 7, pp. 848–859, Jul. 2024, doi: 10.1177/13506501241234981.

[315] I.-J. Kim, 'Surface Engineering for Safer Walking Environments: Optimising Floor Coatings for Enhanced Slip Resistance', *Results in Engineering*, p. 103987, Jan. 2025, doi: 10.1016/j.rineng.2025.103987.

[316] Z. S. Bagheri, N. Patel, Y. Li, K. Morrone, G. Fernie, and T. Dutta, 'Slip resistance and wearability of safety footwear used on icy surfaces for outdoor municipal workers', *Work*, vol. 62, no. 1, pp. 37–47, 2019, doi: 10.3233/WOR-182840.

[317] T. Yamaguchi *et al.*, 'Development of new footwear sole surface pattern for prevention of slip-related falls', *Safety Science*, vol. 50, no. 4, pp. 986–994, Apr. 2012, doi: 10.1016/j.ssci.2011.12.017.

[318] L. Liu, K. W. Li, Y.-H. Lee, C. C. Chen, and C.-Y. Chen, 'Friction measurements on "anti-slip" floors under shoe sole, contamination, and inclination conditions', *Safety Science*, vol. 48, no. 10, pp. 1321–1326, Dec. 2010, doi: 10.1016/j.ssci.2010.04.014.

[319] T. Nishi, T. Yamaguchi, and K. Hokkirigawa, 'Development of high slip-resistant footwear outsole using rubber surface filled with activated carbon/sodium chloride', *Sci Rep*, vol. 12, no. 1, p. 267, Jan. 2022, doi: 10.1038/s41598-021-04102-0.

[320] J. R. Blackford, G. Skouvaklis, M. Purser, and V. Koutsos, 'Friction on ice: Stick and slip', *Faraday Discussions*, vol. 156, pp. 243–254, 2012, doi: 10.1039/c2fd00128d.

[321] E. Lozowski, K. Szilder, and L. Poirier, 'A Bobsleigh Ice Friction Model', *Proceedings of the International Offshore and Polar Engineering Conference*, vol. 24, pp. 1259–1267, Jan. 2013.

[322] M. Irbe, K. A. Gross, J. Viba, and M. Cerpinska, 'Unveiling ice friction and aerodynamic drag at the initial stage of sliding on ice: Faster sliding in winter sports', *Tribology International*, vol. 160, no. February, p. 106967, 2021, doi: 10.1016/j.triboint.2021.106967.

[323] L. Jakobsen, 'Elastomer Friction –Fundamental and Footwear Research', Thesis, Technical University of Denmark, Denmark, 2023. [Online]. Available: www.construct.dtu.dk